TECHNICAL MEMORANDUM

NUREG/CR-2490
ANL-CT-81-17

(Distribution Codes:
RI and XA)

ARGONNE NATIONAL LABORATORY
9700 South Cass Avenue
Argonne, Illinois 60439

HAZARDS TO NUCLEAR POWER PLANTS FROM LARGE LIQUEFIED NATURAL GAS (LNG) SPILLS ON WATER

by

C. A. Kot, T. V. Eichler,*+ A. H. Wiedermann,*+
R. Pape,* and M. G. Srinivasan

Components Technology Division

Manuscript Completed: March 1981

Date Published: November 1981

Prepared for

Division of Risk Analysis
Office of Nuclear Regulatory Research
U. S. Nuclear Regulatory Commission
Washington, D. C. 20555
under Interagency Agreement DOE 40-550-75

NRC FIN No. A2072

*Staff of IIT Research Institute, Chicago, Illinois
+Currently affiliated with ATResearch Associates, Glen Ellyn, Illinois

ABSTRACT

The hazards to nuclear power plants arising from large spills of liquefied natural gas (LNG) on water transportation routes are treated by deterministic analytical procedures. Global models, which address the salient features of the LNG spill phenomena are used in the analysis. A coupled computational model for the combined LNG spill, spreading, and fire scenario is developed. To predict the air blast environment in the vicinity of vapor clouds with "pancake-like" geometries, a scalable procedure using both analytical methods and hydrocode calculations is synthesized. Simple response criteria from the fire and weapons effects literature are used to characterize the susceptibility of safety-related power plant systems. The vulnerability of these systems is established either by direct comparison between the LNG threat and the susceptibility criteria or through simple response calculations.

The analysis and results indicate that the spreading of LNG vapor clouds up to the lower flammability limit is dominated by gravitational effects. Severe fire and blast hazards occur only at locations directly engulfed by the LNG vapor cloud or in its immediate vicinity. Thermal loads resulting from an LNG fire are of short duration and can in general be tolerated by the safety-related power plant systems and components. On the other hand, blast loads from LNG vapor cloud explosions can cause severe damage to those systems. The safety standoff distance between the power plant site and the LNG spill location is primarily dependent on the wind-induced LNG vapor cloud drift. Under strong wind conditions (8.96 m/s) it is estimated, that severe effects on the power plant may be experienced at distances in excess of 10 km in the down wind direction. To reach a no damage level under these adverse conditions a standoff distance of approximately 15 km may be required.

NRC FIN No.	Title
A2072	Hazards to Nuclear Power Plants from Large Liquefied Natural Gas (LNG) Spills on Water Transportation Routes

PREFACE

This report presents the results of an investigation conducted for the U. S. Nuclear Regulatory Commission (NRC), Office of Nuclear Regulatory Research, Division of Risk Analysis. The work was performed under a Standard Order for DOE Work (FIN No. A 2072) with Dr. N. A. Eisenberg, NRC serving as project monitor. His helpful suggestions and reviews are gratefully acknowledged. The work reported herein was a joint effort of the Argonne National Laboratory (ANL) and the IIT Research Institute of Chicago, Illinois.

C. A. Kot, Manager
Structural Systems Analysis Section
Components Technology Division
Argonne National Laboratory
November 1981

TABLE OF CONTENTS

TABLE OF CONTENTS (Cont'd)

LIST OF FIGURES

LIST OF TABLES

Executive Summary

The prime objective of this investigation is to define the hazards to nuclear power plants arising from large LNG spills on water transportation routes. The emphasis is on how the spill environment could affect safety-related systems which are necessary for a safe shutdown of the plant and for subsequent heat removal. Motivation for such a study exists because a sizable number of nuclear power plants are located along navigable waterways. At the same time, some movement of LNG already exists in the costal waters, and this traffic may be expected to increase. Further the shipments of LNG are very large (of the order of 10^5 m^3) and contain immense amount of energy. Hence, the consequences of a massive spill could indeed be catastrophic. A secondary aim of the effort is to provide technical information which will assist the U.S. NRC in formulating guidelines concerning the siting and operation of nuclear power plants as they relate to the threats posed by possible LNG spills on water transportation routes. To achieve these objectives, the scope of this program consists of two major tasks: (1) definition of the LNG spill phenomenology and quantification of the arising threats and (2) assessment of the nuclear power plant susceptibility and vulnerability to the possible threats.

The study was not intended as a major research effort. Rather a synthesis and critical evaluation of existing data, methodologies, and predictive techniques primarily used to obtain estimates of the LNG spill environment and to define were the vulnerabilities of nuclear power plant systems. Since the existing information defining the LNG spill and spreading phenomenology on water was
too disparate and conflicting some developmental work had to be undertaken in this area and the major portion of the program effort was directed towards accomplishing this task.

A global approach, which defines only the most salient features of the phenomenology, but still permits reasonable estimates of the expected threats, has been used in this study. The study is completely deterministic and probabilistic estimates of the hazards are not made. In the vulnerability analysis, simple susceptibility criteria are used for the various plant systems and components. Most of the blast-response vulnerabilities are established by comparing overpressure criteria for various plant systems with the blast environment. Simple calculations are carried out to define the thermal response. In the accident scenario it is assumed that the entire contents of one LNG shipping container, i.e., 25 x 10^3 m^3, are spilled. Ignition is assumed to be possible during all stages of spill development.

The analysis outlined in this report permits an overall description of the phenomena associated with a large spill of LNG on water. A major achievement is the development of a combined LNG spill, spreading, and fire model. This approach permits the simultaneous and coupled computation of all the major aspects of an LNG fire. A tool is thus available to carry out detailed analyses of the fire threat for any postulated scenario and specific power-plant arrangements and sites. Another important result of the analysis effort is the development of an approach for the prediction of air blast in the vicinity of an exploding "pancake-like" vapor cloud. While the method is approximate, the results are scalable with cloud height and therefore are applicable to a broad class of problems. It is believed that those predictions are a better approximation of the air blast field in the vicinity of the vapor cloud than those obtained from TNT equivalency considerations.

Based on the analyses, it is found that the thermal loads resulting from a large LNG fire on water can in general be tolerated by the important safety-related plant systems. This is primarily due to the short durations of the expected fires. On the other hand, it is shown that nuclear power plant systems are very vulnerable to blast effects from an exploding LNG vapor cloud. It is also concluded that all serious effects are limited to the immediate vicinity of the fire/explosion source, i.e., the LNG vapor cloud. Because of this, the standoff distance, i.e., the distance from the LNG spill location, which is required to ensure the safety of the important nuclear power plant systems, is primarily dependent on the wind-induced vapor cloud drift. Under certain atmospheric conditions, i.e., high wind velocities and air humidities, the cloud may drift a long distance in the down wind direction before the LFL is reached. Thus to avoid severe hazards, stand off distances in excess of 10 km are required.

Since nuclear power plants are only affected by the hazards from an LNG spill when the vapor cloud is directly on the plant site or in its close vicinity, safety measures may be taken to mitigate at least some of the hazardous effects. The most obvious is a warning system that will make the operating personnel aware of the impending danger. This can be followed by plant isolation, i.e., closing of all dampers, doors, etc., and elimination of possible ignition sources. The latter requires plant shutdown and the deenergizing of all unnecessary power sources and electrical equipment. Isolation of the plant from the exterior should be quite effective against fire hazards, but will not provide significant protection against air blast overpressure. Such protection can only be achieved by hardening the vital plant systems. The most fragile safety-related system at a typical plant

site appears to be the off-site power supply. It therefore is a prime candidate for blast hardening.

The conclusions of the current study are based on a purely deterministic analysis. Thus, worst-case assumptions are often made, and no consideration is given to the likelihood of the occurrence of an event. In applications to actual power plants, probabilistic considerations must be included, in particular when a preliminary deterministic study indicates significant hazard levels.

The methodology and results of the current study represent a significant improvement in the treatment of the hazard problem arising from large LNG spills on water. The method can be readily used in the analysis of hazards in specific cases. It is particularly valuable as a rapid and inexpensive screening procedure when many possible spill scenarios and environmental conditions must be considered. Coupled with probabilistic analysis, it can become a valuable tool in assessing the risks to nuclear power plants arising from large LNG spills on water transportation routes. It should also be noted that the developed methods can be directly adapted to investigate the spreading and effects of other hazardous materials.

1. INTRODUCTION

In recent years, the effects of off-site hazards have become an important factor in the siting and design of nuclear power plants. There exists particular concern over the shipment of large bulk quantities of hazardous materials, i.e., explosive, toxic, flammable, and corrosive substances, in the vicinity of the plants. The current investigation concerns specifically the hazards that may arise from a large spill of liquified natural gas (LNG) on water-transportation routes. A strong motivation for such a study exists because a sizable number of nuclear power plants are located along navigable waterways. At the same time, considerable movement of LNG already exists in the coastal waters, and this traffic is expected to increase. In at least one case, the separation between an existing plant and an LNG terminal is but a few miles. Further shipments of LNG are very large (of the order of 10^5 m^3) and contain immense amounts of energy. Therefore, the consequences of a massive spill could indeed be catastrophic.

The major objective of the current study is to define the hazards to nuclear power plants arising from large LNG spills on water transportation routes. The emphasis is on how the spill environment could affect safety-related systems which are necessary for a safe shutdown of the plant and for subsequent heat removal. A secondary aim of the effort is to provide technical information which will assist the U.S. NRC in formulating guidelines concerning the siting and operation of nuclear power plants as they relate to the threats posed by possible LNG spills on water transportation routes.

To achieve these objectives, the scope of this program consists of two major tasks: (1) definition of the LNG spill phenomenology and quantification of the arising threats and (2) assessment of the nuclear power plant susceptibility and vulnerability to the possible threats.

A number of research investigations, which deal with the phenomena of LNG spills on water and related areas, have been conducted in the past [1,2] and are now in progress [3]. Although these studies have produced much information, great disparities and uncertainties remain in the obtained results. The purpose of the current program is to reduce some of these uncertainties. However, originally, the study was not intended as a major research effort. Rather a synthesis and critical evaluation of existing data, methodologies, and predictive techniques were planned in order to obtain reasonable estimates of the LNG spill environment. Similarily, in determining the effects of the threats on the power plant, existing information concerning the susceptibility of various systems, components,

and structures is to be used, modified, or adapted to arrive at plant vulnerabilities.

Early in the study, however, it was recognized that existing information defining the LNG spill environment on water is too disparate and conflicting to permit a synthesis into a meaningful predictive tool. Therefore some developmental work had to be undertaken in the area of LNG spill phenomenology, and a large portion of the program effort was directed towards accomplishing this task.

Because of the limited size of the total effort, it was never the intention to develop detailed analyses and computational methods which would require the implementation of large computer codes. Therefore, a global approach, which defines the most salient features of the phenomenology, but still permits reasonable estimates of the expected threats, has been used in this study. Another constraint imposed on the program effort is that a completely deterministic approach has been taken. This program is not intended as a risk analysis, and probabilistic estimates of the hazards and threats are not part of this study. A definition of the problem treated in this study and the approach taken are given in the next section. This is followed by sections that summarize the various phenomenological models for the LNG spill environment as well as the magnitude of threats. A survey of the nuclear power plant safety systems that may be affected by the spill environment is then given, and susceptibilities to the various threats are established. Finally, estimates of plant vulnerabilities are provided, and the limitations of the results are analyzed and discussed. Additional details of the various LNG spill phenomenological models and threat definitions are given in the appendices.

2. PROBLEM DEFINITION

The problem considered here is a large spill of LNG from a tanker ship on an essentially open body of water such as an estuary or wide river. The quantities of LNG carried by a single ship can be in excess of 10^5 m^3. However, regardless of the ship design, the LNG cargo is in general held in compartments not exceeding 2.5×10^4 m^3 in capacity [4]. Since the current investigation relies on a completely deterministic approach and since the rupture of a single compartment appears as the most credible shipping accident, the contents of such a compartment, i.e., 2.5×10^4 m^3, are taken as the maximum credible spill in this study. Although this may appear to be an arbitrary limitation, it was felt that no a priori justification exists for considering the involvement of the remaining tanker compartments and that such justification could only be developed through detailed investigations of possible accident scenarios. However, such an effort is clearly beyond the scope of the current study. Note also that even the contents of a single compartment contain an enormous amount of energy. Since LNG has a density of about 450 kg/m^3(28 lbm/ft^3), there are approximately 10^7 kg or 10 kilotons of fuel in a compartment. Considering that the energy content of hydrocarbon fuels is approximately tenfold that of TNT, this indeed represents a large hazard. For completeness, the case of instantaneous release of the entire cargo of one compartment is included in this study. However, the primary emphasis is on more credible spill scenarios in which the cargo is released over a finite period of time.

Much of the uncertainty in the current estimates of the hazards associated with a massive LNG spill on water arises from the complex phenomenology of such a spill. This complexity in turn is largely due to the physical characteristics of LNG. Being a cryogenic liquid at a very low temperature of -160°C (-256°F) at a density of about 450 kg/m^3(28 lbm/ft^3) [5], LNG upon spilling will float on water and spread in an ever increasing pool. This spreading will be accompanied by violent boiling and vaporization of the LNG with simultaneous ice crystal formation in the water. Since the vaporized LNG remains extremely cold and even after considerable expansion and mixing with air may still be at -73°C (-100°F), moisture in the air will condense and freeze. The density of cold LNG vapor is considerably larger than that of air. Hence the formed vapor cloud will rapidly spread by gravity. At the same time, wind forces will cause a global drift of the cloud. Shear forces and air turbulence, primarily at the upper surface of the essentially pancake-shaped cloud, will induce air entrainment into the cloud, simultaneously heating the mixture and changing its density. The cloud may ultimately reach neutral buoyancy, and further dispersion is then primarily due to atmospheric turbulence and wind-induced drift.

An LNG fuel-air mixture is combustible between the upper flammability limit (UFL) (15% fuel by volume) and the lower flammability limit (LFL) (5% fuel by volume). At the boundary of the vapor cloud flammability conditions will persist at all times until the bulk of the vapor is dispersed below the LFL. Therefore, ignition of the vapors and/or spreading LNG pool is possible at any stage of development and various fire scenarios are possible. These include pool fires, diffusion flame fires in which fuel-rich vapors burn around their periphery, and fires of premixed clouds which may burn very rapidly. In this latter stage of fire development, the possibilities of cloud explosion or rapid deflagration with the accompanying production of significant overpressure or blast waves cannot be excluded. Although no evidence exists that unconfined pure methane-air mixtures will detonate, it must be remembered that LNG is "spiked" with significant fractions of higher hydrocarbons [5]. Some experimental evidence that such mixtures can explode even when unconfined [6]. Partial confinement and/or turbulence induced by obstacles will only enhance this process [7].

The preceding indicates that all phases of the LNG spill phenomenology are interrelated; i.e., fuel dispersion, be it in liquid or vapor form, cannot be separated from the fire phenomenology. None of the past investigations on LNG spills on water have taken into account this fact. Each of the phases, i.e., pool spreading, vapor dispersion, and fire, is treated separately. Thus in addition to the large disparities that exist between various predictions, there is the uncertainty of the effect of coupling between fuel dispersion and fire phenomenology. Therefore, a major aim of the current study is to investigate, at least in a global manner, the interaction between spill, fuel dispersion, and fire phenomena and to provide a more realistic quantitative estimate of the threats produced by the LNG spill environment.

The most prevelant hazard to a nuclear power plant from an LNG spill is due to the fire threat. As pointed out earlier, ignition can occur during any stage of fuel dispersal, and the resulting conflagrations will, in general, cover a large area. Thus significant thermal loads may result at the nuclear power plant, even when the fire is some distance away, simply through thermal radiation.

When a flammable vapor cloud actually reaches the plant site, then in a resulting fire the radiation loads are augumented by direct convective heating of structures, systems, and components. In case of vapor cloud explosion or rapid deflagration, the resulting overpressure loads may be quite high. Since the energies involved are very large, blast durations and

hence drag loads may also be significant. Should a portion of the vapor cloud drift on site and infiltrate some structure volume detonations may result. Even if ignition does not occur, the LNG vapor in itself may constitute a hazard to plant personnel through oxygen depletion. Similarly, the combustion gases constitute a hazard because of their possible toxicity and oxygen displacement. Finally, for a sufficiently close spill, the LNG liquid may represent a hazard, either through ingestion into water intake systems or through its effect on structures, e.g., metal imbrittlement, because of its extremely low temperature.

3. LNG SPILL AND POOL DYNAMICS

The spill and spreading of LNG on a water surface involve many complex hydrodynamic and thermodynamic phenomena. LNG, being lighter than water (density about 45% that of water), will spread away from the spill source driven by buoyant forces and form an ever-increasing pool. The spreading is influenced by both the characteristics of the spill source and the LNG-water interactions at the pool boundaries. In addition, the cryogenic LNG experiences intense heating on contact with the much warmer water and surrounding air. This results in vaporization of the LNG and is the source of the LNG cloud formation. The mass loss from the pool due to vaporization is sufficiently large that it must be taken into account in any realistic representation of the pool dynamics. A schematic of the LNG pool spreading as it might occur when a shipping container is breached is shown in Fig. 1. A complete mathematical formulation and solution of the LNG pool spreading, even under axisymmetric assumption, is very difficult. Neglecting spill source details, viscous forces, and gradients in the vertical direction results in a simplified differential formulation of the gravity spreading for the LNG pool (see Appendix B). To make such a model tractable, the vaporization is represented as a constant liquid mass loss rate per unit area. The boundary conditions at the spill source depend on the actual LNG release mechanisms, and those at the pool's leading edge are dependent on the LNG-water interaction. The system of equations for the described model is hyperbolic and can be solved numerically using the method of characteristics. However, even for such a solution, the many uncertainties involving the boundary conditions require additional assumptions. Further, the complexity of the solution makes it difficult to integrate such a formulation into a global approach for the prediction of the entire LNG spill phenomenology. A detailed examination of this formulation under steady-state conditions (see Appendix B) i.e., when the inflow equals the vaporization mass loss and the pool radius is constant, reveals some interesting characteristics of this model. Most important of these is the result that, under steady-state conditions, physically meaningful solutions are only obtainable when the pool depth decreases with the pool radius. The steady-state solution can be applied to the late stages of pool development when the leading edge of the pool is at considerable distance from the spill source and the behavior is essentially quasi-static.

To treat the early transient behavior of the pool spreading at a level commensurate with a global-model approach, it is further assumed that the pool depth at any instant of time is uniform over the entire pool expanse. This eliminates the spatial dependence of the pool dynamics. Some

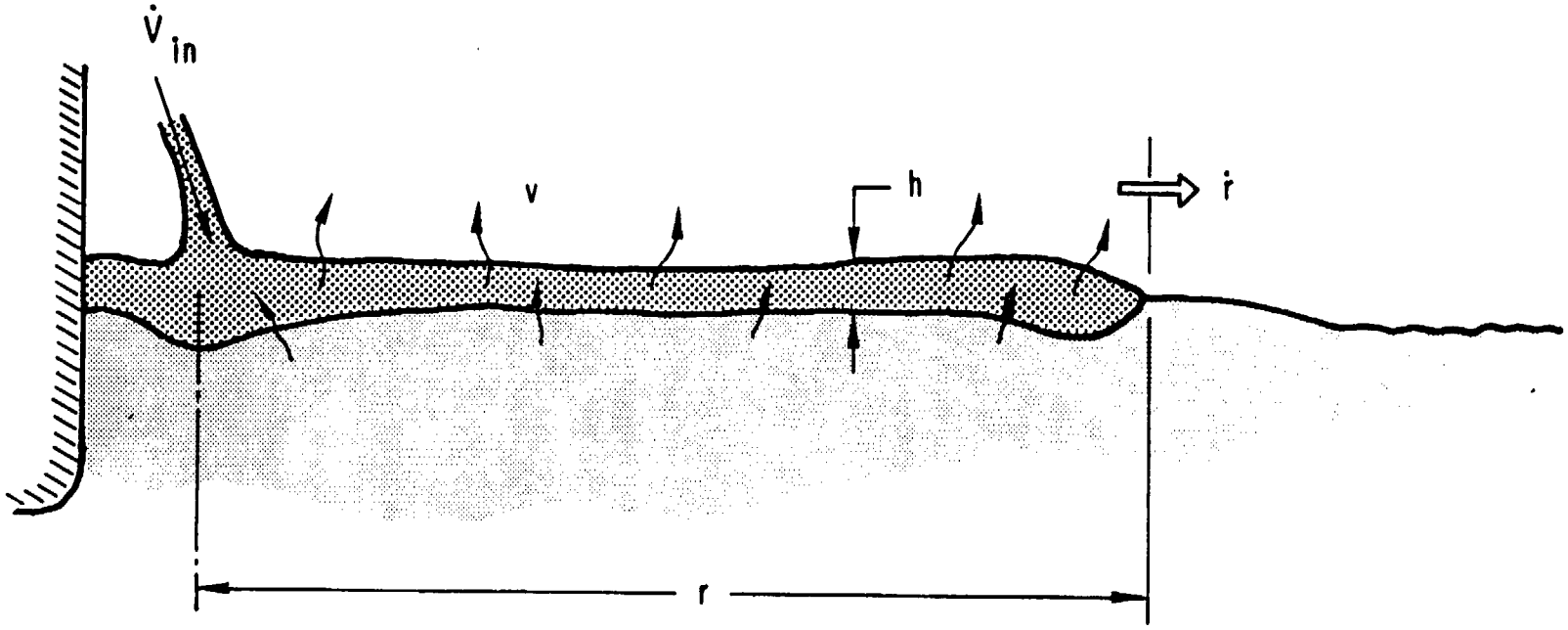

Figure 1. Model of LNG Pool Spread.

experimental evidence exists that this simple model provides reasonable estimates of the pool size as a function of time [1-4]. The equations of motion governing the gravity spreading of a circular pool are then simply reduced to

$$\dot{r} = C\sqrt{h} \tag{1}$$

and

$$\dot{V}_p = \pi r^2 \dot{h} + 2\pi r h \dot{r} = \dot{V}_{in}(t) - \pi r^2 \dot{v}. \tag{2}$$

Here the first equation relates the pool spreading rate $\dot{r}$ to the spatially uniform pool depth h; the second equation expresses the mass conservation in the LNG pool, with r the pool radius, $\dot{V}_{in}$ the time-dependent volumetric inflow to the pool, and $\dot{v}$ the constant volumetric evaporation rate per unit area. The constant C represents the gravitational effect modified by the relative density (or a simple multiple thereof), i.e.,

$$C \propto \sqrt{\frac{g(\rho_w - \rho_L)}{\rho_w}} \tag{3}$$

where ρ_w is the density of water, ρ_L is the density of the LNG and g is the acceleration of gravity. The pool will begin to break up when its thickness reaches a critically small value. This critical value is roughly defined by experimental data. A major drawback of the spatially uniform pool-thickness model is that such a breakup would occur instantly over the entire pool expanse. Similarly, another physically unreal situation arises in a pool of uniforn depth when the entire pool disappears suddenly due to vaporization. To avoid these anomalies, the LNG pool description at late times, when the pool thicknesses are small, is switched from the uniform-depth model to the quasi-steady model described above (see also Appendix B). Although such a change in modeling is arbitrary and produces some abrupt changes in pool behavior, it does allow for an orderly pool shrinkage and receding of the pool leading edge until the pool completley disappears.

The details of the spill source may be expected to influence the dynamics of the LNG pool spreading. For a fixed total (or maximum) release quantity, the major variable is the rate of release. Since LNG is shipped essentially at atmospheric pressure, the release is totally due to gravity flow and is governed by geometric variables such as tank size and shape, as well as the cross-sectional area of the rupture and its location relative to the water surface and tank bottom. Because the LNG contents are not pressurized, it

is reasonable to assume that the size of the rupture is a constant during outflow. Typical results for the outflow from a fully vented tank of uniform cross-sectional area are shown in Fig. 2, where the rupture is assumed to be above the water line (for more details, see Appendix A). The geometric and other primary variables used in defining the dimensionless parameters of the figure are the following: t-time, V-tank volume, A_o-area of opening, H-height of uniform section tank, L-height of opening, ℓ-height of fluid above opening, g-gravitaional constant, ρ_L-density of liquid (LNG). The outflow velocity U and mass flow rate m are then, respectively,

$$U = \sqrt{2g} \tag{3a}$$

and

$$\dot{m} = \rho_L A_o \sqrt{2g}. \tag{3b}$$

Finally dimensionless parameters are defined as follows:

$$\lambda = L/H, \tag{4a}$$

$$\tau = \frac{tA_o \sqrt{2gH}}{V}, \tag{4b}$$

and

$$G = \frac{\dot{m}}{\rho_L A_o \sqrt{2gH}}. \tag{4c}$$

The initial dimensionless mass flow rate is designated as G_o and the dimensionless release duration as τ_f. For gravity outflow from a tank of uniform cross-section, the height of liquid above the opening ℓ decreases proportional to t^2. Hence, the mass outflow decreases linearly with time as shown in Fig. 2. Also indicated are the dependences of mass flow release duration on the location of the opening relative to the tank bottom.

When the cross section of the tank is not uniform, some departure from the above-described behavior may be expected. However, as shown (in Appendix A, Plates 12 and 13) for the extreme of a spherical tank, a linear decrease of mass outflow rate with time is a reasonable approximation for much of the release duration under most conditions of gravity flow. If, the tank rupture occurs some distance below the water line, the outlfow is further modified in that the primary release ceases when the outside water height

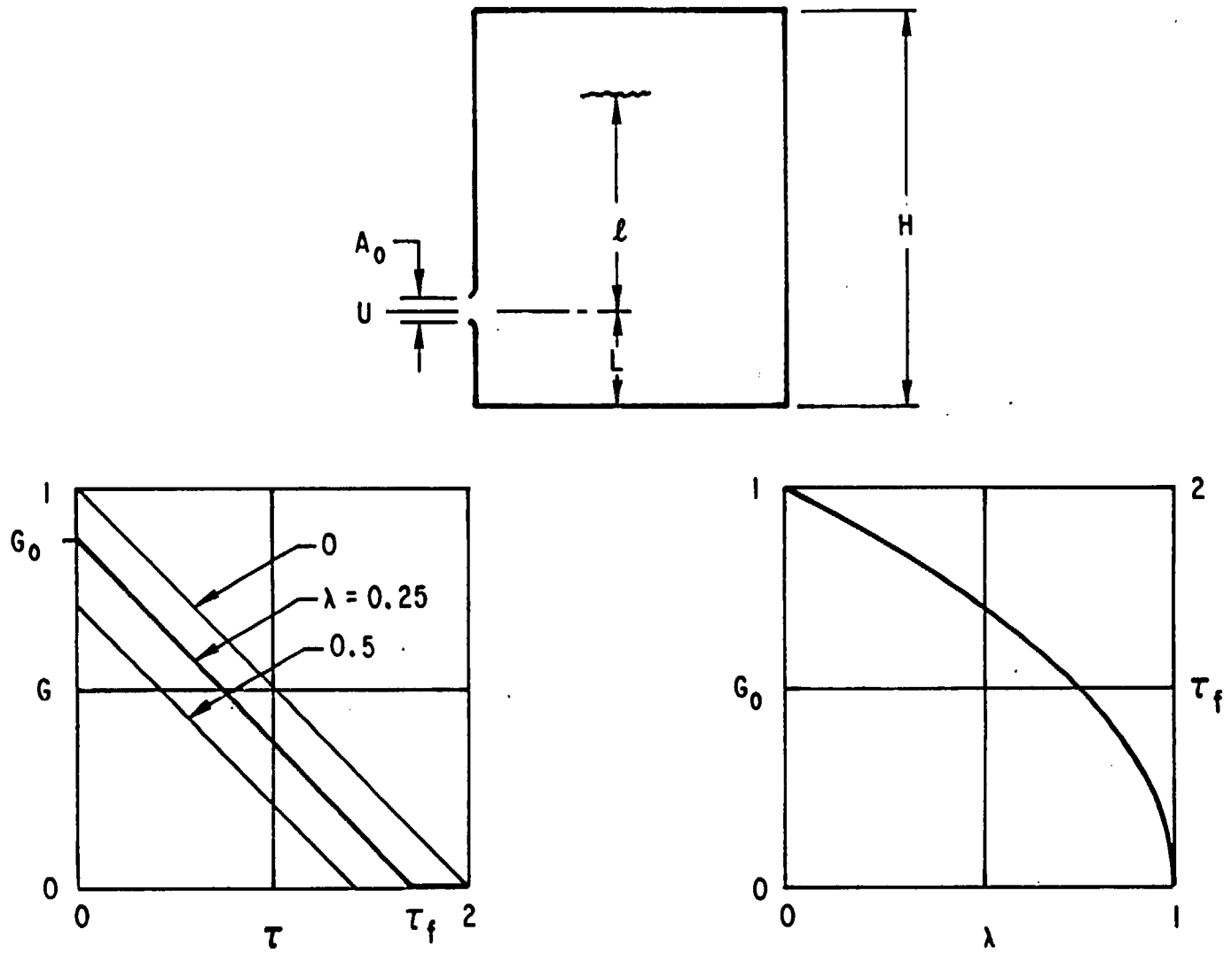

Figure 2. Gravity Outflow from Tank of Uniform Cross Section.

above the opening balances the LNG height above the opening inside the tank (see Plates 14 and 15 of Appendix A). At this point, a secondary release may occur due to the infiltration into the tank of water, which has a higher density than the LNG. This water will sink to the bottom of the tank, displacing the LNG above it and causing an additional release. This process will continue until the water level inside the tank reaches the opening. For a tank of uniform cross section, again the secondary release mass flow varies linearly with time. In most circumstances the secondary release is expected to be a slow process complicated by the rapid evaporation of LNG in intimate contact with the water. Hence, the overall spill will be dominated by the primary release due to direct gravity flow from the tank.

The effect of spill rate on LNG pool size for a linearly decaying (triangular) release is examined in Fig. 3. The influence of the spill rate is seen to be significant during the early pool development, particulary if instantaneous release (t_f = 0) is considered. These differences are markedly reduced by the time the pool reaches its final size, i.e., disappears due to complete vaporization. The variations in the times at which maximum pool growth occurs is even less pronounced. The influence of both rate of release and form of release is illustrated in Fig. 4, by the example of a decaying triangular and a constant mass outflow. Note that the release rate, or duration of spill, has a more pronounced influence on the pool size than the release form. Again, differences are large during the early stages of pool development.

The vaporization rates and vaporization history of the pool are important features for the study of the generation, growth, and spread of the LNG vapor cloud. As indicated earlier, the model adopted here assumes a constant vaporization rate. Figure 5 shows the vaporization history for various spill rates, assuming a vaporization rate of 3×10^{-4} m/s. The effect of spill rate (duration) on the total amount of vapor generated is seen to be significant. For a spill duration of 500 and 1000 s, the pool is completely evaporated before the end of the spill. A secondary pool is then formed, and vaporization continues. This is indicated by the abrupt change in slope in the curves for these spills. The effect of a higher vaporization rate, 6×10^{-4} m/s, is illustrated by the dashed line.

Based on the foregoing results and additional data and analysis given in Appendixes A and B, a two-stage global pool spreading and spill model is adopted. A linearly decaying spill rate appears to be most plausible. The transient stage of the pool spreading is determined under the assumption of spatially uniform average pool thickness, constant vaporization rate, and constant Froude number $F = (r/\sqrt{gh})$. The model then adjusts to a quasi-

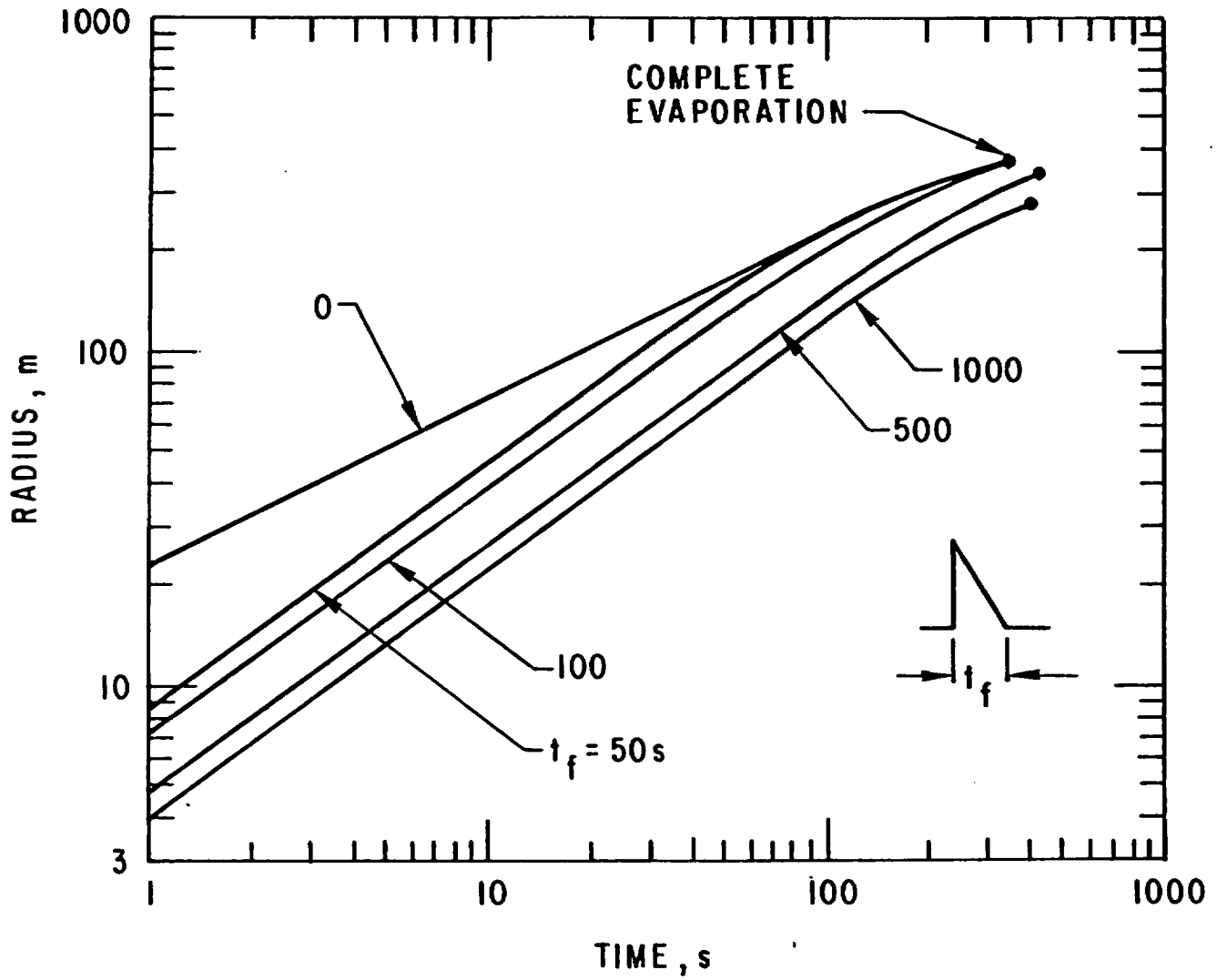

Figure 3. Influence of Release Duration on Pool Spread; Total Volume of Spill = 25,000 m^3.

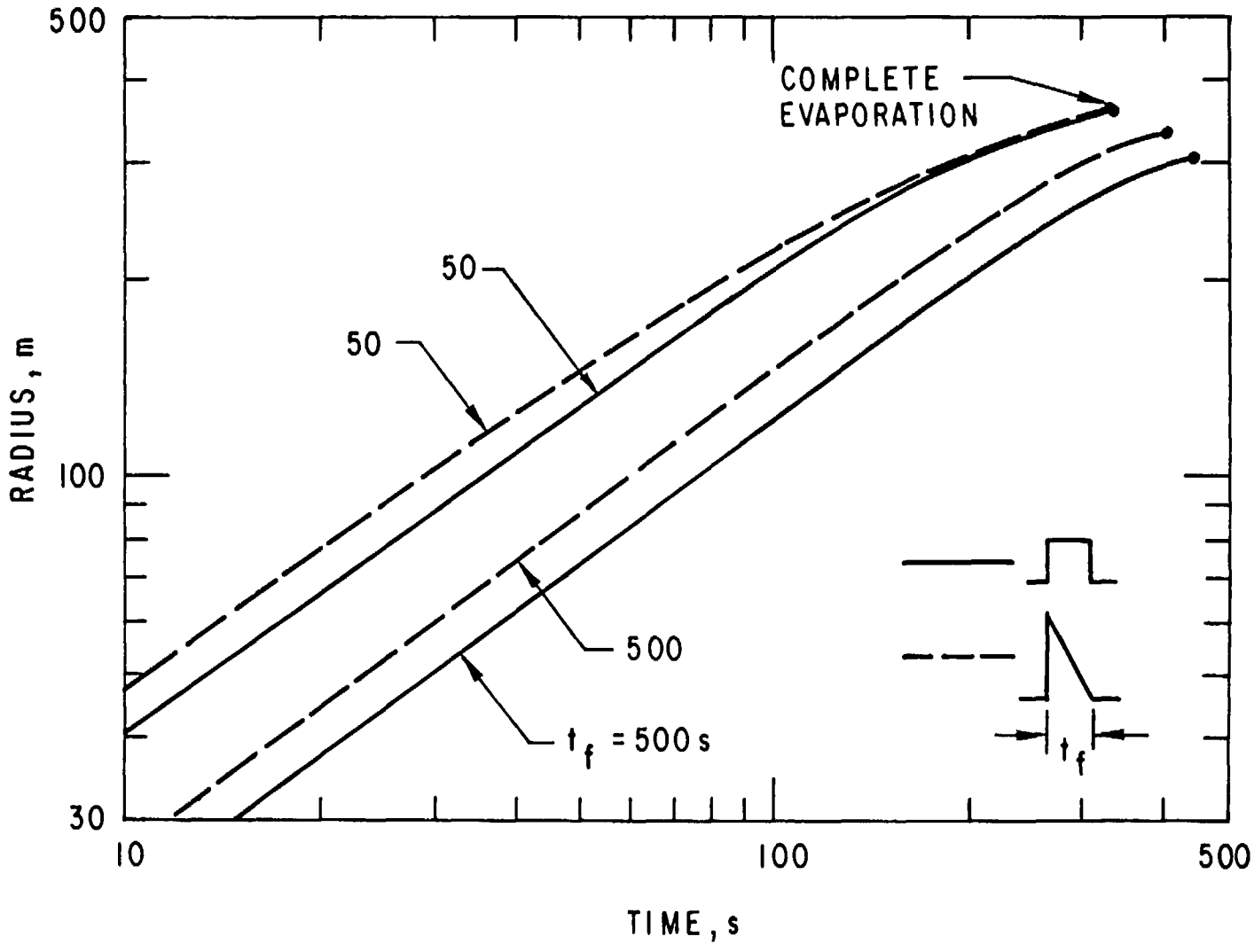

Figure 4. Influence of Release Form on Pool Spread; Total Volume of Spill = 25,000 m^3.

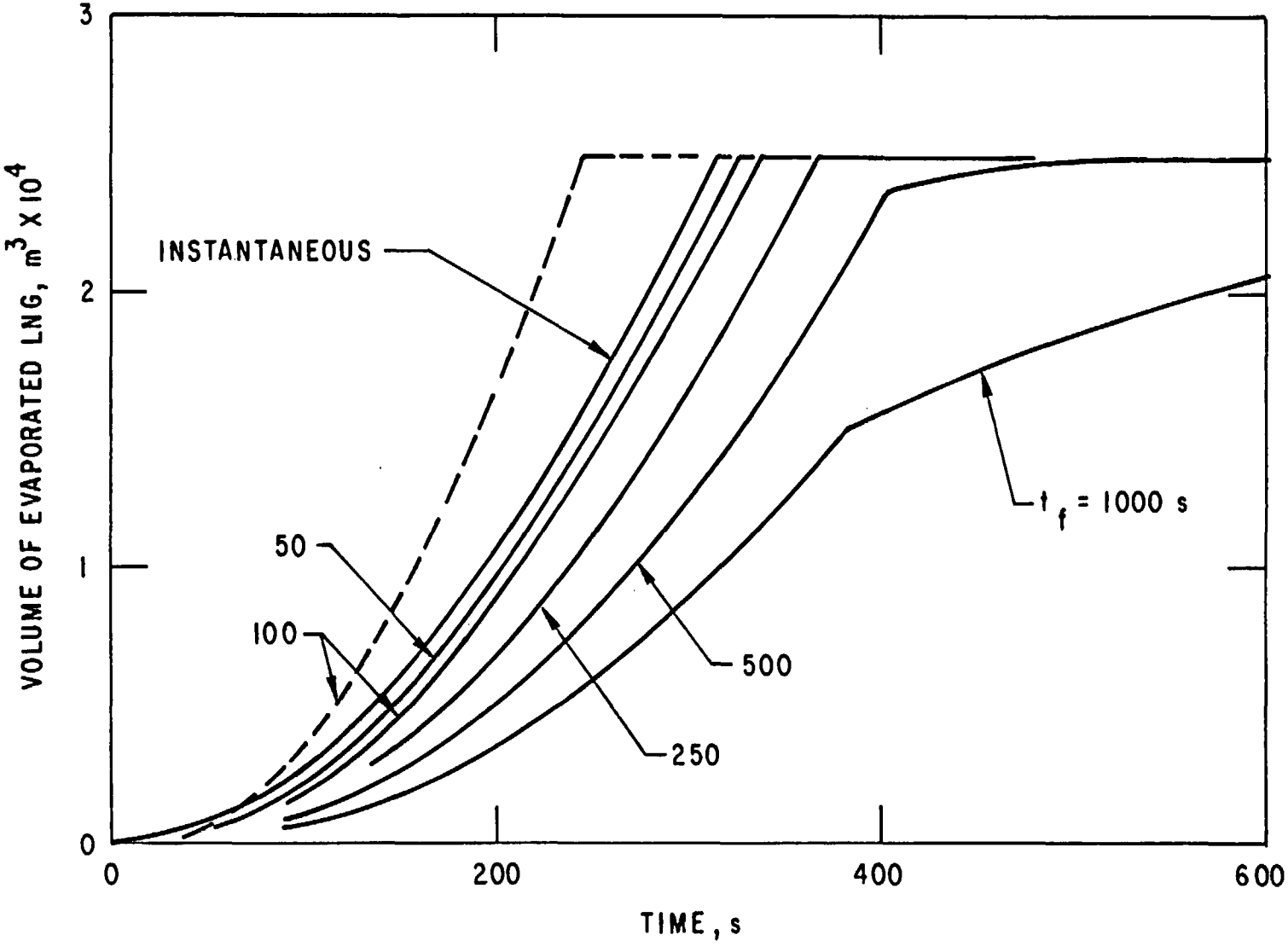

Figure 5. Pool Vaporization Histories; Variation with Spill Duration.
Vaporization Rate: ____ 0.003 m/s, ------ 0.006 m/s.

steady solution when the transient pool thickness suddenly tends to zero due to complete vaporization. This is illustrated in Fig. 6 for a total spill of 25,000 m^3 over a time duration of 600 s. Also shown is the secondary pool growth that would result if the dynamic uniform-thickness pool modeling was assumed valid for the duration of the spill. Although the adopted global model has some shortcomings, such as the abrupt change in size once the maximum dynamic radius is reached, it is believed to give a reasonable representation of a very complex phenomenon and to provide a good basis for the more complex integrated modeling of the LNG vapor cloud spreading and fire phenomena.

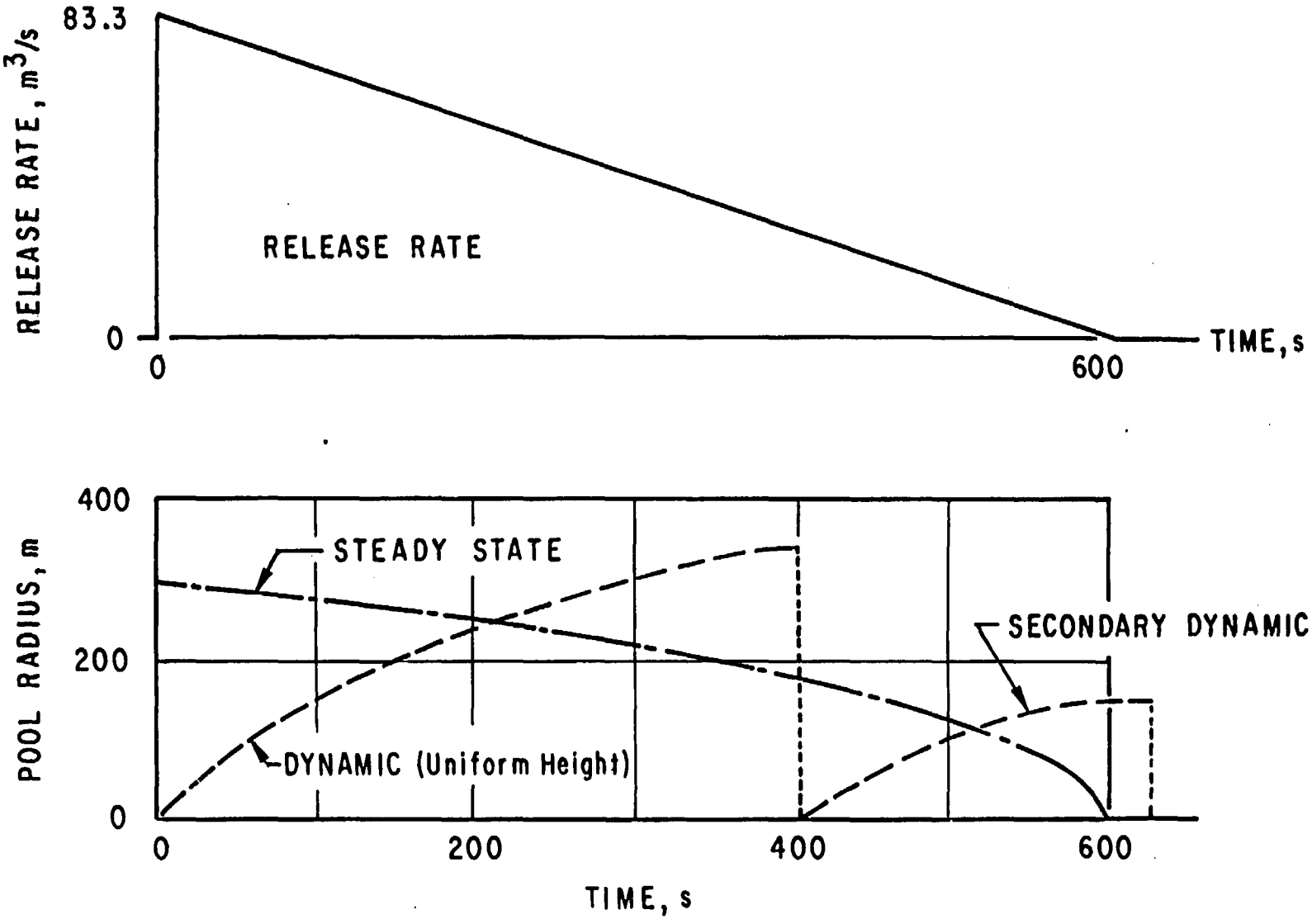

Figure 6. Pool Dynamics.

4. LNG VAPOR-CLOUD DYNAMICS

The problem of a vapor cloud spreading as a result of a spill of cryogenic liquid has been studied by many investigators, and a number of these efforts specifically address the dispersion of LNG vapors. The models developed range from sophisticated three-dimensional computer codes [8] to analytical global representations of the phenomena [1] and also include direct experimental correlations [9,10]. The uncertainties and discrepancies of these past efforts are vividly illustrated in Ref. 11, where for the same spill scenario the predictions for the distance to the lower flamability limit (LFL), obtained by the various models, range from approximately 2.5 to 80 km.

Currently, no published nonproprietary model exists that will reliably predict the size and downwind drift of the LNG cloud resulting from a massive LNG spill on water. At the same time, little guidance can be obtained from the available small-scale experimental data. Limited published results and evaluations of a sophisticated three-dimensional code SIGMET [8] indicate that the cloud geometry is relatively constant, being a somewhat elongated cylinder which drifts downwind. At any instant of time, the primary cloud region appears to be quite uniform in its thermodynamic state. This information suggests that a global model of LNG vapor cloud spreading which assumes a cloud of uniform thermodynamic state and simple shape, and which moves under the influence of wind, may provide a reasonable approximation to the true phenomena. It is further apparent that spreading of the cloud mass is primarily due to gravity and that air entrainment plays an important role [1,8]. From simple thermal-equilibrium considerations, it can be shown (see Appendix B) that, at the upper flamability limit (UFL, 15% by volume), the weight ratio of air to LNG vapor is 12, while at the lower flamability limit (LFL, 5% by volume) this ratio increases to 35. Hence the properties of the ambient air are important in defining the behavior of the vapor cloud. In particular, the humidity of the air, because of the high heat content in the water vapor, may be expected to have significant influence. Another factor that affects the cloud behavior is the heat transfer between the vapor-cloud and the water surface. It can also be shown (Appendix B) that the vapor-cloud spread rate by gravity does not vary much with the dilution of the vapor cloud by the entrained air. This insensitivity to the air dilution suggests a similarity in the cloud-growth histories.

4.1 Vapor Cloud Model

It is assumed that the cloud dynamics can be adequately represented by a

global model. The LNG vapor and entrained air are assumed to be intimately mixed and to be in thermal equilibrium so that the entire cloud expanse is in a uniform state spatially at any instant of time. The model shown in Fig. 7 assumes a cylindrical cloud shape of radius R and height H. The cloud grows laterally due to the action of gravity while retaining it cylindrical shape and drifts downwind under the action of the wind. LNG vapor enters the cloud as a result of time-dependent vaporization from the spreading LNG pool. Air is assumed to be entrained at the upper surface of the cloud region due to the local relative velocity between the cloud vapors and the adjacent ambient air and due to atmospheric turbulence. The effects of air humidity and heat transfer from the water surface may be included. The cloud size is initially of zero radius and height at the start of the LNG release process, and it grows simultaneously with the spill process and the associated LNG pool growth. A gradient wind model is used to describe the atmospheric wind field. To obtain physically meaningful results at all times, it is assumed that if the LNG pool grows radially more rapidly than the corresponding vapor cloud can grow, under the action of gravity, then the cloud radius is governed by the pool spread rate and pool size, which control the region over which LNG vapor is injected into the atmosphere.

The air, LNG vapor, and water vapor (if present) are all treated as perfect gases having a constant average value of specific heat. An energy and mass balance determines the temperature of the vapor cloud and thus its density (see Section 3 of Appendix B). For large relative humidities in the ambient air, the latent heats of the water vapor can have a significant effect on the heat balances.

The cloud dynamics is governed in part by the gravity-spreading velocity relationship, which is based upon the density intrusion concept of Yih [12] (see also Appendix B):

$$\frac{dR}{dt} = \dot{R} = \sqrt{B \; g \frac{(\rho - \rho_a)}{\rho_a} H} \; , \qquad (5)$$

where R is the cloud radius, ρ is the cloud density, ρ_a is the air density, t is time, H is cloud height, and g is the gravitational constant. The factor B may be called a "Froude Multiplier," and sensitivity studies with the cloud dispersion model suggest a nominal value of B = 2 (see Appendix B). The LNG vapor production is controlled by the pool dynamics described in the preceding chapter and is given in differential form as

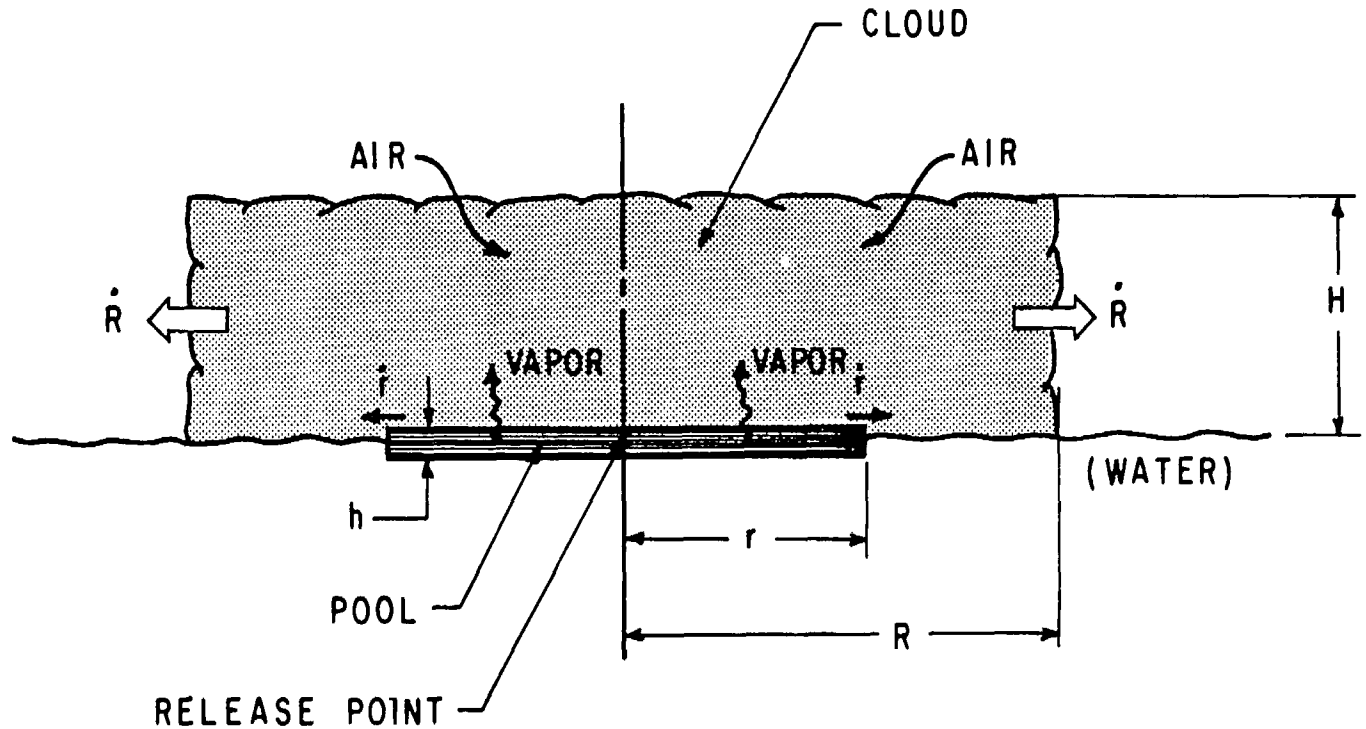

Figure 7. Basic Cloud-Dispersion Model.

$$\frac{d\bar{M}}{dt} = \dot{v}\pi r^2 \rho_L \ , \qquad (6)$$

where r is the time-dependent pool radius, v is the vaporization rate per unit area of LNG liquid, ρ_L is the density of LNG at the saturated liquid state, and M is the mass of LNG vapor in the cloud.

The air entrainment details are similar to the approach used by Germeles and Drake [1], i.e., air is entrained due to the local relative motion between cloud mass and air. Again, in differential form the following equation applies:

$$\frac{dM'}{dt} = \alpha\pi R^2 \rho_a U_e \ , \qquad (7)$$

where ρ_a is the density of ambient air, U_e is the entrainment velocity, M' is the mass of air in the cloud, and α is the entrainment coefficient. The last quantity can be interpreted as being made up of two parts: entrainment due to shear layer effects (between air and vapor cloud) and entrainment due to atmospheric turbulence. While the specific value of α is an input to the model, parametric studies and extrapolation of experimental data (see Appendix B) indicate values of about 0.1. Implicit in Eq. 7 is the neglect of air entrainment at the vertical (side) surfaces of the cloud-mass cylinder. In general, however, this area represents less than 5% of the total area and is therefore neglected.

The entrainment velocity U_e in Eq. 7 is obtained by properly integrating and averaging the local relative velocities over the entire top surface of the cloud (see Appendix B). These relative velocities are the vector sum of the local expansion velocity and the wind velocity. Depending on the wind velocity, the ratio of the entrainment to the spreading velocity $U_e/\dot{R}$ is found to vary from a value of 2/3, when the wind velocity W = 0, to a value approaching W when the latter is large. To facilitate numerical calculations an analytic fit of this relationship is formulated (see Appendix B):

$$U_e/\dot{R} = W/\dot{R} + \frac{2}{3} \exp\ [1.62(\dot{W}/R)] \ . \qquad (8)$$

The simultaneous integration of Eqs. 5-7, subject to the overall energy and mass balance, together with the condition of thermal equilibrium i.e., uniform cloud mixture temperature, yields the cloud volume, V, as a function of time. The cloud radius, R, is directly determined from Eq. 5, and the cloud height H is computed from the geometry, i.e.,

$$H = V/\pi R^2. \qquad (9)$$

Figure 7 illustrates the basic cloud-dispersion model; it includes the LNG pool, which is the source area for the (time-dependent) LNG vapor injection into the cloud. The pool of radius r spreads dynamically at a rate $\dot{r}$, in accordance with the pool-dynamics model described in the preceding chapter. Both cloud and pool are of zero height (or depth) and zero radius at the time of the start of the spill process (t = 0). Thereafter the cloud and pool grow simultaneously until the pool starts to shrink again because the vapor formation outstrips the LNG inflow at the source.

The gradient-height model for the wind field used in the computations is shown in Fig. 8, together with other model details that concern the drift effects of the cloud-dynamics model. The wind magnitude, W, varies with height, H, in accordance with the relation

$$W = W^*(H/H^{*n}), \quad 0 \quad H \quad H^*, \qquad (10)$$

where W* is the nominal wind magnitude at the gradient height H*, and n is the profile exponent. Above the gradient height the wind is constant at the nominal value W*. The recommended values for a water surface are [13]: H* = 228.6 m (750 ft) and n = 0.16.

The drift motion of the LNG cloud is in part due to the horizontal momentum convected into the cloud mass by the entrainment of the moving atmospheric air. The LNG vapor that enters the cloud has no net horizontal momentum; hence, its addition to the cloud mass decelerates the moving cloud. Furthermore, the cloud, which represents a large intrusion into the atmospheric wind field, will distort the streamline of the surrounding air (see Fig. 8) and induce an aerodynamic drag force on the cloud system. This force is here defined in the classical manner, namely

$$F_d = \frac{1}{2}\rho_a U_r^2(2RH)C_d. \qquad (11)$$

Here F_d is the total drag force, C_d is the drag coefficient, U_r is the relative velocity between the cloud and the wind, i.e., $U_r = W - U$, and U is the center of mass cloud velocity.

In the above equation the wind magnitude at the top of the cloud is used; this is a conservative assumption, since it results in the largest drag force and hence the largest cloud drift. The factor $(\rho_a U_r^2/2)$ is the dynamic pressure and 2RH is the projected area in the direction of wind

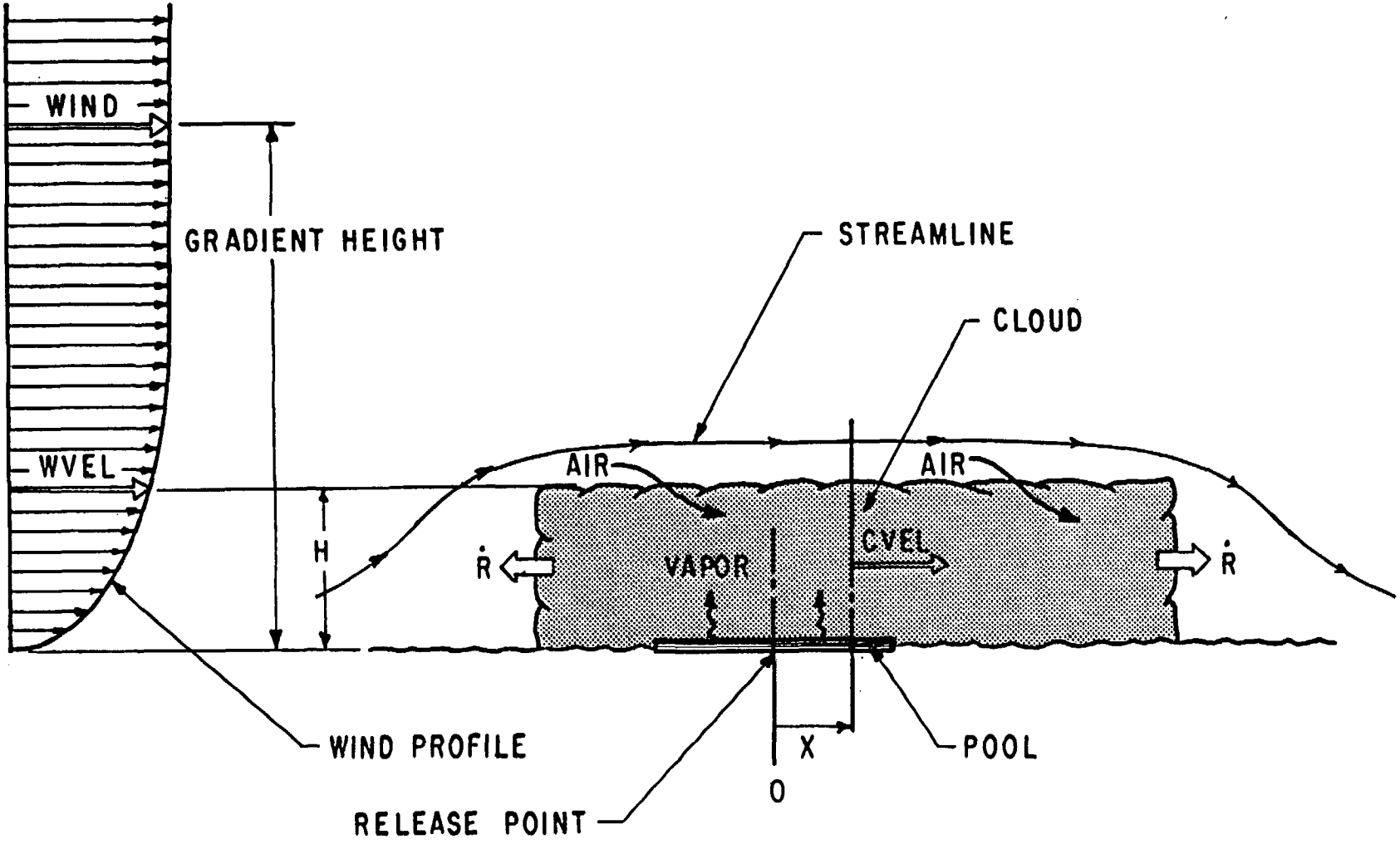

Figure 8. Drift Effects on Cloud-Dispersion Model.

motion. A momentum balance yields the change in cloud velocity, which is given in differential form as

$$dU = \frac{F_d dt + f(W - U)\, dM' - U d\bar{M}}{M' + \bar{M}}, \qquad (12)$$

where $F_d dt$ is the impulse due to the aerodynamic drag force $f(W - U)dM'$ is the momentum increment due to the entrainment of an incremental amount of air (dM'), and UdM represents the momentum that must be imparted to the injected incremental amount of LNG vapor (dM). The denominator of Eq. 12 represents the current total mass of the cloud system. A momentum factor, f, is used to allow for some momentum loss due to internal resistive mechanisms such as mixing. While this is an input parameter, a value close to unity is usually used. On the basis of the cylindrical shape of the cloud, a nominal value of 0.3 is assigned to the drag coefficient. At present, no ground-surface shear resistance is included in the cloud model. Finally, the displacement x (in the wind direction) is computed from its differential form definition

$$\frac{dx}{dt} = U. \qquad (13)$$

Initially, both $x = 0$ (the spill release location) and $U = 0$.

Extensive computational studies were performed to determine the sensitivity of the LNG vapor-cloud dynamics model to the expected range of parameter values and input variables (Section 3 of Appendix B and Section 4 of Appendix C). Using what are considered to be the most typical values of the entrainment coefficient (0.10), wind velocity (4.48 m/s = 10 mph), spill duration (600 s), and the standard spill quantity at 25,000 m^3 we obtain the pool and upwind and downwind cloud trajectories shown in Fig. 9. The result is for dry air and no heat transfer from the water surface. As indicated earlier, the sudden change in pool size at 400 s occurs because the pool description at this point is changed from a spatially uniform-depth dynamic model to a variable-depth quasi-static model. Although this is not completely satisfactory, it does result in the maximum possible pool size and also permits an orderly shrinking of the pool. The most noteworthy result of this computation is that the vapor cloud reaches its LFL in a relatively short time (500 s) and at the moderate downwind distance of 2.8 km. As will be seen later in the result summary these are indeed representative values. Figure 10 is graphic representation of the LFL contours for the same standard spill parameters but different wind speeds. For all but the highest wind speed (8.96 m/s = 20 mph), there is overlap between the pool and cloud at the LFL. In the latter case, some trailing vapor configuration reaching back to the pool should be expected.

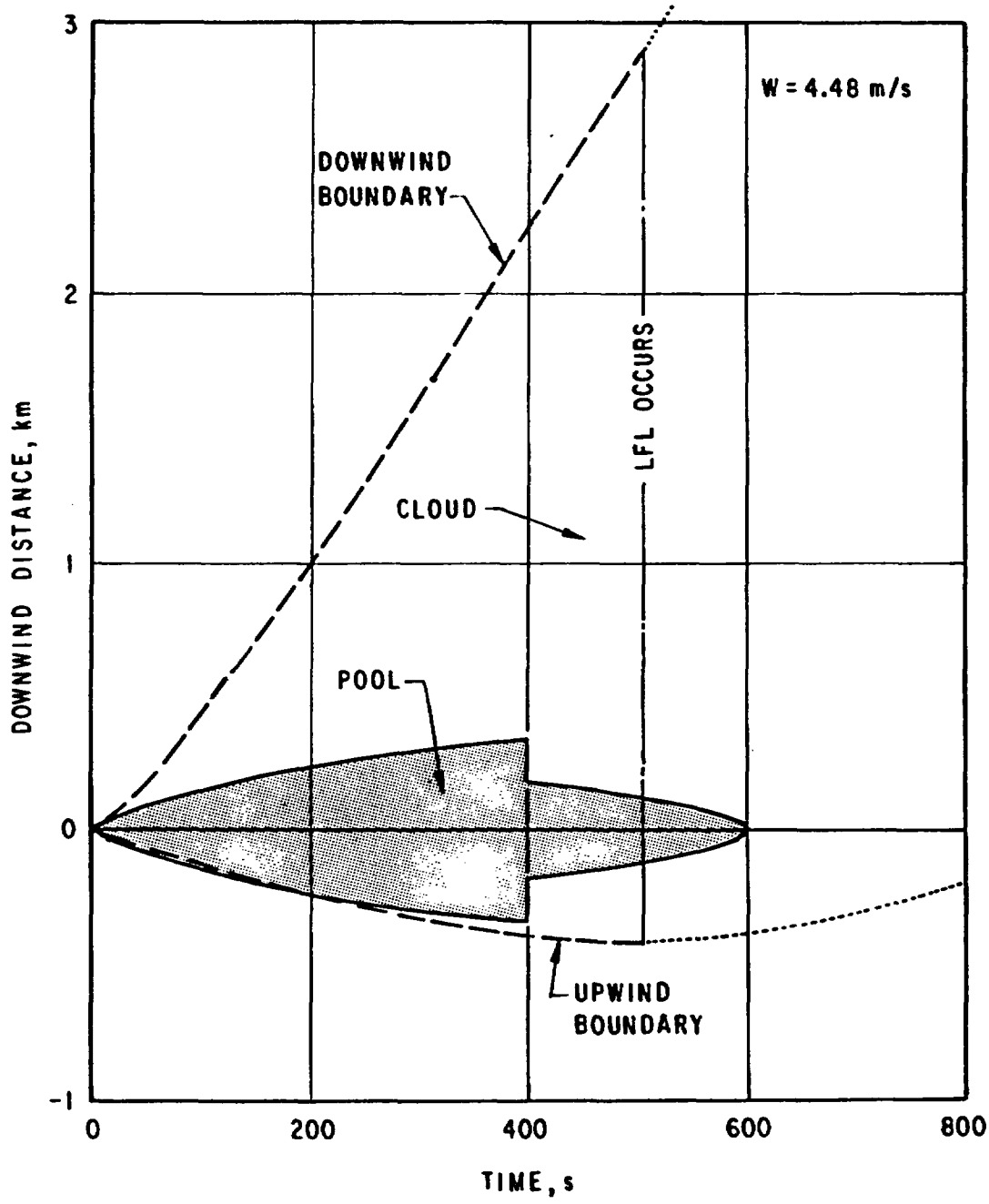

Figure 9. Cloud and Pool Boundary Trajectories.

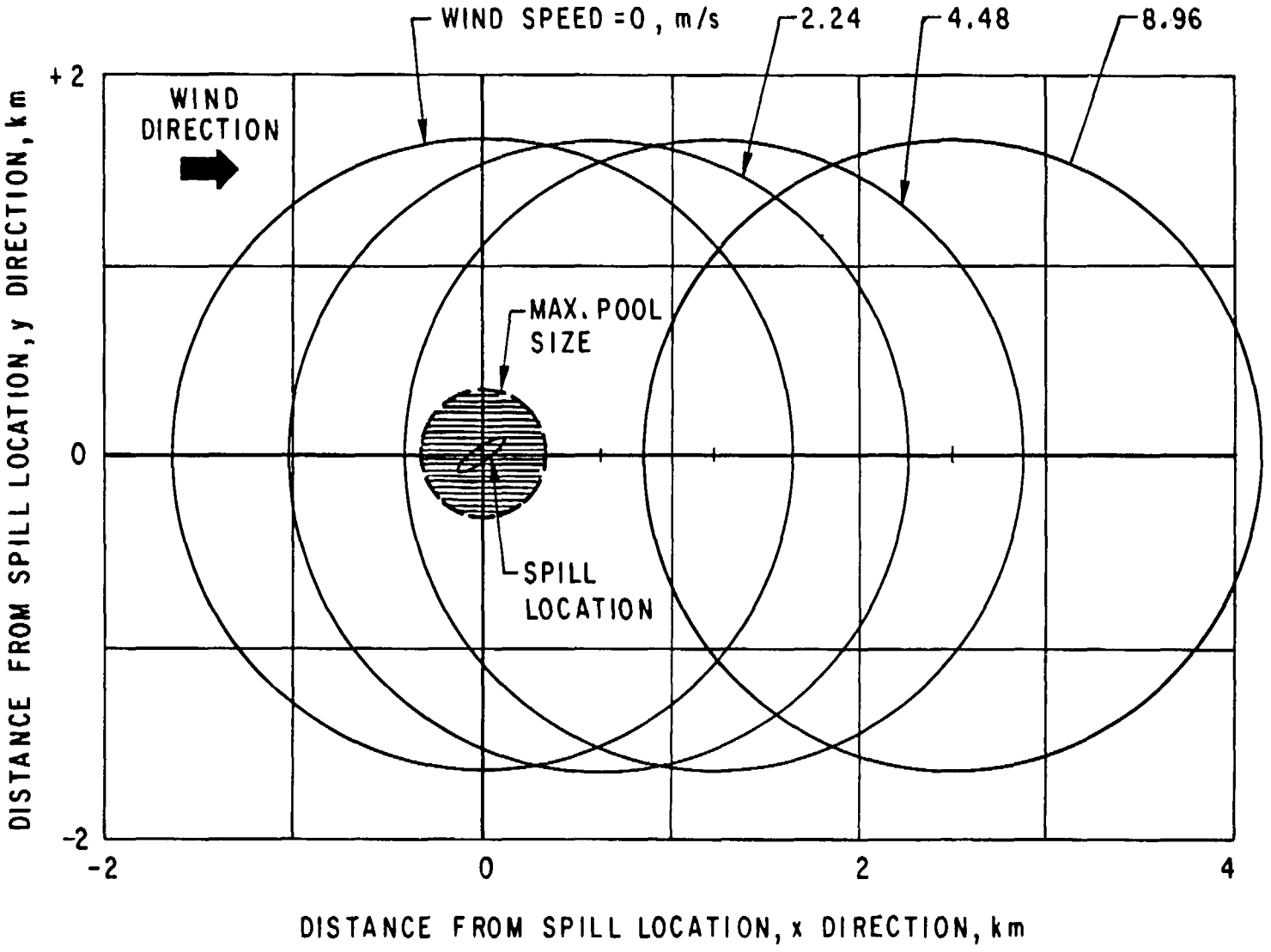

Figure 10. Plan View of LFL Contours.

Since no experimental data exist on large-scale LNG spills on water, the global model developed cannot be validated here. Some limited comparisons with other models were attempted however, (see Section 3 of Appendix B). Figure 11 compares the downwind distance to the LFL for various spill quantities, between the current model, SIGMET-code results [8], and the Germeles and Drake model [1]. Two values of the entrainment coefficient α [0.10 and 0.05] are used for the current model. An instantaneous spill, zero humidity, and a wind speed of 2.24 m/s are assumed. Although the results of all models are reasonable close at moderate spill quantities, the Germeles-Drake model seems to diverge sharply from the other results at the large spill quantities of interest in the current effort. Although this favorable comparison of the present model, with the elaborate computer calculations using the SIGMET code, can by no means be construed as a validation of the vapor-cloud model, it provides some confidence and verification that the obtained predictions are not unreasonable.

The major difference between the current formulation and other global models is the incorporation of global drift of the entire cloud mass. Models that neglect this aspect clearly violate momentum consideration. Numerous parameter studies indicate that, under most conditions, the vapor cloud remains negatively buoyant until the LFL is reached. Dispersion by atmospheric turbulence and the subsequent formation of vapor plumes are expected to play a minor role in the spreading of the LNG vapor in its flammable range. The current formulation therefore does not incorporate any of the Gaussian plume models so frequently advocated for the modeling of cryogenic vapor dispersion [14]. As shown in the sensitivity studies (Section 3 of Appendix B and Section 4 of Appendix C) fuel dispersion to distances larger than those indicated by gravity spreading can be readily accounted for by the global drift of the cloud mass. For predominantly negatively buoyant clouds, the latter dispersion mechanism is much more credible than plume dispersion.

4.2 Result Summary of LNG Vapor-Cloud Spreading

The extensive sensitivity studies carried out [see Appendixes B and C), together with data from the literature [1,3,8,12], provide a basis for standardizing certain of the problem parameters. Although, the selection of the appropriate values involves some engineering judgement, the impact on the overall behavior of the variables that are fixed in the current formulation is in general found to be minor. These values are listed in Table 1; also shown are the variables that must be provided as input to the model and the output that may be expected from a typical computation. Other variables that are fixed for the current application are the total spill

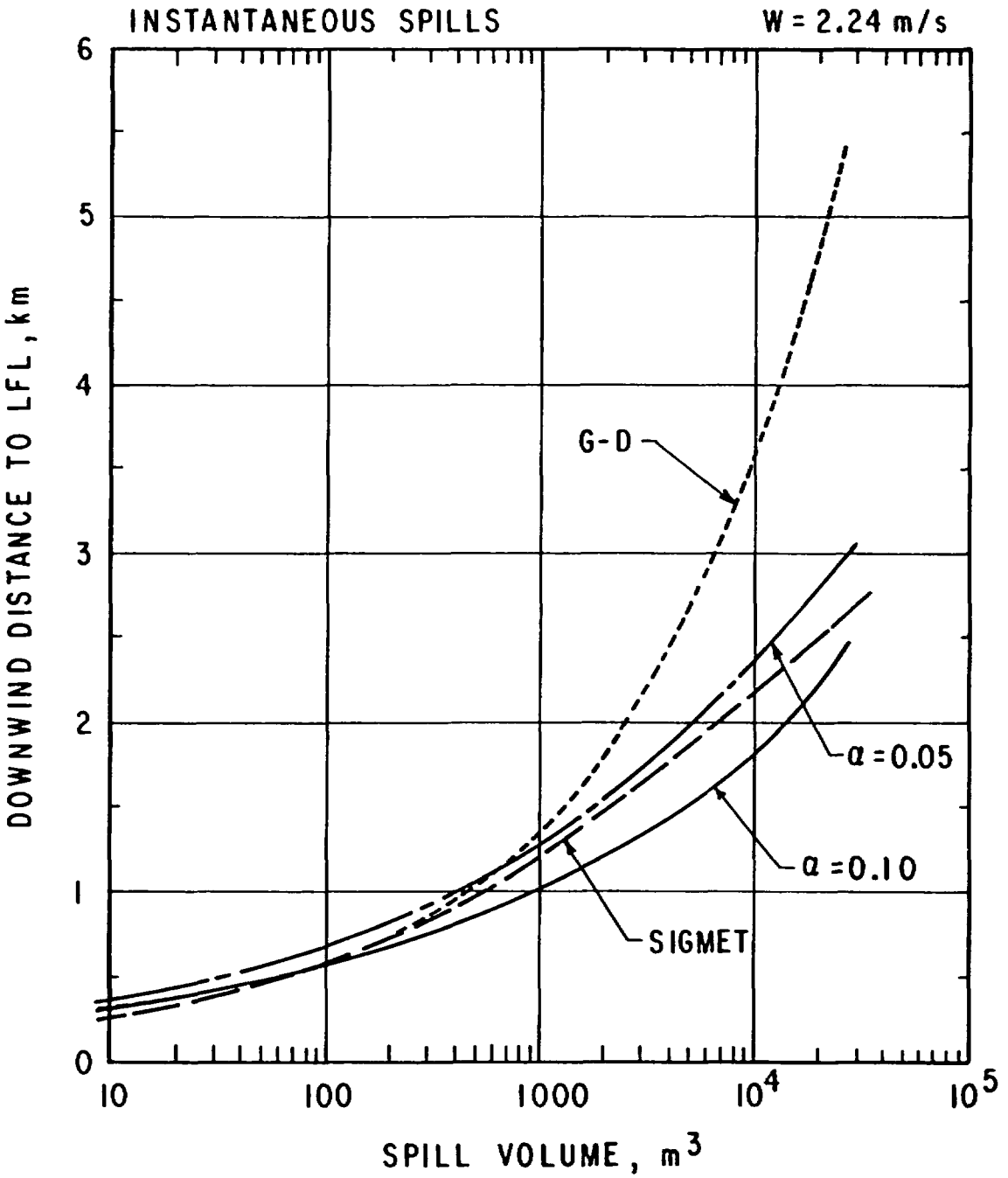

Figure 11. Comparison of Maximum Downwind LFL Distances.

TABLE 1

LIST OF VARIABLES FOR CLOUD DYNAMICS MODEL
INCLUDING CODE DETAILS

PARAMETERS:

Froude multiplier for pool	2
Froude multiplier for cloud	2
Pool breakup depth	.0018 m
Molecular weight of methane	16.0
Molecular weight of air	28.967
Molecular weight of water	18.0
Density of water	1.0 g/cm^3
Density of liquid LNG	.4487 g/cm^3
Temperature of saturated LNG	111.7 K
Specific heat for air	.24 cal/g K
Specific heat for LNG vapor	.48 cal/g K
Specific heat of water vapor	.48 cal/g K
Specific heat of liquid water	1.0 cal/g K
Atmospheric pressure	.101325 MPa
Wind gradient height	228.6 m
Exponent for wind profile	.16
Momentum factor	.90
Drag coefficient	.30

INPUT VARIABLES:

Peak release rate (VOD)	m^3/s
Release duration (TO)	s
Temperature of air (TEMPA)	°C
Temperature of surface (TEMPS)	°C
Relative humidity (RHUM)	%
Molecular weight factor (FMOLWT)	
Entrainment factor (ALFA)	
Wind speed at gradient height (WIND)	m/s
Vaporization rate (VAPR)	m/s

OUTPUT VARIABLES:

Time	s
Cloud radius	m
Cloud height	m
Pool radius	m
Pool depth	m
Cloud spread rate	m/s
Concentation (by volume)	
Cloud velocity	m/s
Cloud drift	m

(Plus many other variables such as:
Cloud Temperature, Energy, Density, etc)

volume (25,000 m^3) and the form of the LNG release, i.e., linearly decaying outflow. Thus the initial maximum spill rate is uniquely determined by the total spill volume and the spill duration.

Among the input variables the influence of ambient temperature, at least for dry air, is found to be minor. Although the effects of some of the other variables may be significant, e.g., vaporization rate, there appears to be sufficient experimental evidence to choose values that are realistic. Thus these parameters were not included in the sensitivity studies. To provide a basis for comparison and to evaluate the influence of various parameters, standard reference conditions were chosen; these are given in Table 2. Also listed in Table 2 are the variables evaluated in the sensitivity studies. The molecular weight factor is used to model, in a approximate way, the influence of LNG composition.

The results of the parameter studies are primarily time histories of such variables as volumetric concentration, cloud radius and height, spreading rate, drift velocity, and drift distance. They are summarized here in a series of tables and are presented in detailed graphs in Appendixes B and C. SI units are used in the tables; thus, all lengths are in meters, time in seconds, and velocities in m/s. The tables present the physical sizes of the vapor cloud at the UFL and LFL as well as the drift distance of the cloud center of mass. To obtain the total downwind range (distance) of the cloud, the cloud radius must be added to the drift distance. Variables not specified in the tables take on the values specified above as reference conditions.

Table 3 summarizes the effect of entrainment coefficient and wind speed. As may be expected, the entrainment coefficient, α, influences primarily the cloud size, i.e., its height and radius, particularly at the LFL. A similar effect is noted (in Appendix B) in the variation of cloud LNG concentration with time. Although a lower value of α appears to give a more conservative answer (larger cloud dimensions), the most realistic experimental estimate of this parameter is around a value of 0.10 (see Appendix B and Ref. 1). When, as is proper, drift is included in the model,the wind speed is seen to have essentially no effect on the cloud dimensions, which are solely goverened by the gravity spreading and air entrainment. The major influence of wind speed is on the drift velocity and cloud travel distance. The drift velocity reaches a value of about two-thirds of the wind speed at the time the LFL is reached. Similarly, the drift distance is proportional to wind speed. This is illustrated in Fig. 12, which shows both the drift and the total downwind distance as a function of wind speed.

TABLE 2

REFERENCE CONDITIONS AND VARIABLES FOR LNG SPREADING

REFERENCE CONDITIONS:

Total spill volume	25,000 m^3
Spill duration	600 s
Entrainment coefficient	0.10
Vaporization rate	0.0003048 m/s
Molecular weight factor	1.00 (Pure methane)
Wind velocity	4.48 m/s
Ambient temperature	21.1 °C
Surface temperature	(Assume no external heating)
Relative humidity	0.0

VARIABLE PARAMETERS:

Entrainment factor
Spill duration
Wind speed
Relative humidity
External heating
Molecular weight factor

TABLE 3

INFLUENCE OF WIND AND ENTRAINMENT COEFFICIENT
ON CRITICAL CLOUD DIMENSIONS

25,000 m^3 SPILL

ALFA	WIND m/s	RADIUS, m		HEIGHT, m		DISTANCE, m	
		UFL	LFL	UFL	LFL	UFL	LFL
** WITH DRIFT **							
0.10	0	664	1646	16.0	37.9	0	0
0.10	2.24	666	1644	16.0	37.7	207	609
0.10	4.48	657	1645	16.0	37.9	412	1225
0.10	8.96	622	1643	15.9	38.7	801	2501
0.05	0	1339	2099	16.0	24.1	0	0
0.05	2.24	1338	2103	16.0	24.1	383	747
0.05	4.48	1331	2095	16.0	24.1	772	1497
** WITHOUT DRIFT **							
0.10	2.24	570	1545	15.6	41.6	-	-
0.10	4.48	397	1353	14.7	50.8	-	-
0.10	5.15	352	1251	14.3	52.0	-	-

CONCENTRATION: UFL = 15%
LFL = 5%

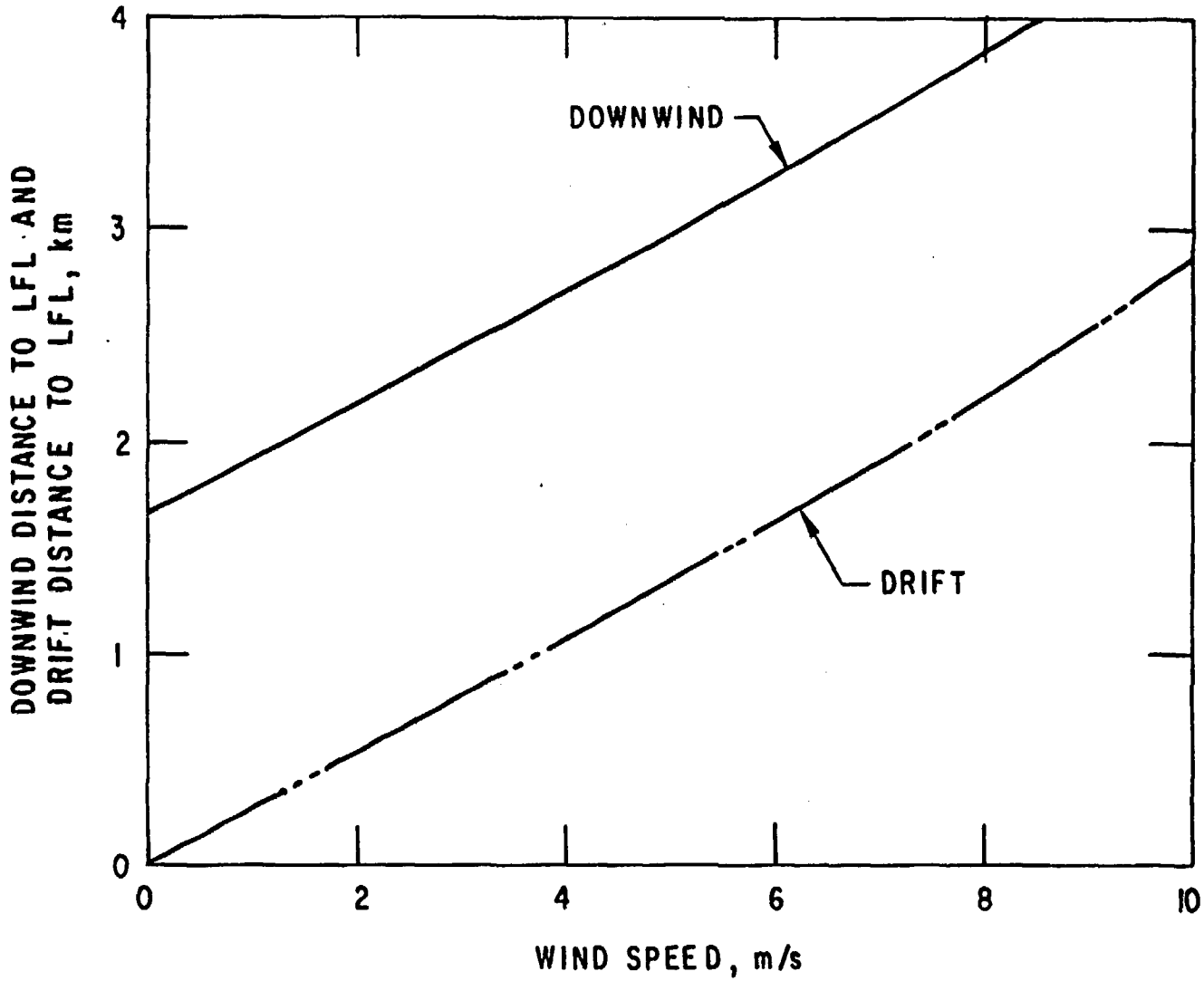

Figure 12. Influence of Wind Speed on Downwind Transport.

The dynamic behavior of a typical cloud variable is illustrated in Fig. 13, which gives the variation of volumetric LNG concentration as a function of time for various wind speeds. Initially, the concentration is 100%. It then decreases rapidly, since the cloud spreading, at early times, is controlled by the pool spreading. As the pool spread rate decreases, gravity spreading of the cloud dominates and the concentration increases again until a maximum of about 50% is reached. Thereafter the dilution (i.e., air entrainment) process dominates, and the concentration decreases until the flamability limits are reached. Ultimately, the concentration reaches a safe diluted state. The LFL is reached in about 500 s for the reference spill duration. This state is indicated by the dot in Fig 13. It is also clear that the concentration history is not significantly influenced by the wind speed. A similar (three-phase) time history is indicated for the other dynamic variables such as the cloud spreading velocity. This and other detailed results are presented in Appendix C.

The effect of spill duration on the cloud dimensions and drift is summarized in Table 4. The results are for the reference wind speed of 4.48 m/s and dry air. All the dimensions appear to attain their peak values in the vicinity of the reference duration, i.e., 600 s. The same holds for all the dynamic variables. This also implies that the time to reach the LFL is the longest for this case. For more rapid spills, including the instantaneous spill, the decrease from the peak values is quite small. However, for long spill durations, the decrease from the peak values is quite significant, so that for spill durations of the order of 10 hours the cloud dimensions are reduced by more than a factor of four. This is illustrated in Fig. 14 for the cloud radius and the total downwind travel.

The influence of relative humidity on the cloud dynamics is investigated together with the effects produced by variations in the average molecular weight of the LNG, i.e., by the presence of some fraction of hydrocarbons other than methane. As indicated earlier, this fraction is controlled in the model simply by a molecular weight factor; all other properties of the LNG are assumed to be the same as those of pure methane. The results are summarized in Table 5. A careful examination of this data indicates that the effects of humidity in changing the cloud dimensions at the LFL and the drift are opposed by the increase of molecular weight.

To understand this phenomenon, we must examine the influence of water vapor alone on the cloud behavior. This influence is complex, because the water in contact with the cryogenic LNG can exist in all three phases (solid, liquid, and vapor). The primary effect of the water is to alter the thermodynamic state of the mixture, and although the quantity of water may

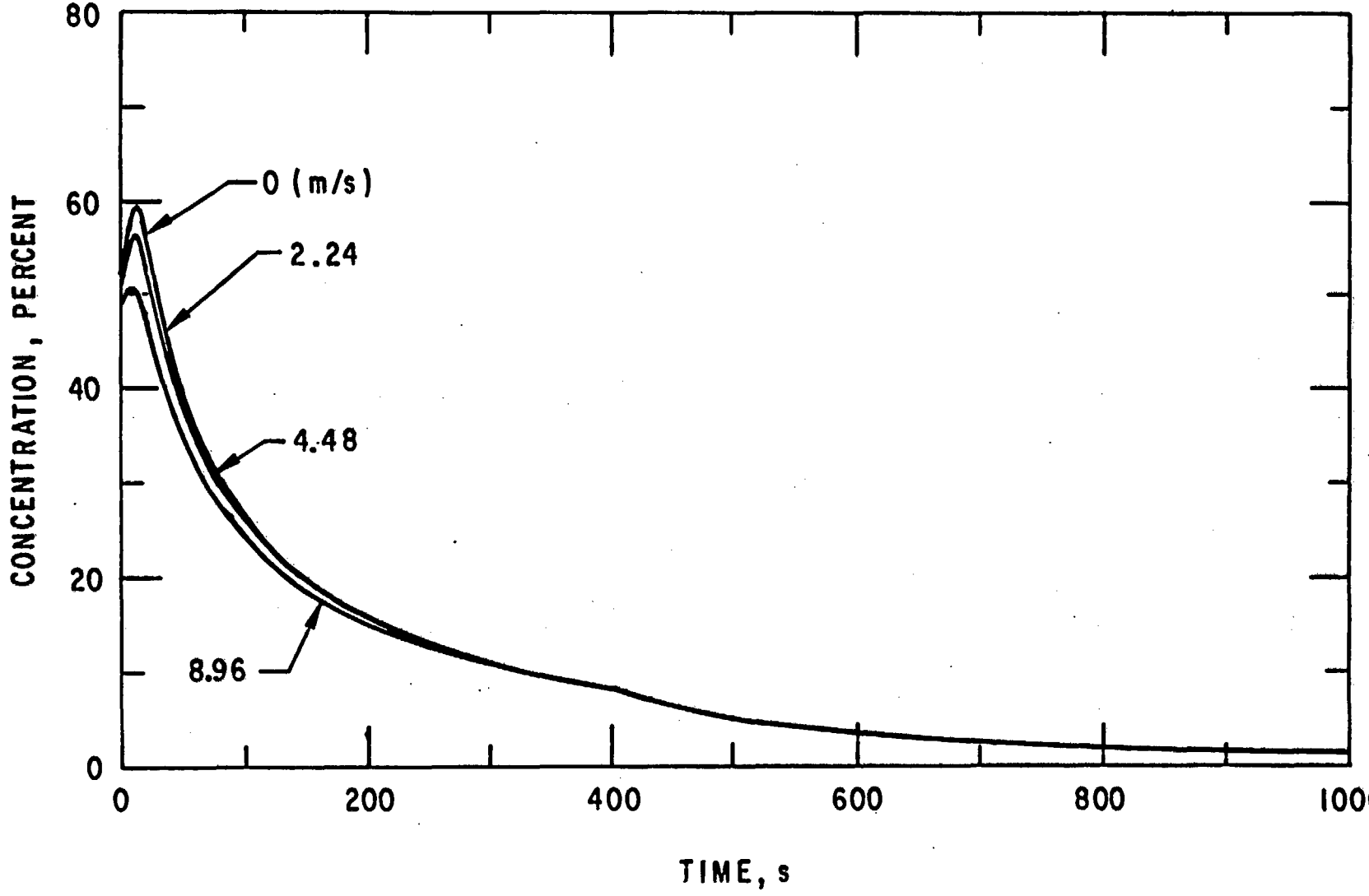

Figure 13. Effect of Wind Speed on Vapor Cloud Volumetric Concentration.

TABLE 4

INFLUENCE OF SPILL DURATION ON
CRITICAL CLOUD DIMENSIONS

25,000 m^3 SPILL

DURATIONS, s	RADIUS, m		HEIGHT, m		DISTANCE, m	
	UFL	LFL	UFL	LFL	UFL	LFL
.06	836	1524	20.3	35.1	439	999
.6	850	1562	20.6	36.0	443	1023
6	891	1591	21.0	36.7	460	1069
60	901	1637	21.3	37.7	473	1087
120	906	1649	21.8	38.0	505	1092
360	751	1667	18.2	38.4	452	1181
600	678	1648	16.1	37.5	421	1216
1200	540	1435	13.1	33.1	361	1156
1800	482	1260	11.8	29.1	336	1059
3600	388	980	9.5	22.7	289	887
5400	344	826	8.5	19.1	267	775
6000	339	798	8.1	18.7	264	785
7200	315	718	7.7	16.7	252	689
18000	234	514	5.7	12.0	205	552
36000	185	390	4.6	9.2	174	455
60000	156	316	3.9	7.5	153	392

CONCENTRATION: UFL = 15%
LFL = 5%

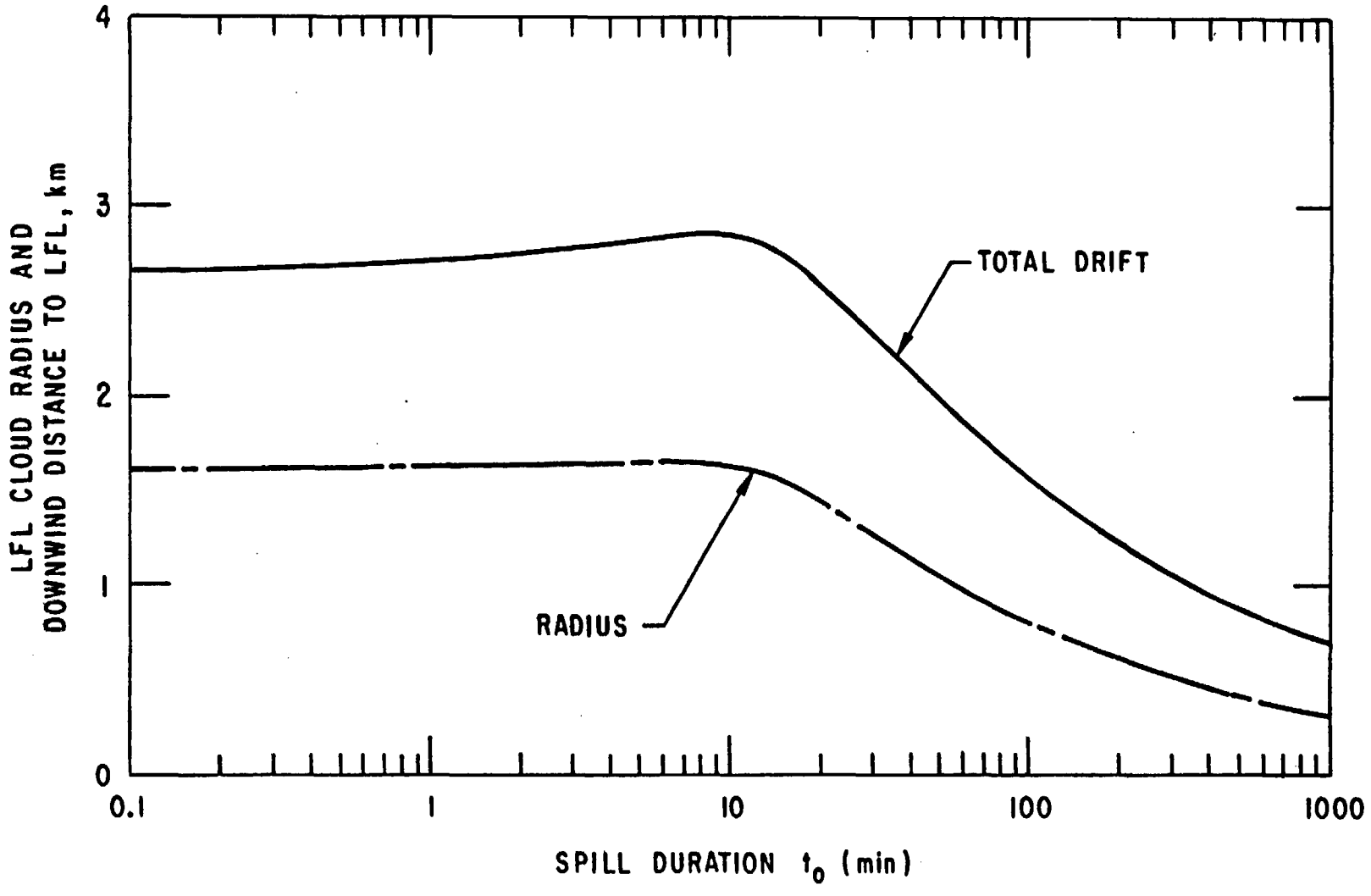

Figure 14. Influence of Spill Duration on Cloud Radius and Drift; Wind Speed = 4.48 m/s.

TABLE 5

INFLUENCE OF HUMIDITY AND MOLECULAR WEIGHT
ON CRITICAL CLOUD DIMENSIONS

25,000 m^3 SPILL

RELATIVE HUMIDITY, %	MOL. WEIGHT FACTOR	RADIUS, m		HEIGHT, m		DISTANCE, m	
		UFL	LFL	UFL	LFL	UFL	LFL
0	1.0	678	1648	16.1	37.5	421	1216
25	1.0	803	1653	19.3	37.5	546	1247
50	1.0	1076	1657	26.6	38.4	907	1576
60	1.0	1089	1652	27.6	38.5	1024	1829
70	1.0	1076	1627	29.0	41.0	1222	2690
75	1.0	984	1420	35.1	52.1	1476	4112
80	1.0	910	1144	41.4	80.7	1638	5772
85	1.0	863	926	45.8	122.8	1741	6752
90	1.0	827	897	50.1	130.6	1839	7195
100	1.0	773	855	57.9	144.6	2026	8159
0	1.1	508	1575	11.8	36.0	282	1111
50	1.1	723	1598	17.5	36.5	486	1262
70	1.1	900	1607	22.3	36.9	691	1418
75	1.1	959	1606	23.9	37.0	767	1569
80	1.1	1018	1603	25.5	37.3	855	1707
90	1.1	1038	1588	26.5	37.9	943	2193
100	1.1	1043	1147	27.4	72.6	1052	4150
0	1.2	408	1490	9.3	33.4	209	953
50	1.2	530	1533	12.6	34.8	314	1107
75	1.2	650	1556	15.9	35.6	430	1281
100	1.2	820	1558	20.5	36.2	620	1633

CONCENTRATION: UFL = 15%
LFL = 5%

be small, the effect may be significant because the latent heat of vaporization is very large. For pure methane and high relative humidities, it is even possible to obtain mixture densities that are slightly smaller than that for air. Thus a stall condition in the cloud spreading may be achieved. This stall process may be only temporary, since the wind effect (if present) will allow the dilution process to continue this dilution, together with the associated thermodynamic effects, may result in sufficient increase in mixture density to permit the spreading by gravity to continue. This process is best understood by examining the radius-time histories for pure methane LNG at various relative humidities, as shown in Fig. 15. For relative humidities up to 50%, the vapor-cloud spreading is little affected. However, for relative humidities in excess of 70%, the above-described stall condition occurs and the cloud radius remains essentially unchanged (spreading velocity is zero). For a relative humidity of 75%, this is seen to be a temporary condition and thereafter the cloud radius increases again rapidly. For 100% humidity, the stall situation persists and the radius remains essentially constant until the LFL condition (dot) is reached at about 7200 s. Significant cloud height growth will occur during stall due to continued entrainment of air at a constant cloud-radius condition. If subsequent spreading occurs, the increased cloud height may drive the cloud to large velocities and some cloud height reduction may actually occur. Finally, the cloud drift distance at the LFL increases, simply (see Table 5) because a longer period of time is needed to achieve this condition.

The cloud radius history for a heavier LNG composition (1.2) is shown in Fig. 16. A much more conventional behavior is observed, and although some differences do occur over the full humidity range, they are significantly reduced as compared to pure methane. Clearly, the mixture density is always greater than the ambient air density. Figure 17 shows the total downwind distance (drift plus radius) as a function of relative humidity for three gas compositions, i.e., pure methane and LNG which is 10% and 20% heavier than methane. The influence of the relative humidity on this critical transport distance is dramatic for pure methane, yielding a downwind distance about three times as large as for dry air. For the intermediate gas composition, stall conditions are just developing when the humidity reaches 90-100%. This causes the downwind distance to be doubled when compared with that for dry air.

The effects of heat transfer from the water surface in combination with other conditions, specifically relative humidity, LNG composition, and spill duration are summarized in Table 6. In general, the influence of heating is insignificant. The only observable effect is on the onset of stall; i.e.,

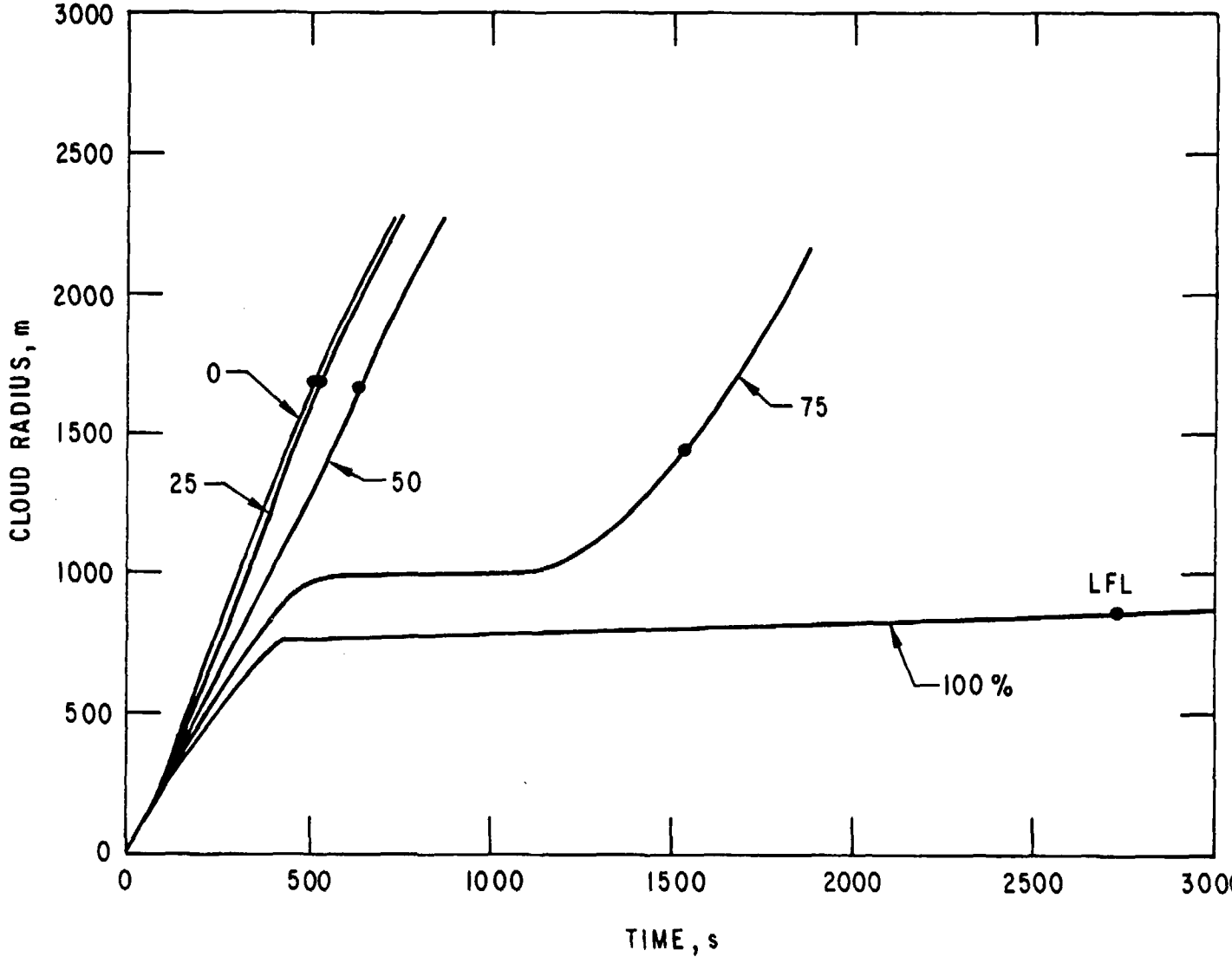

Figure 15. Effect of Relative Humidity on Vapor Cloud Radius for Pure Methane; Wind Speed = 4.48 m/s.

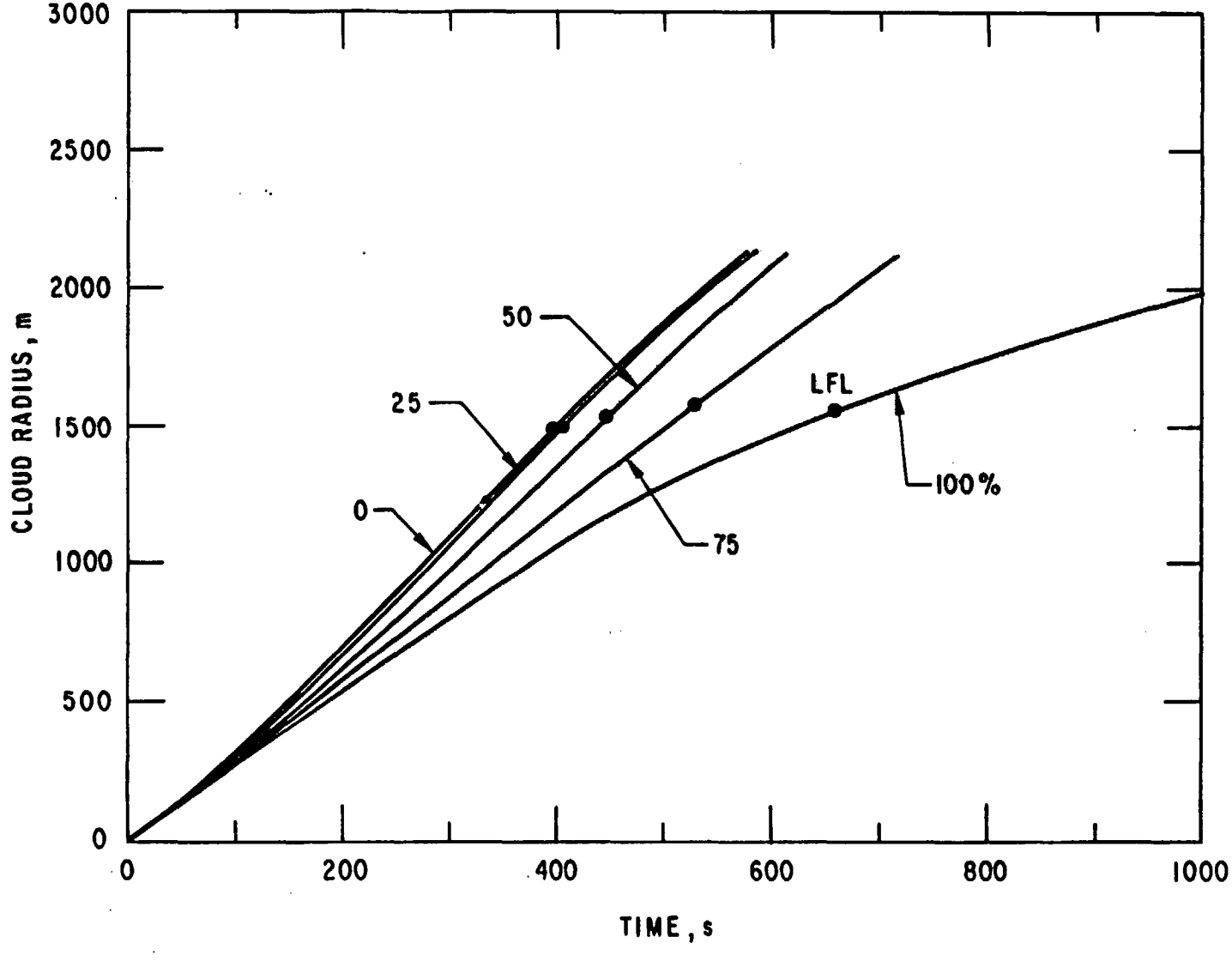

Figure 16. Effect of Relative Humidity on Vapor Cloud Radius for LNG (1.2); Wind Speed = 4.48 m/s.

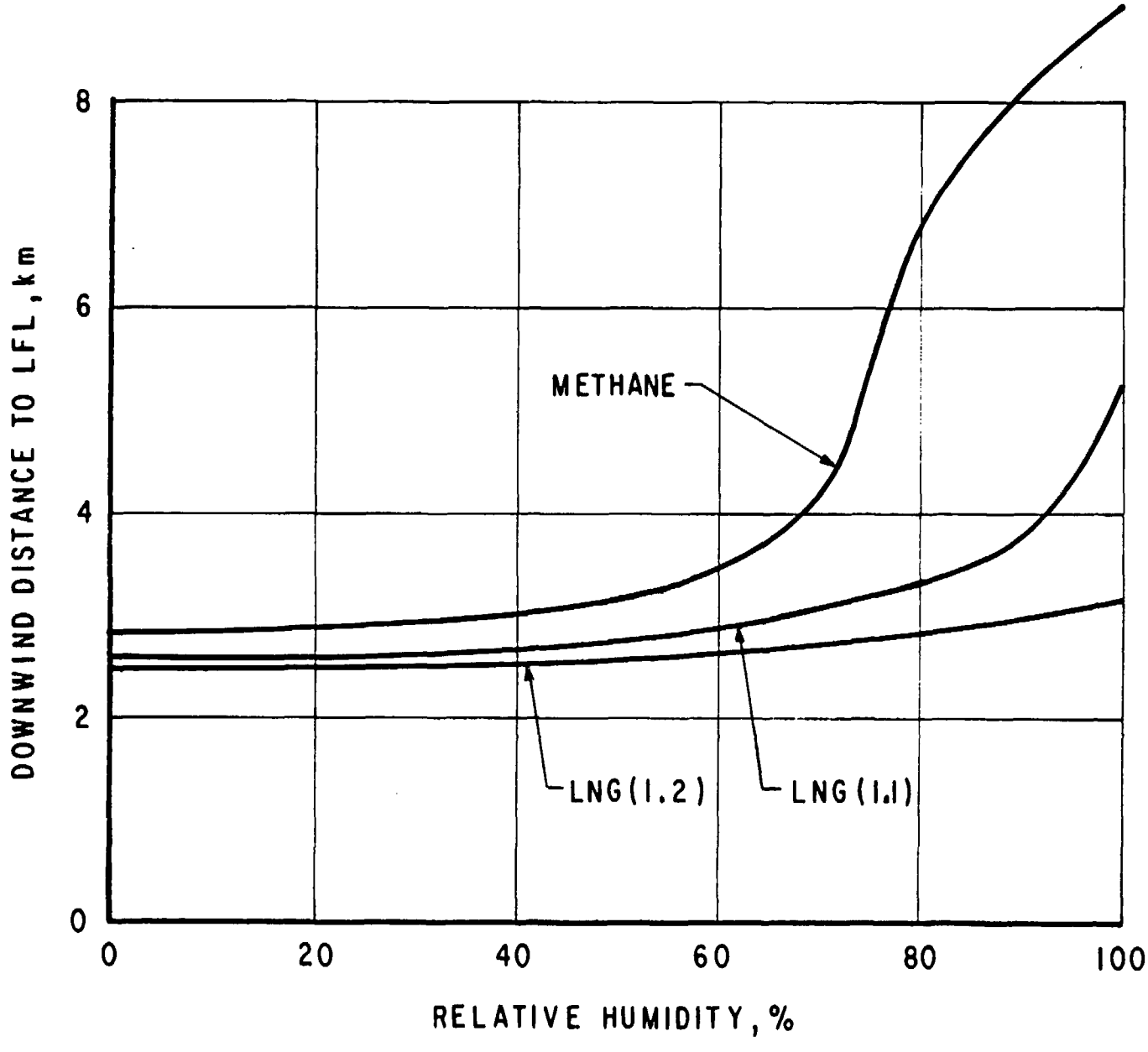

Figure 17. Influence of Relative Humidity and LNG Composition on Downwind Distance to LFL; Wind Speed = 4.48 m/s.

TABLE 6

INFLUENCE OF EXTERNAL HEATING ON
CRITICAL CLOUD DIMENSIONS

25,000 CU M SPILL

RELATIVE HUMIDITY, %	MOL. WEIGHT FACTOR	RADIUS, m		HEIGHT, m		DISTANCE, m	
		UFL	LFL	UFL	LFL	UFL	LFL
** WITH EXTERNAL HEATING **							
0	1.0	698	1651	16.6	38.1	442	1287
50	1.0	1083	1656	26.9	38.4	936	1625
75	1.0	923	1225	40.1	69.8	1601	5362
100	1.0	752	841	61.0	149.6	2099	8498
0	1.2	412	1509	9.4	33.6	216	949
50	1.2	541	1534	12.9	35.1	342	1129
75	1.2	660	1556	16.2	35.6	441	1292
100	1.2	834	1557	20.9	36.4	637	1692
** WITHOUT EXTERNAL HEATING **							
0	1.0	678	1648	16.1	37.5	421	1216
50	1.0	1076	1657	26.6	38.4	907	1576
75	1.0	984	1420	35.1	52.1	1476	4112
100	1.0	773	855	57.9	144.6	2026	8159
0	1.2	408	1490	9.3	33.4	209	953
50	1.2	530	1533	12.6	34.8	314	1107
75	1.2	650	1556	15.9	35.6	430	1281
100	1.2	820	1558	20.5	36.2	620	1633

SPILL DURATION, s	RADIUS, m		HEIGHT, m		DISTANCE, m	
	UFL	LFL	UFL	LFL	UFL	LFL
** WITH EXTERNAL HEATING **						
6	899	1590	21.3	36.8	470	1092
60	915	1636	21.6	37.7	487	1120
600	698	1651	16.6	38.1	442	1237
6000	352	808	8.5	18.9	288	822
** WITHOUT EXTERNAL HEATING **						
6	891	1591	21.0	36.7	460	1069
60	901	1637	21.3	37.7	473	1087
600	678	1648	16.1	37.5	421	1216
6000	339	798	8.1	18.7	264	785

CONCENTRATION: UFL = 15%
LFL = 5%

stall occurs at a slightly lower relative humidity, and hence the cloud drift is somewhat increased.

5. LNG FIRES

The fire that may develop following a massive spill of LNG on water will depend on a number of factors. Foremost of these is the type, location, and timing of the ignition source. Others are the gas composition, cloud homogeneity, cloud turbulence, and possible confinement. Considering only the fire of unconfined, combustible LNG vapor clouds, a recent review of the subject [15] states that the ability to predict the thermal radiation for such a cloud has not been demonstrated. However, other investigators (see section 4 of Appendix B) have shown that, aside from a direct LNG pool fire, the specific fire scenarios that may occur depend primarily on the degree of premixing of fuel vapor and air. Thus, for the fuel-rich mixtures, turbulent diffusion flames may be expected; a premixed cloud, i.e., one with concentrations below the UFL, has a tendency to burn as a fireball or a rapidly moving flame sheet. Using these facts, a simplified LNG global fire model is synthesized that is compatible with the global treatment of LNG pool and vapor-cloud spreading. This model essentially addresses the regime of relatively low flame speeds when the primary hazard is the thermal flux.

5.1 Fire-Model Description

The integrated fire model is based on the current state of the art and treats three separate fire regimes: pool fires; diffusion flames propagating through a fuel-rich vapor cloud, i.e., a cloud having an average concentration above the UFL; and a reaction zone propagating through a premixed cloud, i.e., within the flammability limits.

5.1.1 Pool Fires

The literature [16] identifies three techniques for modeling the heat radiation from LNG fires: (1) rigorous solutions of the gas-radiation problem, (2) point-source models, and (3) emitting surface models. The last approach is found to be most appropriate for the current application (see Appendix B), providing a reasonable balance between model simplicity and accuracy.

The emitting surface model considers the flame to be a solid body of simple geometry, e.g., a cylinder or a cone, which emits radiant energy from its surface as a gray body with an effective emissivity ε_f given by:

$$\varepsilon_f = 1 - e^{-aD} , \qquad (14)$$

where a is the absorption coefficient for the flame and D is the flame

diameter. For large diameters, the emissive power E_f is effectively that of a black body. The radiant energy flux leaving the flame is then given by; $\varepsilon_f E_f$ and the energy flux reaching the target is given as

$$\dot{q} = \tau F \varepsilon_f E_f, \tag{15}$$

where τ is the atmospheric transmissivity and F is the configuration factor. The emitting surface model is illustrated in Fig. 18, and the configuration factor is defined as

$$F = \int_{A_s} \frac{\cos \theta_t \cdot \cos \theta_s}{\pi S^2} dA_s. \tag{16}$$

Here the subscripts s and t refer to the source and target, respectively, and θ is the angle between the ray connecting the incremental source surface element with the target and the appropriate surface normal. The length of the ray is S, and A_s is the surface area of the source. The configuration factor thus defines the flame geometry (height, diameter, and tilt) and the distance and orientation of the target surface. Note that the latter is really a surface element of the total target geometry.

The emitting surface model captures the essential features of the pool fire problem and yet maintains adequate simplicity. Expressions for each of the terms in Eq. 15 are identified either from the literature or from simple physical considerations where the literature is incomplete. Thus, based on the best data available, a value of E_f= 210 kW/m^2 is selected for the optically thick emissive power, and the flame-absorption coefficient a = 0.16 m^{-1} is used (see Section 4.2 of Appendix B for details).

The configuration factor F, needed for computing the heat flux from a pool fire to an arbitrarily oriented surface element of a target, can be rigorously defined by integrating Eq. 16. This integration can in most cases be carried out only numerically, and some computer programs have been developed for simple shapes (see Appendix B). Two options have been provided for the current modeling of pool fires. The incremental target surfaces are assumed to lie in either the vertical or horizontal planes and at specified distances and elevations from the pool center (but not engulfed by the flame). In the first option, a numerical integration of Eq. 16 is performed over a fire surface represented by a number of stacked disks of equal diameter which are staggered along the flame-tilt axis to account for wind drag. This is illustrated in Fig. 19a. This approach is very accurate and should be used for targets situated near the fire column. The other option uses simple analytical expressions for a flat rectangular radiating plane which may also be tilted from the vertical. The geometry is shown in

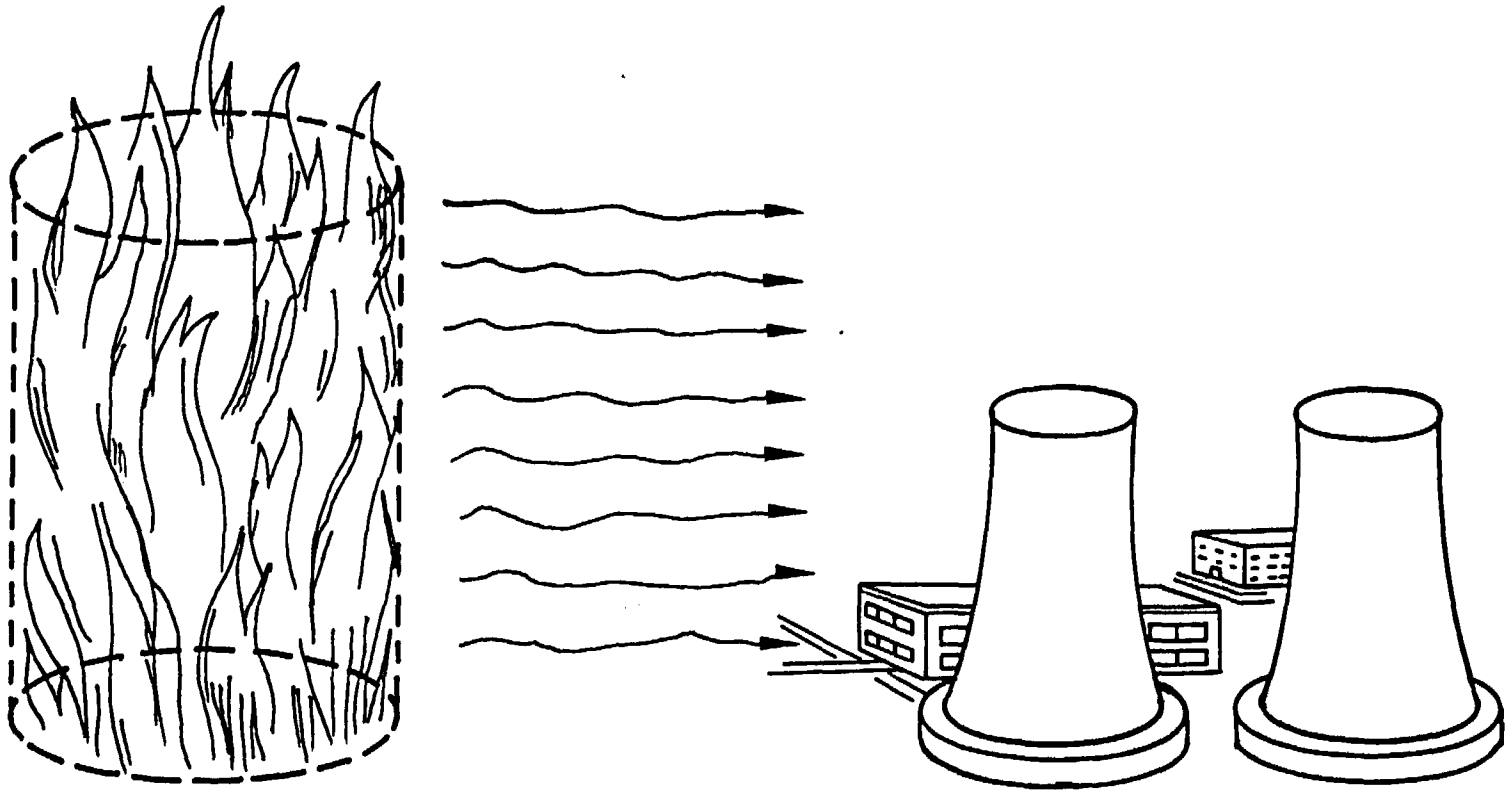

Figure 18. Emitting-Surface Fire Model.

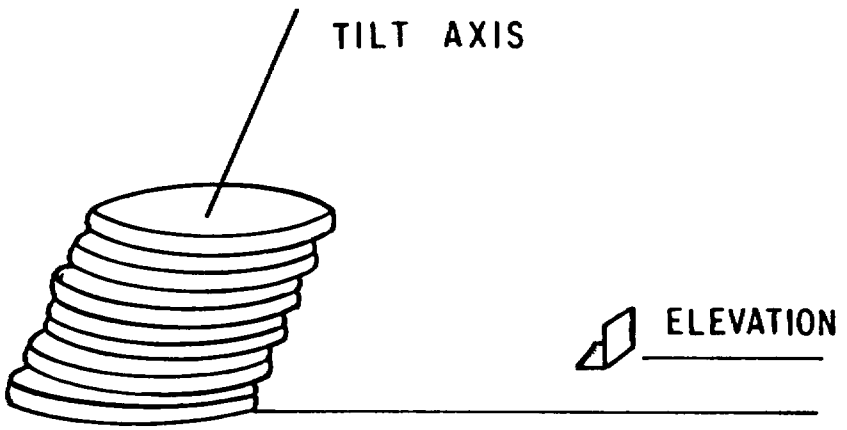

(a) NUMERICAL

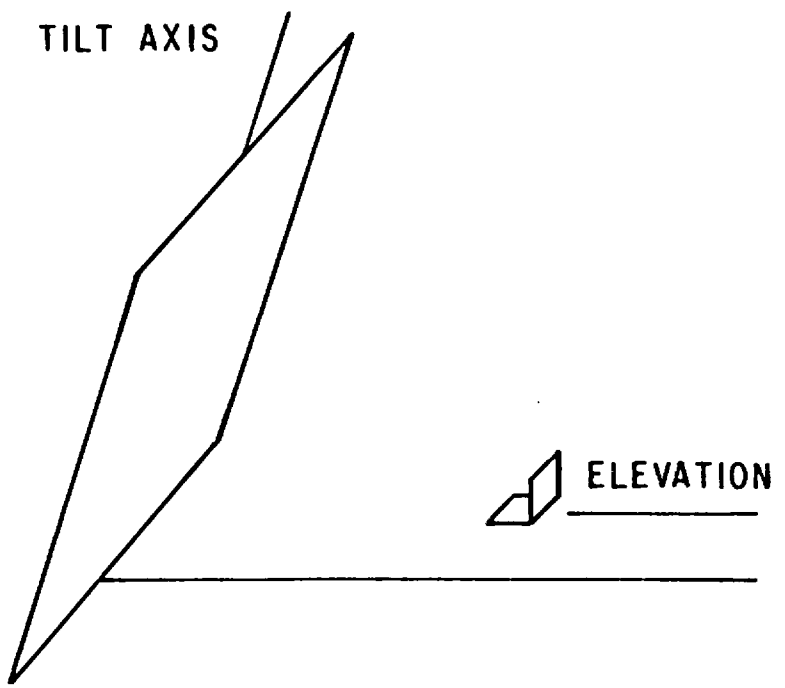

(b) ANALYTICAL

Figure 19. Configuration-Factor Models.

Fig. 19b and is generally accurate for large relative distances to the target. The latter must be downwind when wind tilt is used.

For circular pool fires, which is the assumption in the current model, the flame diameter is merely the LNG pool diameter. To define the flame height, it is necessary to rely on experimental correlations (see Appendix B). The most appropriate for the current application is given by Thomas [17], who identified the dimensionless parameters for correlating experimental flame length data. Thus a dimensionless vaporization rate μ is defined as

$$\mu = \frac{\dot{m}}{\rho_a \sqrt{gD}}, \tag{17}$$

where $\dot{m}$ is the mass vaporization rate per unit area, ρ_a is the ambient air density, g is the gravitational acceleration, and D is the flame diameter. The flame length to diameter ratio L/D is then given as

$$\begin{aligned} L/D &= 26\mu^{0.40}, && 0.1 < \mu, \\ L/D &= 42\mu^{0.61}, && 0.007 < \mu < 0.1, \\ L/D &= 56\mu^{0.67}, && \mu < 0.007. \end{aligned} \tag{18}$$

To account for the effect of wind on plume length, the following expression is used:

$$L/D = 70\mu^{0.86} \left(\frac{W^2}{gD}\right)^{-0.11}, \tag{19}$$

where W^2/gD is the Froude number and W is the wind speed.

The use of the above corrolations requires the knowledge of the vaporization rate. As indicated earlier, the best experimental data currently available [18] suggests as the liquid regression rate for a burning pool a value four times as great as for nonburning pools, i.e., 0.0012 m/s. This regression rate defines the vaporization rate for areas of the pool engulfed by the fire. It corresponds to a heat flux of about 210 kW/m^2, which is the same as the emissive power used for the pool fire flame.

To define the flame-tilt angle θ, experimental correlations must again be used [19]; they are

$$\frac{\tan\theta}{\cos\theta} = 3.3 \left(\frac{DW}{\nu_a}\right)^{0.07} \left(\frac{W^2}{gD}\right)^{0.08} \left(\frac{\rho_g}{\rho_a}\right)^{-0.6} \tag{20}$$

where ν_a is kinematic viscosity of ambient air and ρ_g is the density of the

cold vapor. Flame trailing, i.e., increased fire-base width, is neglected in the current model (see Appendix B). The final parameter needed in the pool-fire model, namely atmospheric transmissivity τ, is a function of specific atmospheric conditions. Based on some studies (see Appendix B), the effect is not thought to be very strong. Thus, a representative transmissivity-versus-distance relation is used for an atmosphere of 50% relative humidity and 21° C, namely,

$$\tau = 1.0 - 0.16 \log_{10} S, \qquad (21)$$

where S is the distance from the emitting surface to the target given in meters.

5.1.2 Diffusion Flames

The second fire regime considered in the current application is a diffusion-controlled flame for the fuel-rich vapor clouds. The wall-fire model of Raj [20] was adapted for this purpose. The flame is assumed to propagate at the turbulent flame velocity. The relationship between flame height H_f and flame width W_f can be obtained from experimental data [21] . The flame width W_f can then be calculated, at least for pure fuel-vapor clouds and a known vapor cloud height H, from the expression [21]

$$\frac{W_f}{H} = \frac{20}{H_f/W_f} \left[\frac{U_f^2}{gH} \left(\frac{\rho}{\rho_a}\right) \frac{\omega(\xi+\omega\rho_a/\rho)^2}{(1-\omega)^3}\right]^{1/3} \qquad (22)$$

$$\text{with } \omega = \left[1 + \frac{\Delta h_c}{\xi C_a T_a}\right]^{-1}.$$

Here U_f is the turbulent flame velocity, g is the gravitational acceleration, ρ is the density of the vapor, ρ_a is the ambient air density, ξ is the stoichiometric ratio, Δh_c is the heat of combustion, C_a is the specific heat of the ambient air, and T_a is the ambient temperature.

In the present fire modeling, Eq. 22 is used to estimate the maximum attainable flame width (or optical thickness) for diffusion flames in the vapor cloud and all concentrations above the UFL. The ratio H_f/W_f is treated as an empirical parameter with a nominal value of 0.5. Similarly, the nominal value of ω is 0.1 [21]. The diffusion-flame velocity U_f is

defined relative to the unburned gas and is also treated as an empirical parameter with values ranging from 1 to 20 m/s. The value of W_f calculated from the equation is compared to a value characteristic of the cloud volume consumed and cloud extent, and the minimum of these is used. The flame height is then computed from the assumed value of H_f/W_f, but is not allowed to be lower than the cloud height. In this way the flame geometry takes account of the finite dimensions of the cloud when most of the vapor is burned-off. It is tacitly assumed that the target is exposed to the maximum emitting surface area presented by the diffusion flame; therefore emissivity is based upon W_f.

5.1.3 Premixed Vapor Flames

Based on observations from a test series [22] with flammable mixtures of hydrocarbon fuels, the simple flame propagation model illustrated in Fig. 20 is developed. As shown, the flame thickness is x_o and the face area is A_o. The flame is moving at a specified velocity U_f, and a linear temperature profile across the flame is assumed. The model is based on the premise that, for steady-state flame propagation (no acceleration), the energy release must equal the total energy loss. For a flame velocity U_f and combustion efficiency η, the total energy release is

$$\frac{\dot{Q}_{total}}{A_o} = \rho_o U_f \chi_f \eta \Delta h_c \, x_o \qquad (23)$$

where ρ_o is the ambient density of the fuel-air mixture ahead of the flame, χ_f is the ratio of fuel mass to total mass of gas in the cloud, and Δh_c is the heat of combustion.

The total energy loss is taken as the radiant loss from the six faces of the rectangular flame slab. This is believed to be the dominant loss; although convective losses are also present, they are considered less important. While the heat loss can be obtained for any temperature profile (see Appendix B), the model is further simplified by assuming a uniform temperature profile T across the flame. The heat loss then becomes

$$\frac{\dot{Q}_{total}}{A_o} 2\sigma T^4 \left[1 - e^{-\alpha x_o} + \frac{x_o}{y_o}(1 - e^{-\alpha y_o}) + \frac{x_o}{z_o}(1 - e^{-\alpha z_o})\right] , \qquad (24)$$

where x_o, y_o, and z_o are the dimensions of the flame slab (see Fig. 20), is the Stefan-Boltzmanu constant, and α is the attenuation coefficient, which has a nominal value of 0.07 m^{-1} [22].

The turbulent flame velocity U_f relative to the unburned gas is of the order of 5.8 m/s [22] and is arrived at (see Appendix B) by the relationship

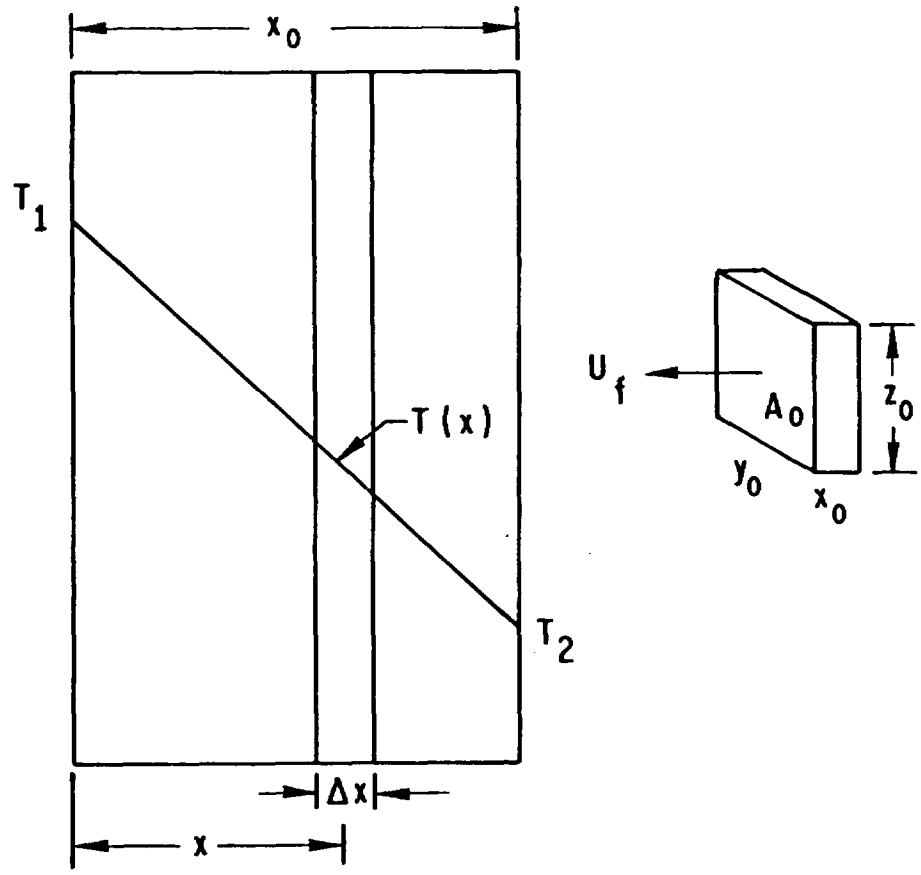

Figure 20. Model for Flame Propagating Through a Premixed Cloud.

$$U_f = \psi \frac{\rho_a}{\rho_f} U_L. \qquad (25)$$

Hear U_L is the laminar flame speed (about 0.37 m/s for a 10 vol % mixture of methane in air); ψ is the empirical turbulence enhancement factor, which has a value of about 2.1, and ρ_a/ρ_f represents the thermal expansion of the gases behind the flame front (value about 7.63). In the actual computational model, the flame-propagation velocity U_f is treated as a basic empirical parameter, which is varied. Similarly, the combustion efficiency η is treated as an empirical parameter with values between 0.4 and 1.0. In all computations, the stoichiometric fuel concentration for methane, i.e., 10 vol %, is used, which gives a mass ratio of $\chi_f = 0.058$. The flame thickness will vary with the flame velocity and flame temperature, and the maximum allowable thicknesses is defined by the iterative solution of eqs. 23 and 24 for x_o. Typical thickness at $U_f = 1$ m/s and $T_f = 2148$ K are 20 m; the width can be as much as 140 m for colder flame zones.

5.2 Integrated LNG Dispersion and Fire Model

It was pointed out earlier that existing models for the estimation of LNG accident consequences are only suited for gross predictions of the possible fire hazard. These models also take no account of the coupling between the dynamic spreading and dispersion of the LNG and the fire phenomenology. A major aim of the current effort has been to overcome some of these shortcomings, and in particular to couple the LNG dynamics and fire phenomena. In the simple global model developed here the coupling is not complete, e.g., while the effect of fire on LNG vaporization is taken into account the effect on cloud buoyancy is not included. Similarly the vapor cloud spreading model takes no account of the asymmetry produced by the propagating flame boundary.

The present combined LNG dynamics and fire modeling assumes that the vapor cloud can, at any stage of its spreading, encounter an ignition source. Accordingly, ignition is assumed to occur along either the upwind or downwind cloud-boundary trajectory. Ignition at the instant of spill is also accounted for an leads to a direct pool fire.

The flame is modeled as propagating through all or a portion of the vapor cloud as either a diffusion or premixed flame at selected values of consumption speed (flame speed relative to the unburnt vapor). The flame is convected by the local cloud spreading and drift and therefore may or may not ignite the pool. The dynamics of the cloud spreading is modified globally to adjust for the effect of cloud consumption. Also, dynamic

influences of the fire upon the cloud are accounted for globally through the estimation of the flame consumption or relative flame speeds. Fire-scenario characteristics include:

- o Pool fire only; immediate ignition condition.
- o Diffusion to premixed flame transition in the cloud at the UFL.
- o Flame extinguishment in the cloud when (1) the LFL is reached, or (2) burn-off of the cloud occurs.
- o Delayed pool ignition when the propagating flame reaches the pool boundary.

The existence of a pool fire modifies both the pool and cloud growths due to an increased (and initially transient) vaporization rate induced by the heat load into the pool.

The capabilities of the combined LNG dynamics and fire model are best illustrated by the distance-time representations of four scenarios given in Figs. 21-24. All are for wind speeds of 4.48 m/s (10 mph) and ignition times of 100 s after the start of the spill. Figure 21 shows the flame trajectory and transition for an assumed consumption speed of 1 m/s and downwind ignition. The pool does not ignite, and only a small portion of the total LNG burns off. At a consumption speed of 5 m/s (Fig. 22), the cloud burns off and the pool is ignited; all LNG spilled is consumed. Upwind ignitions under similar conditions produce a pool fire with the cloud flame extinguished at the LFL for 1 m/s and cloud burn-off at 5 m/s; these are shown in Figs. 23 and 24, respectively. The selected flame speeds in these results are assumed to apply to both the diffusion flame and the burnoff of premixed vapor clouds. It should also be pointed out that real LNG fires may progress somewhat differently and that the results to some extent reflect the idealizations of the model. In particular the assumption of a spatially uniform cloud composition leads to a sudden fire extinguishment at the LFL. In a real cloud some variation in vapor composition is expected, with the heaviest concentrations probably around the cloud center. Hence a more gradual fire extinguishment should be expected.

For any fire scenario the integrated model will also yield the incident radiant flux histories for targets located at arbitrary distances in the downwind or upwind direction. Two flux histories are computed at each location, namely, for vertical and horizontal targets, and the elevation of the target relative to the base of the fire may be specified. Typical radiant flux histories for a pool fire (immediate ignition) and targets at

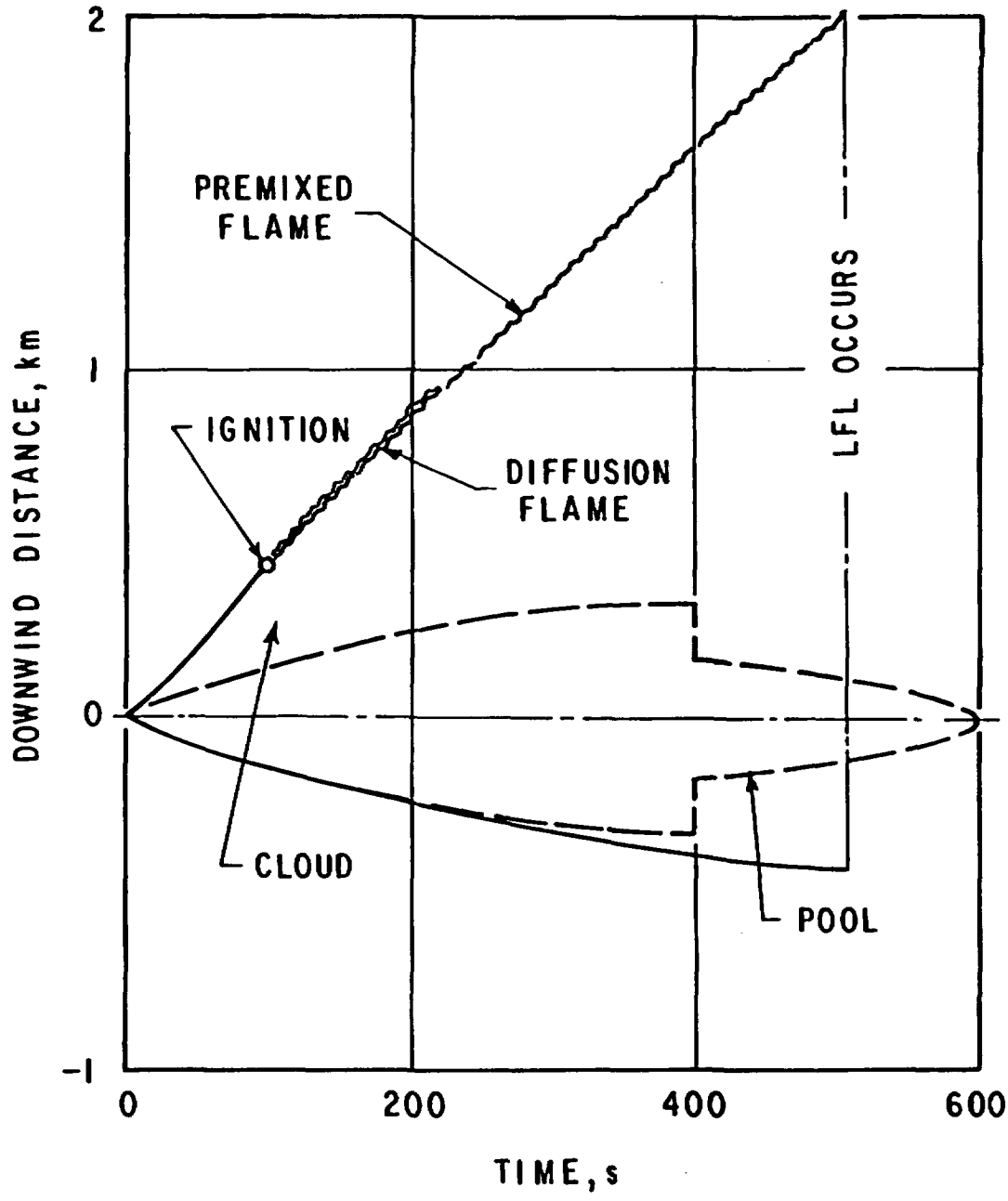

Figure 21. Flame Path for Cloud Fire; Downwind Ignition; Ignition Time = 100 s, Flame Speed = 1 m/s, Wind Speed = 4.48 m/s.

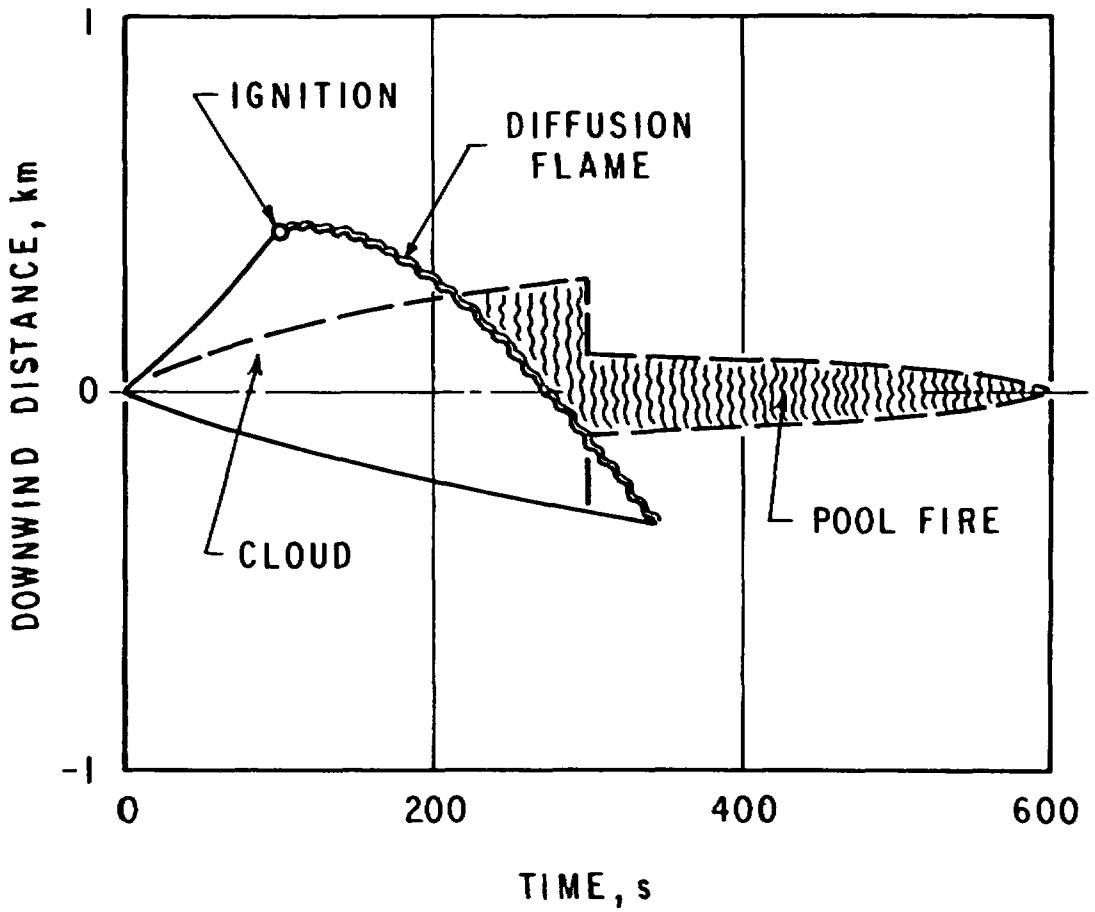

Figure 22. Flame Path for Cloud Fire; Downwind Ignition, Ignition Time = 100 s, Flame Speed = 5 m/s, Wind Speed = 4.48 m/s.

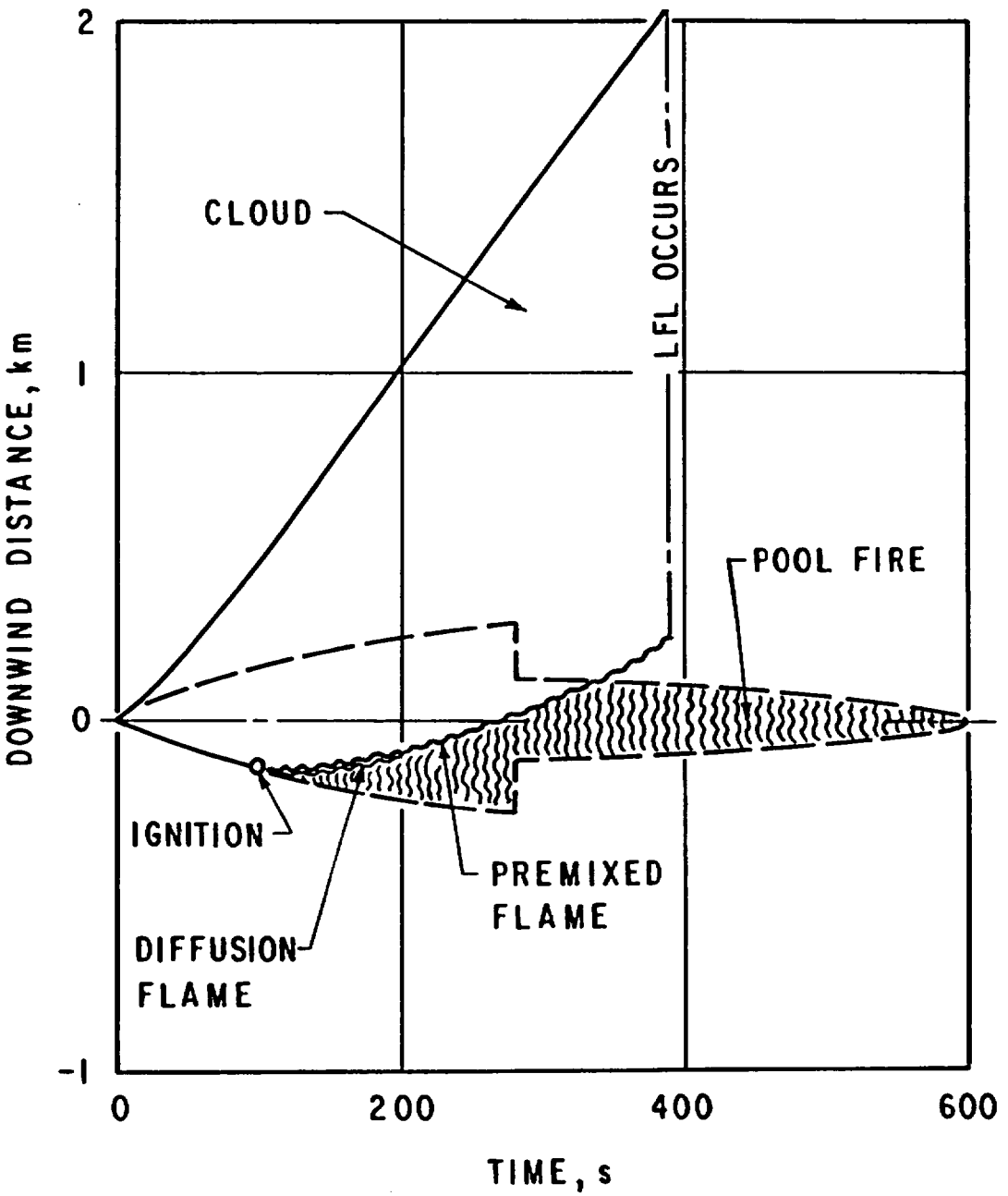

Figure 23. Flame Path for Cloud Fire; Upwind Ignition, Ignition Time = 100 s, Flame Speed = 1 m/s, Wind Speed = 4.48 m/s.

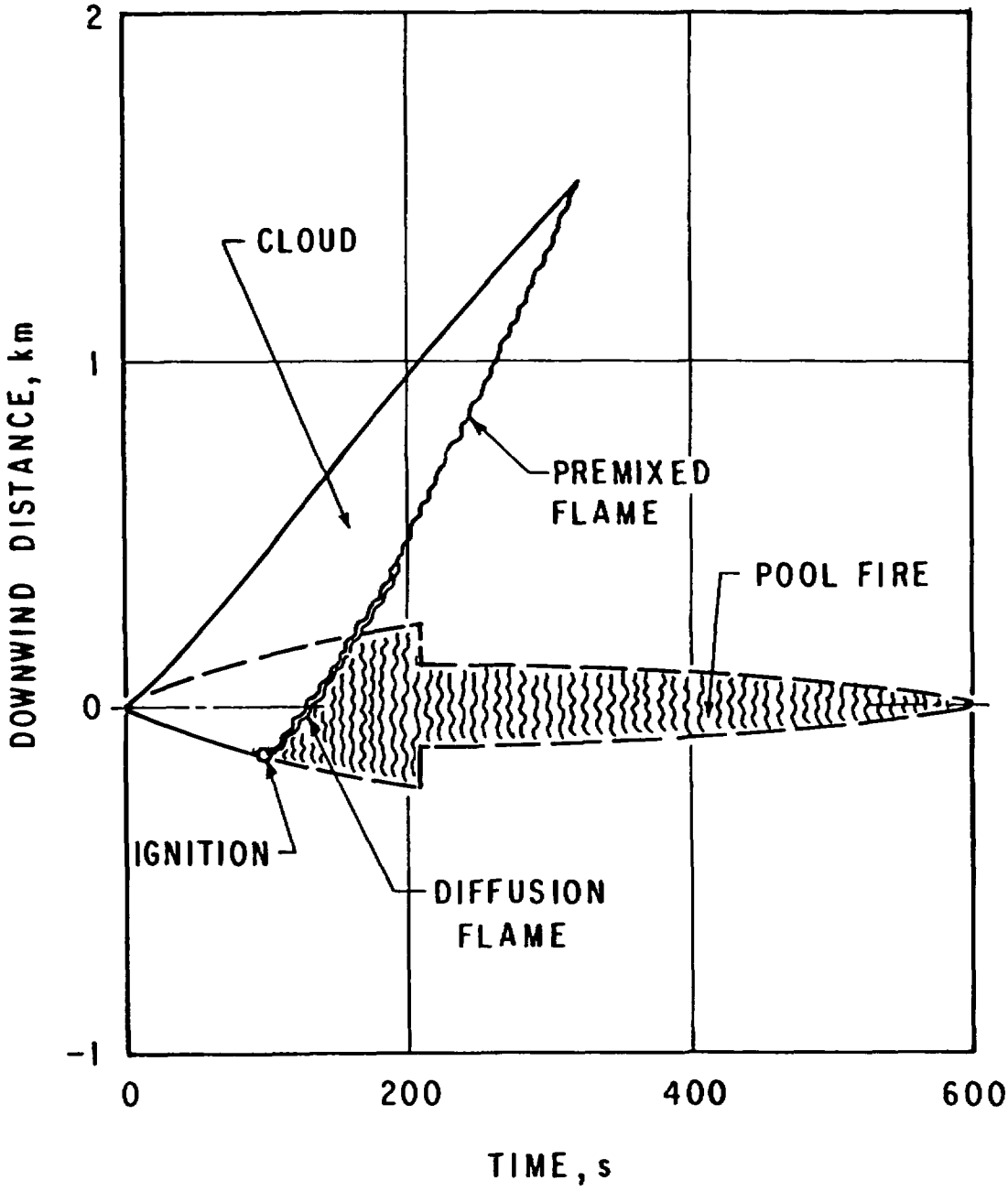

Figure 24. Flame Path for Cloud Fire; Upwind Ignition, Ignition Time = 100 s, Flame Speed = 5 m/s Wind Speed = 4.48 m/s.

zero elevation are shown in Fig. 25. As expected, the fluxes diminish with distance from the fire, and vertical targets (solid lines) receive more incident radiation then horizontal targets (dashed lines). The results shown in Fig. 26 are for vertically oriented targets, downwind ignition at 100 s, flame speed of 5 m/s, and wind speed of 4.48 m/s. In this case, upwind targets (negative sign) receive in general less radiation than downwind targets at comparable distances from the spill site. Detailed flux histories for a wide variation in the fire, spreading, and ignition parameters are presented in Appendices B and C.

The combined LNG dispersion and fire model computes only the heat fluxes arising from radiation at some distance from the fire. Thus targets engulfed by the fire are not treated by the model. Both radiation and convective heat fluxes are important in this case, and the target response cannot be decoupled from the heat input. The heat transfer must be based on the temperatures of the flame and target as well as the heat-transfer coefficient at the target surface. An upper boundary on the heat transfer for this case is readily estimated by assuming that the target-surface temperature quickly (instantaneously) becomes equal to the flame temperature.

5.3 Result Summary for LNG Fires

The foregoing description of the fire models indicates that a great multitude of fire scenarios may occur. It is therefore difficult to assemble a comprehensive result summary, particularly for the expected radiation-flux histories. Even when the problem parameters that only influence the vapor cloud spreading are fixed at their nominal values, it is found (see Appendix B) that at least five major variables influence the incident heat flux at any particular location:

- o Flame speed
- o Wind speed
- o Spill duration
- o Ignition time
- o Ignition location (upwind or downwind)

Although it is not possible to state categorically the order of importance of these variables, it does appear (Appendix B), that the total heat flux is least sensitive to the spill duration, at least for relatively short durations (under 1000 s). Obviously, in addition to the fire variables, the location (relative to the spill site) and orientation of the target will determine the incident heat flux. From the many computations carried out

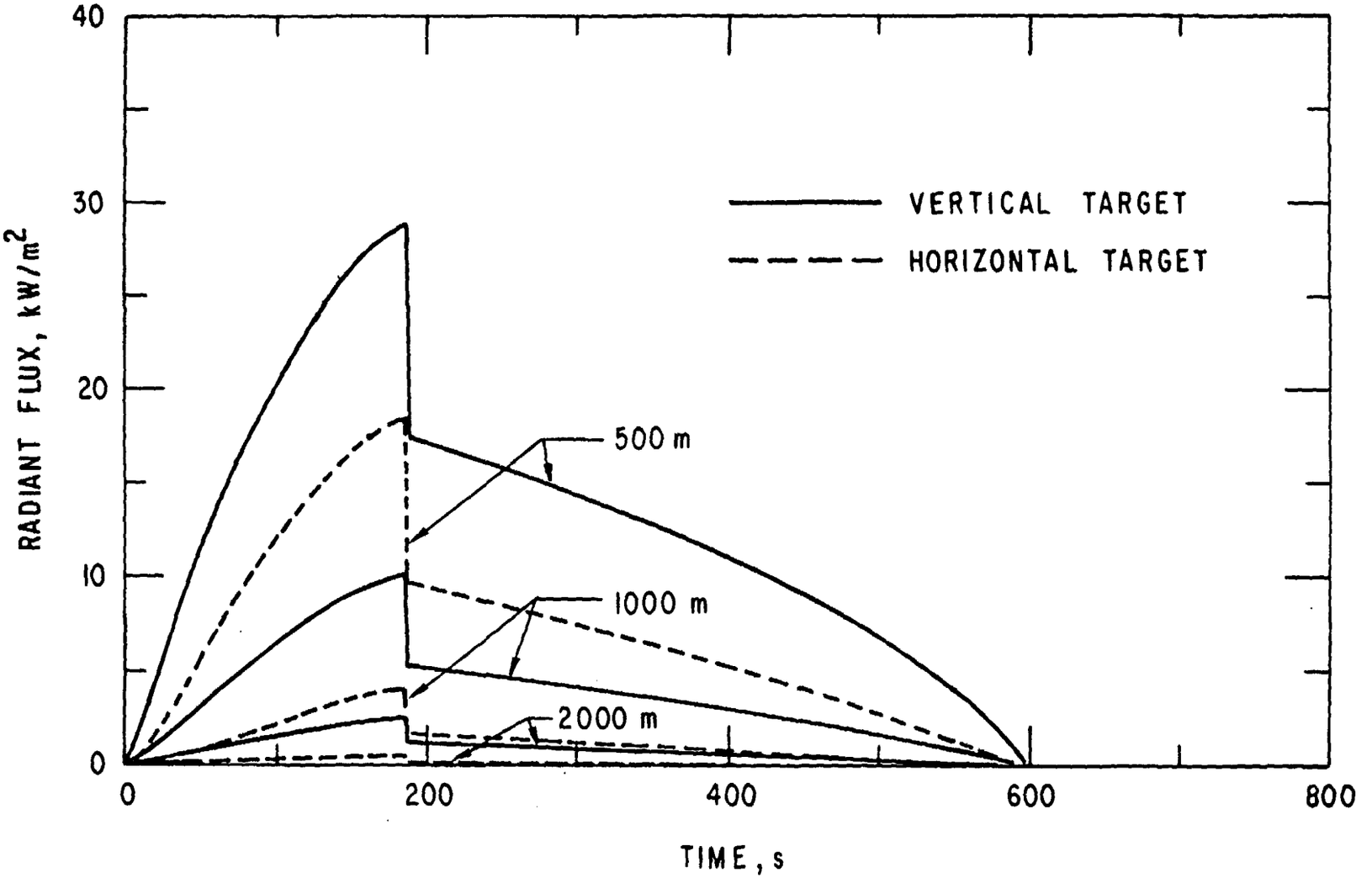

Figure 25. Thermal Radiation Histories for Pool Fire; Spill Duration = 600 s, Wind Speed = 4.48 m/s, Target Evaluation = 0.

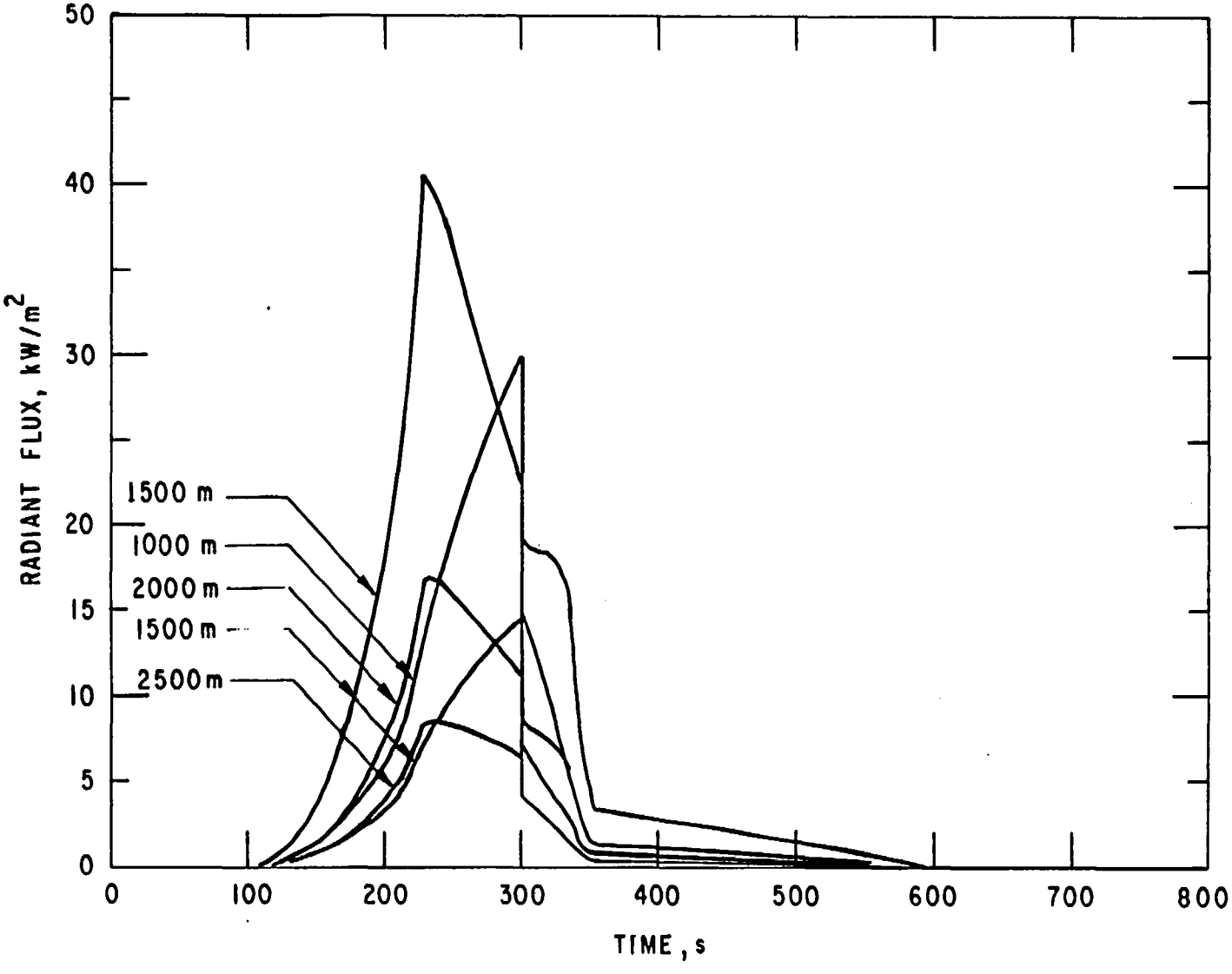

Figure 26. Thermal Radiation Histories at Vertical Targets; Downwind Ignition at 100 s, Spill Duration = 600 s, Wind Speed = 4.48 m/s, Flame Speed = 5 m/s.

(Appendixes B and C), it has also been found that a typical radiation-flux history cannot be defined; i.e., even qualitatively the radiation-time variations are not similar and depend strongly on the fire variables and the target location.

To arrive at certain generalizations, consider first the case of fixed spill duration (600 s) and zero wind speed, which in turn implies no cloud drift. Figures 27-29 show approximately the flame regions for this case as functions of the ignition delay time. The assumed flame speeds are 1, 5, and 10 m/s, respectively, and apply to all fire regimes, i.e., pool fire, diffusion flame, and premixed vapor cloud fire regions. The principal boundaries of the flame region are (1) the ignition boundary along which ignition is assumed to occur at some ignition delay time, (2) the cloud burn-off boundary that is reached if the entire vapor cloud is consumed, and (3) the LFL burnout boundary where the cloud fire is extinguished as its concentration drops below the LFL. Targets within about 2 km of the spill center can be expected to be within range of the flame, and this distance can, of course, increase significantly in the downwind direction if wind is present.

The time durations for the pool, vapor cloud, and total fire at a flame speed of 5 m/s are presented in Fig. 30. The pool and vapor cloud fire generally overlap, and except for spikes due to the cloud fire, the total fire durations are similar at all flame speeds (see Appendix C). The total fire durations are quite moderate, and the maximum duration is associated with immediate ignition, i.e., a direct pool fire. If ignition is delayed too long, the vapor cloud disperses below the LFL and no fire occurs. For similar no-wind conditions but a shorter spill duration (60 s), the total fire durations decrease substantially to about 200 s (see Appendix B). This is due to the fact that for shorter spill durations it takes less time to reach the LFL and the cloud radii are smaller than for the longer spill times.

Another measure of fire severity is the total thermal load incident at a particular location. Its value is obtained by integrating the incident radiant flux over the appropriate fire-duration interval. Figures 31-33 give the total thermal load again for a no-wind condition and the three reference flame speeds of 1, 5, and 10 m/s, respectively. Ignition delay times range from zero (immediate ignition-pool fire) through 400 s in steps of 100 s. Negative distances in these figures indicate the upwind direction or in this case the direction 180° out of phase with the ignition source. Because ignition can occur only at one edge of the cloud, the total thermal-energy distribution, except for immediate ignition, is not symmetric about

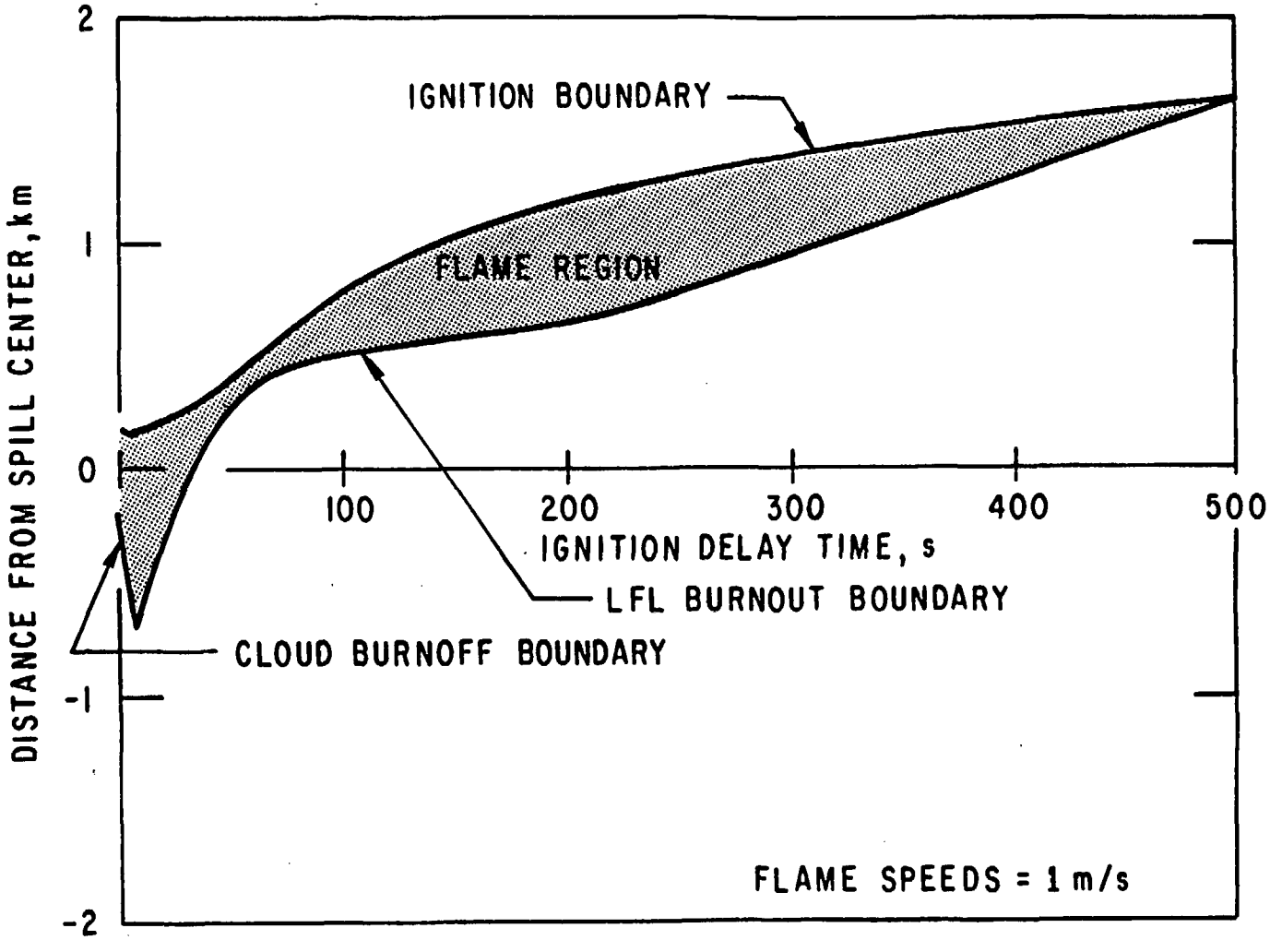

Figure 27. Extent of Flame Region as a Function of Ignition Delay Time for Flame Speeds of 1 m/s; Wind Speed = 0.

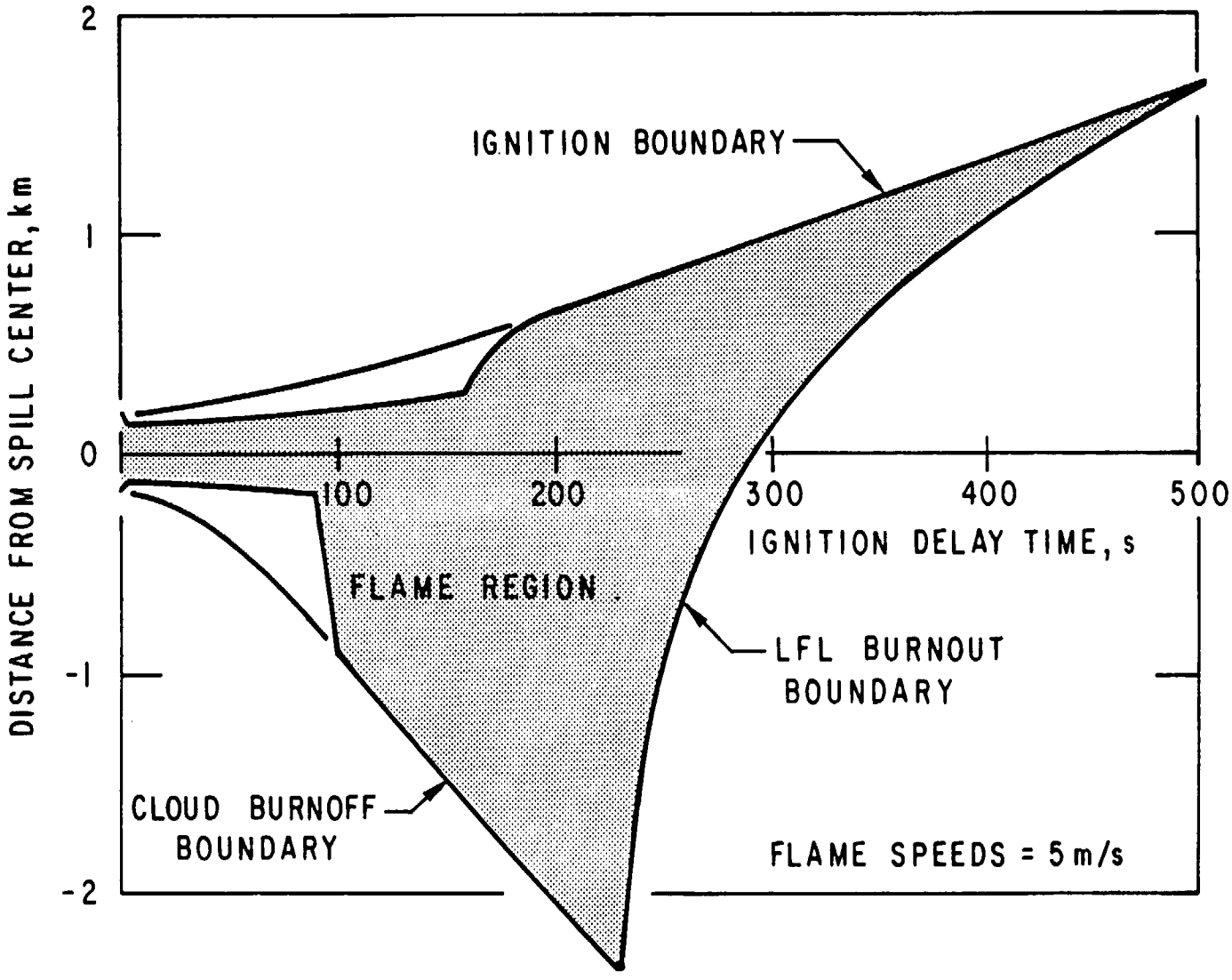

Figure 28. Extent of Flame Region as a Function of Ignition Delay Time for Flame Speeds of 5 m/s; Wind Speed = 0.

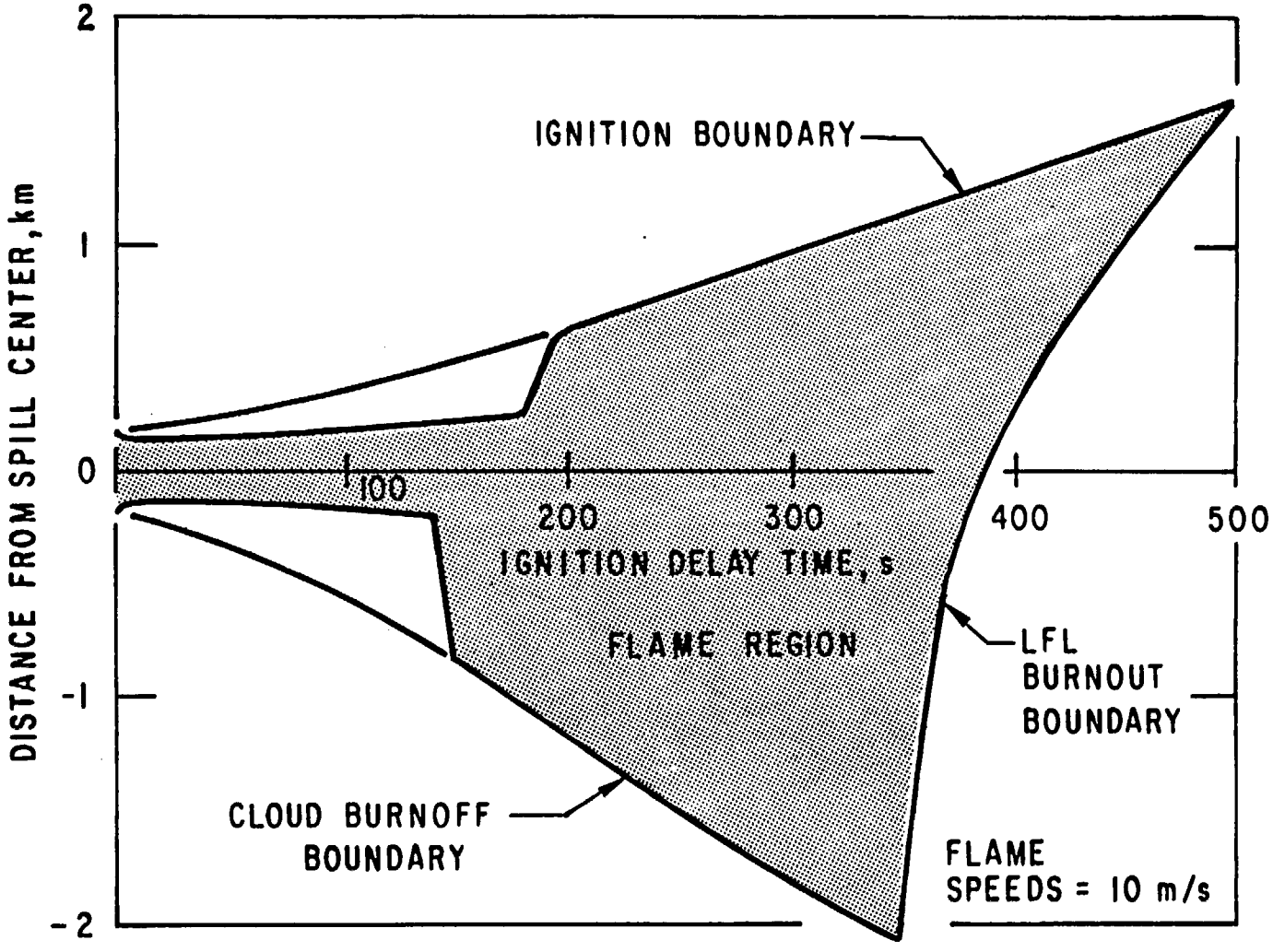

Figure 29. Extent of Flame Region as a Function of Ignition Delay Time for Flame Speeds of 10 m/s; Wind Speed = 0.

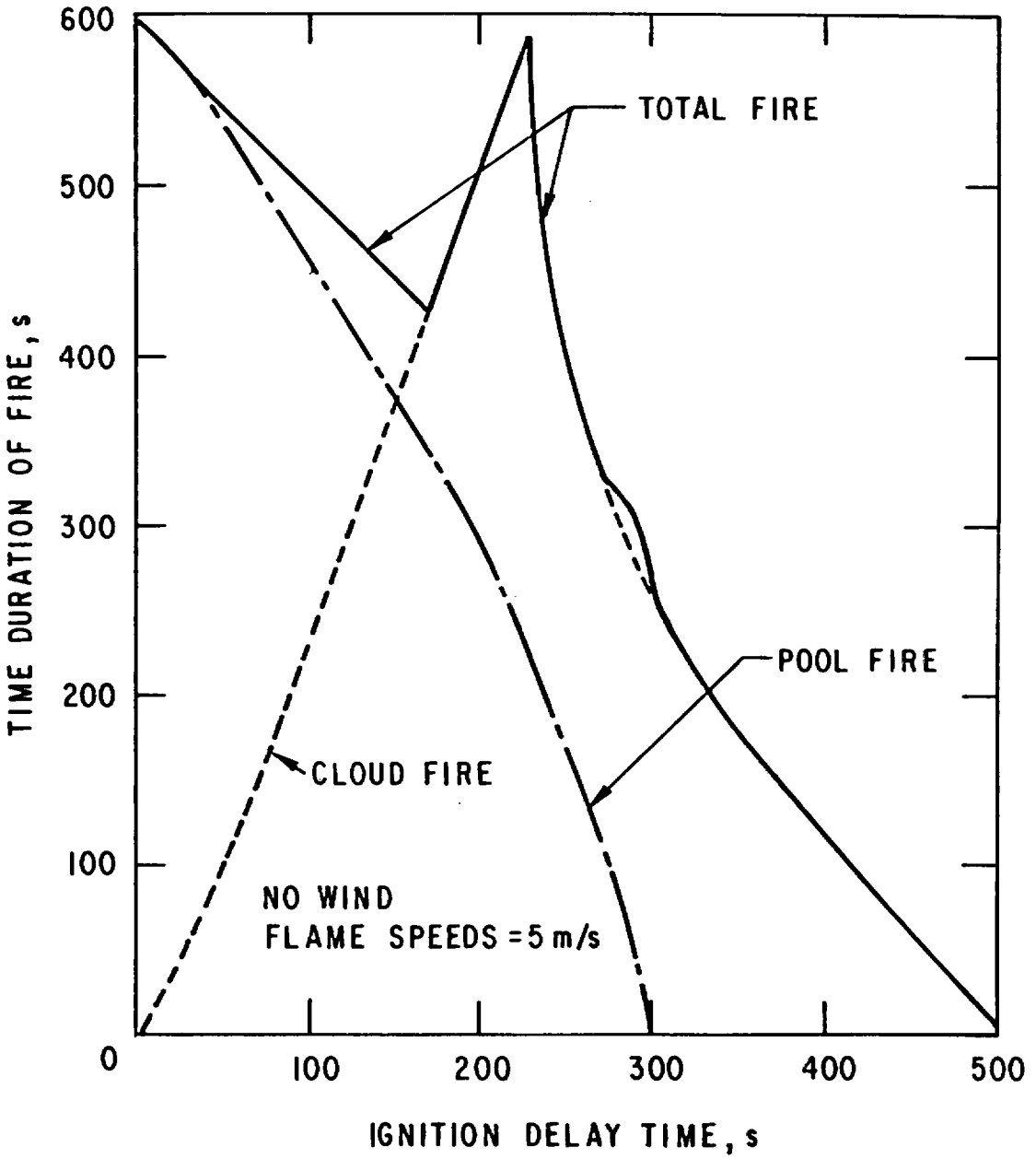

Figure 30. Time Durations of Pool, Cloud, and Total Fires as a Function of Ignition Delay Time for Flame Speed of 5 m/s.

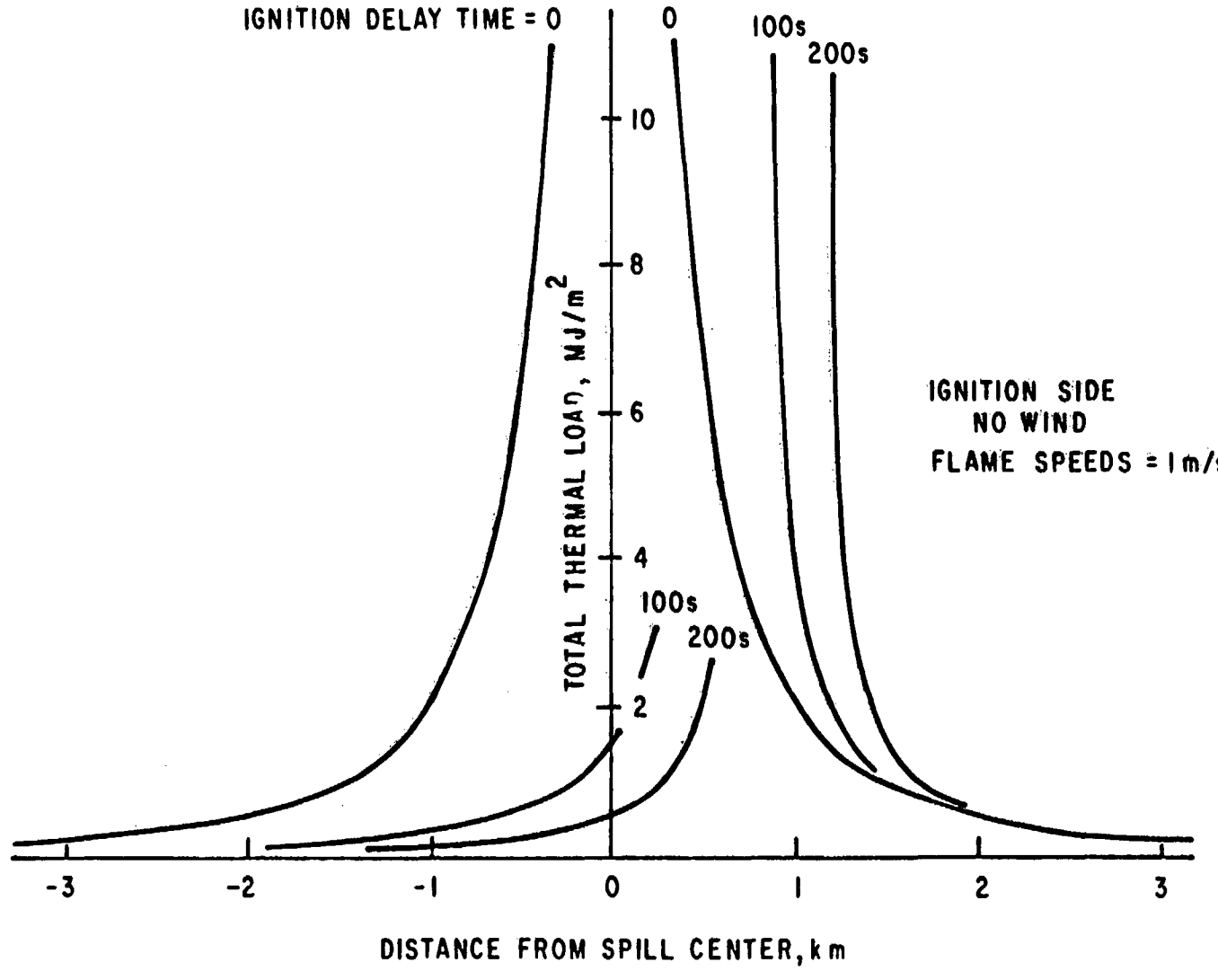

Figure 31. Total Thermal Load Received by Vertical Targets at Ground Level as a Function of Distance and Ignition Delay Time for Flame Speeds of 1 m/s.

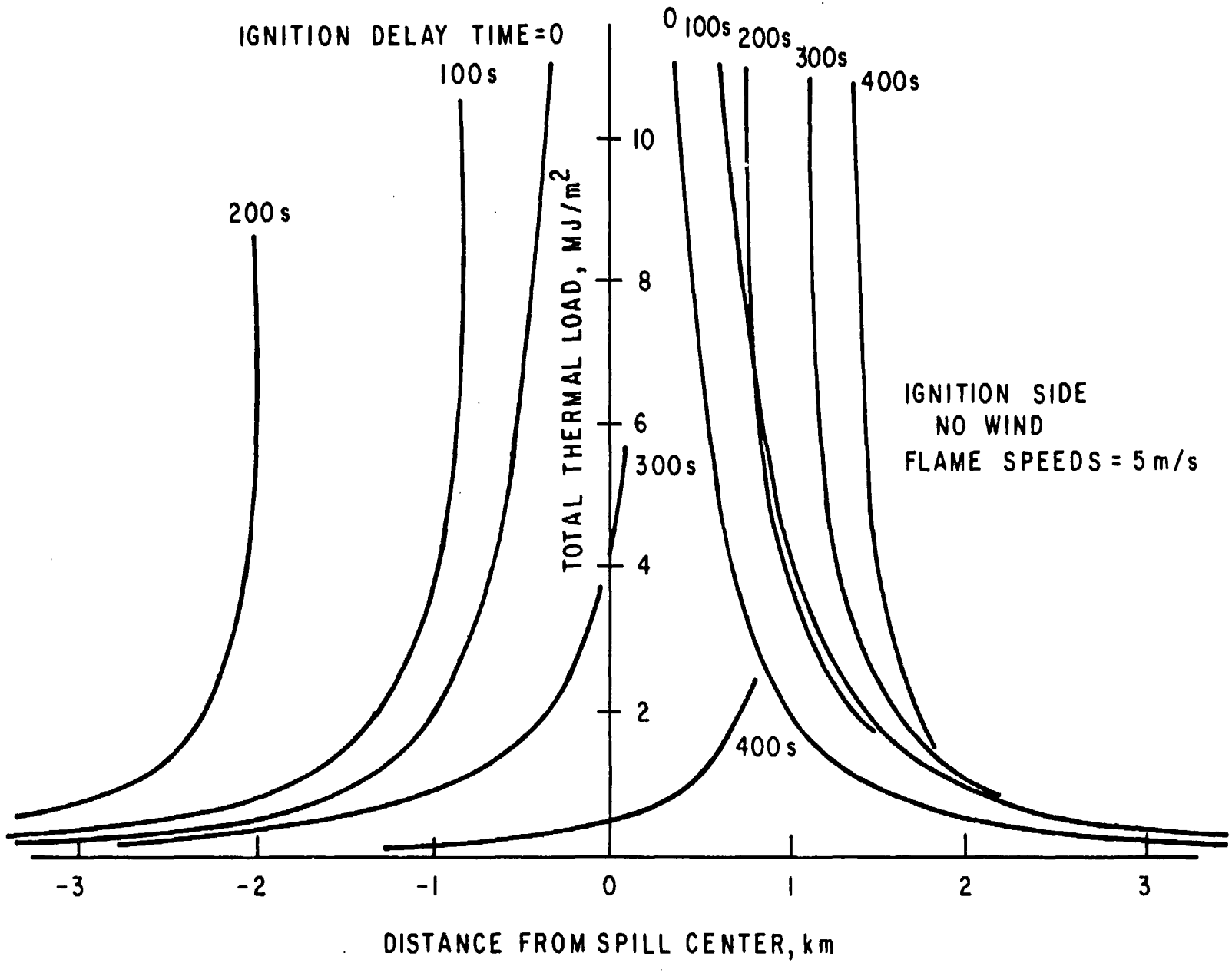

Figure 32. Total Thermal Load Received by Vertical Targets at Ground Level as a Function of Distance and Ignition Delay Time for Flame Speeds of 5 m/s.

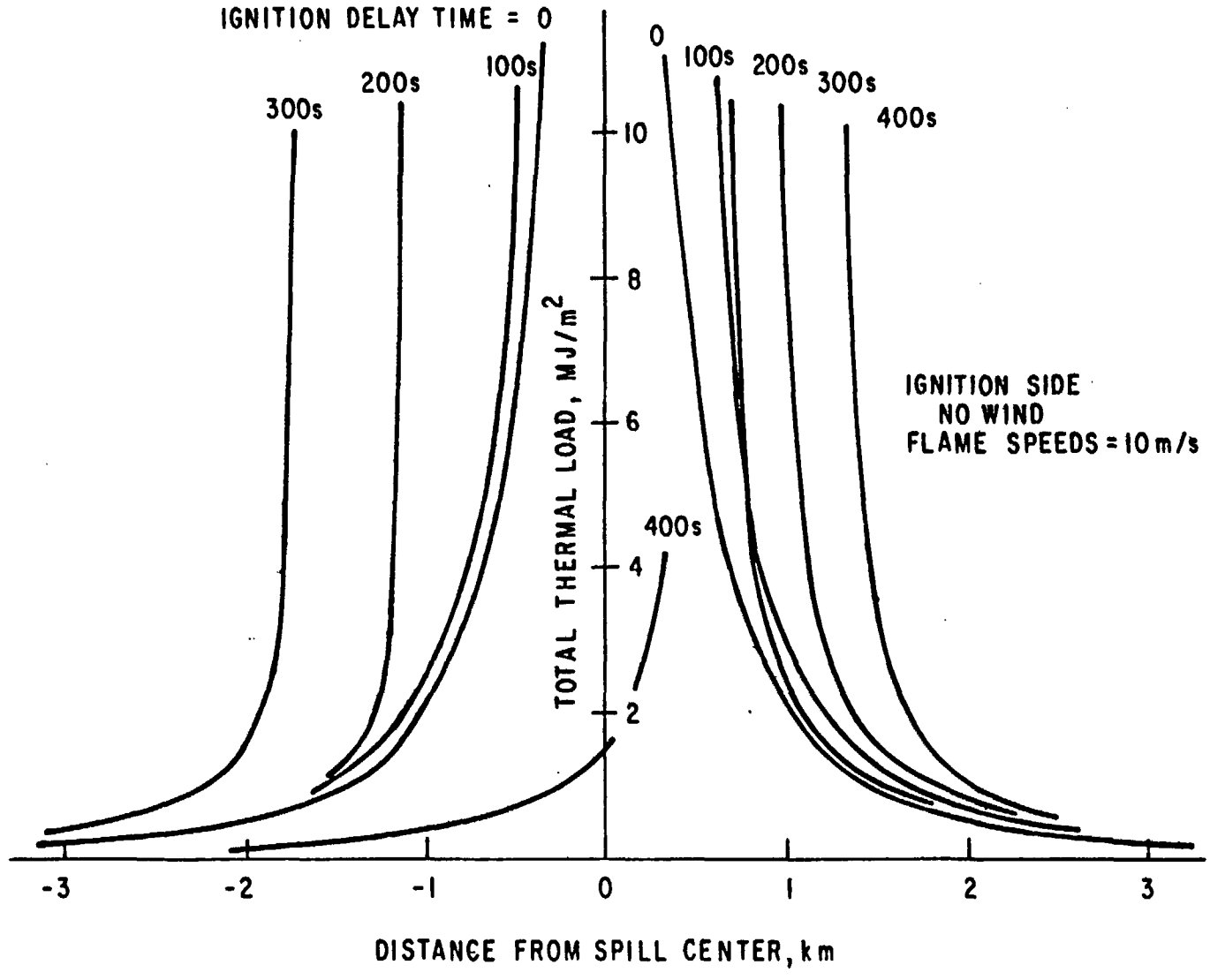

Figure 33. Total Thermal Load Received by Vertical Targets at Ground Level as a Function of Distance and Ignition Delay Time for Flame Speeds of 10 m/s.

the spill origin. In all cases, the total incident thermal load drops very rapidly as the location of interest moves to about 500 m outside the actual flame region. The contribution of the pool fire only to these total loads, expressed as a ratio of pool fire to total load, is given in Fig. 34 for ignition delay times of 100 and 200 s and for flame speeds of 5 and 10 m/s. In many cases at longer distances the pool fire provides the dominant portion of the heat load. Figure 35 compares the total incident radiation loads received by vertically and horizontally oriented targets. A flame speed of 5 m/s is assumed, and comparisions are shown for immediate ignition and an ignition delay of 200 s. As indicated earlier, the vertical targets in general receive larger heat loads, particularly at some distance away from the flame.

Still another measure of fire severity is the peak thermal flux received at a specific location. Figure 36 is a plot of these peak thermal fluxes as a function of distance for several ignition delay times and an assumed flame speed of 5 m/s. The peak loads are seen to vary in a manner similar to the total heat loads. Although the scale in the figure extends to a maximum value of 100 kW/m^2, directly adjacent to the flame the peak radiation flux is much higher. Assuming a flame temperature of 1100°C, the peak flux is in excess of 200 kW/m^2. This provides some measure of how very rapidly the peak radiation flux decays with distance from the flame surface.

The peak-to-average radiation flux ratio is shown in Fig. 37 as a function of distance from the spill location. The average flux is determined by dividing the total thermal load received at a location by the appropriate total duration of the fire. The results are for several ignition delay times and for flame speeds of 5 and 10 m/s. The most noteworthy feature of these plots is that the ratio appears to be nearly constant at locations well outside the flame region, with values of the ratio ranging from less than 2 to about 6. Close to the flame region the ratio becomes quite large, in excess of 10, indicating that short-duration peak fluxes occur at these locations.

The results presented above may be used directly to estimate the gross fire environment resulting from the ignition of LNG under no-wind conditions. Although similar results can be readily produced for other LNG spill and wind conditions, it is also possible to use the no-wind results in conjunction with cloud drift and other dispersion parameters to infer the general nature of the fire environment that my exist in these altered situations. Table 7 compares the total thermal load estimates at fixed distances from the spill source, between a no-wind condition and a wind speed of 4.48 m/s. Both the flame speed and ignition time are varied. For

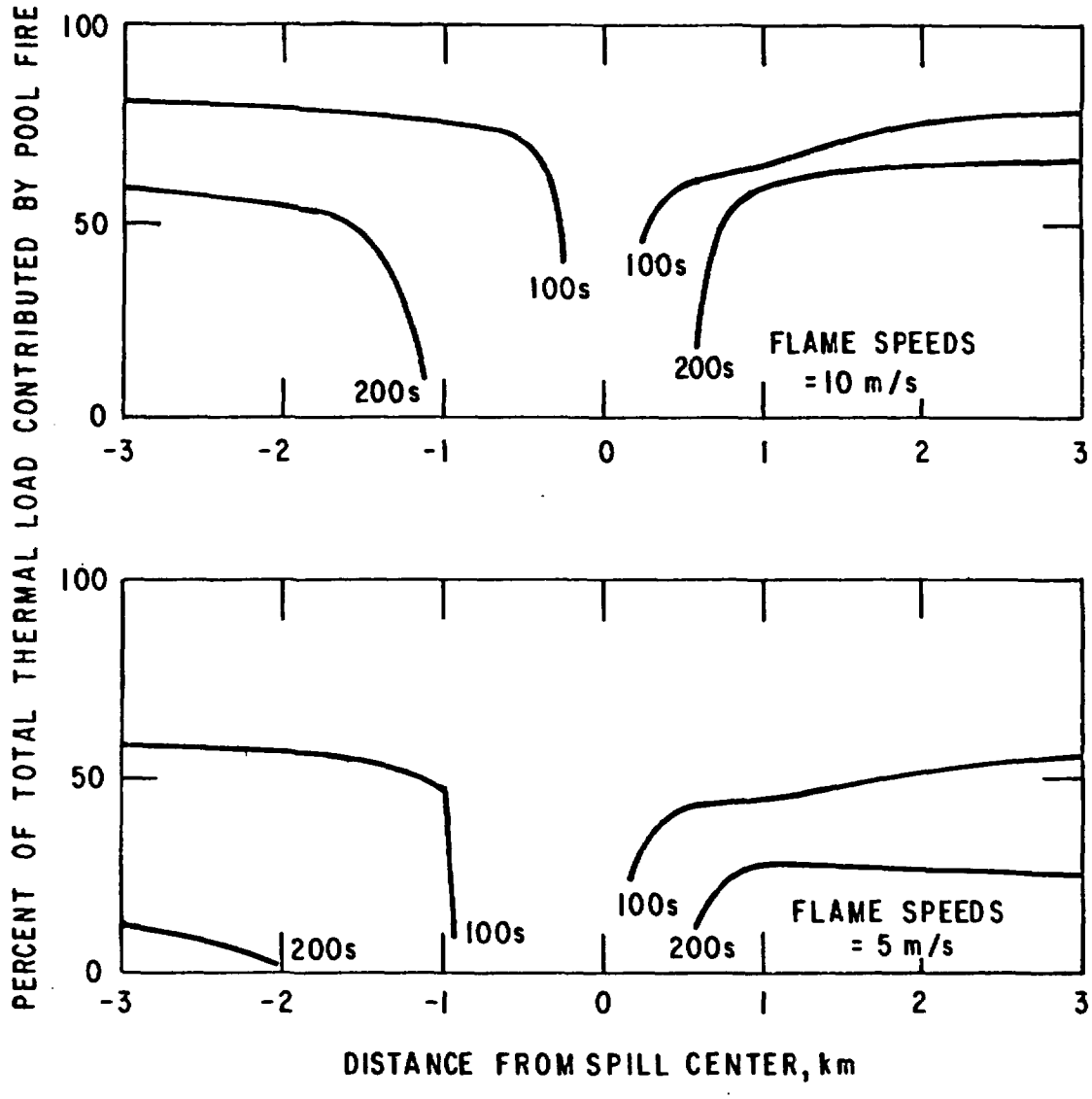

Figure 34. Pool Fire Contribution to Total Thermal Load Received by Vertical Targets at Ground Level with Ignition Delay Time as Parameter.

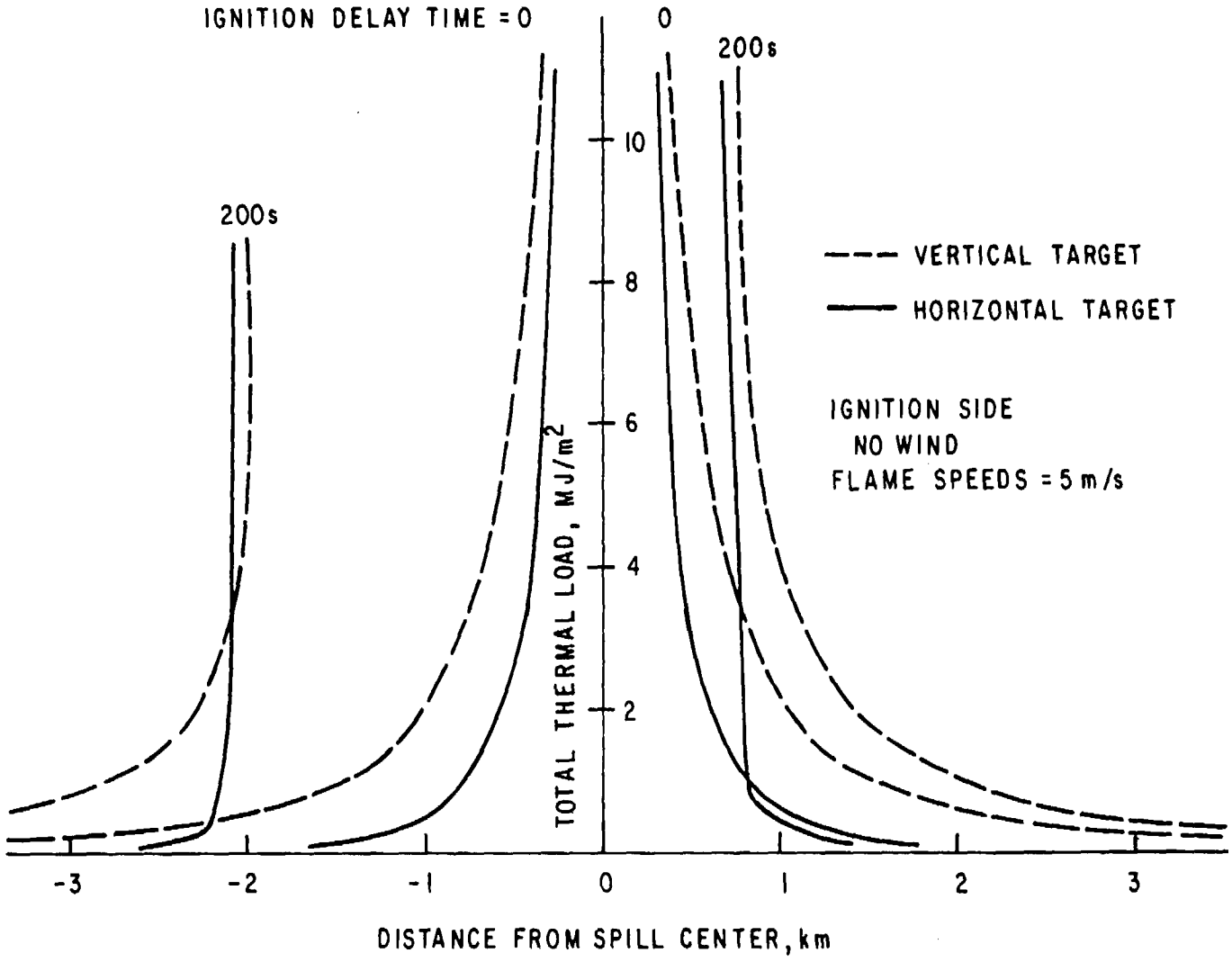

Figure 35. Comparison of Total Thermal Loads Received by Vertical and Horizontal Targets at Ground Plane.

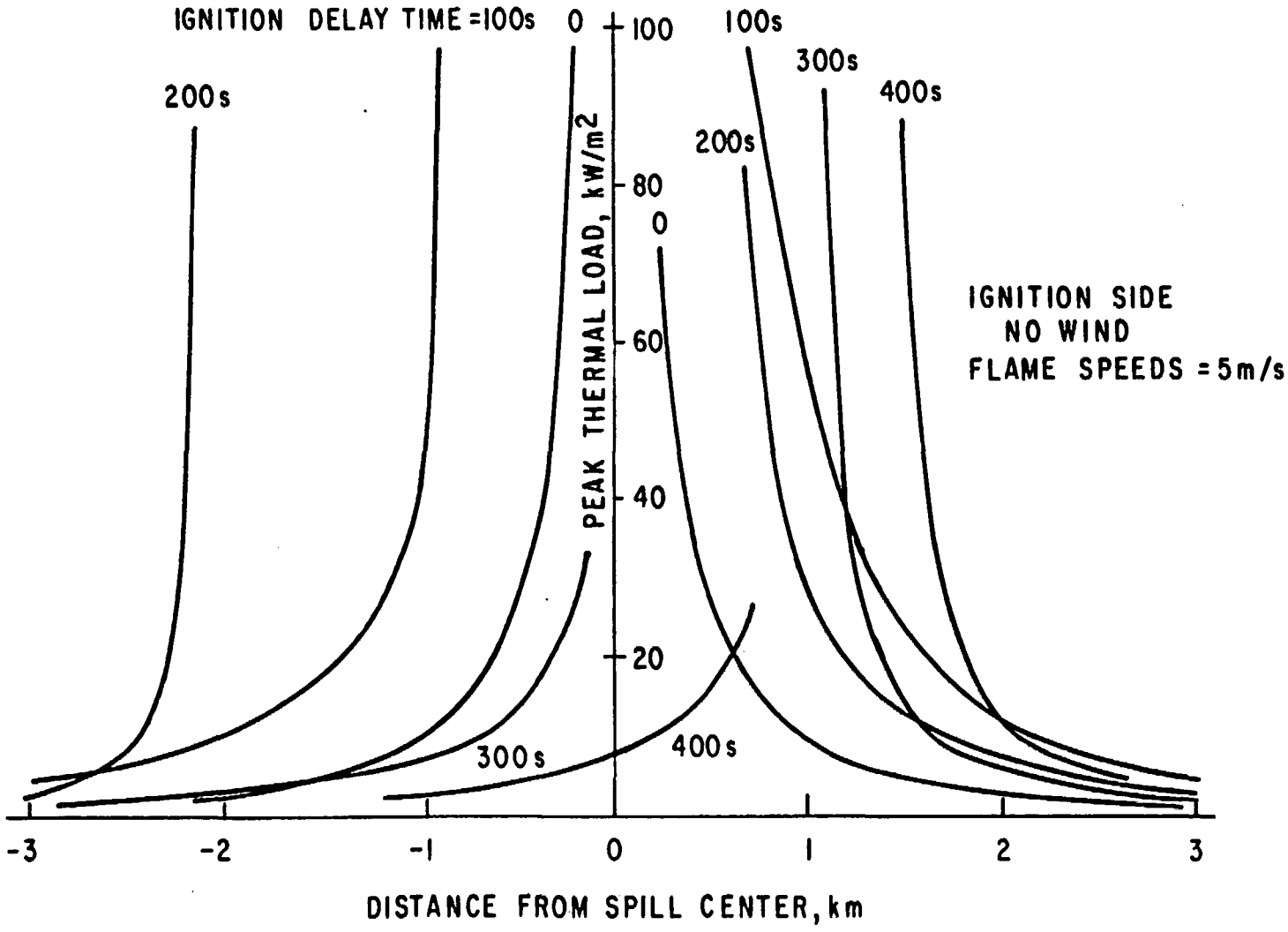

Figure 36. Peak Thermal Load Flux at Vertical Targets at Ground Level as a Function of Distance and Ignition Delay Time for Flame Speeds of 5 m/s.

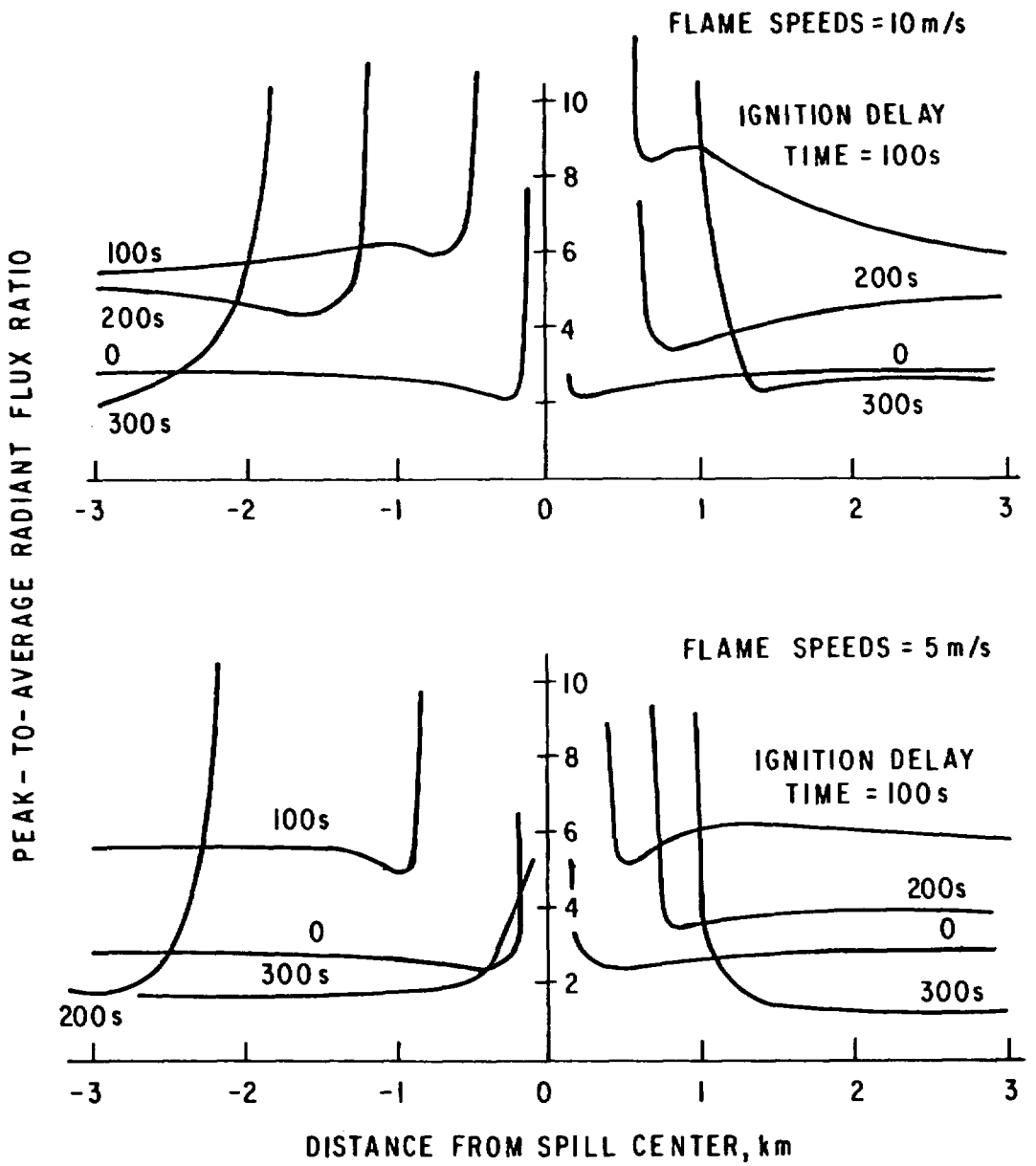

Figure 37. Peak-to-Average Radiant Flux Ratio as a Function of Distance and Ignition Delay Time.

TABLE 7

TOTAL THERMAL LOADS RECEIVED BY VERTICAL SURFACE TARGETS-600s SPILL DURATION

Target to Spill Center Distance (m)	Total Thermal Load (kJ/m^2) Ignition Time (s)						
			Downwind			Upwind	
	0	100	200	300	100	200	300
Wind Speed = 0 m/s							
Flame Speeds = 1 m/s							
2500	311	268	249	191			
2000	498	471	512	466		Same	
1500	903	997	1506	2292		as	
-1500	903	189	90	41		downwind	
-2000	498	126	62	29			
Flame Speeds = 5 m/s							
2500	311	552	579	640			
2000	498	923	910	1113		Same	
1500	903	1783	x	x		as	
-1500	903	1487	x	x		downwind	
-2000	498	801	6446	366			
Wind Speed = 4.48 m/s							
Flame Speeds = 1 m/s							
2500	326	913	1812	4060	335	224	54
2000	531	5677	x	x	529	347	83
1500	985	x	x	x	936	597	138
-1500	985	103	50	21	1143	946	293
-2000	531	74	37	16	618	494	147
Flame Speeds = 5 m/s							
2500	326	1019	952	2204	386	547	365
2000	531	1885	1716	7060	661	928	576
1500	985	4218	4045	x	1849	1969	1017
-1500	985	1541	819	243	985	1080	964
-2000	531	878	529	181	544	611	540

x Indicates vapor cloud reaches target before ignition; model not applicable in this case.

- Indicates distance in upwind direction; when windspeed is zero, the direction away from the ignition source is indicated.

Note: Ignition is assumed at cloud edge.

a direct pool fire (immediate ignition), the differences between the no-wind and finite-wind-speed conditions are minimal. However, when ignition is delayed, the situation changes radically. At slow flame speeds and long ignition delays, many of the downwind locations become engulfed by the flame region in the presence of wind-induced cloud drift. As expected, due to the cloud drift, higher thermal loads are encountered at large distances from the spill source.

6. LNG EXPLOSIONS

The subject of explosion of unconfined LNG/air vapor clouds is currently controversial and poorly understood. On the one hand, there is some indication [23] that enormous amounts of energy are required to explode an unconfined methane/air mixture, and on the other hand, there is experimental evidence that LNG vapor/air clouds may sustain a detonation wave [6]. It has also been shown [24] that to generate substantial overpressures it is not necessary to detonate a fuel-vapor cloud; fast and/or accelerating deflagration is sufficient. In fact, at least for spherical vapor/air mixture clouds, the overpressures and impulses resulting at large distances from the source do not depend significantly on the speed of the combustion reaction, as long as the flame speed exceeds some minimum value [25]. It is therefore reasonable to assume that a large unconfined LNG vapor-air cloud may explode due to the influence of a number of factors including the following:

- A significant fraction of hydrocarbons heavier than methane (e.g., propane, ethane) in an LNG cloud.
- The possibility of strong ignition sources.
- The effects of local confinement and flame-acceleration mechanisms (e.g., the presence of various obstacles in the path of the cloud).
- The potential size of the cloud itself.

Since the velocity of the combustion in an unconfined vapor cloud explosion is ill-defined, it is conservative to assume the worst case of an ideal detonation. This will result in the highest overpressures within the cloud and in its close proximity, while as stated earlier, the pressure fields at large distances are very much alike. It is then necessary to examine the effects of the explosion geometry itself. As indicated earlier, the expected vapor clouds are "pancake like" with a radius many times larger than the cloud height, a ratio of radius to height of 50 being not uncommon. Therefore, as a detonation wave propagates through such a cloud, significant pressure unloading may be expected from the bottom to top surface of the cloud. The most important aspect of the explosion problem is to determine the coupling of the detonation energy to the surrounding air medium and thus the estimation of air-blast wave as a function of time and location. Although this problem can be solved by numerical methods (i.e., using an appropriate computer code), this approach would be very uneconomical because of the unusual geometry of the explosion field. Thus a

two-stage approach is taken here. First, the actual detonation within the vapor cloud is solved by semianalytical methods. The results of this solution are then used as initial conditions for a two-dimensional (axisymmetric) hydrodynamic computer calculation to determine the blast wave propagating into the surrounding air. Blast-wave pressures based on a one-dimensional hemispherical explosion source have been used by other investigators [26] to estimate the pressure field from vapor-cloud explosions. Because of the flat pancake geometry of the LNG cloud, this approach is not felt to be valid in the current application.

6.1 Vapor-Cloud Detonation Parameters

The pressure field inside an exploding vapor cloud and the air blast generated in the near field environment depend both on the thermodynamics of the explosion and on the geometry of the detonating mass. As pointed out earlier, an ideal detonation is assumed in the current application. The parameters governing such an explosion include the ambient conditions, cloud-mixture properties, and the Chapman-Jouget (CJ) detonation state. The general equation that relates the thermodynamic state behind the detonation wave traveling in an ideal gas to the energetics of the gas is given as

$$p = (\gamma - 1)\, e_o + \{ [(\gamma - 1)\, e_o]^2 - \frac{\gamma - 1}{\gamma + 1} (2e_o + 1) \}^{1/2}, \qquad (25)$$

where

$$p = P_d / P_\infty$$

and

$$e_o = \frac{P_\infty}{(\gamma -)\, \rho_\infty} + n_t C_m e_c .$$

The descriptions and the values of the variables defining the CJ state and the ambient cloud conditions, assuming a stoichiometric mixture (≈ 10 vol % of LNG) are tabulated below:

Description	Variable	Value
Detonation pressure	p_d	1.5513 MPa (225 psia)
Detonation wave speed	D	1695 m/s
Detonation particle speed	u_d	741 m/s
Detonatin sound speed	c_d	954 m/s
Detonation temperature	T_d	2511 K
Detonation density	θ_d	2.052 kg/m^3
Ratio of specific heats of detonation products	λ	1.29
Combustion conversion efficiency	η_t	0.71
Low heat of combustion	e_c	49.98 MJ/kg
Ambient pressure	P_∞	0.10135 MPa (14.7 psia)
Mixture temperature	T_∞	292 K
Mixture density	P_∞	1.153 kg/m^3
Mixture mass concentration	C_m	0.06

6.2 Two-Dimensional Explosion Models

The vapor-cloud geometries associated with a large spill of LNG on water have been shown to be rather thin "pancake-like" configurations. Since such extreme geometries have a marked impact upon the airblast environment, it is essential to factor in the source (cloud) shape in computing the resulting pressure fields. To accomplish this, a nominal or generic cloud configuration is selected, and the two-step solution procedure mentioned earlier is adopted. Some aspects of the solution are scalable in terms of the cloud height; hence the solution possesses some universality, and the

results obtained can be extended to most LNG clouds resulting from a spill on water.

A typical cloud configuration is illustrated (to scale) in Fig. 38. The cloud radius is 1.1 km and its height is 25 m; hence its radius-to-height ratio is 44. The volumetric concentration of the fuel at this stage of cloud development is 10%, which corresponds approximately to stoichiometric conditions. The equivalent hemispherical source based upon equal volume is also illustrated in this figure. The equivalent spherical source radius is 350 m. Thus the actual cloud extends out to 3.14 equivalent spherical radii. The extreme geometric dissimilarity between the two sources is quite apparent.

As indicated earlier, it is conservative to assume that an initiation source of sufficient strength can occur and that the cloud composition and size are such that a stable detonation can develop. The assumed explosion scenario is illustrated in Fig. 39 and defines four distinct phases. The first is the initiation phase (a); the initiation can occur anywhere within the cloud region and terminates when a self-sustaining flame or detonation-wave situation occurs. The second phase (b) is a transition phase associated with flame acceleration and the establishment of a stable detonation-wave system. Pressure waves will exist during this phase, and they will spacially precede the chemical-release process. The third phase (c) is the establishment of a stable detonation-wave system in which the detonation front has caught up to any preceding pressure waves in the undetonated mixture and where the compression waves in the air have coalesced into a single air-shockfront. This detonation-wave system will be quasi-steady in nature, and the local explosion environment will be defined by the detonation state and the pressure relief caused by the impedance mismatch with the air above the cloud. The fourth phase (d) is the airblast phase, which starts when local burn-out occurs as the detonation wave reaches the end of the cloud. Thereafter, the chemically released energy is redistributed hydrodynamically, and an outward propagating blast wave will be established. The characteristics (i.e., peak overpressure, impulse, and duration) of this blast environment at locations near the cloud are of prime interest.

Most probably ignition will occur locally, i.e., from a point source. This will lead to a three-dimensional wave system, and hence detonation and airblast environments that vary with respect to the horizontal azimuth. Nonetheless the scenario described in Fig. 39 will still apply, and the blast environment in the direction of detonation-wave propagation will be most severe. A complete three-dimensional solution of the problem is beyond the

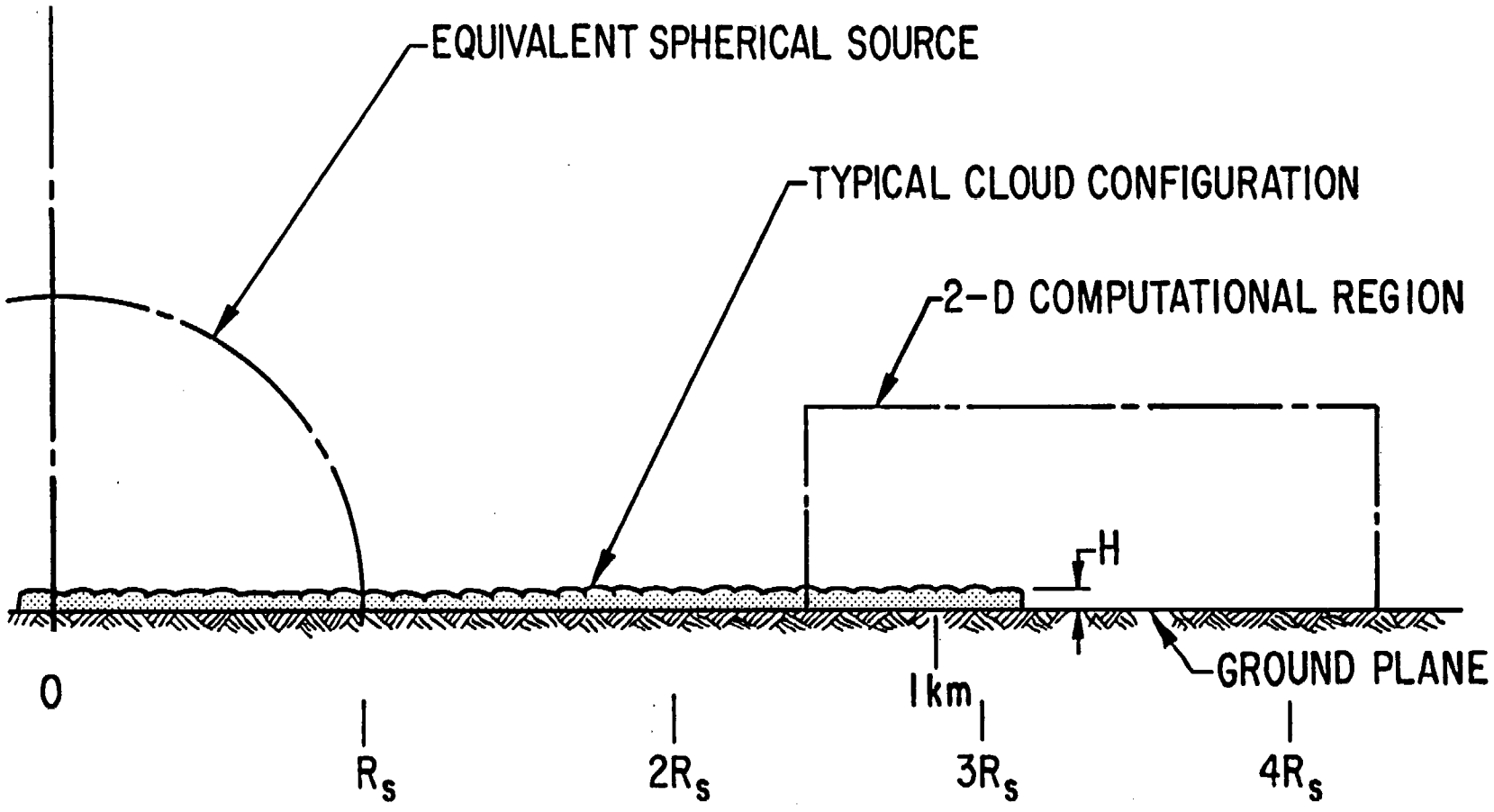

Figure 38. Typical Cloud Configuration at 10% Fuel Concentration.

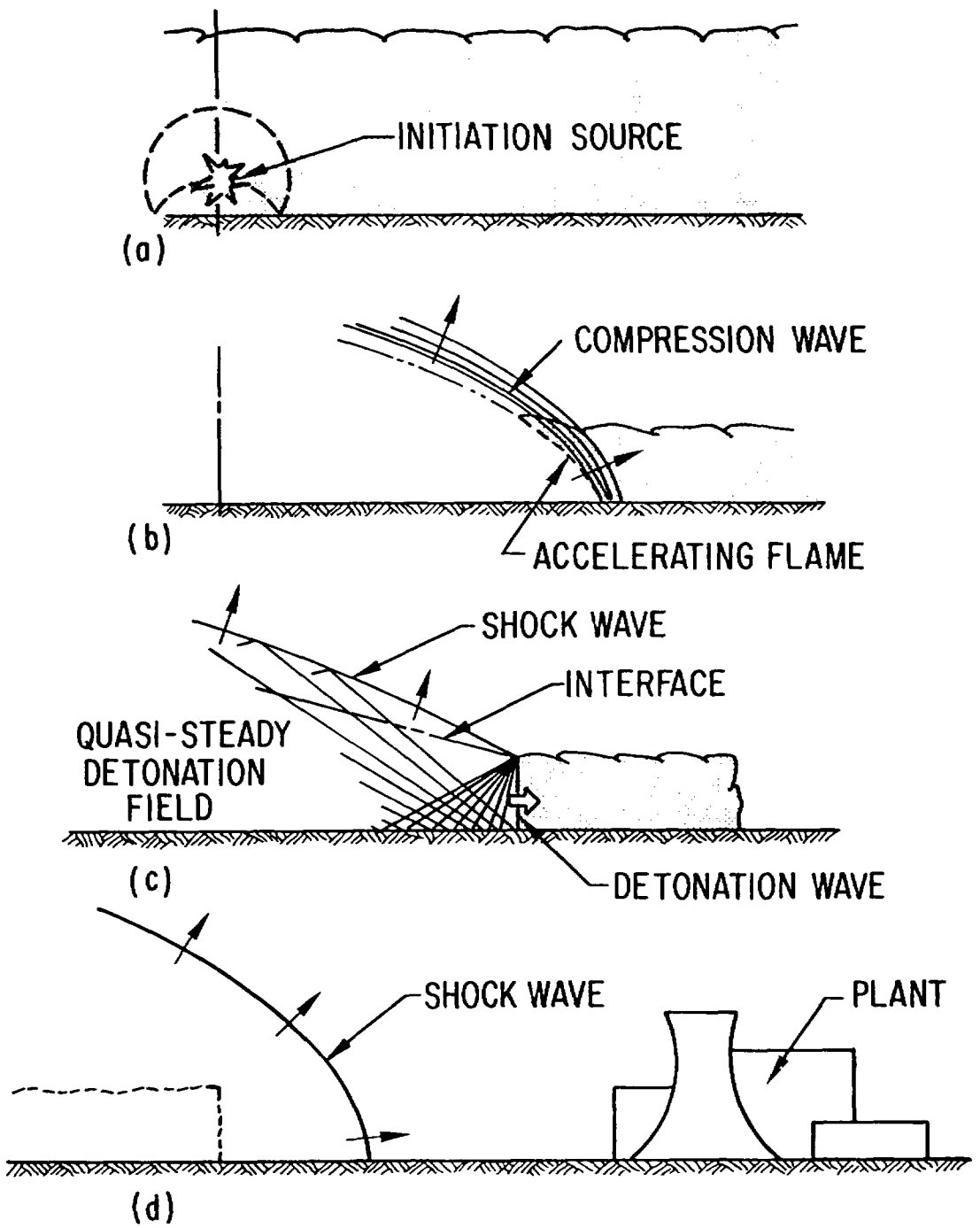

Figure 39. Assumed Explosion Scenario.

scope of the present effort. However, a two-dimensional solution can embody most of the salient features of the phenomenon and represent a conservative (worst-case) estimate of the expected explosion environment.

The two-step approach used to develop the two-dimensional air blast solution consists of first establishing the quasi-steady detonation environment defined in Phase c (Fig. 39c) and then to use this flow field as an initial condition for a two-dimensional axisymmetric hydrocode calculation which starts at the time of local burnout, i.e., when the detonation wave reaches the cloud edge. The computational region used for the nominal cloud configuration is shown in Fig. 38.

6.2.1 Quasi-steady Detonation Field

The large aspect ratio of the LNG vapor cloud, i.e., ratio of radius to height, will tend to make the quasi-steady detonation field planar. Unloading from the top of the cloud because of upward expansion of the reaction products will predominate, making pressure decay due to cylindrical divergence and Taylor-wave expansion near the detonation source less important (see Section 3 of Appendix C). Since, in addition, the detonation wave will propagate through the cloud at constant speed, the estimation of the detonation field can be reduced locally to the solution of a two-dimensional planar and quasi-steady problem. The number of independent variables is thus reduced from three to two; that is, time is eliminated explicitly. The independent variables are then the vertical and horizontal distances z and y; and the only characteristic length associated with the problem is the cloud height H. The latter can be used to define dimensionless similarity variables

$$\zeta = z/H$$

and (26)

$$\eta = y/H.$$

Since the detonation wave and the related pressure field propagate horizontally at a constant speed D, the horizontal distance y represents a measure of time, i.e.,

$$y = Dt. \quad (27)$$

Thus η can also be considered to be the independent time variable. The above scaling renders the results more general, making them applicable to a cloud of any height.

The resulting pressure-wave system is illustrated in Fig. 40 using the dimensionless variables. The system is rendered stationary by using a coordinate system attached to the detonation wave. Thus the combustible mixture approaching the detonation-wave boundary with a constant speed D is converted into reaction products at high pressure and sonic particle velocity. The upward expansion of these products create a shock wave in the air above the cloud and a fan of rarefaction waves in the gases that reflect from the rigid ground surface. A curved interface separates the air from the reaction products. The pressures in the two gases across the interface are equal; however, the tangential velocities on either side may vary due to slip. The air shock wave strength, while variable along its length, is continuous. The solution of this planar, but complex wave system is obtained using the conventional method of characteristic techniques [27]. It provides the pressures and velocities in both the air and combustion gases of the detonation field (see Section 3 of Appendix C).

A specific result of this calculation is the spatial pressure distribution along the ground plane behind the detonation front. This is presented in Fig. 41 in terms of the normalized absolute pressure, which is obtained by dividing the pressure by the (absolute) detonation pressures. Since the horizontal distance variable is also a time variable, the curve can be interpreted as a pressure history. The integration of this result with respect to time yields the impulse per unit area that a surface element experiences as the wave system moves past a given location. This impulse, adjusted to the ambient pressure is

$$I = \frac{0.8\Delta P_d H}{c_d}, \qquad (28)$$

where ΔP_d is the detonation overpressure, c_d is the sound velocity of the detonation state, and H is the cloud height.

6.2.2 Airblast Environment Computations

An existing two-dimensional axisymmetric Eulerian hydrocode called BUNIE [28] is used to compute the airblast environment that exists outside the vapor cloud after the detonation wave reaches the edge of the cloud. The calculation is carried out in terms of height units and thus scales with respect to cloud height. A nominal radius of curvature is used, corresponding to a location of the cloud edge at 50 height units from the

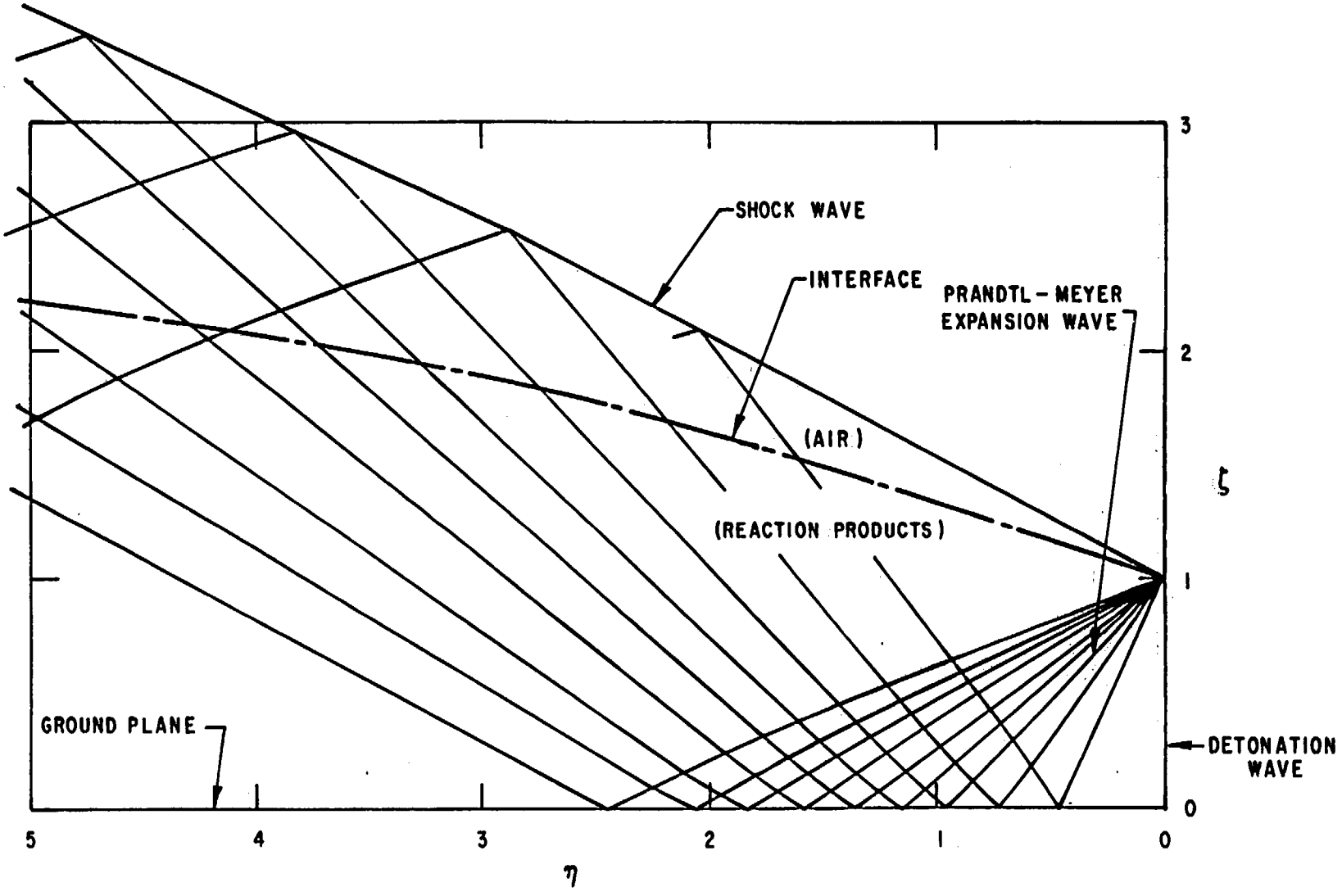

Figure 40. Wave Diagram for Quasi-Steady Detonation Field.

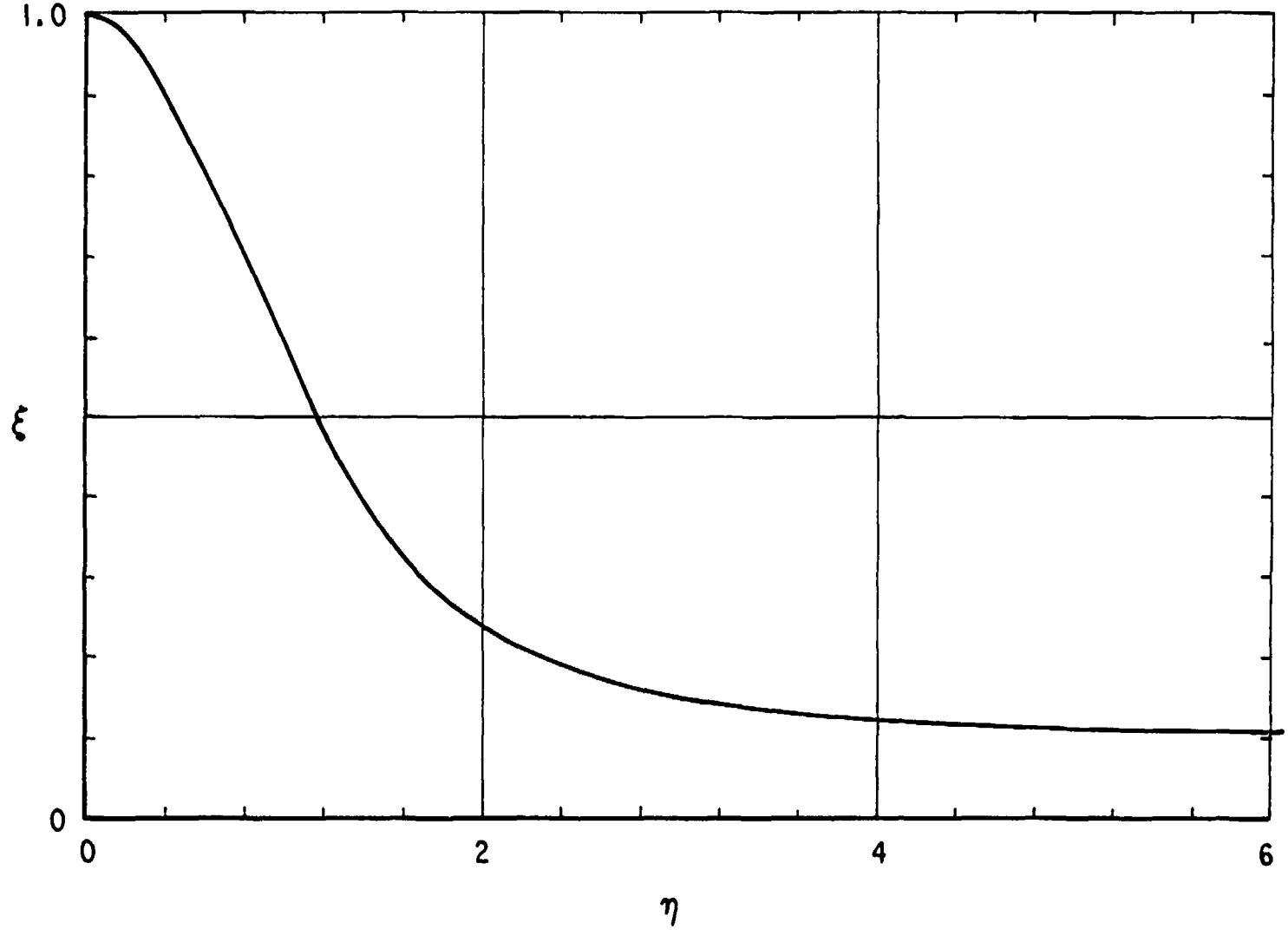

Figure 41. Dimensionless Pressure History/Profile Behind Detonation Front at Ground Level.

origin. Thus blast attenuation due to spatial divergence is approximately accounted for in the solution. Since the computer code is only capable of treating a single continuous perfect-gas region, a compromise value of the ratio of specific heats $\lambda = 1.35$ is used for both the air and combustion gases. This approach has been found satisfactory in earlier applications [28].

The computational region extends up 9 height units, 10 height units upstream, and 16 height units downstreamn. A variable spacing grid is used to provide good resolution in the region of airblast wave formation and at the same time to avoid long computer runs. The total calculation is carried out for 500 time steps corresponding to 33 ms of real time per meter of cloud height. This is the time when the shock wave along the ground passes out of the computational grid. Initial conditions, i.e., pressure, velocities and thermodynamic variables in each computational cell are given by the quasi-steady explosion field obtained from the analytical approach described earlier. Since the finite difference technique used relies on artificial viscosity methods to accommodate shock waves, some smearing of these waves occurs. The computer code is based on the FLIC computational methodology, which used a "donor cell" technique to avoid certain calculational instabilities [28]. This in turn produces a certain amount of unavoidable numerical dispersion. However, the computed results are thought to capture the salient features of the air blast field in the close proximity of the detonating vapor cloud.

6.3 Airblast Result Summary

Once burnout of the vapor cloud occurs and energy input to the system ceases, the expanding airblast is characterized by a rapid decrease of peak overpressure; e.g., after propagating about one height unit along the ground range, the peak shock has already decayed to 55% of its initial value. The pressure field adjacent to the cloud is illustrated by the pressure-time histories given in Figs. 42 and 43 for locations along the ground and at two cloud height units. The horizontal locations correspond to positions 0, 1, 2, ..., to 15 height units downstream from the edge of the cloud. The peak overpressure decays rapidly along the ground immediately in front of the cloud. Note that the overpressure scale differs in the two figures and that the pressure history for the horizontal location four height units downstream from the cloud edge is repeated in both figures for comparison purposes.

The basic characteristics of the airblast environment are best represented in terms of peak overpressure and impulse variations as a function of

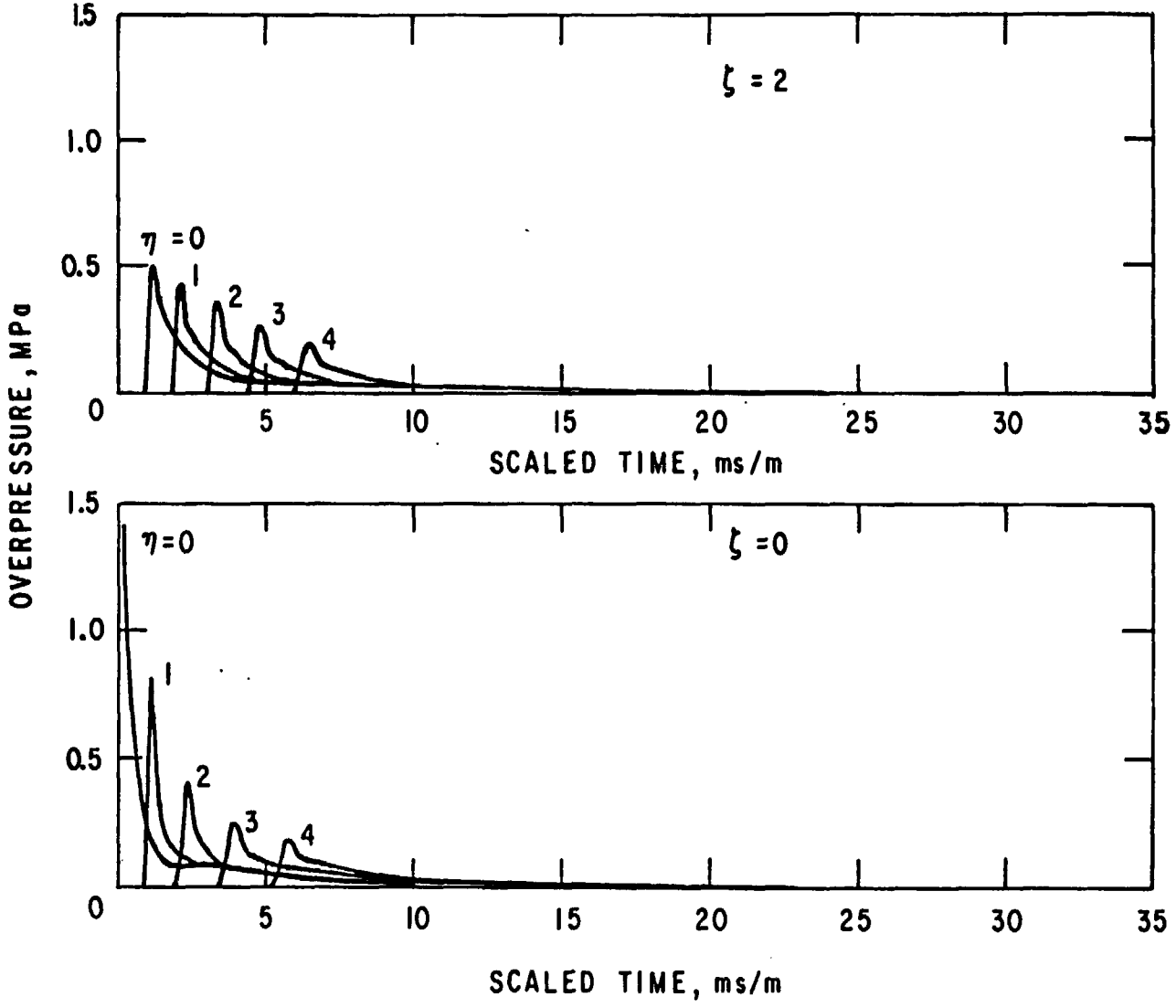

Figure 42. Pressure Histories for LNG Cloud Explosion.

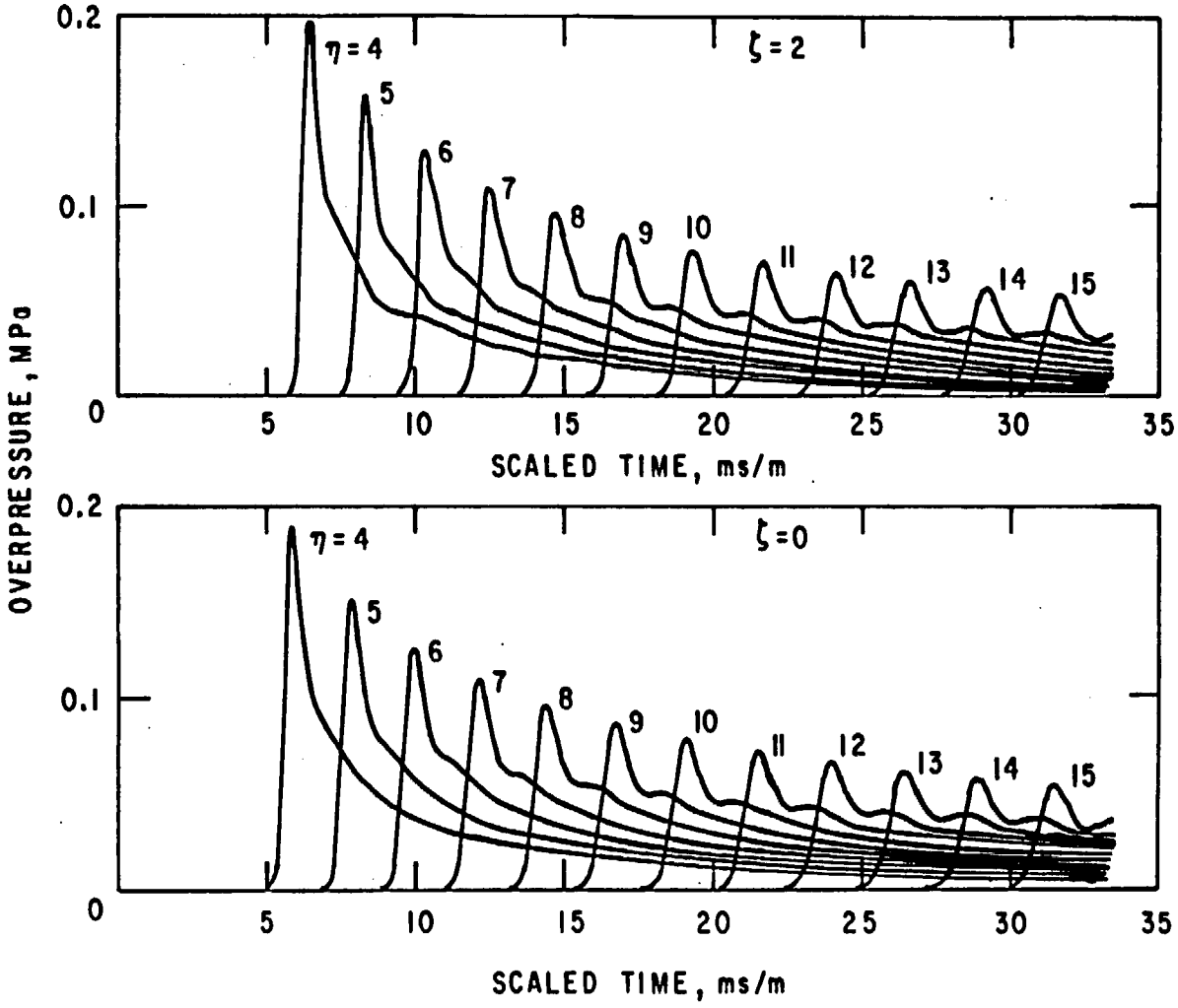

Figure 43. Pressure Histories for LNG Cloud Explosion (Continued).

relative range measured in cloud-height units. These are shown in Figs. 44 and 45 for nominal elevations of zero (ground level), one, and two cloud heights. At the cloud edge, all the curves become very flat for relative ranges less than 1. As a reference value, the detonation overpressure, ΔP_d = 1.45 MPa, is indicated in Fig. 44. The interaction of the detonation wave with the air at the edge of the cloud results in an instantaneous drop in overpressure to 1.16 MPa because of the impedance mismatch of the two gases; this is shown in the results for zero elevation. Close to the detonating cloud, the peak overpressure is highest along the ground level. At relative ranges greater than two, the influence of elevation becomes quite small, with some indication that the overpressure at higher elevations is slightly larger. This effect can be observed in the overpressure histories given in Fig. 43. In this range the overpressure decays approximately as the reciprocal of the horizontal distance. At the limit of the calculations or a range of 15 height units, the overpressure decays to about 0.05 MPa (7 psig). Extrapolating the results to the lowest level of interest or about 0.007 MPa (1 psig), a range of about 100 height units is indicated. For a nominal cloud height of 25 m, this implies a distance of 2.5 km from the cloud edge.

The side-on impulse, i.e., the impulse in the incident blast wave, as a function of relative range is shown in Fig. 45. The values given are in units of MPa ms per meter of cloud height. The impulse obtained from the quasi-steady detonation solution I_d = 1.22 MPa ms/m is indicated in the figure. The impulse decay with range is slow until a relative range value of approximately 8 is reached. Thereafter the decay rate increases sharply. Since the calculations were terminated at a time of 33 ms/m, the impulse values at relative ranges greater than 10 are estimated values and it is not feasible to extrapolate the results significantly beyond the range of the computations. The influence of elevation on impulse is small, some differences existing at close-in locations.

The third important blast-wave characteristic, the duration of the overpressure, has to be estimated from the pressure-time histories. Because of the very flat overpressure decay at late times (see Fig. 43), this quantity is difficult to evaluate. In fact, during the entire computer calculations the overpressure never decays to zero. However, setting an arbitrary low overpressure of about 0.007 MPa (1 psig) as the limit, one finds that the blast-wave durations are 10-20 ms per meter of cloud height.

Applying the above scaled results to the specific example of the vapor cloud shown in Fig. 40, we can make a direct comparison with the often-used equivalent one-dimensional blast estimates. As indicated earlier, this

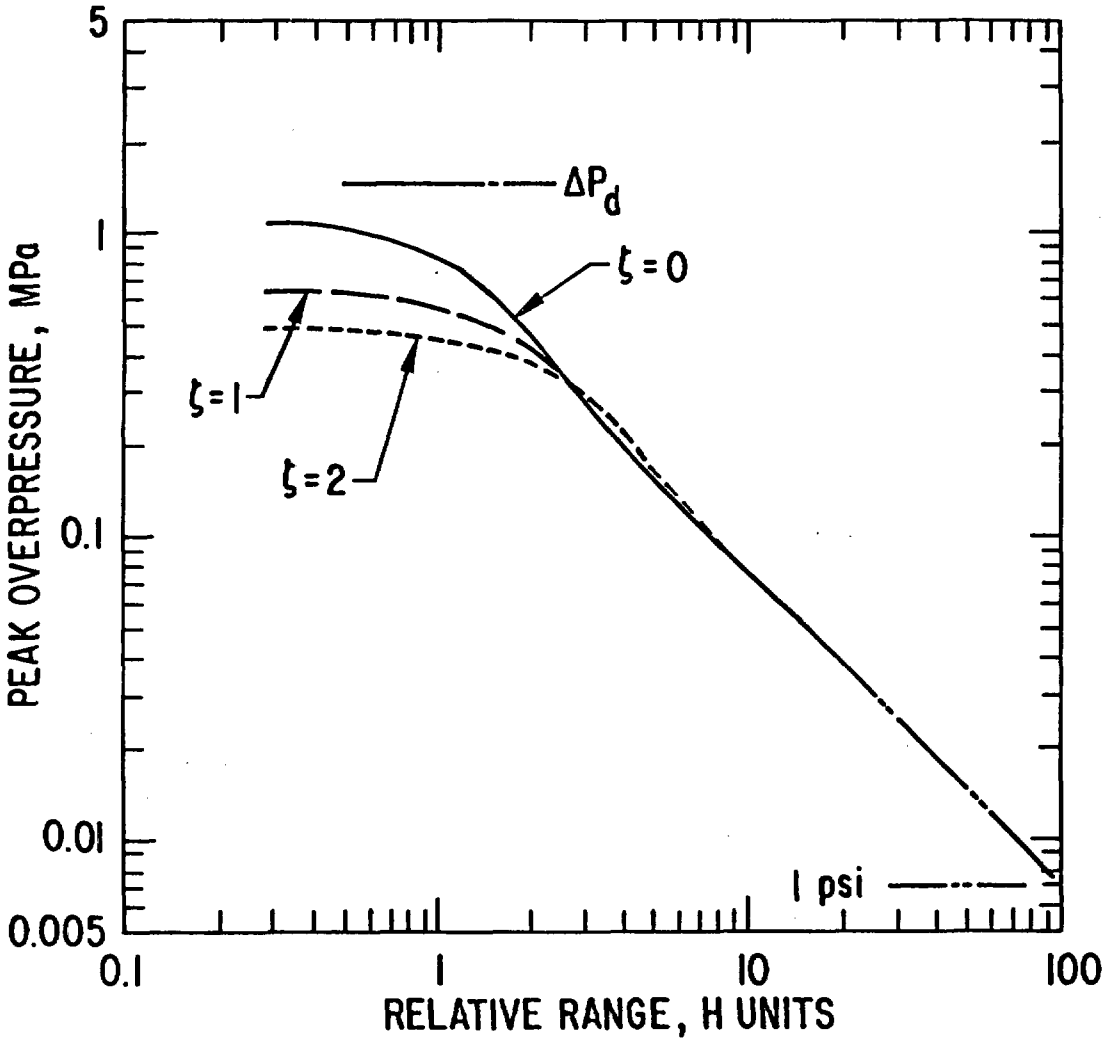

Figure 44. Peak Overpressure Variation for LNG Cloud Explosion.

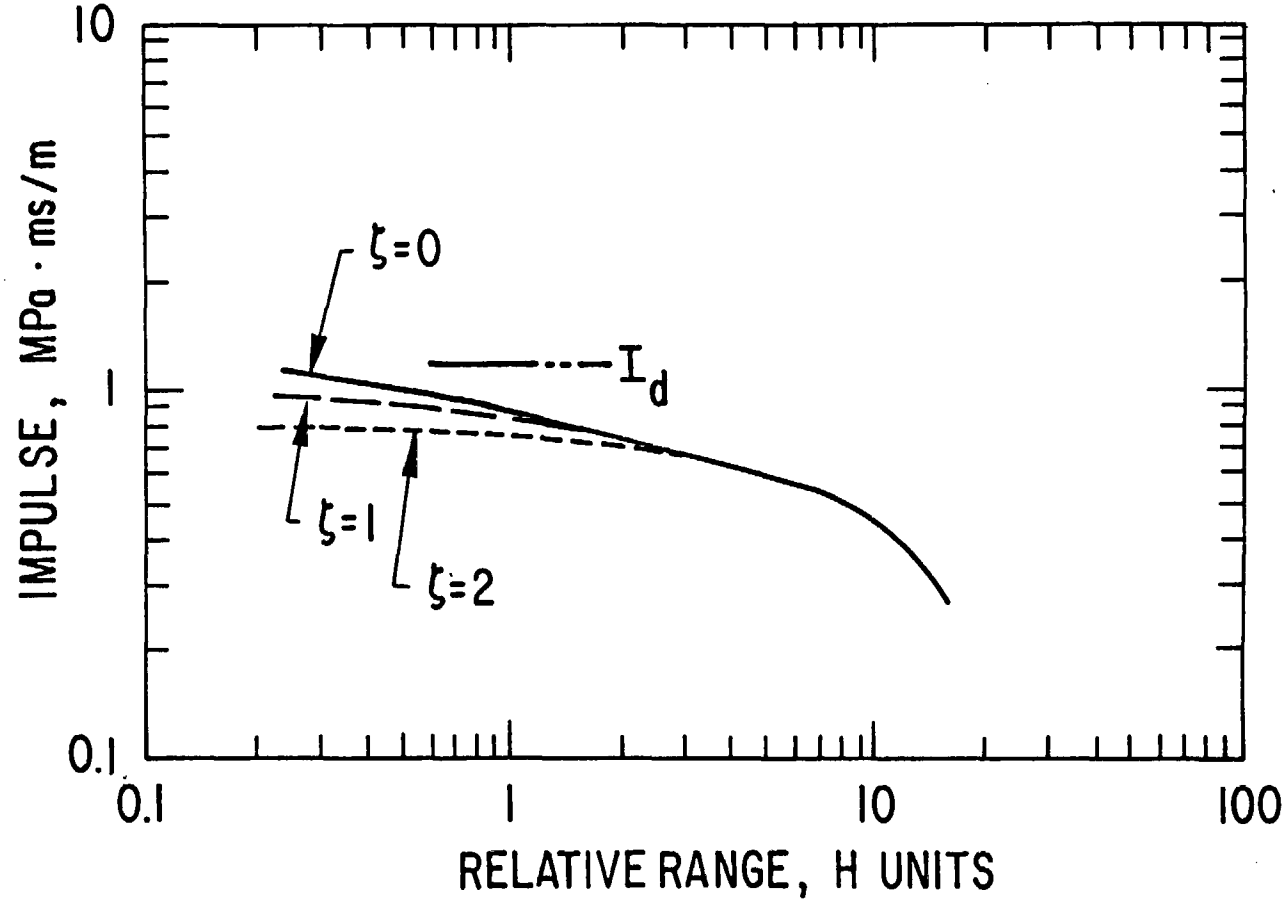

Figure 45. Impulse Variation for LNG Cloud Explosion.

cloud has a height of 25 m and a radius of 1.1 km, while the radius of the equivalent hemispheral cloud is 350m. The peak overpressure comparison is shown in Fig. 46. Here the range is measured from the cloud center (origin), where initiation is assumed to occur. The current two-dimensional results are labeled "LNG Cloud" and show a peak overpressure within the cloud equal to the detonation value of 1.45 MPa. Outside the cloud the pressure decays rapidly, reaching a value of 0.05 MPa (7 psig) at 1.5 km and extrapolating to the 0.007 MPa (1 psig) level at around 3.6 km.

Using a TNT equivalency concept [29], the curve labeled "TNT Equivalence" in Fig. 46 is obtained. Since this curve is based on matching overpressures in the 0.007 MPa (1 psi) range, it can clearly not be applied at significantly higher pressures and definitely takes no account of the geometric distortions embodied in the two-dimensional model. The overpressures are greatly overestimated at close-in ranges, then underestimated at intermediate distances, i.e., ranges of the order of the cloud radius. The curve labeled "Det." corresponds to hemispherical explosions of propane [30], and although the energetics of this system are slightly different than those of LNG, it is clear that this data also grossly underestimates the overpressure at intermediate ranges. The other curves in the figure represent a volume detonation and calculated overpressure curves for various deflagration speeds all assuming a spherical source [30]. It is evident that none of these results are adequate to predict the pressure field resulting from the explosion of a "pancake-like" vapor cloud.

The impulse results for the two-dimensional calculations and for the TNT equivalency method are presented in Fig. 47. (No impulse information is available for the detonating hemispherical gas source.) The impulse estimates obtained from the point-source TNT equivalency methodology are wholly inadequate over the entire range of interest. Thus the current two-dimensional results are the only meaningful impulse estimate available. Similarly, the positive phase durations of the overpressure waves, which are in the range of 0.25-0.50 s for the example cloud, are the only meaningful duration estimates.

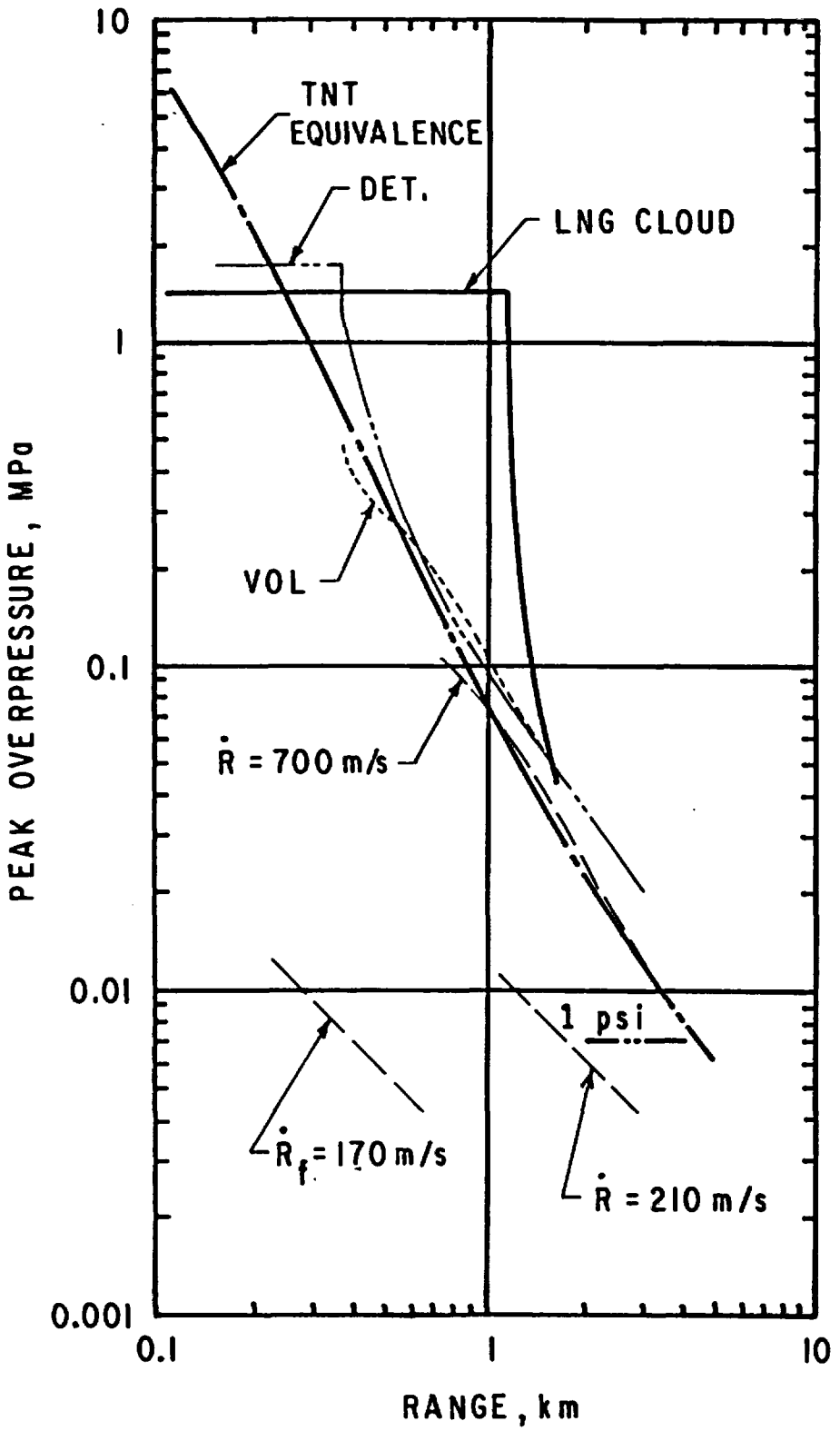

Figure 46. Comparisons of Peak Overpressure Estimates for LNG Cloud Explosion.

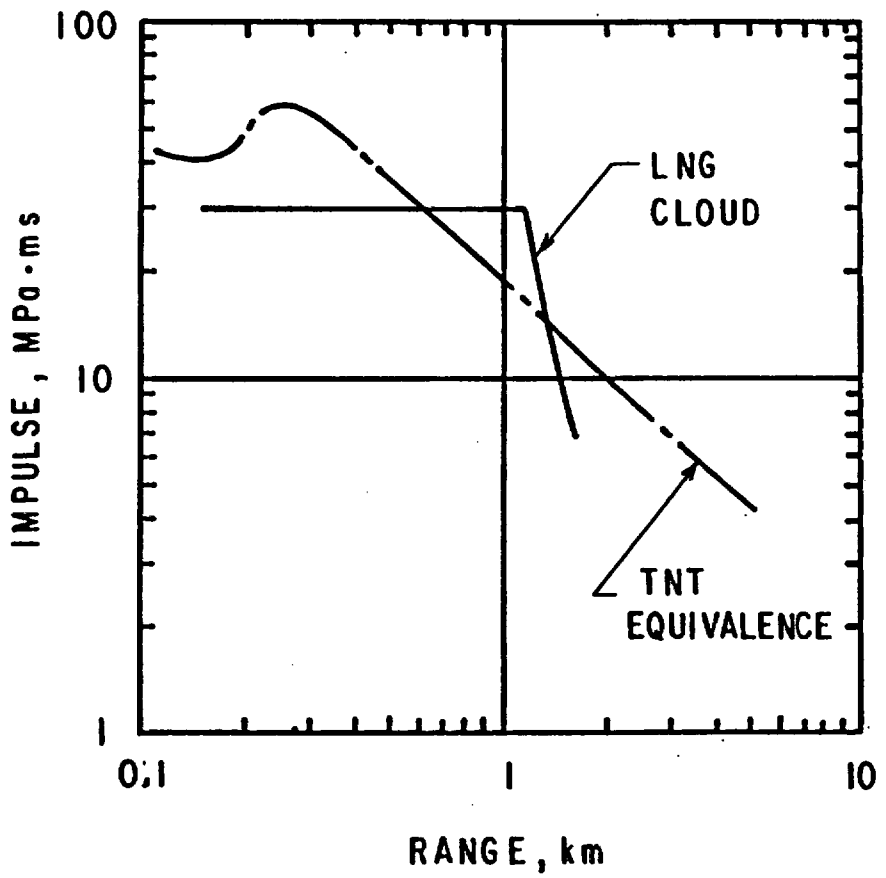

Figure 47. Comparisons of Impulse Extimates for LNG Cloud Explosion.

7. LNG SPILL THREATS

The methods for determining the environment resulting from a massive spill of LNG on water were outlined in the preceding chapters. A result summary was also presented and more detailed data can be found in Appendixes A, B, and C. Based on this information, an attempt is made to estimate the nature and magnitude of the threat from such a spill. Although the term "threat" is not very precise, it is defined here as the extent, intensity, and total magnitude of a particular effect arising from the LNG spill. Thus of interest are the distances and durations of a specific effect as well as fluxes and their time integral. The intent here is to define the credible maxima of these quantities, assuming that the total spill is limited to 25,000 m^3. The threats considered are the LNG liquid, i.e., the pool, the vapor cloud, fire, and explosion. While the actual susceptibility of nuclear power plants will be discussed later, the threat definition provided here obviously takes cognizance of the ultimate application of the results.

7.1 LNG Pool

The major concerns with respect to the LNG liquid is that it may reach a vital plant installation or that is may serve as the fuel source for a pool fire. Thus the size or extent of the LNG pool is of primary importance. This distance depends both on the spill duration and evaporation rate (see Chapter 3 and Appendix A). Because of the latter dependence, the maximum pool radii occur when ignition of the LNG does not take place. Using the most credible evaporation rate (without fire) of 0.000305 m/s, maximum pool radii of the order of 400 m may be expected. The persistence of the LNG pool and quantity of liquid involved are abviously position-dependent, with the longest durations and largest quantities at the spill source. This location is of interest primarily in case of immediate ignition, i.e., for a direct pool fire. At locations some distance from the source, the persistence of the LNG pool can be estimated from the duration of the pool spread. The latter quantity appears to peak at a value of 600 s (see Appendix A) and gives an indication of the upper limit for pool persistence for most locations, except in the immediate vicinity of the source where the duration is equal to the spill duration. Since the average velocity of pool spreading is of the order of 1 m/s, the actual persistence of the LNG pool at most locations will be considerably shorter than the 600 s indicated above. The spreading distance of a spill on water in a particular direction may be enhanced due to current and wave action. However, these are slow effects, which require considerable time [31]. Because of the cryogenic nature of LNG and hence rapid evaporation, the influence of current and wave action is expected to be minor.

7.2 Vapor Cloud

The LNG vapor cloud poses a direct threat to nuclear power plants primarily through its asphyxiating effect on personnel at high enough concentrations. Since LNG usually contains about 85-90% of methane and 15-10% higher hydrocarbons, it can be assumed to act as a simple asphyxiant, i.e., only by the inert dilution of air and thus reduction in oxygen level. The threshold of personnel impairment for such an asphyxiant has been estimated at a volumetric concentration of 28%, which corresponds to an oxygen concentration of 15% [32]. Examining the computational results (Appendixes B and C), we find that for most cases this concentration level of the vapor cloud is reached rather quickly, i.e., usually in times less than 250 s after spill initiation. Variables such as wind speed and spill duration have little effect on concentration. The major effects come from the relative humidity of the air and the initial gas composition. An extreme case arises for high relative humidities (~ 100%) and a pure methane gas. It takes nearly 450 s to reach an LNG concentration of 28%. The corresponding cloud radius at this time is about 750 m. The cloud-drift distance is strongly influenced by wind speed and can be as much as 2200 m for a wind speed of 8.96 m/s (20 mph) (see Appendix C). Thus the furthest possible downwind distance at which LNG vapor concentrations are sufficiently high to result in some personnel impairment due to reduced oxygen levels is about 3000 m from the spill source.

For more usual LNG compositions, i.e., compositions including higher hydrocarbons such that the molecular weight exceeds that of methane by 10%, it is estimated that the critical composition is reached in about 250 s. The cloud radius at this time is estimated to be 800 m, and the cloud drift, even at a high wind speed of 8.96 m/s, does not exceed 500 m. Thus a most plausible distance to the threshold of personnel impairment due to oxygen depletion is about 1300 m.

Since the cloud composition varies only with time, the longest possible duration associated with a condition of severe oxygen depletion is equal to the time when the critical threshold composition is reached and is limited to a region in the close proximity of the spill source. At loctions away from the source, this duration is equal to the time interval starting with the cloud arrival and ending when the threshold composition is reached throughout the cloud. For the extreme case, i.e., pure methane, 100% relative humidity, and 8.96 m/s wind speed, the total durations of oxygen depletion are estimated as follows:

Distance from Spill Source m	Duration s
0	450
1000	300
2000	175
3000	0

Using the more realistic LNG composition, the condition of oxygen depletion appears to last at most 250 s, and at a distance of 1000 m from the spill source, this duration is reduced to about 30 s.

7.3 Fire Potential

The LNG vapor cloud also poses an indirect threat to any installation in that it constitutes the fuel source for severe fires and explosions. Of primary interest, therefore, are the distances and times to reach the flammability limits, i.e., the LFL and UFL. The first of these indicates the maximum extent of possible fire and explosion hazards; the UFL represents the boundary between premixed and diffusion flames and delineates the upper boundary for explosion regions.

In describing the combined LNG dispersion and fire model, we showed how strongly the extent of the flame region depends on the time of ignition (see Figs. 27-29). In defining the threat, this aspect is ignored, however, in order to arrive at a conservative estimate. Figure 17 and Table 5 show the distances to the LFL for various LNG compositions and relative hunidities of the air. These values are for a single wind speed of 4.48 m/s (10 mph). Although wind speed has no effect on the cloud-radius, it does influence the cloud drift. As seen in Table 3, an increase in the wind speed from 4.48 to 8.96 m/s adds an additional 1300 m to the LFL cloud drift for the zero-humidity case.

The times to reach the flammability limits are very sensitive to the LNG composition and relative humidity, but are essentially independent of wind speed. For pure methane and 100% relative humidity it takes 2700 s to reach the LFL and only 800 s to attain the UFL. Thus the cloud remains combustible for 0.75 h, and the risk of an intense fire, in a premixed cloud, and of explosion persists for more than half an hour. Using the more realistic composition (molecular weight 10% higher than methane), the time to LFL is estimated at 1450 s and to UFL at 470 s. Thus the time for possible cloud flammability is reduced to less than 0.5 h and the risk of explosion to about 0.28 h. For lower relative humidities of the air, the

times during which the vapor cloud represents a fire and explosion risk are much reduced. Using the time to reach LFL and estimating the average drift velocity at 6 m/s when the wind speed is 8.96 m/s, it is calculated that, for the worst-case (pure methane, 100% relative humidity), the LFL extends to about 17 km (or in excess of 10 miles). The corresponding distance for the UFL is approximately 4.4 km using an average drift speed of 4.5 m/s. When a more realistic LNG composition is assumed, i.e., a molecular weight 10% larger than that of methane, the maximum distances are: for the LFL, 9.8 km and for the UFL, 3.2 km. All these distances are to the farthest edge of the cloud.

Again, reducing the relative humidities will reduce the distances. However, the assumption of very high relative humidity, i.e., close to 100%, is not unrealistic, considering that the main interest is in a layer of air above a large water surface. Vapor clouds under consideration will probably not keep their coherence for some of the long times required to reach the LFL. This is particularly true for the pure methane case where the time is 0.75 h. Dispersion by air turbulence, which this model neglects, may play some role for these cases. Therefore the most credible estimate of the threats, using the current model, should be based on the heavier LNG composition.

7.4 Fire-Threat Magnitudes

The fire scenarios that may result from an LNG spill on water depend on a large number of variables. It therefore becomes difficult to define a credible fire threat. In all of the examples of flux histories (see Chapter 5 and Appendixes B and C) the durations of the fires are typically less than 600 s, the peak heat fluxes vary from 20 to 50 kW/m^2, and the total thermal loads range from less than 2 MJ/m^2 to about 8 MJ/m^2. These results depend strongly on the time and the location of ignition and are representative for distances of 500-2500 m from the fire source (burning cloud or pool). The fire threat thus appears to be moderate at these locations. However, as shown earlier (Chapter 5), the fire severity increases rapidly as the fire source is approached. Both the fire-peak intensity and the total thermal energy become large. Taking into consideration the long durations of cloud flammability and cloud-drift distances that occur under certain conditions of high humidity and LNG composition (see preceding section), severe fire threats may arise in certain situations.

It has been shown (see Chapter 5) that flame temperatures for hydrocarbon fuels burning as diffusion flames (fuel rich) are about 1373 K, and stoichiometric premixed vapor clouds may burn with flame temperatures as high as 2148K. Assuming ideal conditions, i.e., black body radiation, the

corresponding radiation heat fluxes in the immediate vicinity of the flames (no attenuation) are 201 and 1207 kW/m^2 respectively. The first of these values agrees well with the measured flux of 210 kW/m^2 obtained in pool-fire experiments with LNG [18]. Should a particular target be actually engulfed by the fire, then in addition to radiation heating, convective heating will take place. The latter will depend on the heat-transfer coefficient at the surface of the target. For turbulent flames the maximum value of this coefficient is estimated at 852 W/m^2 K (150 Btu/h ft^2 °F) [33]. Using this value the maximum convective heat flux to a target engulfed by the fire is estimated at 920 kW/m^2 for the diffusion flame and 1,580 kW/m^2 for the premixed vapor burning (2148 K). All the cited heat fluxes represent the maximum possible flux, assuming an initial target-surface temperature of 20°C. As the target-surface temperature increases, the heat flux to the target from both radiation and convection will diminish. However, the quoted heat-flux values provide upper bounds for estimating the threat to targets in contact with the combustion gases.

The second aspect that must be considered is the duration of the fire threat. Given a fixed spill scenario, this duration is primarily determined by the location and time of ignition, as well as the speed of the flame traversing the fuel source. Although most LNG vapor clouds and pools remain flammable only for times of about 10 min, it was shown that for compositions approaching pure methane and for 100% relative air humidity, a cloud may be flammable for as much as 0.75 h. Such a cloud reaches a near constant radius of about 800 m in 500 s (see Appendix C, Figure 4.14). Thus if ignition takes place after this time at one edge of the cloud and the flame speed has a low value say 1 m/s, the duration of the fire, which must burn across the diameter of the cloud, is 1600 s. However, note that the cloud under consideration reaches the UFL at 800 s and that the flame velocity would most likely increase at this point. Assuming a flame speed of 2 m/s in the premixed region reduces the burning time to 950 s while a flame speed of 5 m/s reduces the time to 560s.

For a more realistic LNG composition (molecular weight 10% higher than methane) the nearly constant cloud radius of 1100 m is reached in 450 s. Thus a fire starting at this time and having a flame speed of 1 m/s could burn for about 1000 s until the LFL is reached (1450 s). Since most of the burning takes place in a premixed cloud (UFL occurs at 470 s) higher flame speeds may be expected. At 2 m/s, the fire duration remains at 1000 s, because the LFL is reached before the cloud is burned off. However, at a flame speed of 5 m/s burn-out occurs after a fire duration of 450 s. Note that the above fire threats are essentially independent of the LNG pool. In all cases, to obtain the longest fire durations, ignition is assumed to be

delayed to a time when LNG evaporation is essentially complete.

The range, or distance from the spill site, at which the above fire threats may occur is primarily a function of the cloud drift due to wind action. As shown earlier, the maximum distance for a pure methane cloud at 100% relative humidity and a wind speed of 8.96 m/s is 17 km. For the heavier LNG composition, the corresponding range is 9.8 km. These distances are very large; however, there exists a mitigating factor when the wind velocity is high; namely, the cloud residence time at a given location is short. This in turn reduces the fire threat.

The fire durations estimated above are the total times required to burn off or extinguish the flame regardless of the location and motion of the vapor cloud and flame front. In estimating the threat, however, one is interested in the intense fire duration at a fixed location. The vapor clouds under consideration have a finite size with a diameter of about, 2000 m. Therefore, even for a stationary vapor cloud, a fixed target will experience the high-intensity flame only for a fraction of the total fire duration, because the flame will be either approaching or receding from the target and, as shown earlier, the heat fluxes diminish rapidly as the distance from the target increases. In addition, for a fire approaching the target, the vapor cloud itself will provide some shielding from the heat flux.

With cloud drift present, the situation becomes more complex, since now the residence time of the cloud itself at a given location is a function of the drift velocity. Thus for a 2000 m diameter cloud and a wind speed of 8.96 m/s, which results in an average drift velocity of 6 m/s, the residence time for the cloud at a fixed location is 333 s. For a wind speed of 4.48m/s (drift speed, 3 m/s) this residence time is 667 s. Again as the burning cloud drifts by the target, the actual location of the flame front and thus the source of the heat flux may be aproaching, receding from, or passing the target, depending on the flame speed and ignition location. Therefore, in general, the heat flux received at the target will be smaller than the maximum. The full residence time of the cloud at the target becomes equal to the fire duration at the target only in case the flame speed (relative to the unburned cloud) is equal to the drift speed, and ignition occurs at the downwind edge of the cloud as it first contacts the target. Since drift velocities and flame speeds are of the same order of magnitude, this is probably the most realistic but worst-case fire scenario possible. The farthest location from the spill source, where this full fire duration can be realized, is at least one cloud diameter less then the above-cited distances to the LFL. At greater distances, cloud dilution below the LFL would shorten the fire duration. For the pure methane cloud, 100% relative

humidity, and a wind speed of 8.96 m/s, the farthest location would be 15 km with a fire duration of 333 s. For the more realistic (heavier) LNG composition, the location is about 8 km. When the wind speed is 4.48 m/s and the flame and drift speed are reduced to 3.0 m/s, the farthest target locations are 6.9 km for methane and about 2 km for the heavier LNG, with durations increasing to 667 s. Since for all these cases the cloud composition is in a premixed state, i.e., below the UFL, the target could experience the highest possible heat flux corresponding to a flame temperature of 2148 K. These estimates are based on assuming a constant drift velocity that is reasonable for the times and wind speeds under consideration (see Appendix C). However, for smaller wind speeds this would not apply. These cases are, however, of lesser interest, because the distances would approach the spill source. The above estimates are thought to provide upper bounds for the expected fire threat due to LNG spills on water.

7.5 Explosion Threat

The magnitudes of the overpressure, impulse, and duration from the explosion of a "pancake" shaped LNG cloud are shown in Chapter 6. To ascertain the threat from the explosion, one must determine the distances relative to the spill source at which such explosions may take place. Since the explosion propagates through the cloud at a detonation speed of 1680 m/s, the entire process will be completed even for a large cloud in about 1 s. Relative to the cloud spreading and drift, this is essentially an instantaneous process. The clouds present on explosion threat during the entire time they reside in a premixed state (between UFL and LFL) and out to distances at which the LFL is reached.

While for many spill scenarios these distances and times are moderate, it has been shown (Section 7.3) that circumstances exist (high relative humidity, nearly pure methane) when the threat persists a long time and with appropriately high wind velocities can extend out to long ranges. Thus, for a wind speed of 8.96 m/s (20 mph), a target may experience the detonation overpressure and impulse at a distance of nearly 17 km from the source, assuming pure methane. For a more realistic heavier LNG composition, the range is 9.8 km.

The distance from the cloud edge to the safe overpressure level of 0.007 MPa (1 psi) [29] was earlier estimated as equal to 100 cloud-height units (see Chapter 6). For the cases considered above, these distances would be 14.5 km for the pure methane cloud, which has a height of 145 km and 7.3 km for the heavier cloud, which has a height of 73 m at the LFL (see Table 5).

However, these distances are based on results obtained for a cloud with an aspect ratio (radius to height) of 44 for which planar detonation is a good approximation. For the clouds considered here, the aspect ratio is 5.9 for the methane cloud and 15.8 for the heavier composition. Thus, the above distances are probably overestimates of the true distances. A lower limit for this distance may be obtained by considering the hemispherical explosion of the cloud. The cloud contains approximately a fuel mass of 10^7 kg with a TNT mass equivalency of 2.4 [29]. The 1 psi level from such an explosion is reached at a scaled distance of 18 $m/kg^{1/3}$ [34]. This yields a distance of 5.2 km from the explosion center and should be compared with 15.3 km for the methane cloud and 8.4 k for the cloud of heavier composition, which are obtained with a pancake cloud model. The latter distances are now also referred to the center of the cloud. As pointed out earlier, the estimates based on the hemispherical cloud assumption represent a lower limit of the distance to the 1 psi overpressure level. The actual distance lies probably somewhere between the two extremes. Considering the large drift of the cloud, one finds that the range from the spill source to a completely safe overpressure level is quite large. For the extreme assumption of 100% humidity and pure methane using a credible wind speed of 8.96 m/s (20 mph), this range lies somewhere between 21.4 and 31.5 km. Using the heavier LNG composition and assuming the same atmospheric conditions, the distance to the safe overpressure level is estimated to lie between 13.9 and 16.0 km. As pointed out before, it is somewhat doubtful that for the pure methane composition the cloud will maintain its coherence over the long drift distance predicted by the current model. Atmospheric turbulence coupled with wind action may be expected to cause earlier dispersion below the LFL.

In case an LNG cloud explosion does take place, some degree of damage may be expected, for targets such as a nuclear power plant, at all locations closer to the spill source than the safe 0.007 MPa (1 psi) overpressure level. The degree of damage will depend on the overpressure level, the blast duration, and the hardness of the target. Damage sufficiently severe to affect the safe functioning of a nuclear power plant should probably be expected for overpressures in excess of 0.207 MPa (30 psig). This is the level at which severe damage normally occurs to reinforced concrete windowless structures if the duration of the blast duration is of the order of 0.5 to 2.0.s [35]. From Fig. 43 it is seen that the blast duration for an LNG cloud explosion at this pressure level approaches about 20 ms/m of cloud height. Hence, a cloud height of 75 m will yield a duration of about 1.5 s. While such a cloud height develops only under conditions of high relative humidity (see Table 5), heights of about 50 m and hence durations of 1 s are not unusual. Therefore the 0.207 MPa overpressure level appears to be a

reasonable threshold of severe damage to nuclear power plant structures and functioning.

In case of a "pancake-like" cloud, this threshold occurs at about four cloud-height units from the edge of the exploding cloud (see Figs. 42 and 43). For most cloud configurations, this represents a distance of less than 200 m from the cloud edge, and only in case of high humidity and pure methane may the distance approach 500 m. Therefore, this pressure threshold will depend primarily on the cloud drift. For the most severe case (100% humidity, methane, 8.96 m/s wind speed), the distance from the spill source is 17.6 km, and for the heavier LNG composition, the distance becomes 10.1 km. When a TNT equivalency approach or a detonating hemispherical cloud is used to estimate the pressures from an LNG cloud explosion, the threshold level of interest (30 psi) lies at a distance of 600-650 m from the center of the cloud (see Fig. 46). This, however, is a location that actually lies within the vapor cloud at the time LFL is reached (see Table 5) and thus in reality would experience much higher overpressures. Since the 30 psi overpressure level occurs such a short distance from the cloud edge (4 height units), the estimates based on the pancake cloud should be reasonably accurate and will be used in the current application.

7.6 Threat Summary and Application

The most accurate way of establishing the LNG spill threat in a particular application is to actually perform specific computations for the expected separation distances (spill to target) and the prevailing atmospheric conditions. This, however, is a time-consuming procedure and requires specific site information. To arrive at a first estimate of the expected threat, the results presented in the preceding sections can be used directly. Similarly, in the current application the threat as discussed above will be used to estimate the vulnerability of nuclear power plants. For convenience these results are summarized in Table 8. Both "worst-case" and "typical" threats are presented. The latter approximately corresponds to moderate winds and relative humidities (4.48 m/s and 50%, respectively) as well as a realistic LNG composition (molecular weight 10% larger than methane). The "worst-case" results are for 100% humidity and 8.96 m/s wind velocity and again a realistic LNG composition. The data obtained for pure methane are also listed for the worst case and appear in parentheses. Because of the strong fire-target interaction, it is not possible to estimate the total thermal energies in case of targets engulfed by the fire. It is seen, however, that the initial peak heat fluxes are very intense in this case. Thus the surface temperature of a target engulfed by the fire will increase very rapidly. To estimate the heat transfer into the

TABLE 8

SUMMARY OF LNG THREATS

1. Spill and Pool

Spill duration resulting in maximum pool and cloud size	600 s
Maximum pool duration, no fire	600 s
Maximum pool radius	400 m

2. Vapor Cloud

(a) Asphyxiant (28% LNG by volume)

Max. Range, km	Total Duration, s	Duration at 1 km from Spill Source, s
1.3	250	30
(3.0)	(450)	(300)

(b) Fire Potential

	UFL(15%)		LFL(5%)	
	Max.Range, km	Time, s	Max. Range, km	Time, s
Typical Case	0.8	170	3.5	600
Worst Case	3.2 (4.4)	470 (800)	9.8 (17.0)	1450 (2700)

3. Fire

(a) Typical Targets Not Engulfed by Fire

Distance from spill source, km	0.5 to 2.5
Ignition Delay Times, s	0 to 400
Fire Duration, s	600
Peak Heat flux, kw/m^2	20 to 50
Total Thermal Loading MJ/m^2	2 to 8

(b) Targets Engulfed by Fire

(i) Fire Conditions

	Diffusion Flame	Premixed Flame
Flame Temperature, K	1373	2148
Max. Radiation Flux, kW/m^2	201	1207
Max. Convective Flux, kW/m^2	920	1580

TABLE 8 (cont'd)

(b) Targets Engulfed by Fire (cont'd)

(ii) Worst Case Fire

Max. Range, km	9.8 (17.0)
Total Duration, s	1000 (1600)

(iii) Fire Durations at Targets

Relative Humidity, %	50	100	100
Wind Speed, m/s	4.48	4.48	8.96
Distance, km	2.0	2.0(6.4)	8.0 (15.0)
Duration, s	300	670	330

4. Explosion

	Typical	Worst Case
Detonation: 1.45 MPa		
Distance, km	3.5	9.8(17.0)
Impulse, MPa·ms	37.0	89(176)
Duration, s (Estimate)	0.100	0.250(0.500)
Severe Damage: 0.207 MPa (30 psi)		
Distance, km	3.7	10.1(17.5)
Impulse, MPa·ms	25.0	45(89)
Duration, s (Estimate)	0.5	1.5(2.9)
Safe Overpressure: 0.0007 MPa (1 psi)		
Distance, km	6.5	15(26)

Result Assumptions

	Typical	Worst Case
LNG Molecular Weight, % of Methane	110	110(100)
Wind Speed, m/s	4.48	8.96(8.96)
Relative Humidity, %	50	100(100)

Note: Numbers in parenthesis always refer to pure methane case.

target it is, for most applications, conservative and acceptable to assume that the target surface temperature is equal to the flame temperataure when the target is engulfed by the flame. This approach is used and is justified by more elaborate calculations in the current study.

8. Survey of Safety Systems for Nuclear Power Plants

To ascertain the vulnerability of a nuclear power plant to the threats posed by a large LNG spill on water, one must first identify the vital components of the plant that may be affected by the spill environment. Of primary interest are safety related plant systems particularly those that are required for the safe shutdown and heat removal from the plant so as to avoid any significant incidents that may create a safety hazard for the general public. The current study is not concerned with a particular power plant, i.e., is not site specific; rather, the LNG hazards are to be evaluated in a generic manner. Currently operational nuclear power plants [36] located along water transportation routes or along shorelines are listed in Table 9. As can be seen, there is significant variability in design, size, and age of the plants. Both PWR and BWR systems are represented. The general susceptibility of these plants to the threats posed by an LNG spill may therefore be expected to vary. However, keeping in mind the main concerns, i.e., safe shutdown and heat removal, we can arrive at some generalizations.

To accomplish these operations in a nuclear power plant, the plant must first of all be controllable. This requires not only that certain instrumentation and control systems remain operational, but also that an adequate supply of electric power be maintained and that key operating personnel of the plant be able to function. For plant heat removal, at least one of the major cooling circuits must be available. Also maintained must be an ultimate heat sink, component cooling, and some of the air-conditioning. This in turn implies the continued functioning of certain equipment, such as pumps and valves, and obviously the availability of electric power. It should also be noted that while the durations of the acute threats from an LNG spill may be relatively short (see Chapter 7), all the above-mentioned functions must be maintained for much longer periods following the acute stage. This is most obvious with respect to electric power supply. The period of acute threat may well be handled by the emergency batteries, but in the long run (approximately 2 hours), another power source must become available to the plant to continue the decay-heat removal. Thus severe damage and loss of all offsite power and the emergency onsite diesel generators would indeed constitute a severe incident.

As indicated earlier, the major threats from an LNG spill on water are thermal loads produced by fire and overpressures in case of explosion. Other hazards are oxygen depletion by the vapor cloud, and toxic effects of either combustion gases or vapors released on site, e.g., chlorine, due to the effects of the primary threats. Finally, in some cases a direct threat

TABLE 9

NUCLEAR POWER PLANTS ALONG WATERWAYS

NAME	UNIT	TYPE	MANUF.	OUTPUT MW_t	LOCATION	REMARKS
CALVERT CLIFFS	1&2	PWR	CE	2700	Chesapeak Bay, MD	LNG terminal at Cove Point approximately 5 km away
CRYSTAL RIVER	3	PWR	B&W	2452	Gulf of Mexico, 70 mi N of Tampa,FL	
DIABLO CANYON	1	PWR	W	3338	Pacific Ocean, 10 mi from San Luis Obispo, CA	
	2	PWR	W	3411		
INIDAN POINT	1	PWR	B&W	615	East Bank of Hudson River, 24 mi N of New York	
	2	PWR	W	2758		
	3	PWR	W	3025		
MILLSTONE	1	BWR	GE	2011	Long Island Sound-North Shore 40 mi SE from Hartford, CT	Steel Enclosure Bldg. around containment.
	2	PWR	CE	2700		
PILGRIM	1	BWR	GE	1998	Cape Cod Bay, Western Shore, Plymouth, MA	
SAINT LUCI	1&2	PWR	CE	2570	Hutchison Island near Fort Pierce,FL	Steel Containment Concrete Shield Bldg.
SALEM	1	PWR	W	3350	Delaware River, 8 mi SW of Salem, NJ	
SAN ONOFRE	1	PWR	W	1347	Pacific Ocean Camp Pendleton Marine Station, S of San Clemente, CA	30 ft seawall, Containment Sphere Enclosure Bldg.
SHOREHAM	1	BWR	GE	2436	North Shore of Long Island, NY just N of BNL	
SURRY	1&2	PWR	W	2441	James River (Gravel Neck Point), VA	
TURKEY POINT	3&4	PWR	W	2200	Biscayne Bay, 25 mi S of Miami, FL	4000 acre, 168 mi long grid of closed cycle cooling ponds and canals.

may arise from the LNG liquid pool, either through possible ingestion into the cooling-water system or through the effects of the extremely cold liquid on plant structures located at the water line. As was shown in Chapter 7, both the type of threats and their severity depend on many factors, the most important of which are: distance between the spill location and the plant site, wind conditions, relative humidity, LNG composition, and ignition time and location.

A survey of the vital NPP systems and components [37, 38] readily indicates that most of them are housed inside substantial, usually Class I, structures. Thus, the effects of the LNG spill environment on these systems are in general only indirect, unless the protection provided by the structure is breached. Also, the state of the plant at the time the spill environment or its effects reach the site may be of utmost importance; e.g., has the reactor been shut down, have all ventilation system dampers been closed, has all unnecessary equipment been shut down, has the operating personnel been warned, etc.? In specific cases, an accident scenario must therefore be assumed in order to evaluate the hazard. This in turn, would depend on such plant features as detection and warning systems. The detailed consideration of all these factors is clearly beyond the scope of the present effort. In case the LNG in either vapor or liquid form does not reach the site, the threats are limited to thermal loads due to the radiation from offsite fires and to overpressure effects from a possible offsite explosion. The major hazard in this case may be the possible structural or functional failures of vital systems and components. Ignition of combustibles may also occur, and there is some possibility that heat loads could become excessive for the available cooling capacities. Among safety-related systems, the offsite power supply appears to be the most vulnerable.

If the LNG vapor and/or liquid reach the plant site, additional threats must be considered. Included are oxygen depletion, toxicity, and the earlier mentioned effects of LNG liquid. The fire threat is now enhanced by convective heating, and explosions are more likely and severe because of possible confinement. In particular, volume detonations may occur when combustible mixtures ignite inside a nearly enclosed space. Again the offsite power supply appears to be most vulnerable, but in addition, any space containing vital equipment which is not completely closed off or which cannot withstand the severity of the loading may be vulnerable. This could include auxiliary diesel power, emergency batteries, intake structures, diesel fuel storage, or even the control room and cable spreading room, via their air intake and ventilating systems. Tables 10 and 11 summarize the possible threats, effects, and affected safety systems for offsite and

TABLE 10

SYSTEMS SUSCEPTIBLE TO OFF-SITE LNG THREATS

Threat	Possible Effects	Susceptible Items	Most Likely Affected Safety Systems
Fire (Radiation Only)	Ignition of On-site Combustibles	Fuels (exposed) Wooden Structures Construction Materials Electrical Cables	Off-site power supply
	Excessive Heating of Structures and Components - Structural Failures	Steel Structures Concrete Structures Storage Tanks Electrical Equipment (insulators, transformers etc.)	Off-site power supply
	Excessive heat loads - Insufficient heat removal capability	Ventilation & air conditioning systems Electrical Equipment	Off-site power supply
	Personnel Injuries Burns	Exposed Personnel	
Explosion-Fast Deflagration (Overpressure-Impulse)	Structural & Functional Failures	Electrical Equipment Ventilation Systems Storage Tanks Exposed Pipine Systems All Structures & buildings (except reinforced concrete)	Off-site power supply
	Personnel Injuries	Exposed Personnel	

TABLE 11

SYSTEMS SUSCEPTIBLE TO ON-SITE LNG THREATS

Threat	Possible Effects	Susceptible Items	Most Likely Affected Safety Systems
LNG Pool	Structural & Functional Failures	Intake Structure Cooling Water Circulating pumps	Cooling water circulating pumps
LNG Vapor Cloud	Oxygen Depletion	Personnel-Asphyxiation	Control Room personnel
Fire (Radiation & Convection)	Ignition of Combustibles (exposed)	Fuels Wooden Structures Construction Materials Electrical Cables	Off-site Power supply
	Fire Propagation into Plant Interior	Ventilation Systems Air Intakes and Exhausts	Emergency power battery room, Control room, cable spreading room
	Structural & Functional Failures	Exposed Steel Structures Concrete Structure Storage Tanks Piping Systems Electrical Equipment	Off-site power supply
	Excessive Heat Loads - Insufficient Heat Removal	Ventilation & Air Conditioning Systems, Electrical Equipment, Cooling Systems	Off-site power supply, Control room
	Toxicity-Combustion Gases	Exposed or sheltered Personnel	Control Room Personnel
	Personnel Injuries - Burns	Exposed or sheltered Personnel	Control room Personnel
Explosion-Fast Deflagration (overpressure - Impulse)	Structural & Functional Failures	All exposed equipment Storage Tanks Ventilation Systems All Structures Piping Systems	In order of increasing severity of blast: Off-site power Main Steam or cooling water lines (exposed) Diesel fuel storage-block house Intake structure Auxiliary building Nuclear fuel storage Containment building
Explosion-Fast Deflagration(overpressure - Impulse) (cont'd)	Overpressure Propagation into Plant	Ventilation Systems Air Intake and Exhaust Systems	Control Room Emergency Power Battery Room Emergency Diesel Systems
	Personnel Injuries	Exposed and Sheltered Personnel	Control Room Personnel

onsite LNG situations. It is possible to imagine a whole gamut of effects, and their likelihood and severity, as pointed out earlier, depends very much on the state of NPP, i.e., both its operational status and its degree of isolation from the outside environment. Although many items are identified in the hazards compilations (Tables 10 and 11), only the most likely and severe hazards, i.e., selected systems, components, and personnel, are analyzed for their susceptibilities.

9. Nuclear Power Plant Susceptibility

To estimate the effects of the LNG spill environment on a nuclear power plant, it is first necessary to define the susceptibility of such a plant to the types of threats posed by the spill. As shown in the preceding chapter, only a limited number of plant systems need be considered to assume safe shutdown and heat removal. The approach taken in determining susceptibilities is based on using available information from the literature concerning the generic response or resistance of a system or component to a specific threat, e.g., fire, blast. Thus the process amounts to establishing simple damage criteria, and no detailed analyses are undertaken. It is well known [39] that, regardless of the system considered and the type of threat, the susceptibility may be a function of both the threat intensity and of the time integral of the intensity. The latter provides a measure of the total dosage, impulse, energy, etc., delivered to the system. For each threat and system considered, there usually exist threshold values for both the intensity and its time integral below which the threat will have no effect on the system. Similarly, when a fixed iso-damage level for the system is considered, there again exist minimum values for both intensity and its time integral, which must be exceeded to produce this damage. Therefore in establishing susceptibilities of a system in general, one should consider both factors, i.e., intensity and total amount. Only in the extreme case of a threat of very long duration is it usually possible to define damage criteria or susceptibility limits based only on the intensity. Conversely, for threats of very short durations relative to the response time of the system, criteria may be established using as a basis only the total amount (time integral) of the threat.

In many cases it is possible to define the susceptibility of a system, or at least its first-order estimate, simply in terms of the level of the threat, i.e., its intensity and duration. This usually requires the existence of a large body of experimental data concerning the effects of the hazard under consideration. This approach is usually applicable where the response of the system has little or no effect on the intensity of the threat environment, i.e., the threat environment and the response are not interactive. On the other hand, when the threat and system response are interactive and the times required to produce a response are relatively long, it is difficult to arrive at susceptibilities in terms of the threat levels alone. In these cases it is first necessary to define damage levels or criteria in terms of the response of the system. These can then be used in conjunction with analytical or computational procedures to determine the threat magnitudes required to produce the specified damage level. This approach can be used in all cases. However, as pointed out above, it is

often simpler, when the appropriate data base exists, to go directly to criteria defined in terms of the threat level.

Concerning this latter more direct approach, note that much of the data required for the current application comes from the weapons-effects literature [35,40]. Therefore, the intensities and durations of the blast and thermal threats are not always commensurate with the possible hazard environments created by an LNG spill, and care must be exercised when using these data for the current application. Finally, since the interest here lies in safe operation and shutdown of nuclear power plants, the susceptibility limits must be chosen conservatively, so as to preclude any doubt that the intended functions can be carried out.

9.1 Personnel Exposure Limits

All the threats produced by a large LNG spill on water may to some extent affect or incapacitate the personnel at a nuclear power plant. Many of the effects may be strongly mitigated or completely eliminated for personnel housed inside a structure such as the typical nuclear power plant auxiliary building, which normally contains the control room. The thresholds provided here are therefore primarily for personnel who are found in unprotected areas of the power plant.

The response of the human system, primarily the skin, to thermal loads is a function of both the heat-flux intensity and the duration. Interest here, however, lies in intensity levels that will produce immediate (in less than a few minutes) effects. Although there is some disparity in the literature data, it does appear that intensity levels of 3-5 kW/m^2 provide the threshold for first-degree burns in less than 1 min exposure [39,41,42]. Thus a level of 4 kW/m^2 will be taken to indicate the limit for personnel exposure below which there will be no impairment of function.

It was pointed out earlier that LNG can act as an asphyxiant through oxygen depletion in the atmosphere. Again, the response of the human body to this threat is fairly immediate. Thus, a criterion based solely on the intensity level, in this case, concentration, is acceptable. It is fairly well established that, for a simple asphyxiant, a concentration by volume of 42% or an oxygen depletion in the atmosphere to 12% constitutes the threshold for mental impairment [32]. However, for the current application, where operator performance and not injury is the issue, this oxygen depletion level is considered too low [43]. Therefore a level of 15% of oxygen in the atmosphere will be taken as the limit for the impairment of operator

function. This corresponds to a level of 28 vol % of LNG vapor in the atmosphere.

No direct toxic effects are produced by LNG. However, some secondary or indirect toxic effects may arise from the burning of LNG vapors. The most important of these is the toxicity of combustion gases, which in turn means the concentrations of carbon dioxide and carbon monoxide. The latter produces significant physiological effects, even for concentrations as low as 0.1% [32]. However, long exposures (hours) are required at these low concentrations to produce these effects. Thus, 0.1% of CO is taken as the limit for the current application. While there are some noticeable physiological effects for carbon dioxide concentrations of 2 vol %, e.g., increase in the depth of respiration, no impairment of function is expected at this level [32]. Hence the 2% level of CO_2 is accepted as the limit for the current purpose.

Airblast can produce multiple effects and injuries on exposed personnel. The level of injury strongly depends on both the overpressure and duration. It was seen earlier that the expected blast durations from LNG cloud explosions are quite long (on the order of 0.5-1.0 s); i.e., the duration is comparable with those from nuclear weapons explosions in the high-kiloton or low-megaton range. Since the response time of the body is much shorter than these durations, simple overpressure criteria are acceptable for the determination of susceptibility. In addition to the direct blast effects on personnel, injuries are possible due to secondary effects produced by impacting missiles and debris [35,39]. Also, tertiary injuries arise when the human subject is accelerated and displaced by the blast drag forces and impacts a stationary object or is dragged along the ground surface. However, the aim here is not to determine severity, but to establish thresholds under which the power plant personnel can keep on functioning effectively. An overpressure of 0.0345 MPa (5 psi) is therefore taken as the limit of personnel exposure, since it represents the threshold both for eardrum damage and for injuries due to small-missile (10 g) impact.

9.2 Airblast Effects on Structures and Components

The structures at typical nuclear power plants may range from heavy reinforced-concrete containment buildings to light-wall cinder block structures. Obviously they vary greatly in their resistance to air blast effects and in their natural frequencies. Concerning the latter, even for the most massive structures the response times are of the order of 1 s. These are times comparable in length to the durations of the expected blast waves. It is also a well-documented fact that massive reinforced-concrete

buildings are primarily overpressure sensitive [35,40]. Therefore, simple overpressure criteria will again be used to establish the susceptibility of these structures. Some of the other equipment items of interest, e.g., electric power systems, switchyards, high-voltage power lines, and pipe lines, are primarily drag-sensitive. However, the blast durations are sufficiently long, in comparision to their response times, to permit again the use of a simple overpressure criterion. Using information from the nuclear weapons effects literature [35,39], one arrives at the susceptibility criteria presented in Table 12. These values are considered threshold values at which some damage to the system in question is to be expected. However, its functionality should not be significantly impaired.

In at least one case, namely for reinforced-concrete structures, the overpressure criterion of 0.2069 MPa (30 psi) was thoroughly examined, using structural loading and response analysis techniques that are widely accepted in the design of protective construction [44]. It was found that for a building with dimensions and construction representative of an auxiliary building (20 m high, 20 m deep and 40 m long; 0.45 m thick walls, 0.3 m thick roof, and 3% reinforcing), the displacements produced by a 30 psi peak overpressure blast wave having a duration of 1 s, and approximating that of an LNG explosion, are almost completely in the elastic range. Similar for concrete panels 4.6 m (15 ft) on the side, 0.3 m thick, and with 1% reinforcement, the displacements and stresses were found to be acceptable. The computations provide some confidence that the established susceptibilities are realistic. Further confirmation of the criteria comes from the literature [45], where typical containment structures subjected to blast loadings are analyzed in detail using finite element codes.

9.3 Thermal Susceptibility of Structures

It was brought out earlier that the susceptibility cannot always be defined in terms of threat-environment variables. When the response of the systems is closely interactive with the environment, it is necessary to define criteria in terms of the response variables and then to provide estimates for each case of the system response, given a prescribed environment. The response of structures and components to thermal loads is a good example of this. The heat transfer to the structure is so dependent on the structure itself and on the relative geometry of the fire and structure that it is difficult to define susceptibility criteria in terms of the fire variables alone.

The most widely accepted design criterion for steel structures and structural elements, such as beams and columns, requires that the average

TABLE 12

AIR BLAST SUSCEPTIBILITY CRITERIA -
STRUCTURES AND COMPONENTS

Type of Structure	Overpressure Level MPa	(psi)
Reinforced Concrete Containment Buildings	.3448	50.0
Reinforced Concrete Structures: Auxiliary Building, Intake Structures Fuel Storage Structures, etc.	.2069	30.0
Heavy Industrial Type Building (steel frame): Turbine Building	.0828	12.0
Light Industrial Type or Brick Building: Shops, Offices, Stores	.0345	5.0
Wood Frame or Cinder Block Buildings: Offices, Stores, Guard Posts	.0172	2.5
Large Pipes and Pipe Bridges	.0483	7.0
Electrical Power Systems: Switchyard, substation, high voltage lines	.0345	5.0
Telephone lines	.0241	3.5
Ventilation Stacks (metal)	.0207	3.0

temperature of the elements not exceed 538°C (1000°F) [33,46]. This criterion corresponds to a reduction of the ultimate strength of structural steel to 46% of its value at ambient temperature. It can also be shown [46] that, for a typical steel column under steady-state conditions, i.e., long-duration fires, and under the assumption that the structure is not engulfed by the flame, the above criterion implies a radiation thermal load of 29.5 kW/m^2. Other investigators [42] have suggested that, for uncooled steel structures, the radiation thermal load from long-duration fires be limited to 24 kW/m^2. This corresponds to an average steel temperature of 493°C. Finally, if most (90%) of the ultimate strength of a steel structure must be retained, a limit of 400°C for the steel has been suggested [33]. Again this corresponds to a steady-state thermal load for a steel column of 14.9 kW/m^2. For the general case of unsteady thermal loads, it is best, however, to rely directly on the temperature criteria.

Most of the important buildings on a typical nuclear power plant site are of reinforced concrete construction. Criteria and design guides for reinforced concrete under thermal loading have been developed by many investigators and are well established [33,47,48,49]. Most of these criteria are based on the concept of a critical temperature for the reinforcing or prestressing steel of reinforced concrete structures. When the critical temperatures are exceeded, a structure or structural element is considered unsafe. Although there is some variation among the values used by various investigators or in various countries, these differences are minor. For the current application, a conservative set of temperature criteria has been selected from the literature. Their values are given below and are applicable to both concrete walls and structural elements such as beams and columns.

Temperature Criteria for Reinforced Concrete Structures

Maximum allowable temperature on unexposed face of concrete wall	139°C (250°F)
Maximum temperature of prestressing steel	427°C (800°F)
Maximum temperature of reinforcing steel	500°C (932°F)

A value of 593°C (1100°F) is often used in the literature for the maximum temperature of reinforcing steel [33]. This, however, appears to be too high a value, since it corresponds to a reduction of ultimate strength to 20% of its ambient value. The first criterion is equivalent to the heating of all the concrete in the wall to the above-indicated temperature and implies [49] possible ignition of combustibles on the unheated side of the wall.

The above criteria are developed using standard fire resistance tests [48] in which the average heat flux is 27.5 kW/M^2. The criteria also carry with the assumption that no spalling of the concrete occurs. However, the potential for spalling due to the buildup of steam pressure always exists when the concrete temperature exceeds 100°C. The evaporation of free water in the concrete, the migration of the water vapor, and its possible recondensation are a very complex phenomenon. The potential for spall increases as the critical temperature (100°C) moves to greater depth. This is due to both the greater amount of free water at greater depth and the increase in resistance to steam outflow from the heated surface. The larger amount of water at greater depth is a result of recondensation of steam liberated during the heating of shallower layers. The critical depth for spalling appears to be about 5 cm from the heated surface [33,48]. Explosive spalling may occur early in the fire or at later times, 0.25 to 0.50 hour and may result in exposing the main steel to high temperatures. This can lead to the serious weakening of a structural member, particularly for prestressed beams and heavily reinforced columns. In the current application, the above temperature criteria, together with the critical depth for spalling, will be used as a measure of susceptibility for concrete structures.

9.4 Ignition of Combustibles

The ignition of combustible and flammable materials at a nuclear power plant site is of interest because such ignition may lead to secondary fires directly at the site, and this in turn may result in the damage of a vital plant component. Also, ignition of some materials, e.g., electrical insulation, can directly lead to a failure affecting the plant's operation. Although there may be a variety of combustible materials at a plant site, only a small number of representative materials will be treated here.

In general, wood can be considered as representative of construction materials and may actually constitute part of some less important on-site buildings. Its ignition response under thermal radiation has been thoroughly documented [50], and correlations for the required heat fluxes and times have been derived. Assuming an average thermal inertia for wood, one can obtain simple equations for these correlations [32], for both piloted and spontaneous ignition. The former requires the presence of an ignition pilot, such as a small flame or spark. The expressions governing the ignition of wood are given below. The nomenclature used in these expressions is as follows:

k:	Thermal conductivity	(W/m K)
ρ:	Density	(kg/m^3)
C:	Thermal capacity	(J/kg•K)
I_r:	Incident radiant flux	(kW/m^2)
I_p:	Minimum radiant flux for pilot ignition	(kW/m^2)
I_s:	Minimum radiant flux for spontaneous ignition	(kW/m^2)
t_p:	Time to pilot ignition	(s)
t_s:	Time to spontaneous ignition	(s)
t_{eff}:	Effective duration of incident radiation	(s)

Average thermal inertia of wood:

$$k\rho C = 8.76 \times 10^5 \quad J^2/(m^5 \cdot s \cdot K^5)$$

Pilot ignition:

$$I_p = 13.4 \tag{29}$$

$$t_p = \left(\frac{76.4}{I_r - I_p} \right)^{3/2}$$

Criterion:

$$I_r > I_p \; ; \; t_{eff} > t_p$$

Spontaneous ignition:

$$I_s = 25.4 \tag{30}$$

$$t_s = \left(\frac{83.7}{I_r - I_s} \right)^{5/4}$$

Criterion:

$$I_r > I_s \; ; \; t_{eff} > t_s$$

In either case, two criteria must be met: (1) the incident radiation must be equal to or larger than the threshold value and (2) the duration must exceed the computed minimum value.

For more readily combustible materials, the limits for pilot and spontaneous ignition are often indistinguishable. Some of these examples taken from the literature [32] are provided below. These may be considered as representative of the most easily ignitable materials on site.

Cotton:

$$I_s = 12.5$$
$$t_s = 7.17 \times 10^3 \; I_r^{-1.64} \qquad (31)$$

α-cellulose (paper):

$$I_s = 16.72$$
$$t_s = 4.41 \times 10^6 \; I_r^{-3.64} \qquad (32)$$

Again the criteria for ignition to occur are

$$I_r > I_s \; ; \; t_{eff} > t_s$$

Another group of materials, the ignition of which is of interest, are plastic polymers. These are considered representative of materials used in electrical insulation. Because of their importance in industrial applications, the thermal and ignition response of polymers has been studied extensively [51, 52]. A correlation relationship based on experimental data has been derived for the time required for ignition to occur.

$$t_i = \frac{160(k\,C)^{0.75}\,(T_i - T_a)}{I_r^2} \; . \qquad (33)$$

This equation is dimensional and cannot be converted to arbitrary units. The appropriate units are:

t_i:	ignition time:	s
k:	thermal conductivity:	cal/g s °C
	density:	g/cm^3
C:	heat capacity:	cal/g °C
T_i:	ignition temperature:	°C
T_a:	ambient temperature:	°C
I_r:	radiant flux	cal/cm^2 s

To ascertain if ignition will occur, the values of the ignition temperature must also be known; these can be obtained from the literature [32]. Some representative values are listed below.

Material	kρC	T_i, °C
Silicone rubber	2.363×10^{-4}	720
PVC	1.68×10^{-4}	220

$$T \cong T_a + \frac{2I_r t_{eff}^{1/2}}{(\pi k \rho C)^{1/2}} . \qquad (34)$$

The criteria for ignition to occur are

$$T > T_i \; ; \; t_{eff} > t_i .$$

The actual procedure is first to use Eq. 34 to estimate the surface temperature and to check if it exceeds T_i. Then Eq. 33 is used to compute the time required for ignition at the given radiation level. This time is finally compared to the effective duration of the thermal radiation to see if ignition is possible.

9.5 Fracture of Brittle Materials

Brittle materials such as ceramics play a large role as insulators in electrical substations and power lines. Such materials may fail by fracture when subjected to large temperature changes. The actual stresses generated in an electric insulator subjected to sudden thermal load depend in a complex manner on the geometry and material characteristics of the

insulator. Precise estimates of the response are therefore difficult to obtain. However, using some limiting assumptions, one can get first-order estimates of the response [54-56]. These are based on the concept of thermal-stress-resistance factors. Assuming that either the surface heat-transfer coefficient is very large or that the heat load is so overwhelming that the surface temperature of the body, to a good approximation, changes instantaneously to a new higher value, the thermal resistance factor is given as

$$R = \frac{S(1 - \nu)}{E\alpha}, \tag{35}$$

where S can be the tensile strength (S_t) or the shear strength (S_s); also, ν is the Poisson's ratio, E the modulus of elasticity, and α the coefficient of linear thermal expansion. The case of both tensile and shear failure must be considered. The latter may be the more likely mode of failure in case of sudden heating at the surface. The temperature difference that leads to failure is the expressed as

$$\Delta T_f = A\ R, \tag{36}$$

where A is a factor that depends on the geometry of the body and type of failure mode, i.e., tensile or shear. For a sphere, the factor A takes on a value of 3/2 for failure at the center by tension due to uniform surface heating, or a value of 2 if failure is by shear [54]. This is in reasonable agreement with the values quoted by other investigators [56]. For instantaneous temperature increase at the surface, the maximum tensile stress at the center can be shown to be [57]

$$\sigma = 0.386\ R(T_s - T_a), \tag{37}$$

where T_s is the suddenly applied surface temperature. This maximum stress occurs at a time t given by

$$t = 0.0574\ \frac{b^2 C_p \rho}{k}, \tag{38}$$

where b is the radius of the sphere, C_p the heat capacity, ρ the density, and k the thermal conductivity. The maximum temperature difference to which a sphere can be subjected by convective heating over a wide range of Biot Numbers ($\beta = bh/k$) is approximately given as [56]

$$\Delta T_{max} \quad \frac{2.5S_t(1 - \nu)}{\alpha E}\ [1 + 2/\beta]\ . \tag{39}$$

Here h is the heat-transfer coefficient. When β is large, Eq. 39 reduces to Eq. 37.

If the surface heat-transfer coefficient h is constant and the heating is moderate, the resistance parameter becomes [54,56]

$$R' = \frac{kS_t(1 - \nu)}{E\alpha}, \tag{40}$$

where the nomenclature is the same as used above. The temperature at failure then is [54]

$$\Delta T_f = R'A' \frac{1}{hb}, \tag{41}$$

where b is a characteristic dimension of the body under consideration. For a sphere, a value of A' = 5.0 may be used [56]. Typical of the materials used for insulators in power lines and distribution stations is porcelain. Although some variability in the material constants of insulators is to be expected, the following representative values taken from the literature [54-56] are used in making response estimates.

Density	$\rho = 3996$ kg/m^3
Heat capacity	$C_p = 904.3$ J/kg · K
Heat conductivity (at 400°C]	$k = 1.76$ W/m · K
Linear thermal-expansion coefficient	$\alpha = 6 \times 10^{-6}$ K^{-1}
Modulus of elasticity	$E = 6.2 \times 10^4$ MPa
Poisson's ratio	$\nu = 0.3$
Tensile strength	$S_t = 55$ MPa
Shear strength	$S_s \cong 3S_t$
Thermal resistance (Constant surface temperature--tension)	R = 103 K
Thermal resistance (Constant heat-transfer coefficient--tension)	R' = 182 W/m

It is not possible to obtain accurate results of the thermal response of insulators without performing detailed stress analyses. This holds particularly when the heating is not uniform and when complex geometric shapes are considered. This kind of analysis is, however, beyond the scope of the current effort. Therefore, the above simple expressions will be used to make vulnerability evaluations. The results of such computations should provide order-of-magnitude estimates of the hazard.

10. Vulnerability of Nuclear Power Plants

To establish the vulnerability of nuclear power plants to the hazards arising from large LNG spills on water it is necessary to apply the LNG threats to the identified important plant systems and compare the response with the earlier defined susceptibilities. As mentioned before, it is difficult to perform such an analysis without considering actual spill scenarios including assumptions concerning the state of the plant. Concerning the latter, it is here, in general, assumed that plant personnel are cognizant of the existing hazard and that proper actions have been taken to mitigate as much as possible the consequences of the spill. Hence, among other things, it is assumed that by the time any effects arrive at the plant site, the reactor and all unnecessary equipment has been shut down and that all plant openings such as ventilation-duct dampers, doors, and hatches have been secured. Where, in specific cases, these assumptions are relaxed, it is so stated.

On examining the hazards associated with an LNG spill (see Chapter 7), one sees that some of them pose much greater threats than others. The analysis here will concentrate on the former. It is first noted that the threat posed by the LNG liquid (pool) is probably insignificant. Considering that maximum pool diameters are of the order of 400 m, it not likely that LNG liquid will reach the plant, and even if it does it appears that, at such close-in distances, the effect on the plant arising from other threats such as fire and explosion will be much more severe than those associated with the LNG pool. A similar conclusion can be reached concerning the effects of oxygen depletion where the maximum credible distance to the asphyxiation limit is estimated as 1300 m and durations of threat are very short (about 30 s). With a closed-up plant these effects are then truly minimal. Therefore these two threats, i.e., liquid LNG and oxygen depletion, are not considered in establishing plant vulnerability.

It has also been shown [32] that, even for very large fires, one is not likely to obtain, at ground level, concentrations of combustion products that are toxic. It is possible to envision fire propagating into the plant interior under some circumstances and thus creating a toxicity hazard. However, with the assumption of a closed-up plant this is not likely to be the case. Should fire or smoke nevertheless ingress the plant, then combustion-product toxicity could indeed represent a severe hazard. However, nuclear power plants are in general, at least in the control-room area, equipped with smoke detectors [38]. Thus plant personnel can take evasive actions, e.g., using emergency breathing apparatus, in order to mitigate the combustion-product toxicity threat. To make a reasonable

estimate of the toxicity threat, one must estimate infilitration and air-exchange rates into the plant areas occupied by personnel. Due to the uncertainties concerning the plant configuration and state, it is not possible to make any meaningful estimates of these quantities on a generic basis. Because of this and also because some protective action can be taken against the toxicity hazard, no further consideration is given to this threat. It should, however, be emphasized that this threat is not thought to be negligible and may have to be considered in specific cases.

In estimating the plant vulnerability to other threats, one can organize the results in two ways: (1) by type of threat and (2) by plant system. Although it is convenient to use the latter approach with respect to plant personnel, a presentation by type of threat is used for all other plant systems. Note also that all maximum vulnerability distances presented in the following are obtained using a realistic LNG composition (molecular weight 10% in excess of the value for pure methane), high relative humidity (approaching 100%), and a wind speed of 8.96 m/s (20 mph). Should the LNG vapor composition approach that of pure methane, the maximum vulnerability distances may have to be increased substantially, i.e., on the order of 7-8 km.

10.1 Personnel Vulnerability

Besides the above-discussed threats of oxygen depletion and toxicity, plant personnel are susceptible to thermal loads from fire and overpressure and impulse from explosion-generated airblast. Concerning thermal loads, a limit of 4 kW/m^2 is used here (see Chapter 9) as the threshold value for impairment of personnel functioning. From the results presented earlier (see Chapters 5 and 7), it is readily established that this rather low flux value may extend to a distance of up to 3.0 km from the edge of the fire. At the same time, a realistic estimate for the maximum cloud drift to reach the LFL is 9.8 km. Thus, exposed (in the open) plant personnel may be vulnerable to thermal loads from LNG fires on water up to distances of 13 km from the spill location. On the other hand, personnel located inside a substantial structure, such as the auxiliary building, are essentially completely protected from the threat of thermal loads. The only exception to this is the case of a power plant which has not been closed up before the LNG vapor cloud drifts on site and ignites. Then it is possible for a combustible mixture to enter the plant ventilation system and ultimately pose a threat to personnel. The maximum credible distance from the spill source for such a scenario is about 9 km. However, its occurrence is considered highly unlikely.

The threshold for personnel injury from airblast is 0.0345 MPa (5 psi), which occurs about 1.1 km from the edge of an exploding vapor cloud. This estimate is based on the assumption of a cloud height of approximately 50 m and is reduced for lower clouds and somewhat increased for greater cloud heights. Considering the possible cloud drift, it is estimated that exposed personnel remain vulnerable to airblast up to about 11 km from the spill source.

Again, personnel stationed inside a substantial building are essentially immune to air blast effects, unless the building itself is severely damaged by blast. Although pressure waves can propagate into the plant interior occupied by personnel via a breached ventilation system, it is difficult to estimate the exterior blast-wave overpressure that will lead to this scenario. Details of the ventilation system design, i.e., its geometry and blast resistance, must be known to arrive at a realistic estimate. However, it can be surmised that the occurrence of such an event is not likely. For ordinary ventilation systems, the intake or exhaust stacks may fail at an overpressure as low as 0.0207 MPa (3 psi). Similarly, the flow dampers, which close up the plant, are not expected to act as blast protection devices. Thus, they may be expected to fail at relatively low overpressures. Finally, the ducting itself is probably not designed to resist significant overpressure and will fail when a pressure wave propagates into it. This latter occurrence actually can provide protection, because upon duct failure most of the blast energy will spread out into the space surrounding the duct. Thus, unless the ventilation ducting is very short or can resist substantial overpressures, little blast energy will arrive at the location occupied by personnel. Secondly, even if substantial energies and overpressures propagate into the plant via a ventilation system, only personnel directly adjacent to the duct termination will be severely affected. In the remainder of the room the pressure buildup would be much more gradual and hence much less damaging. Thus it is believed that the free-field overpressures which would lead to injuries of protected personnel (inside the plant) would be of the same level as the pressures that would severely damage the structure itself. For reinforced concrete buildings, these pressures are about 0.2 MPa (30 psi), which occurs only near the edge of an exploding vapor cloud (200 m from the cloud edge for a 50 m cloud height). Thus such events can only occur when the cloud has nearly drifted to the plant site, which for the worst case is about 10 km.

10.2 Ignition Vulnerability

In Chapter 7 (Table 8) it is shown that a duration of a typical thermal exposure for targets outside the vapor cloud is 600 s. For targets inside

the burning vapor cloud, the durations are shorter, about 300 s, but the flux intensities are so extreme (in excess of 200 kW/m^2) that all combustibles engulfed by such a fire are expected to ignite.

For off-site fire the empirical formulas presented in the preceding chapter are used to establish if ignition of combustibles occurs. It is assumed that fire durations are about 600 s and that the peak heat flux (whatever its value) persists for half of this time, i.e., 300 s. Examining typical fire scenarios (see Chapter 5) and the variations of heat flux with distance from the fire, these are believed to be conservative assumptions. Ignition is postulated when the peak radiation flux at the target exceeds the threshold value of the ignition flux for a given material and the time to ignition is less than 300 s. For polymer ignition, the surface temperature is computed from Eq. 34 using the peak radiation flux and an effective duration of 300 s. The obtained value is compared with the ignition temperature specified in the literature. At the same time, Eq. 33 is used to check if the time to ignition for a given flux is less than the assumed 300 s duration. For easily combustible materials, the times for ignition to occur are very short, and hence the radiation heat flux is the governing criterion. Thus for cotton and α-cellulose, ignition may be expected at 12 and 16 kW/m^2, respectively, regardless of the fire duration. Peak radiation-heat-flux values of this magnitude may occur for the case of no wind at distances up to 2 km from the spill center, or about 1 km from the cloud edge. When the vapor cloud is allowed to drift, due to wind, the distance from the cloud edge is more difficult to establish, but can again be taken as about 1 km. Considering that the cloud drift may be as much as 9.8 km under strong wind conditions (8.96 m/s), the ignition hazard extends up to 11 km from the spill source. The same holds for the pilot ignition of wood, where it is estimated that 15 kW/m^2 of heat flux is required for ignition to occur in less than 300 s. Spontaneous ignition of wood requires a heat flux of about 27 kW/m^2. A conservative distance for this flux level from the cloud edge is again about 1 km, and the total distance from the spill, allowing for maximum cloud drift, is 11 km.

The ignition temperatures for polymers that are representative of electrical insulation materials are 220°C for polyvinalchloride (PVC) and 720°C for silicon rubber [32]. With the specified conditions, i.e., 300 s peak flux duration, it takes 17 kW/m^2 to ignite PVC and approximately 35 kW/m^2 to ignite silicon rubber. Although these heat fluxes are for pilot ignition, they are accepted here as being threshold values for all ignition. Since these values are higher than for some of the other combustibles, this assumption is not unreasonable; i.e., ignition sources will probably be present. Again, conservative distances from the burning vapor cloud to the

target are about 1 km for ignition of the PVC and somewhat less for silicon rubber. Hence, the longest distance from the spill source for ignition of either insulating material is again taken as 11 km.

The ignition of combustibles such as wood and fibers does not in itself constitute a hazard to any of the important power plant systems. The threat from such fires is indirect, in that the fire may spread and eventually endanger a plant system. However, since most important systems are housed in substantial buildings, the likelihood of such an occurrence is small. A direct hazard may arise from the ignition of polymer insulation of electric cables, which are exposed to thermal loads. Should the ignition lead to cable failure, important components in an exposed switchyard or substation may eventually fail also. Most important among the systems that could be affected is off-site power. Although its failure alone does not constitute a direct safety hazard, it is the first major link in a chain of events that can lead to such a hazard. Therefore such a failure constitutes a significant increase in the vulnerability of the plant to other effects.

10.3 Thermal-Load Vulnerability

In the preceding section it is shown that the expected durations of LNG fires resulting from spills on water are about 600 s. For these relatively short time spans, it is not expected that steady-state heat-transfer conditions will be established in any of the important plant components and structures that are exposed to the fire thermal load. Thus, to estimate their response to the thermal loading, one must rely on transient analysis.

Most of the vital plant systems required for shutdown and heat removal are housed in rather substantial buildings and are therefore shielded from direct thermal loads. It then becomes important to ascertain if the structures housing this equipment may be sufficiently affected by the thermal loading to preclude its proper operation.

10.3.1 Response of Ceramic Electrical Insulators

A notable exception to this is ceramic electric insulators, which may be used in transmission lines and substations on the plant site. These are directly exposed to the thermal loads, and their failure may lead to a loss of off-site power. As indicated before, the thermal-stress analysis of such complex geomteric bodies represents a difficult problem. Here the simple expressions given in the preceding chapter will be used to obtain first-order estimates of their response. Since ceramic insulators are poor heat conductors, it may be expected that under severe thermal loading their outer

surface will heat up rapidly, while the interior will remain unaffected. This in turn will result in thermal stresses, which could lead to failure by tension toward the center of the body [57]. In the limit it is conservative to assume that the surface temperature changes instantaneously. Using Eq. 36 or 37 together with the material parameters for porcelain (given in the preceding chapter), it is estimated that failure may be expected for temperature differences on the order of 200-300°C. The time required for the surface temperature to increase depends on the thermal load. For a flux intensity of 200 kW/m^2, the time will vary from 4 to 10 s (see Eq. 34)); for an intensity of 100 kW/m^2, 17-38 s is required. It is also estimated, using Eq. 38, that for a body with a characteristic dimension of 50 mm, e.g., radius of a cylinder or sphere, about 250 s is required to reach the maximum or failure stress. This duration is an order of magnitude or more longer than the time required to reach the appropriate surface temperature. Thus the assumption of an instantaneous temperature rise is reasonable. Failure should be expected at these flux levels if they persist for longer than the indicated 250 s. This indeed is the case under the assumptions made earlier. Flux levels of this magnitude, i.e., larger than 100 kW/m^2, occur only directly adjacent to the fire or in the region engulfed by fire. Allowing for maximum vapor-cloud drift, this could occur at distances of up to 10 km from the spill source.

At lower heat-flux values, the assumption of an instantaneous surface-temperature rise is not valid. It is then more difficult to estimate the effect of thermal stress on ceramic insulators, in particular, since the heating is due to thermal radiation. To overcome this difficulty, it is assumed that the radiation flux can be replaced by an equivalent convective heat transfer with a constant heat-transfer coefficient h [53]. The latter is simply estimated by dividing the incident radiant flux by the initial temperature difference between the radiation source (flame) and the target, i.e., the ambient temperature. Assuming the flame temperature at 1100°C (diffusion flame), the ambient temperature at 20°C, and a characteristic dimension (radius) of 50 mm, the maximum allowable temperature difference (surface to center) can be computed for various heat fluxes $\dot{q}$ using Eq. 39. The results are as follows:

$\dot{q}$, kW/m^2	h, $W/m^2 \cdot K$	δT_{max}, °C
50	46.3	649
30	27.8	909
20	18.5	1237
10	9.3	2207

The last two temperature-difference values are obviously impossible. It is also not very plausible that temperature differences as large as those presented above for the first two cases can be attained with the fire durations (600 s) considered here. This is corroborated by graphical results for a flat-plate configuration given in Ref. 54. Thus it can be concluded that failures for ceramic electrical insulators should be expected only when the fire is directly adjacent to, or on, the actual plant site. As indicated above, considering vapor-cloud drift, this results in a maximum distance of 10 km from the spill location.

10.3.2 Effects on Steel Structures and Components

Many of the secondary structures at a typical nuclear power plant site may be of steel-frame construction. Similarly, at some plant designs, steel pipe bridges carrying feedwater or steam lines may be encountered. Although failures of these structures may not represent a safety hazard in themselves, they do contribute to the general plant vulnerability.

Because of the variety and complexity of geometric shapes of structural steel components, it is difficult to arrive at a simple and universal means of estimating their response to thermal loads. Another complication arises from the fact that structural steel has a relatively high thermal conductivity. This precludes the usage of some of the simplifying assumptions used in the previous section; e.g., it is not reasonable to assume, even for high heat fluxes, that the surface temperature changes instantaneously to the value of the surroundings. The only means of making accurate predictions of the thermal response of steel structures are detailed numerical computations. Due to the geometrical and other complexities of steel components, such an approach is considered beyond the scope of the current effort. Numerical data in the literature [53,58] can be used to obtain a first-order estimate of the temperature rise of steel members subjected to thermal loads. Specifically, results for radiation from a medium at a temperature of T_f to a simple slab geometry originally at a temperature T_a can be used. This procedure again replaces the more complex radiation problem, where the heat-transfer coefficient is estimated by dividing the incoming radiant heat flux by the initial temperature difference between the radiation source (flame) and the structure. In calculating the temperature rise in the steel, the following average material properties are used [59]:

Density	$\rho = 7724$ kg/m^3
Heat capacity	$C_p = 618$ J/kg·K

Thermal conductivity $k = 41.5$ W/m•K

Thermal diffusivity $\alpha = 8.694 \times 10^{-6}$ m^2/s

Typical results obtained using the numerical and graphical data from the literature [58] are shown in Fig. 48. The temperature rise in steel plates of various thicknesses is given as a function of heat flux, assuming a constant flux and a duration of 600 s. The temperature values are for the center of a plate of given thickness heated on both faces. They also apply for a plate of half the thickness heated on one face and insulated, or having minimal heat loss, at the other face.

In these results it was noted that, due to the high thermal conductivity, the temperature varied little (less than 10%) across the thickness of the steel plate, in particular at high-heat-flux values. An approximate solution based upon the assumption of a spatially uniform (across the plate thickness) temperature therefore suggests itself. For the equivalent convective problem, the equation governing the response of the steel slab is then simply

$$s\rho C_p \frac{dT}{dt} = \dot{q}_f + \dot{q}_a \,, \tag{42}$$

where $\dot{q}_f$ and $\dot{q}_a$ represent, respectively, the heating of the plate and any heat losses that may occur. They can be expressed as

$$\begin{aligned} \dot{q}_f &= h_f(T_f - T) \\ \dot{q}_a &= h_a(T_a - T). \end{aligned} \tag{43}$$

In Eqs. 42 and 43, T represents the temperature, t is time, s is the plate thickness, ρ is the steel density, and C_p is the specific heat. Subscripts f and a refer to the heat source (flame) and the ambient (or initial) conditions, respectively. The heat-transfer coefficients h_f and h_a are assumed to be constant. The former is obtained by the procedure outlined earlier; the latter is assumed to have a value typical for the cooling of a steel plate in the atmosphere [58], i.e., $h_a = 11.35$ W/m^2•K = 2 Btu/h•ft^2• °F. Under these assumptions Eq. 42 can be integrated analytically:

$$T = \frac{1}{b}\left[a - (a - b\,T_a)e^{-bt/s\rho C_p}\right], \tag{44}$$

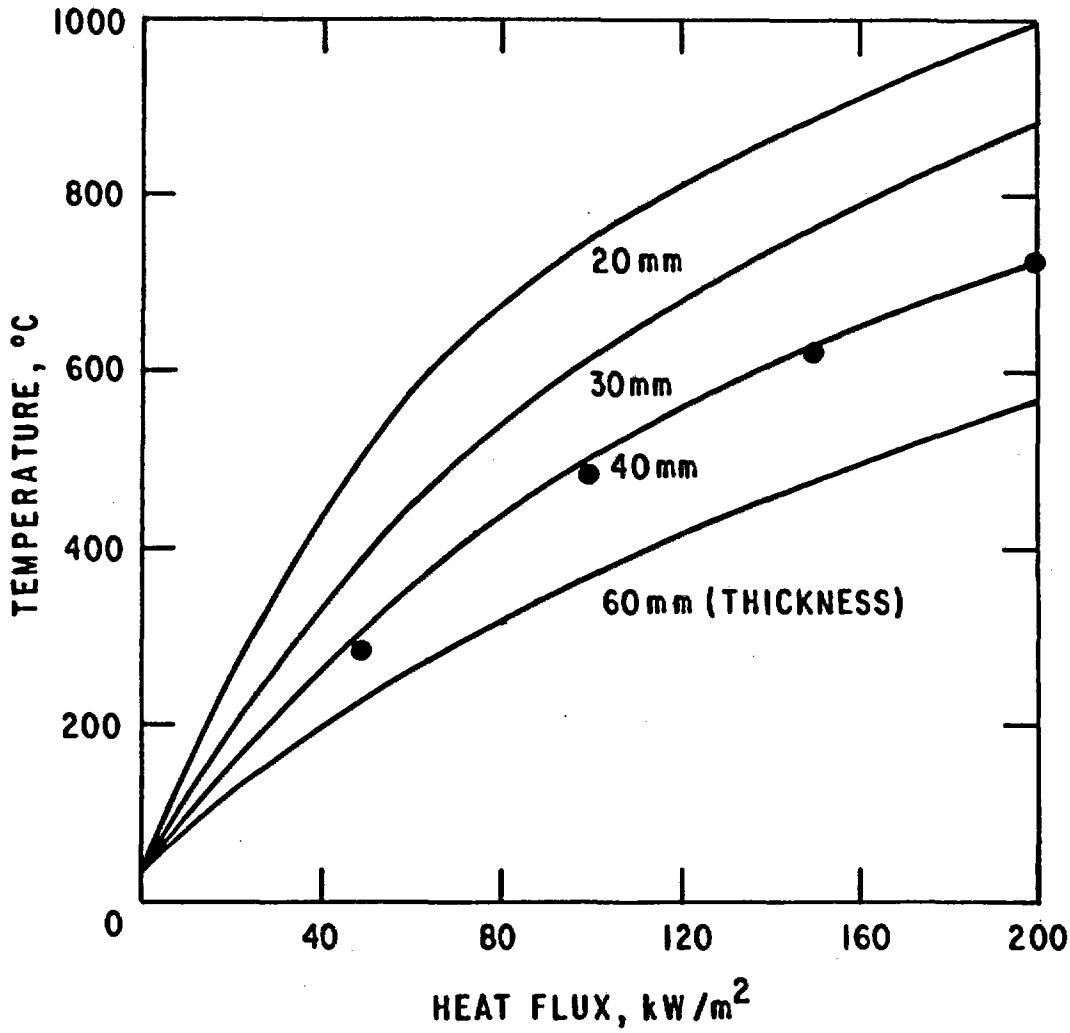

Figure 48. Temperature Rise in Steel Plate vs. Heat Flux; Flux Duration 600 s.

where

$$a = h_f T_f + h_a T_a$$

and

$$b = h_f + h_a .$$

The results from Eq. 44, for a slab of 40 mm thickness (or 20 mm thickness when heated on one side), are shown as the solid dots in Fig. 48. The agreement with the exact solution is quite good, particularly for high heat-flux values. Encouraged by this result, and also because there is considerable doubt as to the equivalency of convective heat transfer as a substitute for radiation, the actual problem is treated again by assuming a uniform spatial temperature across the steel slab. When a structure is not engulfed by fire, the radient flux is incident only on one face of the slab; however, heat losses by reradiation and convection occur on both faces. The equation governing the thermal response of such a steel plate can then be written as

$$s\rho C_p \frac{dT}{dt} = \dot{q}_r - 2[\sigma(T^4 - T_a^4) + h_a(T - T_a)] . \qquad (45)$$

The notation is the same as used earlier, $\dot{q}_r$ is the specified incoming radiant flux. The factor 2 accounts for losses on both faces of the slab. An analytical solution to Eq. 45 is not readily evident. Therefore a numerical solution is obtained with the assumption of constant heat flux $\dot{q}_r$ and heat-transfer coefficient h_a. Using the simplest possible integration scheme, we can express Eq. 45 in finite-difference form as

$$T_{n+1} = T_n + [\dot{q}_r/2 + \sigma T_a^4 + h_a T_a - (\sigma T_n^4 + h_a T_n)] \frac{2\Delta t}{s\rho C_p} . \qquad (46)$$

Here Δt is the time step and the subscripts n and n + 1 refer to the preceding and current time step, respectively. Figure 49 shows the temperature rise as a function of time for two values of heat flux and two plate thicknesses, and Fig. 50 presents the temperature increase as a function of heat flux for flux durations of 600 and 300 s. Comparing the results of Fig. 50 with those of Fig. 48 for the equivalent convective problem, i.e., the 40 mm curve (20 mm if heated on one face), we see that for heat fluxes of up to 100 kW/m^2, the agreement is good. However, at higher heat fluxes the actual radiation solution results in higher temperatures than the equivalent convective solution. The numerical radiation solution is therefore used to estimate the thermal response of steel structures. In Figs. 49 and 50, the maximum allowable temperature for

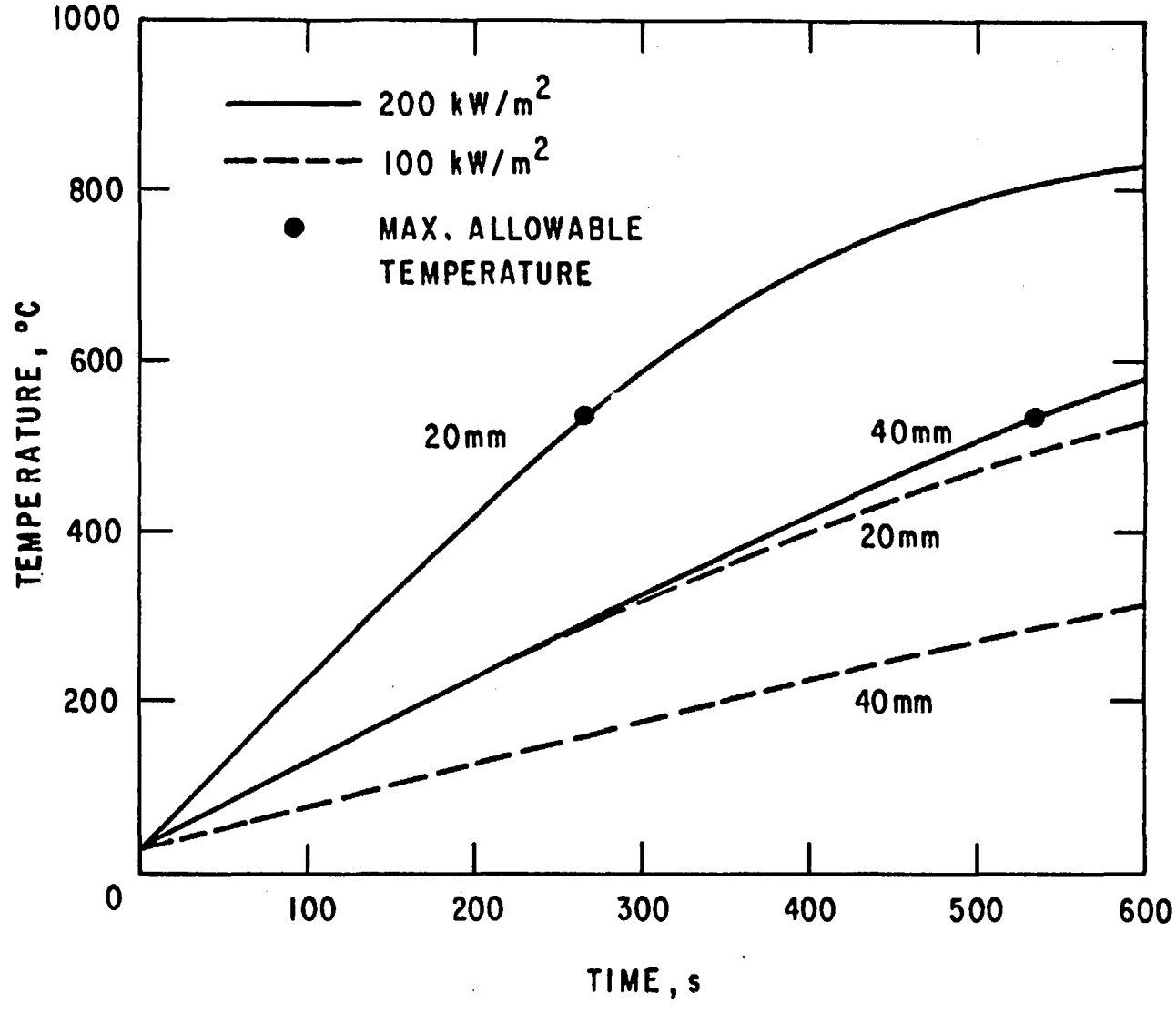

Figure 49. Temperature Rise in Steel Plate not Engulfed by Fire; Constant Radiant Heat Flux.

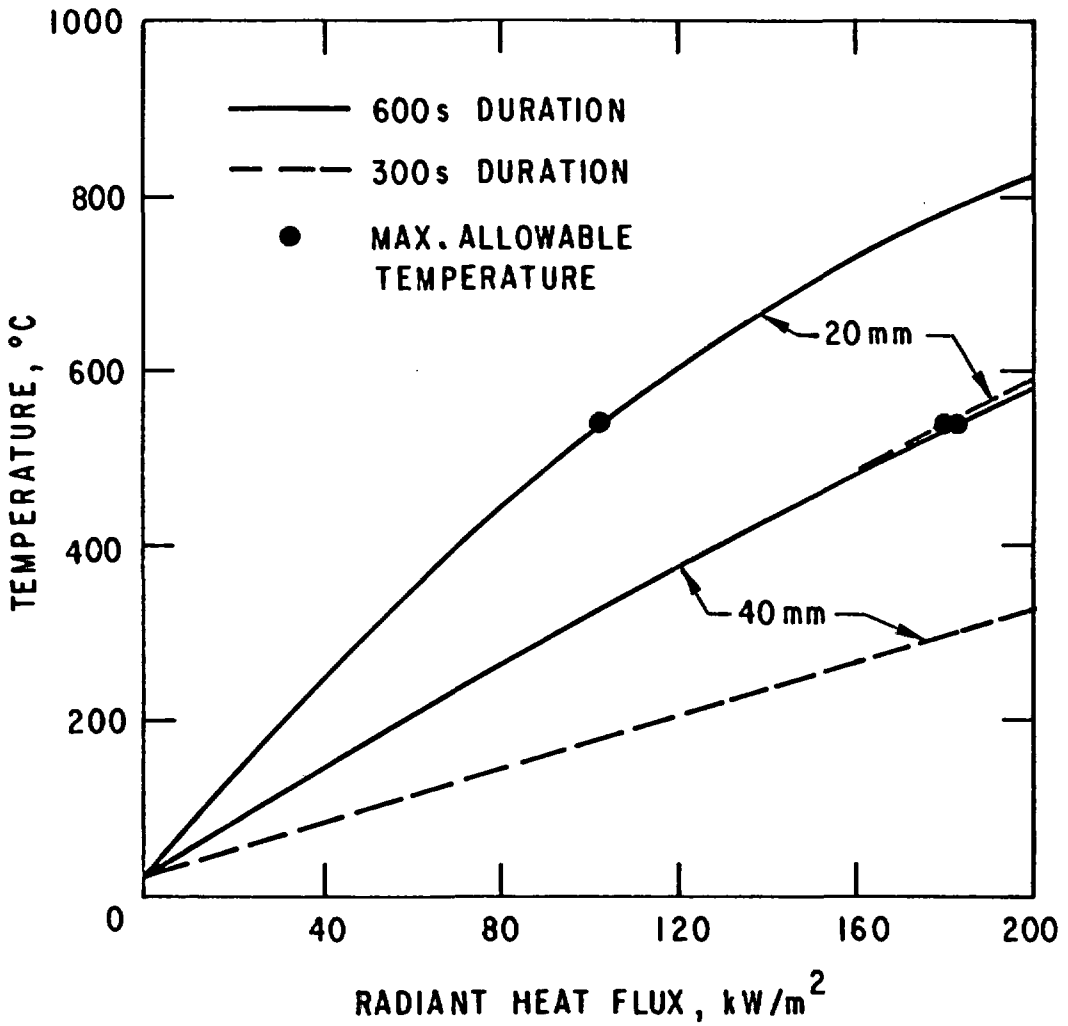

Figure 50. Temperature in Steel Plate not Engulfed by Fire as Function of Heat Flux.

structural steel, i.e., 538°C (see Chapter 9), is indicated where appropriate. For heating durations of 300 s or less, it appears (see Fig. 50) that heat fluxes up to 180 kW/m^2 can be tolerated even for very thin steel sections (20 mm). Thicker steel sections (40 mm) can withstand heating at similar levels for 600 s. For these longer durations, a 20 mm plate can tolerate up to 100 kW/m^2. Reviewing the results on fire threats (Chapter 7), we find that these high-level fluxes occur only in the direct vicinity of the fire. Hence, taking vapor cloud drift into account, they may occur at distances of up to 10 km from the spill source. Since for most real scenarios the heating duration at peak levels is much shorter than the times indicated here (see Chapter 5), typical steel structures should be relatively immune to the thermal loads from an LNG fire on water unless they become actually engulfed by the fire.

To examine the response of steel components engulfed by fire, we again assume that the spatial variation in temperature, across the steel section, can be ignored. Heat input to the steel is now both by radiation and convection. For the latter it is necessary to define a heat-transfer coefficient h_f. There is considerable variation in the literature as to the appropriate value of h_f. A conservative value of $h_f = 170\ W^2 \cdot K \cong 30\ Btu/h \cdot ft^2 \cdot °F$ is used for the current appliction [46]. The equation governing the heat transfer to a steel slab engulfed by fire can be written as

$$s\rho C_p \frac{dT}{dt} = \sigma(T_f^4 - T^4) + h_f(T_f - T) , \qquad (47)$$

where T_f is again the temperature of the flame. All shielding by the combustion gases, which could diminish the radiant flux, is neglected in this expression. As written, Eq. 47 represents heating on one face of the slab with the other face insulated or experiencing minimal heat loss. For reasons of symmetry, the results obtained from the integration of this equation are equally applicable to a slab of twice the thickness, totally engulfed by fire, and heated on both faces. The simplest finite difference form is

$$T_{n+1} = T_n + \left[\sigma T_f^4 + h_f T_F - (\sigma T_n^4 + h_f T_n)\right] \frac{\Delta t}{s\rho C_p} . \qquad (48)$$

Figure 51 shows numerical results obtained for the temperature rise, as a function of time, in various slab thicknesses. As given, the thicknesses are for steel plates completely engulfed by fire, i.e., heated on both faces. The results of each curve are equally applicable to slabs of one-half the indicated thickness which are heated only on one side. The assumed

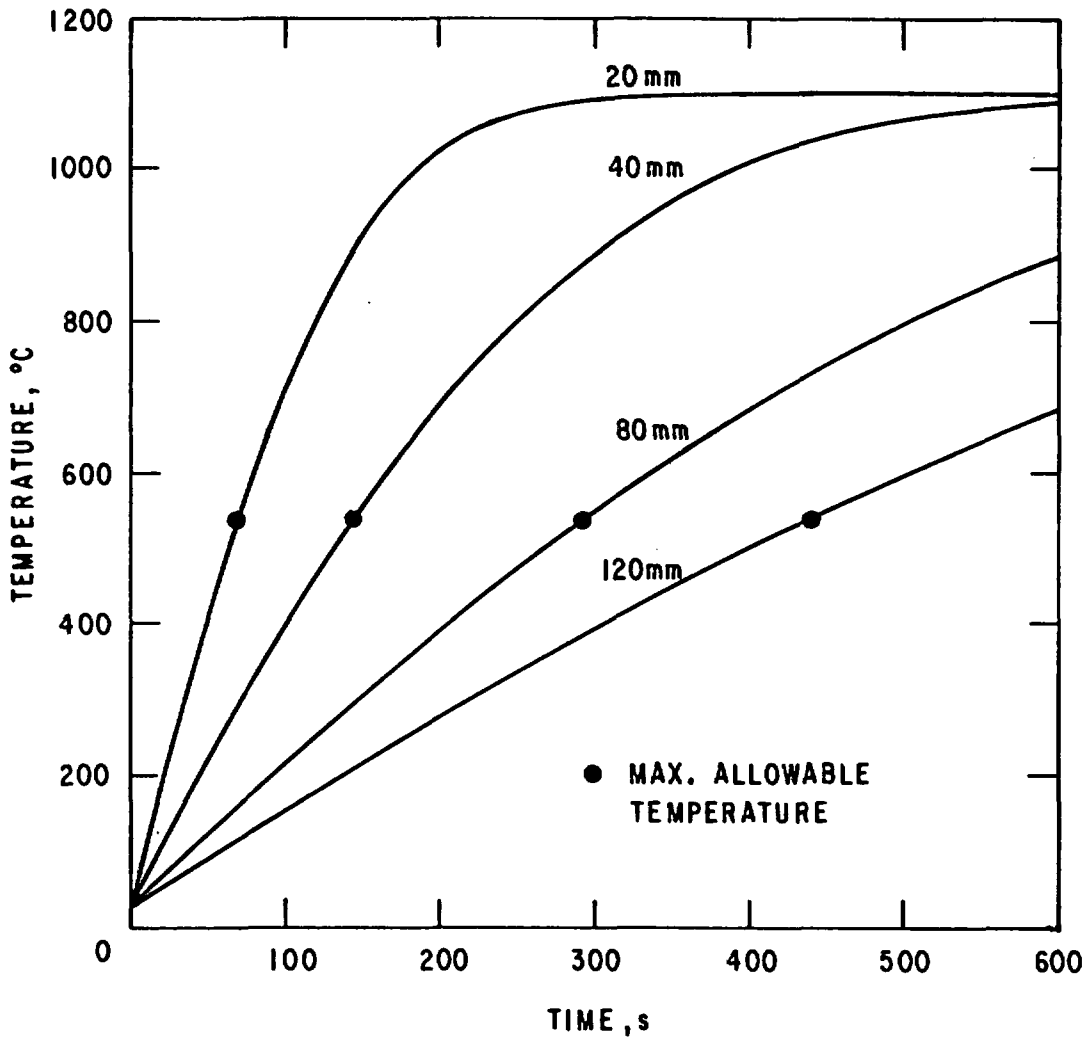

Figure 51. Temperature Rise in Steel Plate Engulfed by Fire.

fire temperature of 1373 K is that of a turbulent diffusion flame. Again the maximum allowable temperature for structural steel is shown in the figure. It is clearly evident that thin steel sections can tolerate the fire environment only for short durations. Since the maximum duration of a vapor-cloud fire at a fixed location is about 300 s (see Chapter 7), it appears that a steel section of 40 mm, if heated on one side, or 80 mm if totally engulfed by the fire, is required in order to avoid serious weakening of the structure. Most nuclear power plant structures are expected to be contiguous without any free-standing structural components. Thus the 40 mm slab section and heating from one side appear to be indicated as the safe limit. Since the structure must be engulfed for some time to experience a substantial temperature rise, it is estimated that taking cloud drift into account, the furthest distance from the spill location at which such a scenario is possible is about 9 km.

It is realized that considerable variability prevails in the size and geometry of structural components, none of them being truly flat plates. However, the results given here permit a first-order estimate of the response and vulnerability of steel structures at nuclear power plants subjected to thermal load from LNG fires. Using the reasonable assumption of uniform temperature across a steel section, we can readily carry out more accurate calculations for actual structural steel shapes. The procedure is also easily adapted to the case of time-varying heat flux, where the latter may be obtained from an actual spill, ignition, and fire scenario. The most important result of the current analysis is that steel structures at nuclear power plants are probably immune to thermal loads from LNG fires, unless the plant is actually engulfed by the fire. In the event the later is true, a closer examination is necessary, in particular for cases in which important structural components have sections with thermal inertias less than that of 40 mm thick flat slab.

10.3.3 Thermal Response of Concrete Walls

Most important safety-related equipment in modern nuclear power plants is housed inside substantial reinforced concrete buildings. The response to the expected thermal loads of concrete structures is thus of utmost importance in analyzing the vulnerability of such plants. Typical material constants of concrete that are important for the thermal response are [33]:

Density	$\rho = 2082$ kg/m^3
Specific heat	$C_p = 837.4$ J/kg·K

Thermal conductivity $k = 2.77$ W/m•K

The most significant of these parameters is the rather low value of the thermal conductivity. It suggests that, unless heating persists for very long times (hours), severe thermal response of a concrete structure will be limited to a rather shallow layer adjacent to the heated surface. The wall thicknesses in nuclear power plant structures vary substantially from building to building, but are not expected to be less then 0.3 m. Preliminary estimates for such a wall, based on data for the literature [53], indeed indicated that for thermal-load durations typical of LNG fires, say less than one-half hour, significant heating is limited to the vicinity of the exposed surface.

The above findings suggest certain conservative simplifications in calculating the response of concrete walls. For a structure engulfed by the fire, it is therefore assumed that the exposed surface temperature changes instantaneously to the flame temperature. Calculations of the thermal response are then readily carried out, for any wall configuration, using existing heat-transfer computer codes [60]. For the estimates used here to assess the vulnerability of concrete structures, the response of a simple slab is computed.

When the structure is not engulfed by the fire, heating is due to radiation, and the incident heat flux can be obtained from the integrated LNG spreading and fire model. Reradiation to the surroundings, which are at ambient temperature must, however, be taken into account, in order to avoid a gross overestimate of the heating effect. An existing procedure [61] for the computation of the thermal response in a semi-infinite slab is adapted for the prediction of the temperature rise in a concrete wall subjected to a radiant heat flux. Figure 52 shows typical results of the temperature, as a function of time, at the heated surface and at various depths for a constant heat flux of 50 kW/m^2 and in Fig. 53 for a heat flux of 201.4 kW/m^2. The latter flux value corresponds to radiation from a diffusion flame (1373 K) without any loss or attenuation. Already, at a depth of 100 mm, the temperature rise even for the higher flux is quite moderate. The calculations also show, that at a depth of 300 mm the temperature remains essentially unchanged after 1800 s of heating. While some temperature rise at these greater depths may be expected at later times after the radiant flux has ceased, the increases are minimal. This is born out by the results given in Fig. 54, which represent the response to a variable heat flux of finite duration with the extreme peak value of 100 kW/m^2.

Figure 55 shows the temperature rise, as a function of incident radiant heat

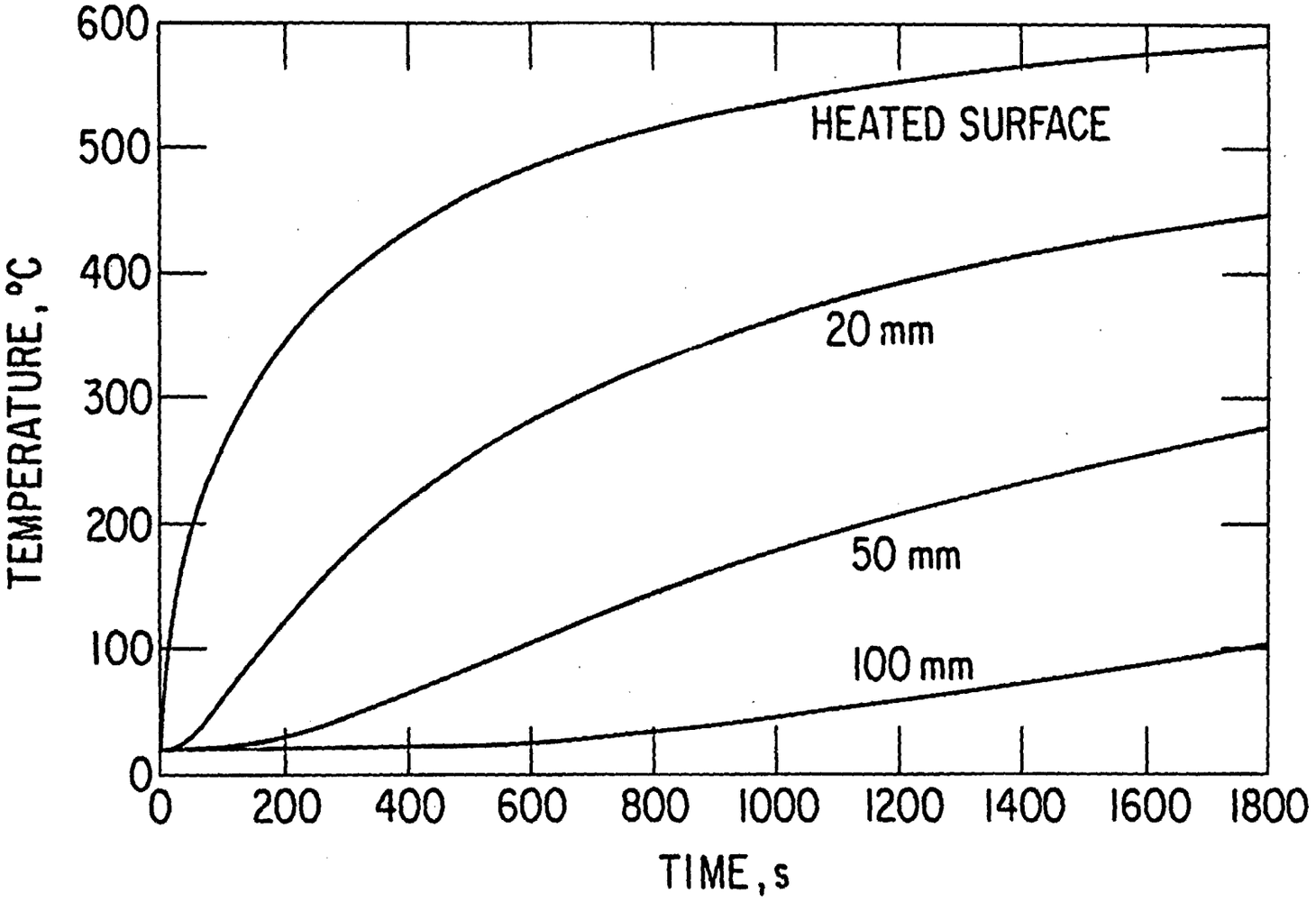

Figure 52. Temperature Histories in Concrete Slab at Various Depths; Radiant Flux = 50 kW/m^2.

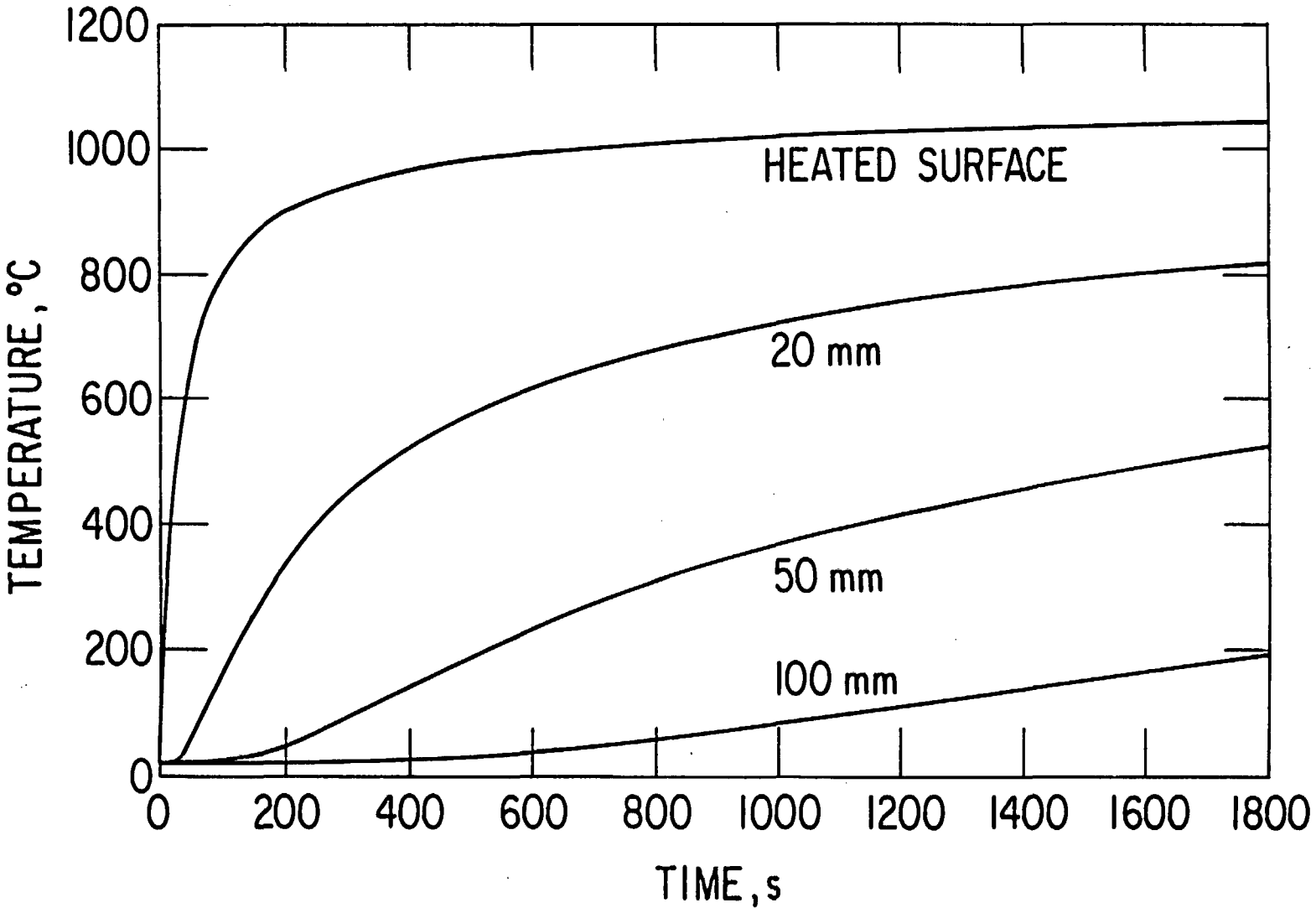

Figure 53. Temperature Histories in Concrete Slab at Various Depths; Radiant Flux = 201.4 kW/m^2 (T_R = 1373 K).

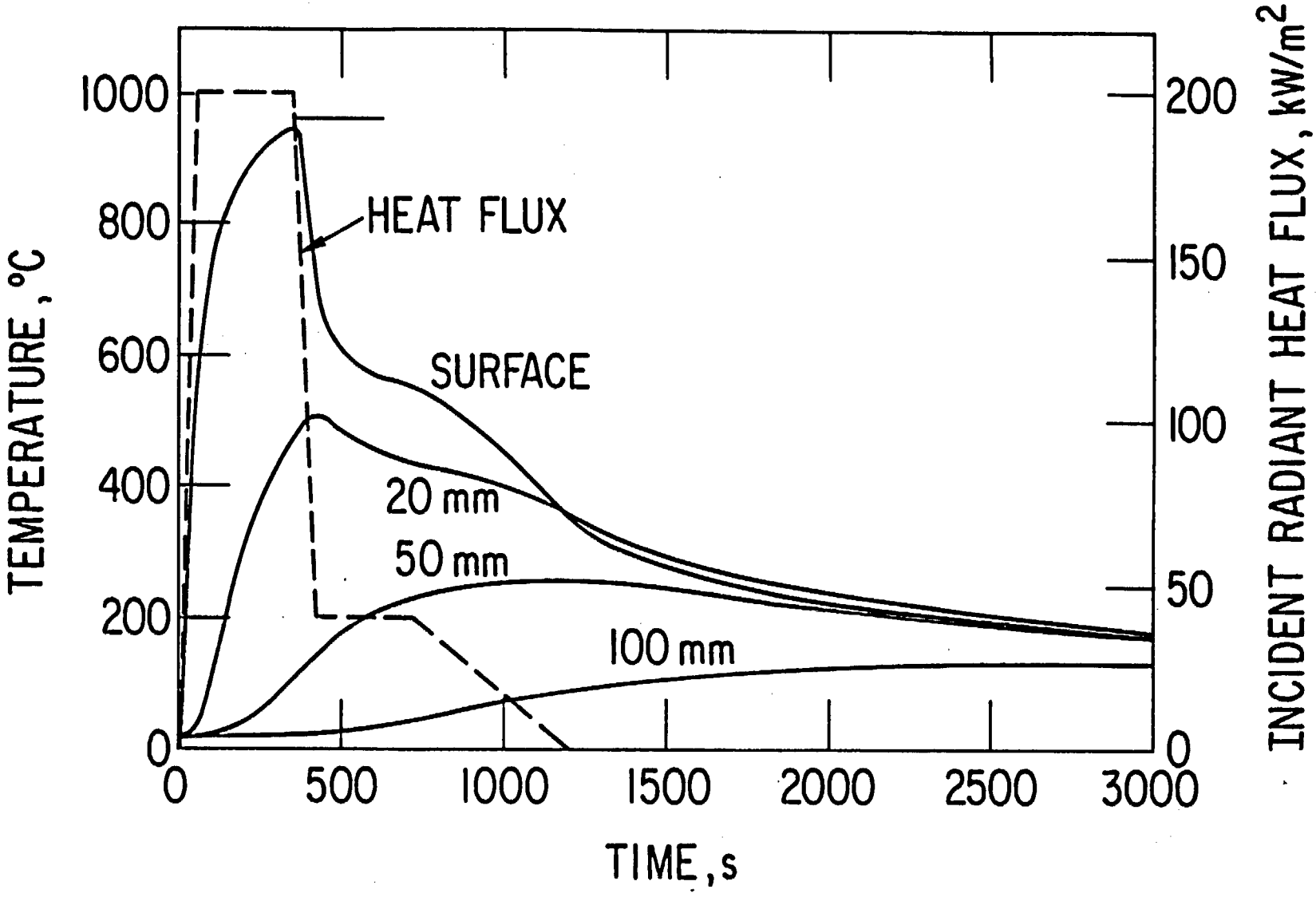

Figure 54. Temperature Histories in Concrete Slab at Various Depths.

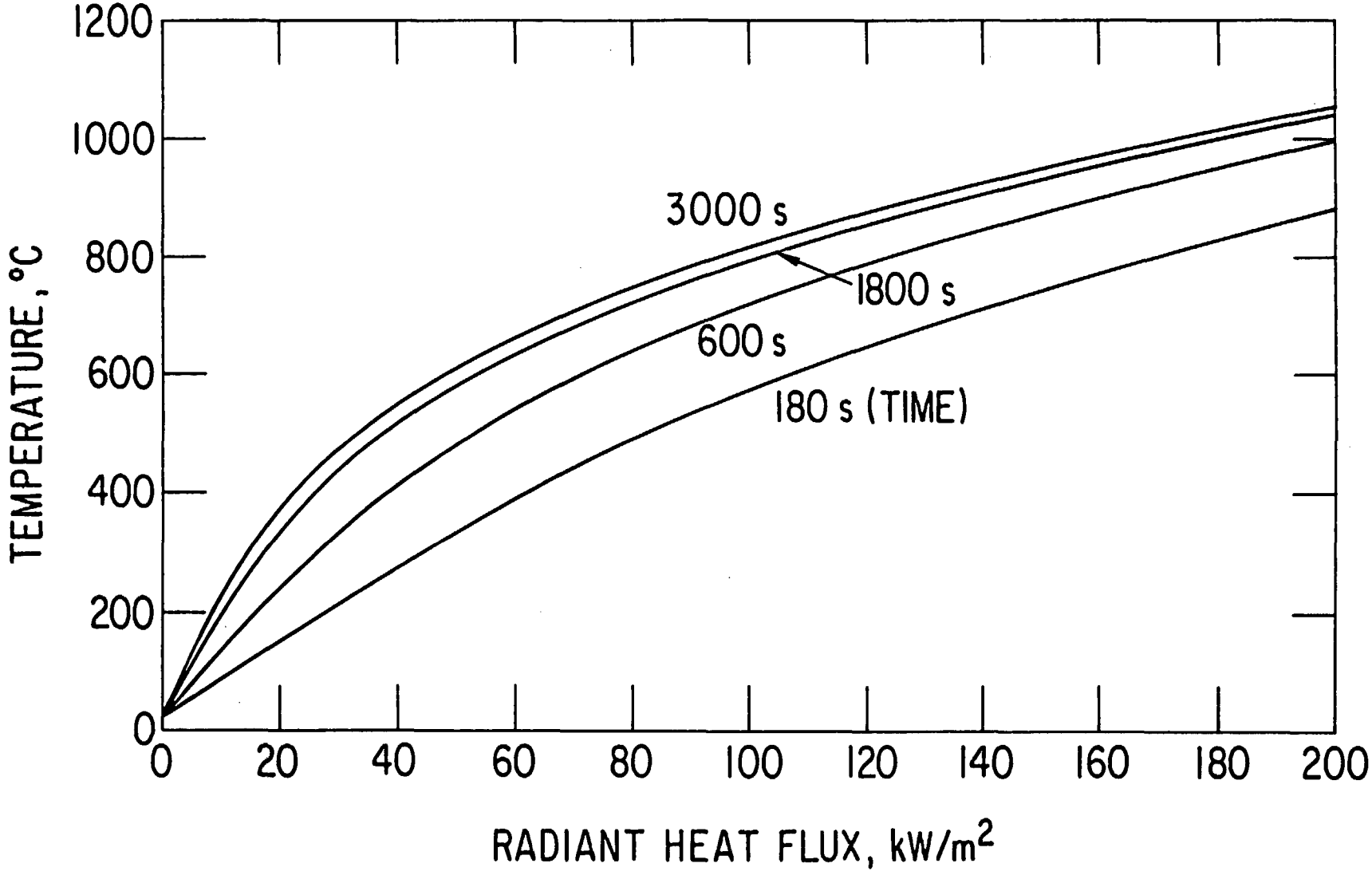

Figure 55. Surface Temperature of Concrete Slab as Function of Incident Radiant Heat Flux.

flux, at the surface of the slab and for various durations. Similar results for a depth of 50 and 100 mm from the heated surface are given in Figs. 56 and 57, respectively. Since expected fire durations are of the order of 600 s and peak fluxes persist for considerably shorter times, the heating of the layer of concrete adjacent to the exposed face appears to be very moderate. The maximum allowable temperature increase for reinforcing steel is 500°C. This temperature is only exceeded at a very shallow depth of 20 mm for an extreme heat flux (200 kW/m^2) and an exposure duration in excess of 360 s. In most massive concrete structures, the first layer of reinforcing is expected to lie at a depth of about 50 mm, for which an exposure duration of 1660 s is needed to exceed the critical temperature. Thus the heating appears to have little detrimental effect on the reinforcing and thus structural integrity. Similarly, prestressing steel, which can tolerate a temperature rise up to 400°C (see Chapter 9), should be unaffected, since it is normally located at depths greater than 100 mm.

Some surface spalling may be expected, however, since the water-vaporization temperature (100°C) is exceeded for larger heat fluxes at the critical depth of 50 mm. The effect of such spalling is difficult to estimate. However, direct exposure to the radiant heating of the reinforcing could lead to substantial weakening of the structure. A mitigating circumstance is the fact that, even for the severest flux (200 kW/m^2), a duration in excess of 300 s is required to raise the temperature to 100°C at the 50 mm depth. At a lesser heat flux (50 kW/m^2), this time is in excess of 600 s. Thus, considering the actual durations of the fires, it is not expected that, for the off-site fire, the combination of concrete spalling and reinforcement exposure to heat flux will lead to any significant degradation of the concrete structures.

The thermal response of concrete structures engulfed by the fire is based on the assumption of a sudden surface temperature jump to the value of the flame temperature. Two cases are considered: a diffusion flame fire at 1373 K and the fire of a premixed LNG vapor cloud at 2148 K. Both are illustrated by the example of a 0.3 m thick wall. Results for the former are shown in Figs. 58 and 59. The first of these presents numerical results [60] for the temperature rise with time at various depths from the heated surface, and Fig. 59 is the temperature profile through the wall after a fire duration of 1800 s. First, note that, even after this long time, the temperature at the far face is still unaffected by the thermal exposure. It takes in excess of 1350 s to reach the critical temperature (500°C = 773 K) for reinforcement steel at a depth of 50 mm, and the critical temperature (400 °C = 673 K) for prestressing steel is never reached at the 100 mm depth within the first half-hour of fire exposure. At a shallow depth of 20 mm

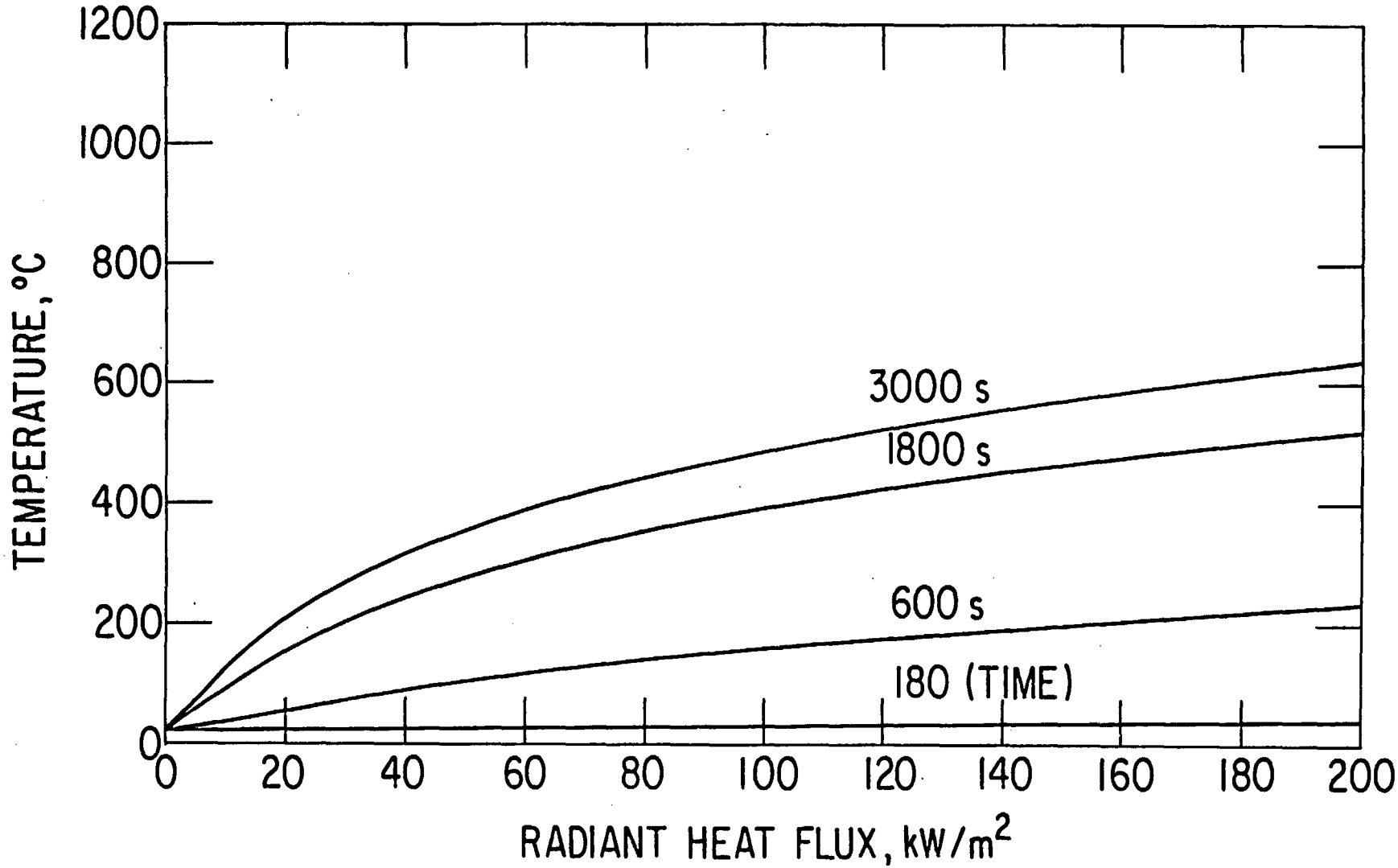

Figure 56. Temperature in Concrete Slab as Function of Incident Radiant Heat Flux; Depth - 50 mm from Heated Surface.

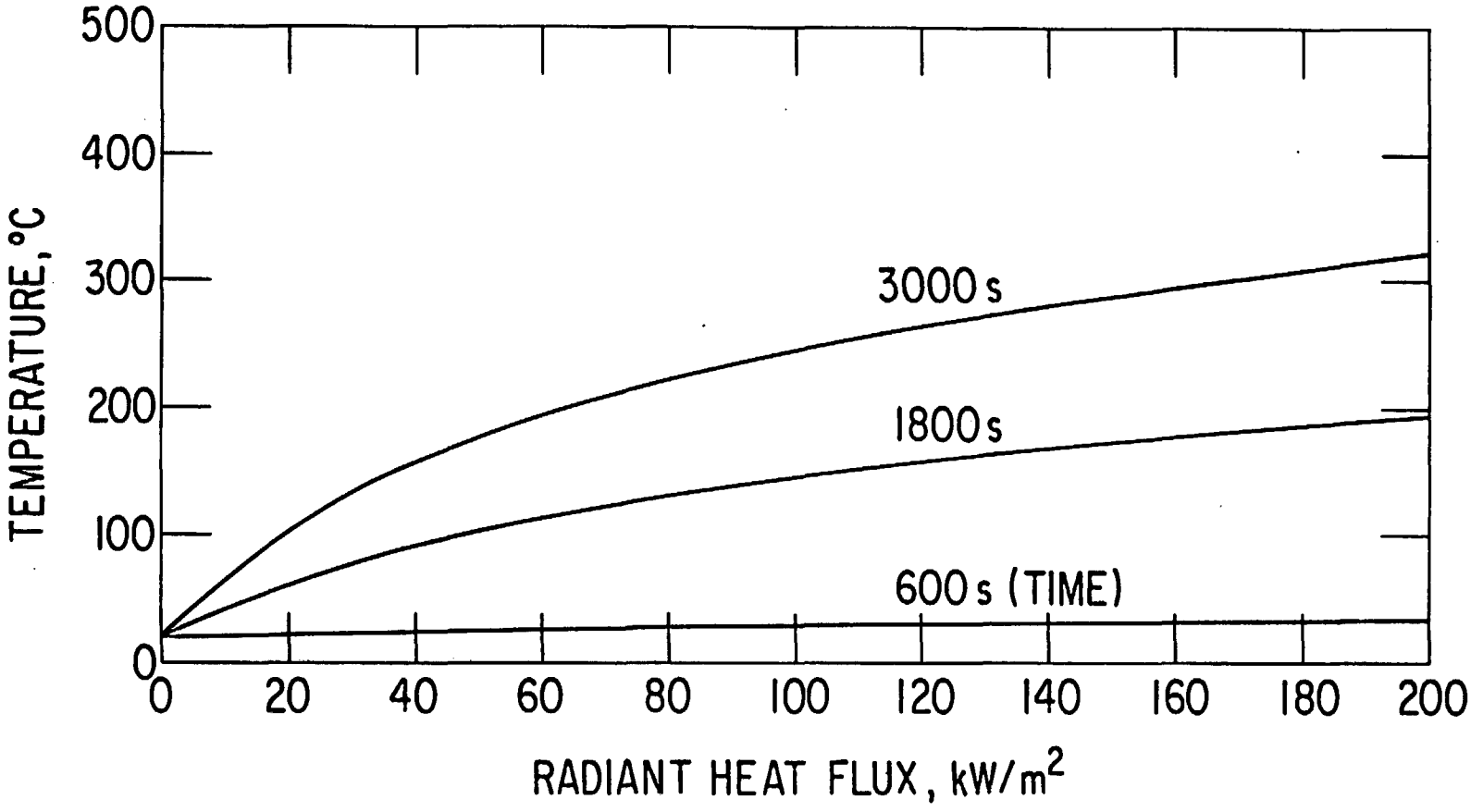

Figure 57. Temperature in Concrete Slab as Function of Incident Radiant Heat Flux; Depth - 100 mm from Heated Surface.

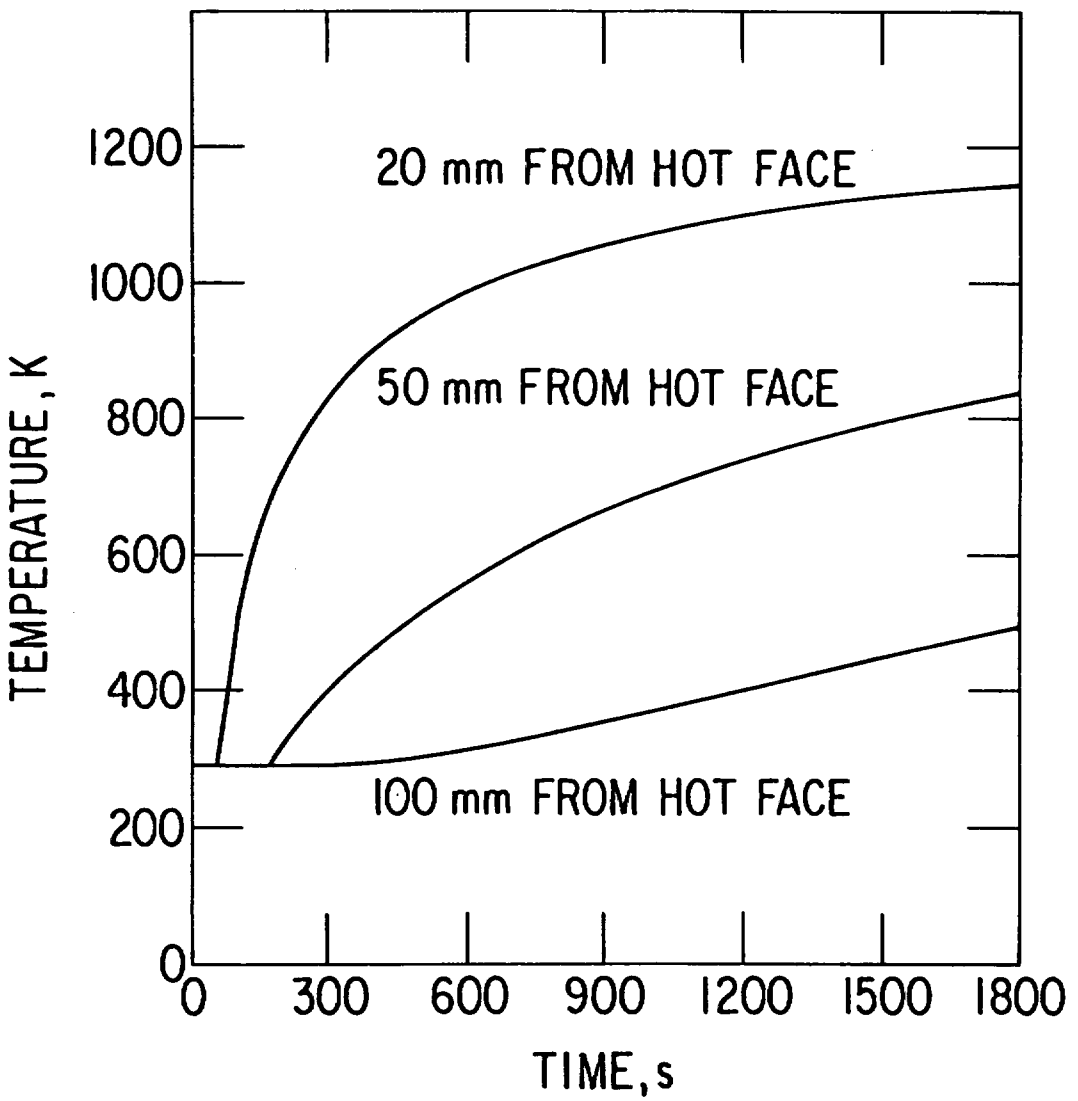

Figure 58. Temperature Rise with Time in Concrete Wall 0.3 m Thick; Constant Surface Temperatures = 1373 K, Initial Temperature = 293 K.

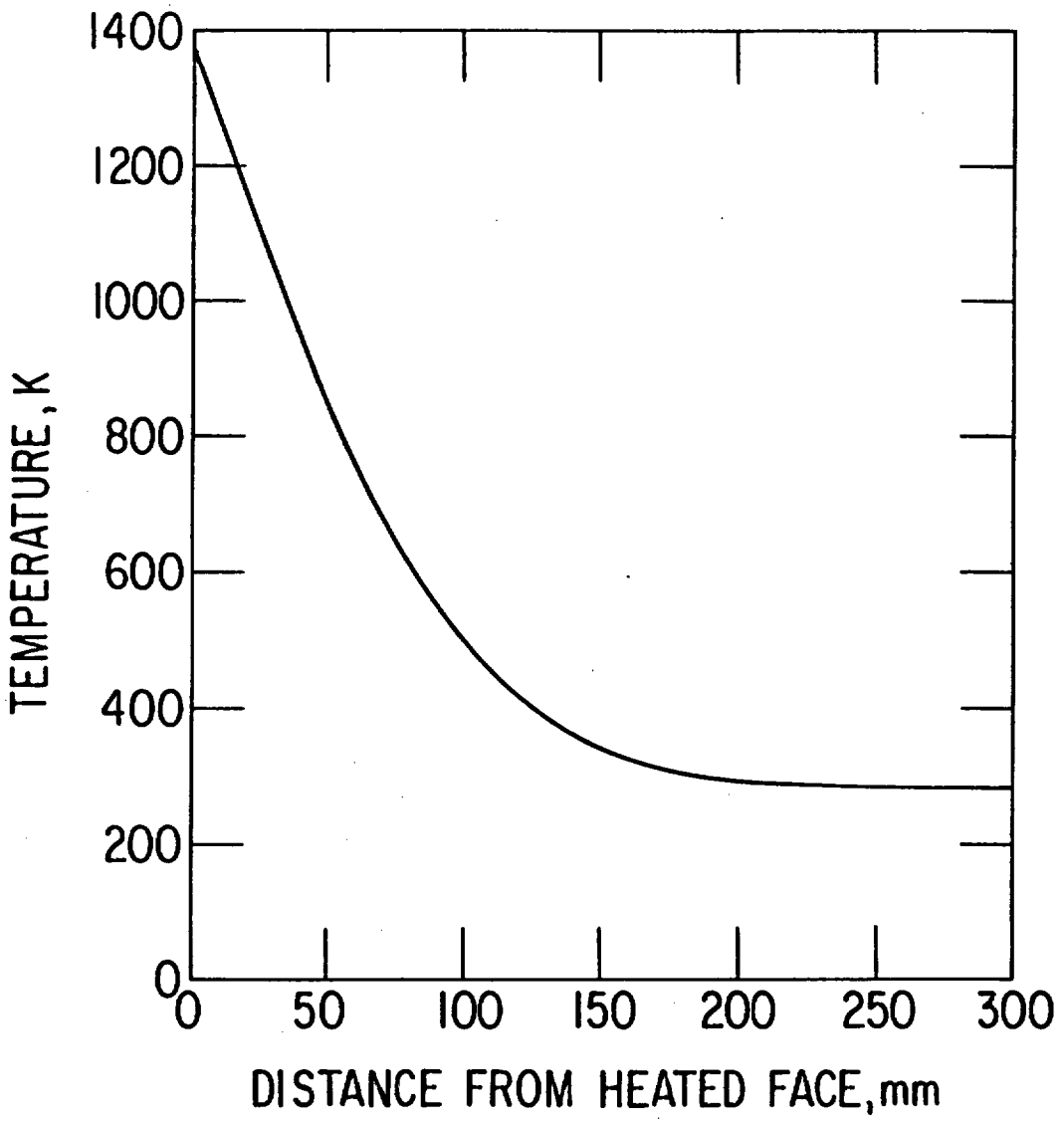

Figure 59. Temperature Variation Across 0.3 m Thick Concrete Wall at Time t=1800 s; Constant Surface Temperature = 1373 K, Initial Temperature = 293 K.

the 500°C limit is reached within 230 s. However, as pointed out earlier, the concrete cover over the reinforcement is expected to be substantially thicker than the 20 mm. Again spalling of concrete is to be expected, but considering the approximately 300 s duration of the fire (see Chapter 7), no significant structural degradation is anticipated. In general, this case is very similar, both in thermal load and structural response, to the case of high radiant heat flux.

Finally, the burning of a premixed vapor cloud on the plant site is analyzed. The temperature rise with time at various depths from the heated surface is presented in Fig. 60, and the temperature profile through the wall after one-half hour is given in Fig. 61. Again, the far face of the wall is seen to be unaffected. Similarly, the critical temperature for prestressing steel (400°C) is never reached at a depth of 100 mm or larger. The 500°C limit for reinforcing steel now obtains in 600 s at a depth of 50 mm. Thus, if fires of this duration should occur, then significant structural effects might be expected. However, this is not a likely event for a premixed cloud. Although the time between UFL and LFL may exceed the 600 s under some circumstances very slow flame motion and cloud drift, relative to the stationary site, would be required to achieve such durations. In addition, the slow cloud drift would limit the occurrence of such an event to the close proximity of the spill location. Thus this is not considered a viable scenario. Again, the spalling conditions at a depth of 50 mm are reached in a time somewhat in excess of 200 s. At shallower depth this occurs much earlier. Hence, spalling is a likely occurrence, and the remote possibility exists that a combination of spalling and heating may ultimately lead to some structural degradation. The effect of fire engulfment followed by a rapid decay of surface temperature is illustrated in Fig. 62. It is seen that at some distance from the heated surface (100 mm), the maximum temperature occurs long after the surface temperature has decayed. After a long time, the entire slab reaches an essentially uniform temperature.

Based on the foregoing, it is ascertained that concrete structures can sustain the effects of LNG fires very well. Although some spalling of concrete is to be expected, no structural degradation is in general anticipated. Even the spalling can only be significant when the heat fluxes are large, which implies on-site or near-site fires. Considering cloud drift, such effects may occur out to distances of 9-10 km from the spill source.

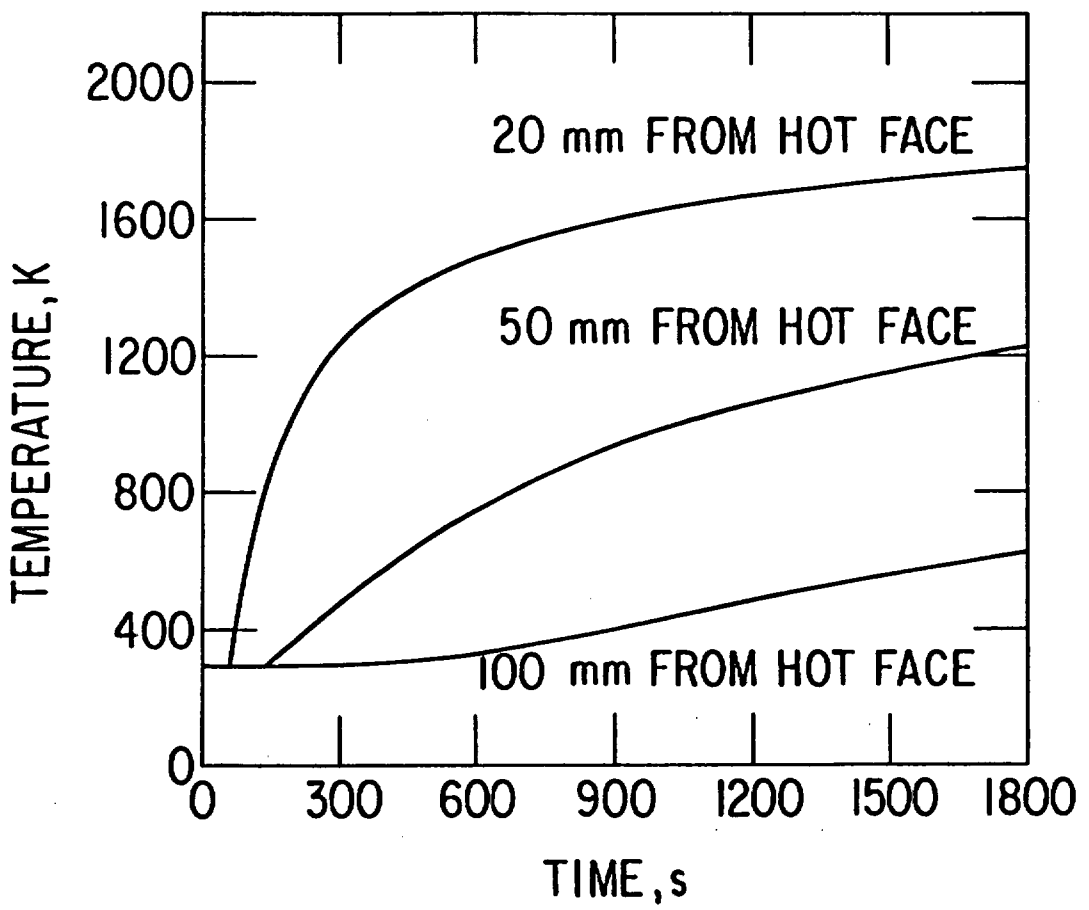

Figure 60. Temperature Rise with Time in Concrete Wall 0.3 m Thick; Constant Surface Temperature = 2148 K, Initial Temperature = 293 K.

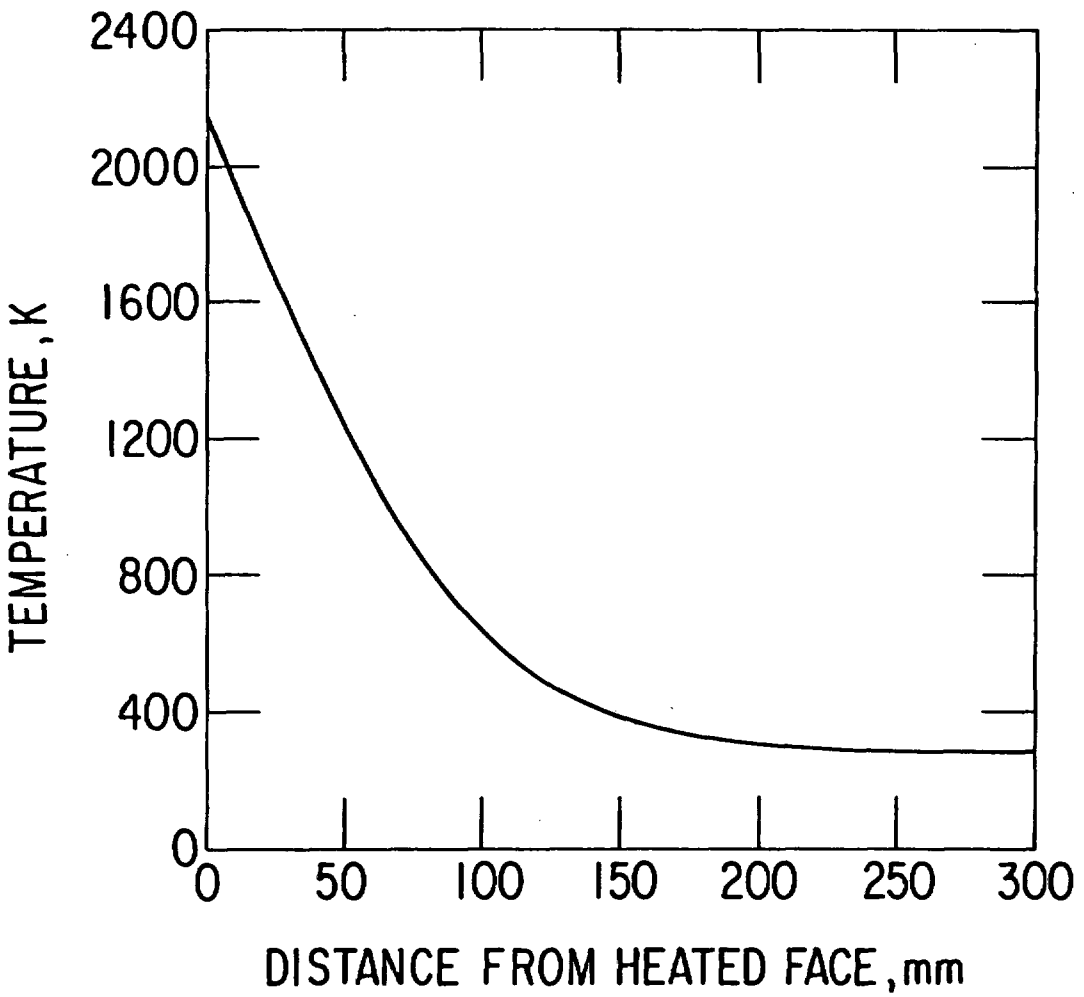

Figure 61. Temperature Variation across Concrete Wall 0.3 m Thick at Time t=1800 s; Constant Surface Temperature = 2148 K, Initial Temperature = 293K.

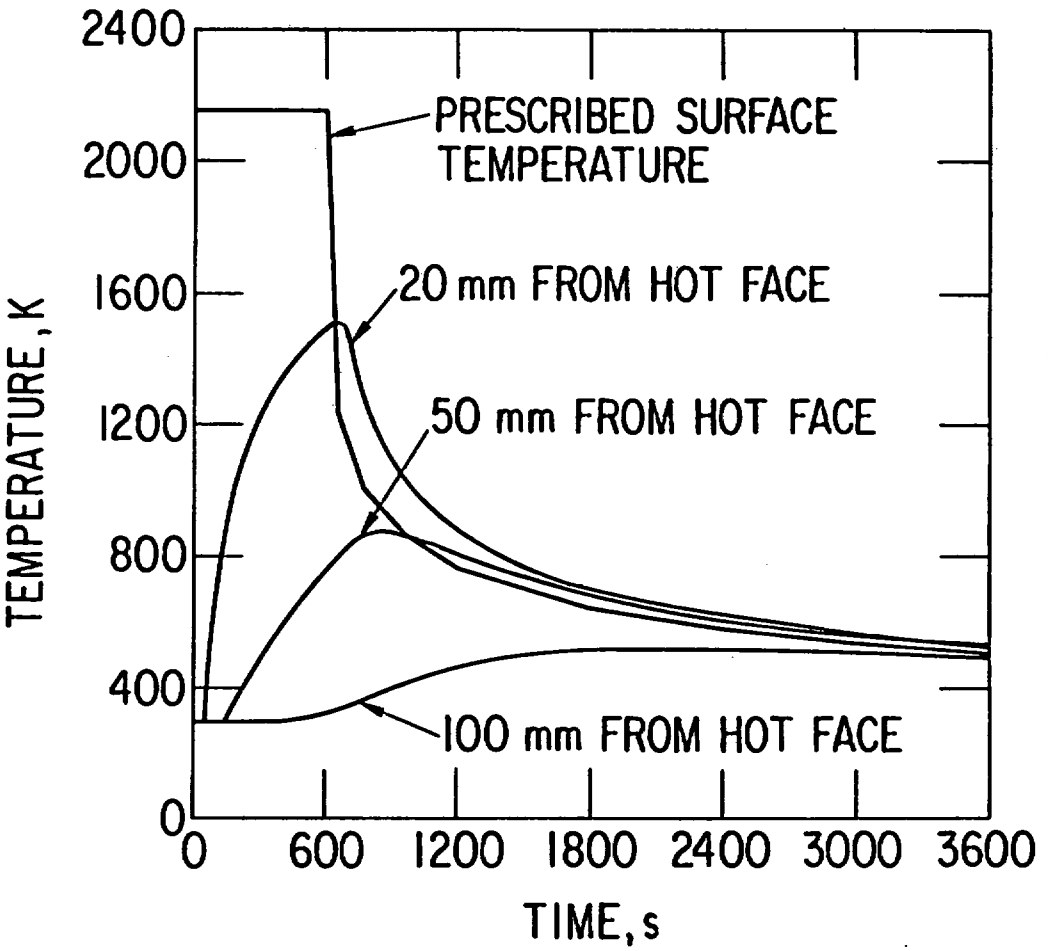

Figure 62. Temperature Rise with Time in Concrete Wall 0.3 m Thick; Initial Temperature = 293 K.

10.4 Air Blast Vulnerability

A detailed structural response analysis of the important nuclear power plant buildings subjected to air blast from an LNG vapor-cloud explosion is beyond the scope of the current effort. Therefore, the structural resistance criteria summarized in Table 12 will be used to assess the power plant vulnerability. As pointed out earlier (Chapter 9), the expected blast durations are sufficiently long to permit the employment of simple overpressure criteria. The distance to a particular overpressure level from the edge of the exploding vapor cloud is a function of cloud height (see Chapter 6), which realistically may be expected to vary from 25 to 75 m. The following estimates of distance are based on the average value of cloud height, i.e., 50 m.

Starting with the most severe blast scenario, i.e., an actual cloud detonation on the plant site that produces an overpressure of 1.45 MPa, it can readily be seen from Table 12 that all the plant structures would be extremely
vulnerable. In fact, destruction or severe damage may be expected for all buildings. The consequences of such an event are difficult to ascertain, but significant radiation release is quite probable.

A more moderate scenario is one involving volume explosions on the plant site. Again this requires the vapor cloud to drift to the site. Infiltration by the premixed LNG vapor into nearly completely confined spaces and subsequent ignition may lead to this event. The overpressure generated by a volume explosion is approximately one-half the detonation value [29], or 0.73 MPa in the present case. Again none of the plant structures are designed to withstand such an internal overpressure. Thus, severe damage would result. All structures that are not closed off from the atmosphere, are susceptible to such an event. Since LNG vapor, even in the premixed state, is heavier than air, infiltration by gravity into any opening engulfed by the cloud is to be expected. The containment is generally closed to the atmosphere and is therefore not a likely candidate for such an event. The most vulnerable structures appear to be concrete block houses used for the protection of diesel fuel and condensate water tanks against the effects of tornados. The intake structure could also be affected in this manner, as well as areas of the auxiliary building, e.g., battery rooms if not closed off or positively ventilated. The only mitigating circumstance is the fact that some plant openings may not be reached by the vapor mixture because of the limited cloud height. Both of the described events, i.e., on-site detonations and volume explosions, require LNG vapor cloud drift to the site location. Under strong wind

conditions (8.96 m/s), it is estimated that the farthest distance from the location of spill at which these events can occur is about 9.5 km.

The effects from a volume explosion could serve as the initiation source for a general vapor-cloud explosion, thus involving additional structures. Another secondary effect of consequence could be the debris problem. Although debris is generated whenever blast pressure results in significant structural damage, the problem could be particularly severe for volume explosions. The reason for this is that in such an event, rather substantial concrete structures may
be blown apart, resulting in very massive high-velocity missiles. The impact of such missiles may lead to secondary damage of important safety-related components and structures. Particularly vulnerable appear to be exposed pipe lines and electrical equipment, such as distribution stations and off-site power installations.

The maximum overpressure level to which reinforced concrete containment buildings can be exposed without sustaining significant damage is estimated at 0.345 MPa (see Table 12). For substantial reinforced concrete structures, such as the auxiliary building, the corresponding overpressure level is 0.207 MPa. The distances from the cloud edge to these overpressure levels are, respectively, 2.5 and 4.0 cloud-height units or 125 and 200 m. Since the maximum cloud drift is 9.8 km (see Table 8), the maximum distance from the spill source can, for both thresholds, be taken as about 10 km. Any substantial damage to the concrete structures, and particularly to the containment building, would indeed be serious.

Moderate damage to heavy industrial-type structures, of which the turbine building may be representative, is estimated to occur at overpressures of about 0.083 MPa (see Table 12). Such overpressure levels can occur at distances of 450 m (9 cloud-height units) from the edge of the exploding vapor cloud. Accounting for cloud drift, the maximum distance from the spill source is 10.3 km. Although damage to such buildings by itself may not constitute a safety hazard, it is again possible to envision secondary effects, caused by debris or other actions, which may result in such a hazard. In this category would be any disruption of the cooling system. Since main steam lines often run exposed through the turbine building, such a possibility cannot be excluded.

A similar possibility exists at even lower overpressures such as 0.048 MPa (see Table 12), when main coolant lines (feedwater and stem) run exposed between buildings as is the case in some older existing plants. This overpressure persists at a distance from the cloud edge of 850 m (17 cloud-

height units) or including cloud drift about 10.7 km from the spill source.

A loss-of-coolant accident is always considered a grave matter, but may be particularly dangerous when coupled with failures of other vital equipment. For air blast overpressure, this may indeed be the case, because electrical power systems may sustain damage of overpresures as low as 0.035 MPa (see Table 12). The vulnerable items are substations, switchyards, and high-voltage lines, the damage of which can result in the loss of off-site power. Since the off-site power supply is more susceptible to blast than large piping runs or the turbine building, failure of power supply should be expected when the latter items sustain damage. The distance from the cloud edge at which electrical systems may be damaged is estimated at 1100 mm (22 cloud-height units). Including cloud drift the maximum distance from the spill source for such an event is 10.9 km.

Damage to other buildings, systems, and components can result at still lower blast overpressures (see Table 12). The loss or damage of none of these items, however, appears to pose a direct or indirect threat to the safety of the power plant. The dynamic pressures, and hence, drag forces at these pressure levels, i.e., 0.035 MPa or below, are comparable with those resulting from the design tornado [62]. Hence, at these overpressures, the expected damage to power plant structures should be equivalent to that resulting from a toranado.

As with plant personnel, some potential for damage exists due to the propagation of pressure waves into the interior of the plant via a breached ventilation system, access hatch, or door. The overpressure levels for breaching to occur and the resulting damage are so design-dependent that it is not possible to make any meaningful generic vulnerability estimates. The purpose of it being mentioned here is simply to indicate that this problem must be considered and to point out that approaches and methodologies exist [63,64] to make reasonable predictions of the blast-wave propagation into the plant interior in specific cases.

10.5 Summary of Vulnerabilities

Only a limited number of hazardous effects arising from a large LNG spill on water were considered in the generic vulnerability analysis of the preceding sections. Many other vulnerabilities can probably be identified for individual power plants. This, however, requires the consideration of specific plant design and siting details and will not be pursued here.

One additional generic question that may be asked is how well a typical

plant can cope with the overall thermal-loading incident on the plant or a specific building. That this is a legitimate question can be readily seen by comparing the cooling or heat-rejection capability provided in a typical containment cooling (air-conditioning) system with the heat received by the building from a severe fire. For typical modern PWR designs, the maximum instantaneous containment cooling is about 7×10^4 kW [38]. On the other hand, the instantaneous heat load on the building, when engulfed by a massive LNG fire, can readily be 200 kW/m^2, or for typical containment building dimensions (diameter 30 m, height 50 m), a total load of about 10^6 kW. Thus the ratio of the instantaneous heat load to the cooling capacity is nearly 15.1. It was shown earlier that the durations of intense LNG fires are rather short, say 600 s. Assuming an average concrete wall thickness of 0.75 m for the containment building, we find that, even neglecting all heat losses, the building possesses sufficient heat capacity to limit the average temperature rise in the wall to less than 85°C. This is an acceptable value, and hence it is thought that no significant hazard arises from the overall heating of concrete buildings, which house most of the critical systems of a modern nuclear power plant.

To facilitate an overall evaluation of nuclear power plant vulnerability, Table 13 summarizes the important generic hazards due to an LNG spill on water. The hazards are listed together with their threshold vulnerability distances, i.e., the maximum distances from the spill source at which a plant may be vulnerable to a particular effect. Items marked with an asterisk are considered to constitute a direct safety hazard. Essentially all these items pertain to blast effects on the power plant. Thus, if LNG vapor cloud explosions are possible and occur in the vicinity of a nuclear power plant, then the safety of the plant may be endangered.

On the other hand, the effects produced by fire and thermal loading on the nuclear power plant seem, in general, to be tolerable. Although specific safety-related components might be affected, the plant's backup and engineered safety system should permit a safe shutdown and subsequent heat removal. The major reason for this limited effect of thermal loads is the short duration of the expected fires. Heat loads similar in magnitude to those produced by the LNG fire, but of much longer duration, could not be tolerated as well.

The data in Table 13 establishes also another very important point; namely, the vulnerability threshold distances for all the considered hazards are approximately the same. Using a single value of about 10.0 km for all of them would result in very little error, at least for the most severe effects. The reason for this is twofold. First, the thermal and blast

TABLE 13

SUMMARY OF NUCLEAR POWER PLANT VULNERABILITY

Plant System, Threat and Effect (Comment)	Standoff Distance, km
Personnel	
Exposed - Fire - Skin Burns (4 kw/m^2)	13.0
Exposed - Air Blast (.0345 MPa)	11.0
Protected - Air Blast (.2069 MPa)	10.0*
Ignition	
All combustibles including electric insulation	11.0
Thermal Loads	
Ceramic insulators (100 kw/m^2)	10.0
Steel Structures - Not engulfed (100 kw/m^2)	10.0
Steel Structures - Engulfed (40 mm thickness safe)	9.0
Concrete Structures - Not engulfed (200 kw/m^2; 360 s)	10.0
Concrete Structures - Engulfed (300 s safe, no spalling)	9.0
Air Blast	
Detonation on Site (1.45 MPa - Severe Damage all Structures)	9.5*
Volume Detonation (Severe Damage-Concrete Bunkers)	9.5*
Containment Building (.3448 MPa)	10.0*
Concrete Structures (.2069 MPa)	10.1*
Heavy Industrial Structures (.0828 MPa)	10.3*
Exposed Piping Systems (.0483 MPa)	10.7*
Electrical Equipment (.0345 MPa)	11.0*

*Direct Effect on Safety System

effects are only severe enough to affect the plant in the close vicinity of the fire/explosion source, i.e., at distances of about 12.0 km from the edge of the LNG vapor cloud. Second, the overall vulnerability threshold distance (maximum distance from spill source) is dominated by the LNG vapor cloud drift. The cloud drift distance represents, in general, 90% or more of the total distance.

On the basis of Table 13 and the foregoing analysis, it is also observed that, among the safety-related plant systems, exposed electrical equipment and specifically off-site power appears to be most vulnerable to the LNG spill hazards. Ignition of cable insulation, failure of ceramic insulators, and damage by relatively low overpressure blast waves are considered here. Other damage mechanisms seem also plausible, e.g., overheating and subsequent failure of oil-filled transformers. From a safety point of view, off-site power is primarily important for long-term decay heat removal. As mentioned earlier, the failure of off-site power alone does not constitute a direct safety hazard. However, in combination with other failures, e.g., emergency power diesel failures or loss of all diesel fuels, the loss of off-site power, for any extended period of time, may result in a grave situation.

11. Discussion, Conclusions, and Recommendations

The analysis outlined in Chapters 3-6 of this report permits an overall description of the phenomena associated with a large spill of LNG on water. The models are based on simple engineering analysis and rely on a global approach to arrive at a reasonable definition of a complex process. Although the limitations of the models are recognized, it is believed that the most salient features of the problem have been included. Sensitivity studies were used to establish the importance of various parameters.

One major achievement of this effort was the development of a combined LNG spill, spreading, and fire model. This approach permits the simultaneous and coupled computation of all the major aspects of an LNG fire. A tool is thus available to carry out detailed analyses of the fire threat for any postulated scenario and specific power plant arrangements and sites.

Another very important result of the analysis effort is the development of an approach for the prediction of air blast in the vicinity of an exploding "pancake-like" vapor cloud (Chapter 6). The method has its shortcomings in that it is not a unified procedure and depends on both simplified analytical calculations and the use of two-dimensional hydrocodes. However, the obtained results are scalable with cloud height and therefore are applicable to a broad class of problems. Although the limitations of the procedure are recognized, it is believed that the predictions are a much better approximation of the air blast field in the vicinity of the vapor cloud than those from the normally employed TNT equivalency concept, which is based on a hemispherical vapor cloud-shape assumption.

In carrying out the effects and vulnerability analysis (Chapter 10), we use simple susceptibility criteria for the various plant systems and components. Also, the analysis itself is much less detailed than the descritpion of the LNG spill environment. This approach was taken because of limitations on the program effort and also because detailed response analyses are thought to be more appropriate for site specific studies. Most of the blast-response vulnerabilities are established by comparing overpressure criteria for various plant systems with the blast environment. Simple calculations are carried out to define the thermal response.

Based on this analysis, it is found that the thermal loads resulting from a large LNG fire on water can in general be tolerated by the important safety-related plant systems. This is primarily due to the short durations of the expected fires. On the other hand, it is shown that nuclear power plant

systems are very vulnerable to blast effects from an exploding LNG vapor cloud. It is also concluded that all serious effects are limited to the immediate vicinity of the fire/explosion source, i.e., the LNG vapor cloud. Because of this, the standoff distance, i.e., the distance from the LNG spill location, which is required to ensure complete safety of the important nuclear power plant systems, is primarily dependent on the wind-induced vapor-cloud drift. For most of the severe hazardous effects and under the assumption of a strong wind (8.96 m/s = 20 mph), the required standoff distance in the downwind direction is found to be somewhat in excess of 10 km.

The results of the vulnerability analysis are all based on the predictions of the models that describe the LNG spill environment. To gain some confidence as to the correctness of the results, verification of these models is required. This would best be accomplished by comparison with experimental data. Although some small-scale tests of LNG spills on water have been conducted [6,9,10], the data is either inadequate or not documented well enough to provide the needed verification. The validity of scaling this information to the large LNG spill is also questionable. The other approach to verification, of the methods used here, is by comparison with much more detailed analytical and computational procedures. One such comparison with an elaborate computer code [8] has been carried out and found acceptable. However, much more is required to obtain true verification of the employed methodologies. Because of their dominant importance in defining plant vulnerability, two aspects in particular deserve precise scrutiny. These are: (i) the wind-drift predictions for the LNG vapor clouds and (ii) the assumption of LNG detonability (explosion).

Nuclear power plants are only affected by the hazards from an LNG spill when the vapor cloud is directly on the plant site or immediately adjacent to it. This suggests that safety measures may be taken to mitigate at least some of the hazardous effects. Since nuclear power plants are not likely to be located in the immediate area of the LNG spill source, it should be possible to institute a warning system that will make the operating personnel aware of the impending danger. This in turn will permit some mitigating actions.

Actions that come to mind are plant isolation and elimination of possible ignition sources. The first of these would involve the closing of all dampers, hatches, doors, etc., to prevent the ingress of combustible mixtures into the plant interior. Shutdown of the plant and the deenergizing of all unnecessary power sources, such as electrical equipment

and diesel engines will remove many of the possible ignition sources, thus reducing the hazards further. Isolation of the plant from the exterior should be quite effective against fire hazards. However, with current plant designs it is not believed that isolation will prevent the propagation of air blast pressure waves into the plant interior, e.g., via ventilation shafts.Effective isolation against air blast can only be provided by blast-hardening of the structures and components, as in military protective design. Although this approach does not appear practical for the entire plant complex, it may be applicable to selected plant systems.

As pointed out earlier, the most vulnerable safety-related system at a typical plant site appears to be the off-site power supply. It therefore is a prime canditate for blast hardening, e.g., by providing a completely underground power supply to the plant. Multiple redundancy of safety systems is another approach to reducing nuclear power plant vulnerability. Finally, the best protection is provided by sufficient standoff distance from the LNG spill source. Based on the current analysis result, this distance is in excess of 10 km and may not always be achievable for specific plant sites.

It should also be remembered, that the conclusions of the current study are based on a purely deterministic analysis. Thus worst-case assumptions are often made, and no consideration is given to the likelihood of the occurrence of an event. In applications to actual power plants, probability considerations must be included, in particular when a preliminary evaluation of the effects indicates significant hazard levels. In many cases, the stochastic analysis may indicate that the risks are still acceptable.

The methodology and results of the current study represent a significant improvement in the treatment of the hazard problem arising from large LNG spills on water. The method can be readily adapted to the analysis of hazards in specific cases. It is particularly valuable as a rapid and inexpensive screening procedure when many possible spill scenarios and environmental conditions must be considered. Coupled with probability analysis, it can become a valuable tool in assessing the risks to nuclear power plants arising from large LNG spills on water transportation routes. Verification of the results in specific cases can be obtained by comparing some aspects of the predictions with more detailed and precise deterministic procedures; e.g., cloud development and drift can be compared with the results of precise hydrocode calculations.

The main improvement in the accuracy of the prediction for specific cases can be achieved by introducing more elaborate and detailed structural and

thermal-response analysis. This can be readily achieved with existing procedures and computer codes. Improvements in the descrption of the LNG spill environment can also be introduced. Further sensitivity and parameter studies may provide a better definition of the various problem constants used in the analysis. It is also believed that the methods are readily adaptable to treating the influence of solid boundaries, such as shore lines, on the development of the LNG pool, vapor cloud, and fire scenario. Finally the methods developed here for the treatment of LNG spills on water can be extended to land spills and may also be used to analyze spills of other hazardous materials. Specifically any material whose spill results in the formation of negatively buoyant vapor clouds may be treated by the approach used here for LNG.

REFERENCES

1. Germeles, A. E., and Drake, E. E., "Gravity Spreading and Atmospheric Dispersion of LNG Vapor Clouds," Proceedings of the Fourth International Symposium on Transport of Hazardous Cargoes at Sea and Inland Watterways. Jacksonville, FL, October 25-30, 1975, NTIS No. AD/A023505, pp. 519-539, Oct. 1975.

2. Fay, J. A., "Unusual Fire Hazards Tanker Spills," Combustion Science and Technology, Vol 7, pp. 77-79, 1973.

3. Department of Energy, "Liquified Gaseous Fuels Safety and Environmental Control Assessment Program: Second Status Report," DOE/EV-0085, Oct. 1980.

4. Cookhill, M., "LNG Shipping: Past, Present and Future Directions," Proceedings of the Sixth International Conference on Liquified Natural Gas, Session III, paper 1, Kyoto, Japan, Apr. 7-10, 1980.

5. American Gas Association, LNG Fact Book, Planning and Analysis Group, AGA, Arlington, VA, 1977.

6. Parnarouskis, M. C., Taylor, M. W., Lind, C. D., Raj, P. P. K., and Cece, J. M., "Vapor Cloud Explosion Study," Proceedings of the Sixth International Conference on Liquified Natural Gas, Session III, paper 12, Kyoto, Japan, Apr. 7-10, 1980.

7. Moen, I. O., Donato, M., Knystantas, R., and Lee, J. H., "Flame Acceleratin Due to Turbulance Produced by Obstacles," Combustion and Flame, 1980.

8. Havens, J. W., "A Description and Assessment of the SIGMET LNG Vapor Dispersion Model," U. S. Coast Guard Report CG-M-3-79, Feb. 1979.

9. Feldbauer, G. F., Heigl, J. J., McQueen, W., Whipp, R. H., and May, W. G., "Spills of LNG on Water-Vaporization and Downwind Drift of Combustible Mixtures," Esso Engineering and Research Company, Report No. EE61E-72, May 24, 1972.

10. Boyle, G. J., and Kneebone, A., "Laboratory Investigation into the Characteristics on LNG Spills on Water, Evaporation, Spreading and Vapor Dispersion," Shell Research Ltd., Report to the API Projection LNG Spills on Water, Ref. 6A32, March 1973.

11. Havens, J. A., "Predictability of LNG Vapor Dispersion from Catastrophic Spills on Water: An Assessment," U. S. Coast Guard Report CG-M-09-77, NTIS AD/A-040525, Apr. 1977..

12. Yih, C. S., Dynamics of Nonhomogeneous Fluids, MacMillan Co., New York, 1965.

13. Houghton, E. L. and Carruthers, Wind Forces on Buildings and Structures: An Introduction, John Wiley & Sons, New York, 1976.

14. Parker, R. O., and Spata, J. K., "Downwind Travel of Vapor from Large Pools of Cryogenic Liquids," paper presented at LNG-1 Conference, Chicago, IL, 1968.

15. Schneider, A. L., "Liquified Natural Gas Research Overview," U. S. Coast Guard Report No. CG-M-01-09, Dec. 12, 1978.

16. Raj, P., and Atallah, S., "Thermal Radiation from LNG Spill Fires," Conference on Advances in Cryogenic Engineering, Georgia Insitute of Technology, August 1973.

17. Thomas, P. H., "The Size of Flames from Natural Fires," Proceedings of the Ninth International Symposium on Combustion, pp. 844-859, 1962.

18. Lind, C. D. and Whitson, J. S., "China Lake Spill Tests," Report L, An Approach to Liquified Natural Gas (LNG) Safety and Environmental Control Research, U. S. Department of Energy, DOE/EV-0002, Feb. 1978.

19. Welker, J. R. and Sliepcevich, C. M., "Bending of Wind-Blown Flames from Liquid Pools," Fire Technology, vol. 2, no. 2, May 1966.

20. Raj, P. K., "Calculations of the Thermal Radiation Hazards from LNG Fires - A Review of the State-of-the-Art," Paper No. 2, Session 18, AGA Transmission Conference, St. Louis, MO, May 1977.

21. Stewart, F. R., "Prediction of the Height of Turbulent Diffusion Buoyant Flames," Combustion Science and Technology, vol. 2, pp. 203-212, 1970.

22. Lind, C. D. and Whitson, J. C., "Explosion Hazards Associated with Spills of Large Quantities of Hazardous Materials," Phase III, U. S. Coast Guard Report No. CG-D-85-77, Nov. 1977.

23. Boni, A. A., Wilson, C. W., Chapman, M., and Cook, J. L., "A Study of Detonation in Methane/Air Clouds," Acta Astronautica, vol. 5, no. 11/12, pp. 1153-1169, 1978.

24. Kurylo, J., Dwyer, H. A., and Oppenheim, A. K., "Numerical Analysis of Flow Field Generated by Accelerating Flames," AIAA Journal, vol. 18, no. 3, pp. 302-308, March 1980.

25. Kuhl, A. L., Kamel, M. M., and Oppenheim, A. K., "Pressure Waves Generated by Steady Flames," Proceedings of the 14th Symposium (International) on Combustion, The Combustion Institute, Pittsburgh, PA, pp. 1201-1215, 1973.

26. Strehlow, R. A., "Unconfined Vapor Cloud Explosions - An Overview," Proceedings of the 14th Symposium (International) on Combustion, The Combustion Institute, Pittsburgh, PA, pp. 1189-1200, 1973.

27. Shapiro, A. H., The Dynamics and Thermodynamics of Compressible Fluid Flow, Vol. I, The Ronald Press Company, New York, 1954.

28. Eichler, T. V., and Wiedermann, A. H., "Review of Quantity Distance Protection - Blast Wave Diffraction Over Barricades," IIT Research Institute, Final Report, Phase IIA, Project J6194J05, Oct. 1970.

29. Eichler, T. V. and Napadensky, H. S., "Accidental Vapor Phase Explosion on Transportation Routes Near Nuclear Power Plant," NUREG/CR-0075, Apr. 1977.

30. Eckhoff, R. K., Fuhre, K., Krest, O., Guiro, C. M., and Lee, J. H. S., "Some Recent Large Scale Gas Explosion Experiments in Norway," Chr. Michelsen's Institutt, Norway, Report CMI No. 790750-1, Jan. 20, 1980.

31. Kalelkav, A. S. and Everett, J. L., "Fire Ingestion Risks Due to Massive Spills Resulting in Flammable Chemicals at Water Intakes of Power Plants," Paper presented at ASCE Conference on Probabilistic Methods in Engineering, Stanford University, Stanford, CA, 23-25 June 1974.

32. Dausch, A. H., Eisenberg, N. A., and Lynch, C. J., "Continuing Development of the Vulnerability Model," Enviro Control, Inc., Report No. CG-D-53-77, Feb. 1977.

33. Harmathy, T. Z., "Design to Cope with Fully Developed Fires," Design of Buildings for Fire Safety, ASTM STP 685, E. E. Smith and T. Z. Harmathy, Eds., American Society for Testing of Materials, pp. 198-276, 1979.

34. U. S. Nuclear Regulatory Commission, "Evaluations of Explosions Postulated to Occur on Transportation Routes Near Nuclear Power Plants," Regulatory Guide 1.91, Revision 1, Feb. 1978.

35. Glasstone, S., and Dolan, P. J. (Editors), The Effects of Nuclear Weapons, U. S. Department of Defense and U. S. Department of Energy, 1977.

36. U. S. Department of Energy, "Nuclear Reactors Built, Being Built or Planned in the United States, as of Dec. 31, 1979," TID-8200-R40, 1979.

37. U. S. Nuclear Regulatory Commission, "Reactor Safety Study: An Assessment of Accident Risks in U. S. Commercial Nuclear Power Plants," NRC Report WASH-1400 (NUREG-75/014) NTIS, Oct. 1975.

38. Baltimore Gas and Electric Company, "Calvert Cliffs Nuclear Power Plant - Units 1 and 2, Final Safety Analysis Report," Jan. 1971.

39. Eisenberg, N. A., Lynch, C. L., and Breeding, R. J., "Vulnerability Model: A Simulation System for Assessing Damage Resulting from Marine Spills," Enviro Control, Inc., Report No. CG-D-137-75, AD/A-015-245, June 1975.

40. Baker, W. E., Cox, P. A., Westine, P. S., Kulesz, J. J., and Strehlow, R. A., "A Short Course on Explosion Hazards Evaluation," Southwest Research Institute, San Cantonio, Texas, 1979.

41. U. S. Department of Transportation, "Liquified Natural Gas Facilities; Federal Safety Standards; Final Rule and Proposed Rule Making," 49 CFR Part 193, [Docket-OPSO-46], Federal Register, vol. no. 29, pp. 9183-9237, Feb. 11, 1980.

42. Baltimore Gas and Electric Company, "Investigations and Literature Survey to Establish the Hazard Implications of LNG Spills at the Columbia LNG Corporation Receiving Terminal at Cove Point, MD, on the Calvert Cliffs Nuclear Power Plants," Wesson & Associates, Inc., Norman, OK, March 12, 1976.

43. Baltimore Gas and Electric Company, "LNG Contingency Plan," Calvert Cliffs Nuclear Power Plant, Docket Nos. 50-317 and 50-318, Sept. 11, 1978.

44. Biggs, J. M., Introduction to Structural Dynamics, McGraw-Hill Book Company, New York, NY, 1964.

45. Kiciman, Ö. K., "Finite Element Analysis of Reactor Containments under Blast Loading," Transactions of the 5th International Conference on Structural Mechanics in Reactor Technology, Vol J, paper no. J10/6, Berlin, Germany, 13-17 Aug. 1979.

46. American Iron and Steel Institute, Fire-Safe Structural Steel, A Design Guide, AISI, Washington, DC, 1979.

47. "Guides to Good Practice - FIP/CEB Recommendations for the Design of Reinforced and Prestressed Structural Members for Fire Resistance," Cement and Concrete Association, Wexham Springs, England, June 1975.

48. Allen, D. E., and Lie. T. T., "Fire Resistance of Reinforced Concrete Columns and Walls," National Research Council Canada, DBR Paper No. 784, NRCC 16818, from Proceedings of the Canadian Structural Concrete Conference, Ottawa, Canada, June 1977.

49. Gustaferro, A. H., "Temperature Criteria at Failure," Fire Test Performance, American Society for Testing and Materials, ASTM STP 464, pp. 68-84, 1970.

50. Lawson, D. I., and Simms, D. L., "The Ignition of Wood by Radiation," British Journal of Applied Physics, vol. 3, pp. 288-292.

51. Hallman, J. R., Welker, J. R., and Sliepcevich, C. M., "Ignition of Polymers," SPE Journal, vol. 28, pp. 43-47, Sept. 1972.

52. Hallman, J. R., Welker, J. R., and Sliepcevich, C. M., "Ignition Times for Polymers," Polymer Plastics Technology and Engineering, vol. 6, no. 1, pp. 1-56, 1976.

53. Carslow, H. S., and Jaeger, J. C.,- Conduction of Heat in Solids, 2nd edition, Oxford Press, 1959.

54. Kingery, W. D., "Factors Affecting the Thermal Stress Resistance of Cermic Materials," Journal of the American Ceramic Society, vol. 38, no. 1, pp. 3-15, Jan. 1955.

55. Hasselman, D. P. H., "Unified Theory of Thermal Shock Fracture Initiation and Crack Propagation in Brittle Ceramics," Journal of the American Ceramic Society, vol. 52, no. 11, pp. 600-604, Nov. 1969.

56. Hasselman, D. P. H., "Thermal Stress Resistance Parameters for Brittle Refractory Ceramics: A Compendium," Ceramic Bulletin, vol. 49, no. 12, pp. 1033-1037, Dec. 1970.

57. Timoshenko, S., and Goodier, J. N., Theory of Elasticity, McGraw-Hill Book Company, New York, NY, 1951.

58. Jakob, M., Heat Transfer, vol. I, John Wiley & Sons, Inc., New York, NY, 1949.

59. Hanford Engineering Development Laboratory, Nuclear Systems Materials Handbook, vol. 1 - Design Data, TID 26666 Revision 3, 1 Sept. 1978.

60. Southern Services, Inc. - Engineering Computer Applications, Computer Program HEATING II, Program No. EN8705SS, May 1975.

61. Swatosh, J. J. Jr., Anderson, D., Eichler, T. V., and Wiedermann, A. H., "Nuclear Weapons Effects: Dust and Air Temperature Environment," IIT Research Institute, Final Technical Report for Office of the Chief of Engineers, U. S. Department of the Army, Construction Engineering Research Laboratory Technical Manuscript S-2R, Feb. 1971.

62. U. S. Atomic Energy Commission, "Design Basis Tornado for Nuclear Power Plants," Regulatory Guide 1.76, 1974.

63. Kot, C. A. et al., "Air Blast Attenuation," IIT Research Institute, Final Technical Report for the Office of the Chief of Engineers, U. S. Department of the Army, Construction Engineering Research Laboratory Technical Manuscript S-1R, Feb. 1971.

64. Kriebel, A. R., "Airblast in Tunnels and Chambers," URS Research Company, Final Report URS 7050-2 for Defense Nuclear Agency, DASA 1200-II, Supplement 1, Oct. 1972.

APPENDICES

The appendices of this report contain the detailed phenomenological studies which lead to the development of global models describing all aspects of a large LNG spill on water. Since these models have been amply outlined in Chapters 3, 4, 5 and 6 and because of the large volume of the detailed material, the appendices are here included in microfiche form.

The studies presented in the appendices were conducted for Argonne National Laboratory (ANL) by the IIT Research Institute (IITRI) Chicago, Illinois. Each of the appendices addresses different aspects of the LNG spill phenomenology and corresponds to an IITRI Technical report submitted to ANL as follows:

Appendix A

T. V. Eichler, A. H. Wiederman, R. Pape, "Study of Liquid Natural Gas (LNG) Spill Phenomenology on Water," IITRI Final Report J6456, December 1978, Revised May 1979.

Appendix B

T. V. Eichler, A. H. Wiedermann, R. Pape, "Study of Liquid Natural Gas (LNG) Spill, Dispersion, and Combustion Phenomenology," IITRI Final Report J6481, May 1980.

Appendix C

T. V. Eichler, A. H. Wiedermann, R. Pape, "Study of Explosions and Fast Deflagrations of LNG Vapor," IITRI Final Report J6517, September 1980.

Distribution for NUREG/CR-2490 (ANL-CT-81-17)

Internal:

E. S. Beckjord
C. E. Till
R. S. Zeno
G. S. Rosenberg
M. G. Srinivasan (2)
H. C. Lin
J. B. van Erp
C. A. Kot (35)
ANL Patent Dept.
ANL Contract File
ANL Libraries (2)
TIS Files (3)

External:

NRC, for distribution per RI and XA (220)
DOE-TIC (2)
Manager, Chicago Operations Office, DOE
President, Argonne Universities Association, Argonne, Ill.
Components Technology Division Review Committee:
A. Bishop, U. Pittsburgh, Pittsburgh, Pa. 15261
F. W. Buckman, Consumers Power Co., 1945 Parnall Rd., Jackson, Mich. 49201
R. A. Greenkorn, Purdue U., West Lafayette, Ind. 47907
W. M. Jacobi, Westinghouse Electric Corp., P. O. Box 355, Pittsburgh, Pa. 15230
M. A. Schultz, 124 Lakeshore Drive, North Palm Beach, Fla. 33408
E. E. Ungar, Bolt, Beranek and Newman, Inc., 50 Moulton St., Cambridge, Mass. 02138
J. Weisman, U. Cincinnati, Cincinnati, O. 45221
R. M. Bernero, Div. Risk Analysis, USNRC, Washington (50)